Effective Mass and Valence-band Structure in $Ga_xIn_{1-x}As/InP$ and $Ga_xIn_{1-x}P/AlGaInP$ Quantum Wells

Von der Fakultät Physik der Universität Stuttgart

zur Erlangung der Würde eines Doktors der Naturwissenschaften (Dr. rer. nat.) genehmigte Abhandlung

vorgelegt von

Jun Shao

geboren in Jiangsu, China

Hauptberichter :	Prof. Dr. M. H. Pilkuhn
Mitberichter :	Prof. Dr. G. Denninger
Tag der Einreichung :	04. Dezember 2001
Tag der mündlichen Prüfung :	30. Januar 2002

4. Physikalisches Institut der Universität Stuttgart
2002

Contents

Effective Mass and Valence-band Structure in $Ga_xIn_{1-x}As/InP$ and $Ga_xIn_{1-x}P/AlGaInP$ Quantum Wells

Zusammenfassung

Im letzten Jahrzehnt waren bei der Realisierung und industriellen Herstellung optoelektronischer Bauelemente wie z.B. von Halbleiterlasern und Modulatoren GaInAs/InP-Quantenfilmsysteme von großer Bedeutung. Zur gezielten Optimierung dieser optoelektronischen Strukturen ist die Kenntnis von Bandstrukturparametern wie der effektiven Masse und der Exzitonenbindungsenergie vonnöten. Deshalb besteht seit einigen Jahren ein besonderes Interesse an der Bestimmung eben dieser Parameter [1–7]. Trotz der Einfachheit ihres experimentellen Aufbaus stellt die Magnetoabsorption eine äußerst wichtige und vielseitige Methode zur Vermessung der Bandstruktur nahe des Zentrums der Brillouin-Zone dar. In druckverspannten und unverspannten Quantenfilmen waren die Exzitonenbindungsenergie sowie die reduzierte *in-plane* (in der Wachstumsebene) effektive Masse des Exzitonengrundzustands bereits mit guter Genauigkeit bestimmt worden [6]. Im Falle von zugverspannten Quantenfilmsystemen lieferten Absorptionsmessungen jedoch wegen zu breiter und schwacher Exzitonenlinien keine verläßlichen Werte für diese Parameter [6]. Neben umfassenden Voraussagen, die auf der $\mathbf{k} \cdot \mathbf{p}$-Theorie basierten [6, 8], und der Beobachtung einer indirekten Valenzbandstruktur in zugverspannten Quantenfilmen mittels der zeitaufgelösten Lumineszenzspektroskopie lagen bisher keine experimentellen Ergebnisse aus magnetooptischen Messungen vor, die die Valenzbandstruktur in der Nähe des Zentrums der Brillouin-Zone darstellen konnten. Auch waren bislang im Materialsystem GaInAs/InP keine verbotenen Übergänge beobachtet worden. Ein wichtiger Vorteil bei der Beobachtung solcher verbotener Übergänge liegt darin, daß damit die optischen effektiven Massen von Elektron und Loch sowohl in der Quantenfilmebene als auch in z-Richtung (Wachstumsrichtung) gleichzeitig bestimmt werden können [9, 10]. In Anbetracht dieser Tatsachen war eine verbesserte magnetooptische Untersuchung nötig.

GaInP/AlGaInP-Heterostrukturen besitzen eine große Bedeutung für effiziente elektrooptische Anwendungen im sichtbaren Spektral-

bereich. Beispiele hierfür sind u.a. Quantenfilmlaser [11–13] zum optischen Beschreiben von Medien mit hohen Speicherdichten sowie die Datenkommunikation mittels der günstigen Kunststofflichtwellenleiter. Im kürzerwelligen Spektralbereich bestehen jedoch noch Schwierigkeiten, die das Erreichen ähnlich guter Leistungen verhindern. Für die weiter Optimierung ist auch in diesem Fall eine zuverlässige Kenntnis der Materialparameter äußerst wichtig. Obwohl viele Berichte zu den Banddiskontinuitäten der GaInP/AlGaInP-Strukturen existieren [14–19], gab es über die effektive Masse bisher nur eine einzige experimentelle Arbeit. In der Veröffentlichung [20] wurden erstmals die Exzitonenbindungsenergie und die effektive Masse aus Magnetoreflexionsmessungen bei magnetischen Flußdichten von bis zu 45 T gewonnen. Die Ergebnisse waren jedoch insofern nicht zufriedenstellend, daß keine Leichtlochübergänge beobachtet wurden. Daneben ist bereits gezeigt worden, daß unter geeigneten Wachstumsbedingungen in GaInP eine *CuPt*-Ordnung entlang der $[111]_B$-Richtung auftritt [21]. Die herausragenden Ordnungseffekte wie die Valenzbandaufspaltung und die Bandlückenreduzierung [22–32] wurden in GaInP experimentell und theoretisch untersucht. In GaInP/AlGaInP-Quantenfilmen sind Ordnungseffekte jedoch meist ingnoriert worden [17–20, 33, 34]. Nach unserem Wissen existiert bisher keine Veröffentlichung, die den Einfluß der oben erwähnten Ordnungseffekte auf die Banddiskontinuitäten, die effektiven Massen und die Exzitonenbindungsenergie behandelt.

Als mächtiges Instrument zur theoretischen Analyse der Valenzbandstruktur wird häufig die $\mathbf{k} \cdot \mathbf{p}$-Methode verwendet [8, 35–39], u.a. auch im Falle von $Ga_xIn_{1-x}P$/AlGaInP-Quantenfilmen [33, 40–44]. Nach der Voraussage von Moritz [43, 44] sollte die weit verbreitete axiale Näherung hier nicht mehr anwendbar sein. In der Literatur existierte bislang jedoch kein grundlegender Vergleich zwischen $\mathbf{k} \cdot \mathbf{p}$-Rechnungen mit bzw. ohne die Einbeziehung der axialen Näherung, wobei letztere ausdrücklich eine anisotrope Bandstruktur beinhalten.

In der vorliegenden Arbeit werden grundlegende magnetooptische und theoretische Untersuchungen von Exzitoneneffekten und Valenzbandstrukturen in verspannten und/oder geordneten GaInAs/InP- und GaInP/AlGaInP-Quantenfilmen vorgestellt. Unter Anwendung der

Magnetoabsorptionsspektroskopie werden dabei in druckverspannten GaInAs/InP-Quantenfilmen verbotene optische Übergänge beobachtet und für zugverspannte Quantenfilme die effektiven Massen mittels der Ableitung der Absorptionsspektren bestimmt. Unter Verwendung dieser Daten wird die indirekte Valenzbandstruktur in zugverspannten Quantenfilmen anhand einer $\mathbf{k} \cdot \mathbf{p}$-Simulation weiter diskutiert. Um geordnete GaInP/AlGaInP-Quantenfilmen zu beschreiben, wird eine modifizierte *model-solid*-Methode entwickelt und die Wirkung der Ordnung auf die effektive Masse untersucht. Zusätzlich wird eine 6-Band-$\mathbf{k} \cdot \mathbf{p}$-Simulation präsentiert.

Die Arbeit gliedert sich in vier Teile.

Im ersten Teil werden die theoretischen Grundlagen bereitgestellt, die zum Verständnis der Absorption und der Reflexion im Magnetfeld nötig sind. Daneben werden die speziellen experimentellen Methoden beschrieben, die im Laufe der Arbeit zum Einsatz kamen.

In Kapitel 2 wird zunächst ein Überblick über die theoretischen Modelle zur Berechnung der Exzitonenübergänge im Magnetfeld gegeben: Ein Exziton kann in Analogie zum Wasserstoffatom durch die Bindungsenergie E_B und den Bohrschen Radius a_B charakterisiert werden. Setzt man eine Quantenfilmstruktur einem homogenen Magnetfeld senkrecht zur Wachstumsebene aus, zeigen die exzitonischen Übergänge eine diamagnetische Verschiebung. Zur Analyse dieser Verschiebung wird in der vorliegenden Arbeit eine quasi-zweidimensionale Effektive-Masse-Gleichung [45–47] mit Hilfe eines numerischen Integrationsverfahrens [48] gelöst. Zur Beschreibung der Band-Band-Übergänge werden hierbei die *model-solid*-Theorie [49–51] und ein Potentialtopfmodell [52] verwendet. Es folgt eine $\mathbf{k} \cdot \mathbf{p}$-basierte Simulation der Einflüsse der Verspannung auf die effektiven Elektron- und Lochmassen [6,8,53]. Dazu wird als numerisches Verfahren zur Lösung des 6-Band-$\mathbf{k} \cdot \mathbf{p}$-Problems eine Finite-Differenzen-Methode vorgestellt. Außerdem werden die Ordnungsphänomene in $Ga_xIn_{1-x}P$ [23, 24, 29, 30] kurz beschrieben.

Eine Darstellung der experimentellen optischen und magnetooptischen Meßmethoden findet sich in Kapitel 3. Um die Methode der numerischen Ableitung spektroskopischer Daten einzuführen, werden

kurz deren Eigenschaften [54] diskutiert. Ebenfalls detailliert erklärt wird, wie Fabry-Pérot-Oszillationen, die in der optischen Spektroskopie von Schichtstrukturen häufig Probleme bereiten, effektiv reduziert werden können.

Im zweiten Teil (Kapitel 4) werden verspannte $Ga_xIn_{1-x}As/InP$-Quantenfilme mit Hilfe der Magnetoabsorption untersucht.

Die Anpassung der theoretischen Berechnungen durch geeignete Parameterwahl an die experimentellen Daten zur diamagnetischen Verschiebung zeigt, daß in den Absorptionsspektren druckverspannter Proben neben den erlaubten S-artigen Übergängen zwei Typen von verbotenen Übergängen sichtbar sind. Nach sorgfältiger theoretis cher Analyse läßt sich der erste als sogenannter P- bzw. D-artiger Übergang (magnetische Quantenzahl $m = \pm 1$ bzw. $m = \pm 2$) identifizieren, der durch den Galliumgehalt und die damit verbundene Verspannung verursacht wird. Beim zweiten Typ handelt es sich um einen Band-Band-Übergang zwischen Niveaus mit verschiedenen Hauptquantenzahlen ($\Delta n \neq 0$). Mittels verbotener und erlaubter Übergänge werden aus den Daten die effektiven Elektron- und Lochmassen sowohl *in-plane* als auch in z-Richtung gewonnen. Anhand der Ergebnisse wird eine theoretische Voraussage zum Verhältnis der effektiven Elektronenmassen an der Bandkante des Volumenhalbleiters, in der Wachstumsebene und der Wachstumsrichtung $m_{\Gamma_6} < m_{e,\rho} < m_{e,z}$ [6] im druckverspannten ($x_{\mathrm{Ga}} < 0.468$) Bereich überprüft. Die erhaltene *in-plane* effektive Masse des Elektrons stimmt mit dem Wert überein, der sich aus Magnetolumineszenzmessungen an n-modulationsdotierten Einfachquantenfilmen gleicher Quantenfilmbreite [55] ergab. Die effektiven Lochmassen werden mit den von Sugawara bestimmten [6] verglichen.

Um die effektiven Massen auch in zugverspannten Quantenfilmen zu erhalten, müssen die exzitonischen Resonanzenergien ebenso genau bestimmt werden, wie dies im Fall der druckverspannten Proben möglich war. Die sehr breiten und schwachen exzitonischen Linien in den Absorptionsspektren lassen dies jedoch zunächst nicht zu. Um die erforderliche Genauigkeit dennoch zu erreichen, wird deshalb die Methode der numerischen Ableitung der optischen Spektren ange-

wandt. Es wurde bereits nachgewiesen, daß eine solche Ableitung die Breite der Exzitonenlinien drastisch vermindern und die Hintergrundabsorption wirksam unterdrücken kann [56, 57]. Ableitungen bis zur achten Ordnung im Kombination mit Glättungsoperationen (*smoothing*) werden zunächst für die Spektren aller Proben sorgfältig durchgeführt. Im Falle der druckverspannten Proben zeigen diese Ableitungen bei der anschließenden Auswertung keinerlei Einfluß auf die effektiven Massen. Bei den zugverspannten Proben vermindern sich jedoch durch dieses Vorgehen sowohl die Linienbreiten als auch die Hintergrundabsorption deutlich, so daß die Resonanzenergien nun genau genug bestimmt werden können. Allgemein sind die Ableitungen stabil und zeigen für höhere als vierte Ableitungen keinen sichtbaren Unterschied in der Auswertung der effektiven Massen mehr. Die Ableitungen der Absorptionsspektren bilden deshalb die Grundlage bei der Auswertung der Messungen an zugverspannten Proben. Sie liefern neben den genauen Positionen von Leichtloch- und Schwerlochübergängen des Exzitonengrundzustands auch höhere Übergänge, die in den originalen Absorptionsspektren nicht erkennbar sind. Die Exzitonenbindungsenergie und die reduzierten effektiven Massen für Leichtloch- und Schwer- lochexzitonen bis zum Zustand $5S$ werden so erstmals zuverlässig bestimmt.

Ein Vergleich der effektiven Massen mit Werten aus Magnetolumineszenzmessungen an n-modulationsdotierten Einfachquantenfilmen [55] ist nun für Galliumgehalte zwischen 30% und 70% möglich. Während die Lumineszenzübergänge in n-modulationsdotierten Quantenfilmen vom Leitungsband ins Valenzbandmaximum erfolgen ($\Delta\mathbf{k} = 0$), zeigt der Vergleich, daß die Absorptionsübergänge in undotierten Mehrfachquantenfilmen exzitonischer Natur sind, d.h., der Grundzustandsübergang ($1S$) erscheint dicht am Zentrum der Brillouin-Zone ($\mathbf{K} = 0$). Übergänge aus höher angeregten exzitonischen Zuständen ($2S$, $3S$, ...) erfolgen demnach im $\mathbf{k}$-Raum an Stellen mit $\mathbf{K} > 0$, wobei immer $\Delta\mathbf{k} = 0$ angenommen wird. Die große Bedeutung dieser Erkenntnis liegt darin, daß die Valenzbandstruktur der Quantenfilme so durch die Auswertung der effektiven Massen einer "Zustandsleiter" von angeregten Exzitonzuständen experimentell dargestellt werden kann. Während in druckverspannten und unverspannten Proben die

effektiven Massen der verschiedenen Schwerlochexzitonenzustände durchweg positiv sind, ergibt sich in zugverspannten Proben ($x_{\mathrm{Ga}} = 0.6$ and 0.7) eine negative effektive Masse zum Grundzustand des ersten Leichtlochexzitons, aber wiederum positive Werte für höher angeregte Zustände. Nach der Definition der effektiven Masse $m_h^* = -\hbar^2/(\partial^2 E/\partial k^2)$ bedeutet der Vorzeichenwechsel der effektiven Masse von negativen ($1S$) zu positiven Werten ($2S$, $3S$, ...), daß das Valenzbandmaximum nicht im Zentrum der Brillouin-Zone ($\mathbf{K} = 0$) sondern bei $\mathbf{K} > 0$ liegt. In zugverspannten Proben existiert also ab einem Galliumgehalt von etwa 60% eine indirekte (Typ II) Valenzbandstruktur. Dieses Ergebnis stimmt mit zeitaufgelösten Lumineszenzuntersuchungen an undotierten GaInAs/InP-Quantenfilmen [58,59] überein. Auch die Magnetoabsorption eignet sich deshalb neben der zeitaufgelösten Lumineszenz [60] sehr gut zum experimentellen Nachweis der indirekten Valenzbandstruktur. Desweiteren wird gezeigt, daß man eine gute Beschreibung der Valenzbandstruktur auf der Grundlage von $\mathbf{k} \cdot \mathbf{p}$-Rechnungen nur mit einem geeigneten Satz von Luttinger-Kohn-Parametern erhalten kann. Verglichen mit den von Sugawara *et al.* mittels magnetooptischer Spektroskopie ermittelten Werten, sind zur Interpretation unserer Ergebnisse im Fall der Druckverspannung kleinere, für Zugverspannung jedoch größere Luttinger-Kohn-Parameter notwendig.

Im dritten Teil der Arbeit (Kapitel 5) werden die Ergebnisse der systematischen Untersuchungen zu den Einflüssen von Ordnungseffekten auf die Banddiskontinuitäten und Übergangsenergien in geordneten $\mathrm{Ga}_x\mathrm{In}_{1-x}\mathrm{P}$/AlGaInP-Quantenfilmen dargestellt. Daneben werden Ergebnisse für die effektive Masse sowie die Exzitonenbindungsenergie präsentiert, die sich aus Magnetoreflexionsmessungen ergeben. Zunächst werden hier die experimentellen Schwierigkeiten erläutert, die sich bei Absorptionsmessungen an den erwähnten Proben ergeben, und anschließend eine auf Reflexionsmessungen optimierte Probenstruktur vorgeschlagen. Die Übergänge in verspannten und geordneten GaInP/AlGaInP-Quantenfilmen werden dann mittels Photolumineszenz (PL) und anregungsabhängiger Photolumineszenz (PLE) identifiziert. Dabei wird im Gegensatz zu den Linienprofilen der Lumineszenzspektren von geordnetem GaInP-Volumenmaterial für Quan-

tenfilme nur eine Linie beobachtet. Die Breite dieser Linie (FWHM, full width at half maximum) beträgt für unverspannte und stark geordnete Proben etwa 12.2-15.3 meV, für teilweise geordnete Proben 18.6-23.2 meV. Druckverspannte Proben zeigen in den jeweiligen Fällen Linienbreiten von 20 meV bzw. 27.1 meV. Anders als im Volumenmaterial verschiebt die PL-Linie der Quantenfilme bei Erhöhung der Anregungsdichte zu höheren Energien hin (Blauverschiebung), und zwar zunächst schnell ($P \leq 20$ W/cm^2), dann etwas langsamer und schließlich nicht mehr ($P > 40$ W/cm^2). Die Linienbreite verringert sich unter diesen Bedingungen ebenfalls (bei Anregungsdichten zwischen 5 W/cm^2 und 20 W/cm^2 auf Werte von 2.5 meV bis 0.5 meV). Sehr interessant ist dabei, daß die Linie trotz der Blauverschiebung exzitonisch bleibt, wie durch Magnetolumineszenzmessungen nachgewiesen wurde. Dieses Verhalten kann nicht mit dem bekannten Modell für die Bandkantenstruktur in geordnetem GaInP-Volumenmaterial [61–65] erklärt werden, das auf Piezoelektrizität oder Bandausläufen besteht. Stattdessen wird ein anderes Modell vorgeschlagen, das im wesentlichen von einer statistischen Verteilung geordneter Bereiche ausgeht: (i) wegen der Ordnungseffekte bildet sich keine indirekte Bandstruktur aus, (ii) die PL-Intensität resultiert vorherrschend aus Domänen mit hohem Ordnungsgrad und kleiner Bandlücke, (iii) bei ausreichend hohen Anregungsleistungen werden die Domänen mit kleiner Bandlücke vollständig besetzt, und die PL-Linie zeigt danach keine Blauverschiebung mehr.

Anhand der Magnetolumineszenzmessungen werden zudem die Exzitonenbindungsenergie und die reduzierten effektiven Massen bestimmt, wobei sich beide Größen als ordnungsabhängig erweisen. Im Gegensatz zu Reflexionsmessungen kann im Photolumineszenzspektrum prinzipiell leider nur eine einzelne Linie beobachtet werden. Um die Bandstruktur genau zu vermessen sind deshalb Reflexionsuntersuchungen nötig, bei deren Auswertung die Kenntnis des Ordnungsgrads erforderlich ist.

Auf der Basis der bekannten *model-solid*-Theorie [49–51] wird nun eine modifizierte *model-solid*-Methode entwickelt, die die Einflüsse der beiden wichtigsten Ordnungseffekte, nämlich der Valenzbandaufspal-

tung und der Bandlückenreduzierung, beinhaltet. Auf diese Weise können die Ordnung in (111)-Richtung, die Verspannung entlang der (001)-Richtung sowie die Spin-Bahn-Kopplung berücksichtigt werden. Neben der Berechnung der Band-Band-Übergangsenergie wird die Aufteilung der Banddiskontinuitäten auf Valenz- und Leitungsband in Abhängigkeit vom Ordnungsgrad und/oder der Verspannung bestimmt. Außerdem werden an den (un)verspannten und geordneten GaInP/AlGaInP-Quantenfilmen Reflexionsuntersuchungen in Kombination mit dem oben beschriebenen numerischen Ableitungsverfahren durchgeführt. Für die drei obersten Valenzsubbandübergänge können die exzitonischen Übergangsenergien genau bestimmt werden. Durch die Anpassung der theoretischen Berechnungen an die experimentellen Ergebnisse mittels geeigneter Parameterwahl kann gezeigt werden, daß die modifizierte *model-solid*-Theorie die Band-Band-Übergänge in geordneten GaInP/AlGaInP-Quantenfilmen zufriedenstellend vorhersagen kann. Der Ordnungsgrad kann anhand der ersten Übergangsenergie bestimmt werden. Unter sonst gleichen Wachstumsbedingungen der Proben zeigt die Druckverspannung die Tendenz, die Ordnungseffekte zu reduzieren. Es wird nachgewiesen, daß die experimentell bestimmte Verkleinerung der Bandlücke von $\Delta E_g(\eta = 1) = -0.471$ eV die beste Übereinstimmung für unverspannte Proben liefert, während Werte, die hierauf basieren aber zusätzlich eine theoretisch vorhergesagte Verspannungskorrektur berücksichtigen, sich besser zur Beschreibung von druckverspannten Proben eignen. In bezug auf die Frage der Banddiskontinuitäten ergibt die *model-solid*-Methode, daß zunehmende Ordnung eine Zunahme der Leitungsbanddiskontinuität Q_c verursacht. Für unverspannte und druckverspannte Quantenfilme liegt Q_c im Bereich von 0.58 bis 0.7, während der Ordnungsgrad η von 0 bis 1 steigt. Fast identische Werte von $Q_c \approx 0.58$ ergeben sich für ungeordnete, unverspannte und druckverspannte Quantenfilme. Um die reduzierten effektiven Massen sowohl von Schwerloch- als auch von Leichtlochexzitonen in geordneten GaInP/AlGaInP-Quantenfilmen bestimmen zu können, werden die exzitonischen Übergänge in Reflexion untersucht. Mit Hilfe des Ableitungsverfahrens und der Anpassung der theoretischen Parameter werden sie identifiziert. Wegen apparativer Beschränkungen können die Reflexionsmessungen nur

unter einem Winkel von 45° zur Wachstumsrichtung ausgeführt werden, weshalb als maximale magnetische Flußdichte nur ein Wert von $B_{\max} = \cos 45° \times 6.8\,\mathrm{T} \approx 4.8$ T erreicht werden kann. Trotz dieser Einschränkung können in der vorliegenden Arbeit die exzitonischen Schwerloch- und Leichtlochübergänge ausdrücklich identifiziert und die Übergangsenergien bestimmt werden. Die Leistungsfähigkeit der Kombination aus Reflexionsmessungen mit dem numerischen Ableitungsverfahren wird bei der Untersuchung von GaInP/AlGaInP- Quantenfilmen so eindrucksvoll demonstriert. Die Ergebnisse bezüglich der diamagnetischen Verschiebung lassen sich folgendermaßen zusammenfassen: (i) in mittleren magnetischen Feldern ist für unverspannte und ungeordnete Proben keine diamagnetische Verschiebung zu detektieren, (ii) da für druckverspannte Proben die effektive Masse aufgrund der isotropen Verringerung der Bandlücke reduziert ist, wird die diamagnetische Verschiebung sichtbar und kann zur Auswertung der effektiven Masse genutzt werden, (iii) effektive Masse und Exzitonenbindungsenergie sind ordnungsabhängige Größen.

Im letzen Teil (Kapitel 6) wird schließlich die Ordnungsabhängigkeit der effektiven Massen und damit der Valenzbandstruktur analysiert. Ordnung in GaInP/AlGaInP-Quantenfilmen kann als Zugverspannung in der (110)-Richtung bzw. als Druckverspannung in der (-110)-Richtung interpretiert werden [30, 66]. Um sowohl die Anisotropie des Valenzbands deutlich sichtbar zu machen als auch die Unterschiede in Rechnungen mit bzw. ohne Verwendung der axialen Näherung zu überprüfen, wird ein modifiziertes 6-Band-$\mathbf{k}\cdot\mathbf{p}$-Modell mit expliziter Winkelabhängigkeit vorgestellt. Es basiert auf der bekannten 6-Band-$\mathbf{k}\cdot\mathbf{p}$-Theorie zur Berechnung der Valenzbandstruktur mit einem Hamiltonoperator nach Luttinger und Kohn [8, 35–39]. Zusätzlich werden jedoch die beiden wichtigsten Ordnungseffekte berücksichtigt. Die Valenzbandstruktur kann so zum einen im Rahmen einer axialen Näherung, zum andern als gesamtes unvereinfachtes 6-Band-Problem numerisch simuliert werden. Dabei wird nachgewiesen, daß etwa 13% der ordnungsinduzierten Verringerung der Bandlücke durch eine Verschiebung des Valenzbands nach oben realisiert werden. Diese Tatsache spricht gegen eine TypII Valenzbandstruktur in geordneten GaInP/AlGaInP-Quantenfilmen, wie sie in Veröffentlichungen

zu geordnetem GaInP-Volumenmaterial häufig verwendet wird [61–65]. Da für die Luttinger-Parameter $\gamma_1 \neq \gamma_2$ gilt, ist die Valenzbandstruktur insbesondere in druckverspannten und unverspannten Quantenfilmen stark winkelabhängig. Die maximalen Energien und effektiven Massen des Valenzbands treten dabei in Richtungen mit Winkeln von $(2n+1) \times 45^\circ$ gegen k_x $(n = 0, 1, 2, 3)$ auf. In zugverspannten Quantenfilmen ist dieses Phänomen nur sehr schwach ausgeprägt. Als weiterer Effekt wird hierdurch ein sogenanntes *warping* verursacht, das ebenfalls für Zugverspannung sehr klein, für unverspannte und druckverspannte Proben jedoch stark ist. Es ergibt sich also, daß die axiale Näherung für zugverspannte, ungeordnete oder sehr schwach geordnete Quantenfilme gerechtfertigt ist, so daß die Rechenzeit deutlich geringer gehalten werden kann. Im Falle der Druckverspannung ist jedoch eine Lösung des vollständigen 6-Band-$\mathbf{k} \cdot \mathbf{p}$-Modells ohne die axiale Näherung nötig.

Es wird gezeigt, daß durch die Ordnung die effektive Masse der obersten beiden Valenzbänder in der (110)-Richtung erhöht und diejenige des obersten Valenzbands in der (-110)-Richtung reduziert wird. Um einen Vergleich der experimentell aus Magnetoreflexions- und Lumineszenzmessungen bestimmten effektiven Massen anstellen zu können, wird ein Durchschnittswert der ordnungsabhängigen effektiven Masse über die Winkel in der Filmebene gebildet. Für druckverspannte und unverspannte Quantenfilme erhöht sich die effektive Masse des obersten Valenzsubbands aufgrund der Ordnung, während die effektive Masse des zweiten Valenzsubbands abnimmt. Im unverspannten Fall verursacht die Ordnung eine Zunahme der effektiven Massen der obersten beiden Valenzsubbänder im Bereich von $0 \leq \eta \leq 0.4$. Eine Abnahme der effektiven Masse des ersten Valenzsubbands sowie eine Zunahme für das zweite Subband ergibt sich im Bereich der Zugverspannung für $0 \leq \eta \leq 0.45$. Die aus der experimentellen Auswertung von Magnetoreflexions- und Magnetolumineszenzmessungen erhaltenen effektiven Massen für druckverspannte GaInP/AlGaInP-Quantenfilme stimmen mit diesen theoretischen Vorhersagen überein.*

*I'm greatly indebted to Miss Anne Hasenkopf for her critical reading of this *Zusammenfassung*.

Abstract

In this dissertation, main interests are focused on exciton effects and on the valence-band structures in $Ga_xIn_{1-x}As$/InP and $Ga_xIn_{1-x}P$/AlGaInP quantum-well (QW) systems.

Theoretically, in order to obtain exciton binding energy and effective mass from magneto-optical absorption and reflectivity measurements, and to explain the experimental phenomena, we have employed a model-solid theory together with a finite square QW model to reasonably determine the transition energies in GaInAs/InP QW systems [Sec. 2.2.1, 2.2.2]. We have numerically solved a quasi two-dimensional effective-mass equation of excitons in magnetic fields by direct integration [Sec. 2.2.3, 2.2.4], and evaluated the effective masses of up to $5S$ states of the $1e$-1h exciton in the QW systems. A quantitative description of the valence-band structure has been achieved. This enables a judgment if a 6-band second-order $\mathbf{k} \cdot \mathbf{p}$ theory can quantitatively describe the valence-band structures or not [Sec. 4.6.2]. The direct and indirect valence-band transition for tensile strained GaInAs/InP QWs has been evidenced by simulating a 6-band second-order $\mathbf{k} \cdot \mathbf{p}$ Hamiltonian equation with the finite-difference method [Sec. 2.3].

To understand the CuPt-type ordering effect in GaInP/AlGaInP QWs, we have constructed a modified model-solid method by incorporating two important ordering effects into the model-solid method [Sec. 5.6], and measured the transition energies of the heavy-hole (hh), light-hole (lh) and spin-orbit (SO) excitons by reflectivity measurements. By correlating the theoretical and the experimental results we showed that the modified model-solid method can well predict the band-edge electronic structures in the QWs with the ordering.

Further, we established an ordering-included 6-band $\mathbf{k} \cdot \mathbf{p}$ model to simultaneously deal with the effects from (001) elastic strain, SO coupling, and (111) CuPt-type ordering [Chap. 6], and made the necessary matrix-transform to simplify the analysis of the difference caused by using or not using an axial approximation. We found that the ordering drastically changes the valence-band structure: for compressive

strain, the ordering results in an increase of the effective masses of the hh- and lh-like subbands, for absence of strain, the ordering causes the effective masses of the first subband (hh-like) to slightly increase in a range of $\eta \lesssim 0.4$; for tensile strain, the effective mass of the first subband (lh-like) decreases. That of the third subband also decreases in a range of $\eta \lesssim 0.45$ (1hh), as ordering increases.

Experimentally, we employed a Fourier-transform-infrared spectrometer to realize absorption measurements on $Ga_xIn_{1-x}As$/InP QWs under up to 6.8 T (Tesla) magnetic fields, and traced out two types of forbidden transitions in the compressively strained $Ga_xIn_{1-x}As$/InP QWs [Sec. 4.3]: one of which is due to the $P-$ and $D-$type exciton states, the other is between conduction- and valence-band states with different principle quantum numbers. Together with the allowed transitions they provided a chance to evaluate all the z-direction and the in-plane effective masses of electrons and holes simultaneously, which give a direct evidence supporting Sugawara *et al.*'s theoretical prediction of a relation among the three effective masses of the electrons as $m_{\Gamma_6} < m^*_{e,\rho} < m^*_{e,z}$ in the compressively strained $Ga_xIn_{1-x}As$ on InP. We borrowed the derivative technique widely used in the area of chemistry to analyze the absorption spectra [Sec. 3.3] in the tensile strained QWs, and showed that it is stable, accurate and easy to perform, and can present a more detailed and reliable description of the exciton states. We have accurately determined the exciton binding energies and effective masses in the tensile strained QWs, which were rarely evaluated before [Sec. 4.4.2]. Comparing the effective masses of different exciton states for all the $Ga_xIn_{1-x}As$/InP samples, we showed that for the tensile strained samples there is a direct-to-indirect valence-band structure transition around a Ga fraction of 60% [Sec. 4.6], and pointed out that evaluating the effective masses of different exciton states is a good pathway to identify the indirect valence-band structure.

For $Ga_xIn_{1-x}P$/AlGaInP QW systems, we performed excitation-intensity dependent photoluminescence (PL) and magneto-PL measurements at a low temperature on ordered and compressively strained/lattice-matched samples [Sec. 5.4.1, 5.4.3]. The results suggests that ordering in the QWs may not induce a type-II valence-band struc-

ture to the well-layer. We have adjusted the samples' structures to fit reflectivity measurements. With the assistance of the derivative technique, we were able to determine the exciton resonance energies with an accuracy range of ∼0.3 meV, and obtained ordering parameters for four series of strained /lattice-matched and ordered samples based on the calculations and the experimentally determined band-to-band transition energies. We also obtained the ordering-dependent band-offset ratio in this QW systems [Sec. 5.7.3], and compared it with those obtained based on a *totally disorder* assumption. By performing magneto-optical reflectivity measurements, we obtained the effective masses and exciton binding energies for strained and/or highly ordered samples [Sec. 5.5.2]. A primary comparison of the strain and ordering effects on the effective mass and exciton binding energy was also performed, and showed that just as tensile strain, the order increases the effective mass and exciton binding energy in the compressively strained QWs. The results are qualitatively in agreement with the theoretical analysis.

Briefly, we have obtained the following results in this work,

- the observation of two types forbidden transitions. The electron and hole effective masses were simultaneously determined.
- the introduction of the derivative method. It enables an accurate evaluation of the effective masses in tensile strained GaInAs/InP and ordered GaInP/AlGaInP QWs.
- the effective masses of up to $5S$ exciton states in $Ga_xIn_{1-x}As$/InP QWs. A direct evidence for direct and indirect valence band was obtained.
- the adjustment of the GaInP/AlGaInP QW structures. Magneto-reflectivity study was realized. The transition energies were determined in an uncertainty range of 0.3 meV.
- a theoretical study of the band-edge electronic structure in ordered and strained GaInP/AlGaInP QWs.
- an ordering-included 6-band $\mathbf{k} \cdot \mathbf{p}$ model. With it, ordering effects on the effective masses of valence subband were analyzed.

Chapter 1

Introduction

The $Ga_xIn_{1-x}As$/InP quantum-well (QW) system has attracted a lot of attention in the last several years [1–7,67–75], due to its great importance for electronic and photonic applications, such as quantum-well lasers, light emitting diodes, infrared detectors and optical-confinement Bragg reflectors. As crucial parameters for optoelectronic device design and modeling, the effective masses of the carriers and the exciton binding energy in this material system are of particular interest.

For the compressively strained and lattice-matched QWs, the exciton binding energy and in-plane reduced effective mass of the exciton ground state were evaluated reliably. However, the data for the tensile strained QWs were more difficult to determine, due to the larger full-width at half-maximum (FWHM) of the excitonic transitions and an additional underlying background absorption [6].

Moreover, there were no experimental data from magneto-optical measurements describing the valence-band structure near the Brillouin-zone center in $\mathbf{k}$ space, though theoretical predictions based on the Luttinger-Kohn $\mathbf{k} \cdot \mathbf{p}$ theory have been presented by many groups [6,8]; and it has been concluded from the time-resolved recombination of carriers that the valence-band structure in the tensile strained QWs is indirect [58, 59].

Also, optical forbidden transitions, which were recently detected in undoped InGaAs/Ga(PAs) QWs by polarization-dependent photoluminescence excitation (PLE) under high magnetic field [9], were not observed in GaInAs/InP QW systems. An important usage of the forbidden transitions is, from a technical point of view, that they can be employed together with allowed transitions to determine the optical in-plane effective masses of electrons and holes simultaneously [9, 10].

A detailed magneto-optical study is therefore called for. This forms the first part of this work.

$Ga_xIn_{1-x}P$/AlGaInP heterostructures possess a great potential for efficient, visible electron-optical applications, e.g., quantum-well lasers [11–13,76–78] for high density optical recording (digital versatile disk-DVD), data communications using inexpensive plastic optical fiber, and printing, as they represent the largest direct band gap in the III-V low-dimensional semiconductor systems apart from nitrogen-containing compounds. To aid the device design, sufficient knowledge of the material properties and parameters is necessary. In the past few years, many efforts have focused on structures incorporating strain ($x \neq 0.52$) in ternary QW active region [18, 19, 22, 79, 80]. Band-edge electronic structure in the strained QWs has been intensively studied [14, 15, 17, 19, 81, 82].

However, none of the reports took into account the CuPt-type atomic ordering, which is well established to exhibit along the $[111]_B$ directions in epitaxially grown $Ga_xIn_{1-x}P$ alloy under proper growth conditions. The ordering has two prominent effects of band-gap reduction and valence-band splitting [23–25, 31]. Ignoring these effects would cause the electronic-structure prediction to be doubtful.

On the other hand, in contrast to GaInAs/InP QW systems, very limited literature is available on the determination of exciton binding energy and effective mass. The only paper, to our knowledge, was about magneto-optical reflectivity study under up to 45 T magnetic fields, but still with big uncertainty in the determination of excitonic resonance energy and ignoring the ordering effects.

Therefore, a proper theoretical model including the ordering effects for the band-edge electronic-structure analysis is important. Also, new experimental method are expected to increase the accuracy in resonance energy determination and to enable a proper evaluation of the exciton binding energy and effective mass in the GaInP/AlGaInP QW systems. Both of these issues will constitute the second major part of this work.

In $Ga_xIn_{1-x}P$/AlGaInP QW systems, the Luttinger-Kohn $\mathbf{k} \cdot \mathbf{p}$ theory has been used by many authors [33,40,42–44] in analyzing valence-band structures under different assumptions. Domen *et al.* [42] compared the difference in valence-band structure caused by either in-

cluding or not including the spin-orbit split-off band. Moritz *et al.* included the ordering effects in their full 6-band calculations [43, 44]. Nevertheless, it was still not clear how the difference will be by using the axial approximation, which was widely used in $\mathbf{k} \cdot \mathbf{p}$ simulations. Attempting to get the answer and further, to find out ordering effect on valence-band effective mass, will form the last part of the work.

The dissertation is organized as follows. In Chapter 2, a theoretical picture of excitonic transitions in magnetic fields are composed by using a model-solid theory, a finite square-well model, and an effective-mass equation of an exciton in magnetic fields. Using certain numerical methods, the equations are solved numerically. This enables us to establish a quantitative relation between the theoretical prediction and the experimental data, which leads to the determination of crucial parameters, and the identification of new phenomena. Then, a brief description is dedicated to the strain effect on electron- as well as hole-effective masses. A strain-included $\mathbf{k} \cdot \mathbf{p}$ model is provided for the valence-band-structure analysis. Also a short introduction is made on the CuPt-type ordering effects in the $GaInP_2$ alloy.

In Chapter 3, a brief description of the magneto-optical spectroscopy used in this work, i.e., absorption, PL and reflectivity, is made, and the schematic diagram of the Fourier transform infrared (FTIR) spectrometer (DA3.01) as well as its related components is given. Also, the theoretical basis of using the derivative method to analyze magneto-optical spectra is established. By analyzing the reason of harmful multiple-beam interference in the GaInP/AlGaInP QW structures, a pathway of diminishing the interference is suggested.

Detailed magneto-optical absorption studies on GaInAs/InP QW systems are presented in Chapter 4. Both experimental and theoretical evidence are given for two types of optical forbidden transitions in the compressively strained $Ga_xIn_{1-x}As$/InP QWs. Based on an analysis of the forbidden as well as allowed transitions, all the in-plane and z-direction effective masses of electrons and holes are simultaneously determined [83]. It is shown, by a careful study of derivative operation on absorption spectra, that derivative can drastically increase the accuracy of spectroscopic-position determination, thereby enabling an

accurate evaluation of the exciton binding energy and effective mass in the tensile strained QWs [54]. The reduced as well as the hole effective masses of different exciton states are obtained for all the samples with the Ga fraction varying through 0.30 to 0.70 (corresponding to lattice-mismatch of ε_ρ from -1.16% to $+1.6\%$). With aid of a 6-band $\mathbf{k}\cdot\mathbf{p}$ simulation, it is also illustrated that the determined hole effective masses of different exciton states can provide a good description of the valence-band structure in the Brillouin-zone center. With them, the indirect valence-band structure in the tensile strained samples is evidenced [83].

In Chapter 5, the difficulty occurring in the absorption measurements on the GaInP/AlGaInP QW systems is pointed out, and a new sample structure is proposed for reflectivity measurements. Using PL, excitation-dependent PL and magneto-PL, ordering-related properties are investigated, and the exciton binding energy as well as reduced effective mass is estimated. Then, derivative-assisted reflectance measurements are carried out, which provide a pathway to accurately determine the spectroscopic position of the excitonic transitions in the spectra. A modified model-solid method [84] is established to predict the band-edge electronic structure in the ordered QW system. It enables us to estimate the ordering parameter in the QWs by only measuring the energy of the first excitonic transition. Also, it is shown that, the exciton binding energy and reduced effective mass can be evaluated even under low magnetic fields, with the derivative-assisted reflectivity method, and primary results are provided [85].

Finally in Chapter 6, a full 6-band $\mathbf{k}\cdot\mathbf{p}$ model is established to include all the ordering, strain, and spin-orbit split-off effects. The purpose that it should be easy to make a comparison of using and not using an axial approach is taken into account. By employing the finite-difference method, an example calculation for a GaInP/AlGaInP QW is made with and without axial approach, respectively, and the validity of the axial approximation in this material system is verified. Based on numerically solving the full 6-band problem, the anisotropy of the valence-band dispersion is identified, and ordering effects on the valence band-edge effective mass are investigated.

Chapter 2

Theoretical considerations

2.1 Introduction

In this work, most of the experimental part is concentrated on exciton-related phenomena, e.g., exciton diamagnetic shift, exciton binding energy, and exciton reduced effective mass.

An exciton is formed when an electron is lifted from the valence band across the band gap into the conduction band, and attracts each other via the Coulomb force with the hole left by the lifted electron in the valence band. It is most probably the case in semiconductor when temperature and excitation are low [45]. The exciton in semiconductors is called Wannier exciton, for which the electron and the hole are separated by many inter-atomic spacing. In general, as an exciton is a two-particle system, the problem of calculating its energy levels is in principle very complicated. Fortunately, for the Wannier exciton the effective mass approximation (EMA) can be used and the problem can be simplified enormously.

The essential point of the EMA is that, near the extremes of the conduction and valence bands, the kinetic energies of the electron and the hole are positive quadratic function of the change in momentum $\hbar(\mathbf{k}-\mathbf{k}_m)$, where $\hbar\mathbf{k}_m$ is the momentum at the extreme. For a simple isotropic non-degenerated band extreme at the zone center ($k_m = 0$) the kinetic energy is [86]

$$E_k = \frac{\hbar^2 k^2}{2m^*}\,, \tag{2.1}$$

where m^* is the effective mass (m_e^* for the electron, m_h^* for the hole). In other words, the net effect of the crystal potential on the electron (hole) kinetic energy is to change the electron (hole) mass from the value in free space to the effective mass m^*. As a result this approximation is known as the EMA. Though there is no known case in

nature to which this simple theory strictly applies, it indeed exhibits most of the essential features of the exciton, and provides an excellent approximation in our case. Correspondingly, the Coulomb potential can be written as [86]

$$V(\rho) = -\frac{e^2}{4\pi\varepsilon_0\varepsilon_r\rho}\,,$$

where ρ is the electron-hole separation, ε_0 is the dielectric constant and ε_r is the relative permittivity. Such a potential gives rise to an infinite series of discrete hydrogenic bound states, with energies and radii given by [86]

$$E_n(\mathbf{k}) = -\frac{e^2}{8\pi\varepsilon_0\varepsilon_r a_n} + \frac{\hbar^2\mathbf{K}^2}{2M}\,, \qquad a_n = \frac{4\pi\varepsilon_0\varepsilon_r\hbar^2 n^2}{\mu e^2}\,, \tag{2.2}$$

where $n = 1, 2, \ldots, \infty$, $\mu^{-1} = (m_e^*)^{-1} + (m_h^*)^{-1}$, $M = m_e^* + m_h^*$, $\hbar\mathbf{K} = \hbar(\mathbf{k_e} + \mathbf{k_h})$ is the momentum of the center of mass, and E_n is measured from the band edge E_g. The values of E_n and a_n for $n = 1$ and $\mathbf{K} = 0$ are known as exciton binding energy and effective Bohr radius of the ground state:

$$E_b = \frac{e^2}{8\pi\varepsilon_0\varepsilon_r a_B}\,, \qquad a_B = \frac{4\pi\varepsilon_0\varepsilon_r\hbar^2}{\mu e^2}\,.$$

Note that E_b is inversely proportional to the square of the background dielectric constant. As the background dielectric constant describes the screening of the Coulomb interaction in an unexcited crystal, and the screening requires virtual interband transitions which becomes more and more unlikely for materials with larger band gap E_g, the exciton binding energy is therefore large for the wide-gap materials [47].

From 3-dimensional (3D, bulk) semiconductors to the limiting exact 2-dimensional (2D) case, i.e., for a quantum-well with well-width $L \ll a_B$, the exciton binding energy will dramatically increase, $E_{b,2D} = 4E_{b,3D}$, for the infinitely deep well. Such an increase can be understood by considering quantum well structures with decreasing width. The wavefunction tries to conserve its spherical symmetry since the admixture of P-wavefunction is energetically unfavorable. Confinement parallel to the quantum wells is therefore accompanied by a decrease

in the Bohr radius perpendicular to the wells. In the ground state, the 2D exciton radius is only $a_B/2$. The increase in exciton binding energy has a profound influence on quantum-well properties. It allows, for example, GaAs-based quantum-wells to have their optical properties dominated by exciton effect even at room temperature. In the quantum well, the degeneracy of the valence band is removed, due to the reduction in symmetry along the axis of growth, and the presence of band discontinuities at the interfaces. Strain also lifts the valence band degeneracy. Thus the valence subbands may be treated as isolated set of bands from the point of view of exciton formation. This leads to the formation of two exciton systems, i.e., the heavy-hole (hh) exciton and the light-hole (lh) exciton. Under an external magnetic field, the exciton shows magnetic related phenomena, such as diamagnetic shift. This provides an pathway to determine the exciton binding energy and reduced effective mass μ.

In this chapter, a theoretical picture of excitonic transitions in magnetic fields are composed in Sec. 2.2. A finite square-well model together with a model-solid theory is used to calculate band-to-band transition energies. To analyze excitonic diamagnetic shifts, an exciton effective-mass equation is employed, and numerically simulated by direct integration. In Sec. 2.3, strain effects on electron- and hole-effective masses are considered. A strained-included $\mathbf{k}\cdot\mathbf{p}$ model is selected to analyze valence-band structures in GaInAs/InP QWs. The finite-difference procedure in $\mathbf{k}\cdot\mathbf{p}$ simulation is briefly described. The relation between the effective masses of electrons in strained GaInAs is established, which will be experimentally verified in Sec. 4.3. Finally in Sec. 2.4, a short description of ordering effects in the $GaInP_2$ alloy is made, serving as an introduction to the detailed theoretical analysis of the ordering effects in the (Al)GaInP QWs.

2.2 The exciton in a magnetic field

Under a magnetic field perpendicular to quantum-well layers, the exciton resonance energy in the well is [6]

$$E_{\rm ex} = E_A + E^z_{c,n} + E^z_{h,n} + E_r + E_{\rm sp}\,, \tag{2.3}$$

where E_A is band gap energy of the quantum-well material, $E^z_{c,n}$ and $E^z_{c,n}$ are the electron and hole energy levels in finite quantum well, respectively. $E_{\rm sp}$ is the spin-splitting energy of the exciton resonance,

$$E_{\rm sp} = \pm\mu_{\rm B}\xi B\,,$$

where + for $M_J = 3/2$ and $1/2$, and − for $M_J = -3/2$ and $-1/2$, $\mu_{\rm B} = e\hbar/2m_0$, $\xi = g_e/2 - 3\kappa - 27q/4$ for heavy-hole exciton, and $\xi = \pm g_e/2 - \kappa - q/4$ for light-hole exciton, g_e is the g factor of the conduction-band electron, and κ and q are Luttinger-Kohn valence-band parameter [87]. Since no spin-splitting has been observed in this work and previous studies [6], we neglect $E_{\rm sp}$ in our discussion*.

2.2.1 Electron and hole levels in a finite quantum-well

We first consider E_g, $E^z_{c,n}$ and $E^z_{h,n}$ in Eq. (2.3). In quantum wells, electron and hole states in the growth direction (z-direction) can be described in the regime of the EMA [52] by the Schrödinger equation

$$\left[-\frac{\hbar^2}{2m^*_s(z)}\frac{\partial^2}{\partial z^2} + V_s(z)\right] Z_s(z) = E_{s,n}\, Z_s(z)\,, \tag{2.4}$$

where $m^*_s(z)$ is the electron (hole) effective mass of the well-layer (w) or barrier (b) material, $V_s(z)$ is the potential well for the electron (hole), $Z_s(z)$ is the confined-state envelope wave function of the electron (hole). Under the square-well assumption and if the well has a reflection symmetry $V_s(z) = V_s(-z)$ around the center of the well taken as the center of coordinates (Fig. 2.1), the solution of Eq. (2.4) can only be even or odd. They can be written as [47, 88]

$$Z_s(z) = \begin{cases} \cos kz & |z| < L/2\,, \\ B\, e^{-\kappa(|z|-L/2)} & |z| > L/2\,, \end{cases} \tag{2.5}$$

for even states, or

$$Z_s(z) = \begin{cases} \sin kz & |z| < L/2\,, \\ B\, e^{-\kappa(|z|-L/2)} & |z| > L/2\,, \end{cases} \tag{2.6}$$

*As a rough estimation, a splitting of ~ 1 meV per Tesla was expected. With regard to the width of the $1S$ exciton of ~ 6 meV, the splitting should be observable in the range of the magnetic fields available in this work. We guess that the quantum confinement effect may significantly reduce the splitting, probably due to the reduction of the g_e and/or the κ and q parameters.

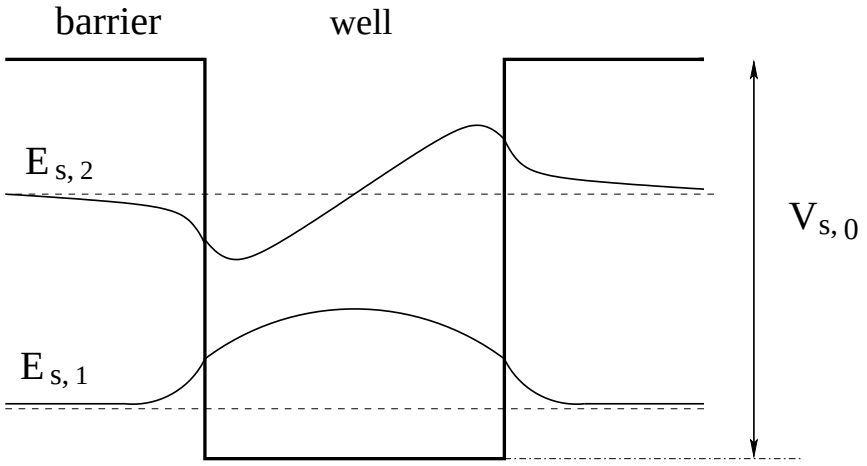

Figure 2.1: First two bound energy levels and wave functions in a finite quantum well. The cusps for the wave functions at the boundaries are introduced by the different values of the effective mass in the well and barrier layers, respectively.

for odd states. Here L is the width of the quantum well. The energy eigenvalue is determined by $E_{s,n} = \hbar^2 k_{s,n}^2 / 2m_{s,\mathrm{w}}^*$, or $E_{s,n} = V_s - \hbar^2 \kappa_{s,n}^2 / 2m_{s,\mathrm{b}}^*$, and $0 < E_{s,n} < V_{s,0}$. For the solution of Eq. (2.5), the continuity conditions at $z = \pm L/2$ yield

$$(k_{s,n}/m_{s,\mathrm{w}}^*)\,\tan(k_{s,n}L/2) \;=\; \kappa_{s,n}/m_{s,\mathrm{b}}^* \tag{2.7}$$

for even states. Similarly, Eq.(2.6) yields

$$(k_{s,n}/m_{s,\mathrm{w}}^*)\,\tan(k_{s,n}L/2) \;=\; \kappa_{s,n}/m_{s,\mathrm{b}}^* \tag{2.8}$$

for odd states. These lead $k_{s,n}$ and $\kappa_{s,n}$ to be finally determined by:

$$\kappa_{s,n} \;=\; \begin{cases} (m_{s,\mathrm{b}}^*/m_{s,\mathrm{w}}^*) k_{s,n} \tan(k_{s,n}L/2)\,, & \text{if } \tan(k_{s,n}L/2) > 0\,, \\ -(m_{s,\mathrm{b}}^*/m_{s,\mathrm{w}}^*) k_{s,n} \cot(k_{s,n}L/2)\,, & \text{if } \tan(k_{s,n}L/2) < 0\,, \end{cases} \tag{2.9}$$

and

$$k_{s,n} \;=\; \begin{cases} k_{s,0} \left(\frac{m_{s,\mathrm{w}}^*}{m_{s,\mathrm{w}}^* + m_{s,\mathrm{b}}^* \tan^2(k_{s,n}L/2)} \right)^{1/2}, & \text{if } \tan(k_{s,n}L/2) > 0\,, \\ k_{s,0} \left(\frac{m_{s,\mathrm{w}}^*}{m_{s,\mathrm{w}}^* + m_{s,\mathrm{b}}^* \cot^2(k_{s,n}L/2)} \right)^{1/2}, & \text{if } \tan(k_{s,n}L/2) < 0\,, \end{cases} \tag{2.10}$$

with

$$k_{s,0} \;=\; \left(\frac{2m_{s,\mathrm{w}}^* V_{s,0}}{\hbar^2} \right)^{1/2}. \tag{2.11}$$

To fully describe the electronic energy levels of strained heterostructures, it is important to have information about the effects of the strain on the properties of the well-layers. These include strain-induced changes in energy gaps, splitting due to the lowering of symmetry, and variations in effective masses. We will follow the "model-solid" theory to determine $V_{s,0}$ in Sec. 2.2.2.

2.2.2 Model-solid theory for band-edge alignment

The model-solid theory was first proposed by van de Walle and Martin [49, 89, 90], followed by others [50, 51, 91], to calculate strain effects on the band lineups.

Pseudomorphic (or commensurate) growth of strained layers on a (001) substrate (Fig. 2.2) subjects these layers to a biaxial strain $\epsilon_{\parallel}$

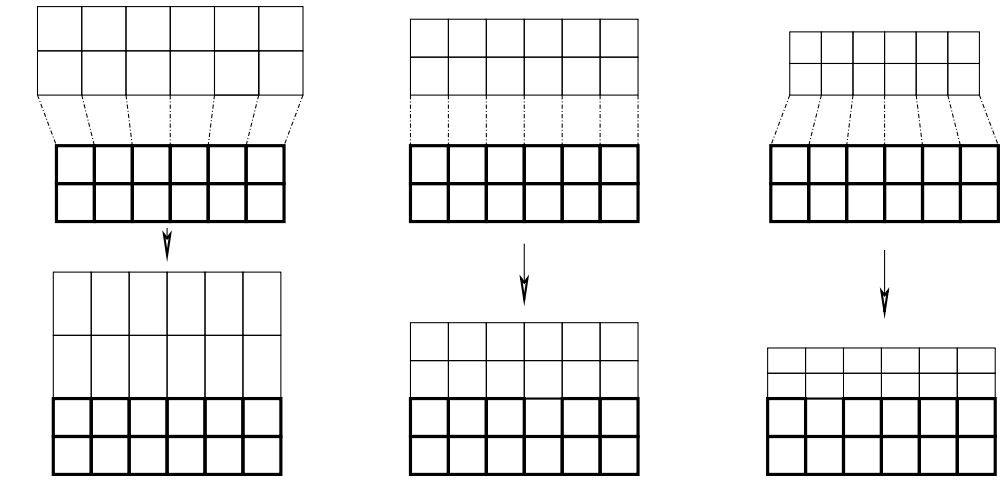

Figure 2.2: Schematic of the strained layer on (001) substrate.

parallel to the plane of the interface and a uniaxial strain $\epsilon_{\perp}$ perpendicular to it:

$$\epsilon_{\parallel} = \frac{a_0}{a_f} - 1\,, \quad \epsilon_{\perp} = \left(-\frac{2C_{12}}{C_{11}}\right)\epsilon_{\parallel}\,, \tag{2.12}$$

where a_0 denotes the lattice constant of the substrate and a_f the equilibrium lattice constant of the layer material. The strain effect on the

energy levels of zinc blende-type semiconductor at Γ point can be decomposed into hydrostatic and shear contributions. The hydrostatic strain component leads to shifts of the conduction-band energy E_c and the average valence-band energy $E_{v,av} = (E_{\rm hh} + E_{\rm lh} + E_{\rm so})/3$:

$$\Delta E_c^{\rm hy} \;=\; a_c \left(2\epsilon_{\parallel} \,+\, \epsilon_{\perp}\right) , \quad \Delta E_{v,{\rm av}}^{\rm hy} \;=\; a_v \left(2\epsilon_{\parallel} \,+\, \epsilon_{\perp}\right) , \qquad (2.13)$$

where a_v and a_c are the hydrostatic deformation potentials for the valence band and conduction band, respectively. The shear contribution does not affect the conduction band at Γ. However, it couples to the spin-orbit interaction and results in an additional splitting of the valence-band energies. The energy shifts for the $|J, m_J\rangle = |\frac{3}{2}, \frac{3}{2}\rangle$ valence subband (or $E_{\rm hh}$), the $|\frac{3}{2}, \frac{1}{2}\rangle$ subband (or $E_{\rm lh}$), and the split-off band $|\frac{1}{2}, \frac{1}{2}\rangle$ (or $E_{\rm so}$) relative to their average ($E_{v,{\rm av}}$) are given by

$$\begin{aligned}
\Delta E_{\rm hh}^{\rm sh} &= \frac{\Delta^{\rm so}}{3} + \frac{\Delta_{001}^{\rm sh}}{3} \qquad (2.14)\\
\Delta E_{\rm lh}^{\rm sh} &= -\frac{\Delta^{\rm so}}{6} - \frac{\Delta_{001}^{\rm sh}}{6} + \frac{1}{2}\left[(\Delta^{\rm so})^2 - \frac{2}{3}\Delta^{\rm so}\Delta_{001}^{\rm sh} + (\Delta_{001}^{\rm sh})^2\right]^{1/2}\\
\Delta E_{\rm so}^{\rm sh} &= -\frac{\Delta^{\rm so}}{6} - \frac{\Delta_{001}^{\rm sh}}{6} - \frac{1}{2}\left[(\Delta^{\rm so})^2 - \frac{2}{3}\Delta^{\rm so}\Delta_{001}^{\rm sh} + (\Delta_{001}^{\rm sh})^2\right]^{1/2}
\end{aligned}$$

where $\Delta^{\rm so}$ is the spin-orbit splitting in the absence of strain, and $\Delta_{001}^{\rm sh}$ is given by

$$\Delta_{001}^{\rm sh} = 3b\,\frac{C_{11} + 2C_{12}}{C_{11}}\epsilon_{\parallel}\,. \qquad (2.15)$$

The quantity b is the shear deformation potential for the strain of tetragonal symmetry.

For the stress-free case, $\Delta_{001}^{\rm sh} = 0$, therefore $\Delta E_{\rm hh}^{\rm sh} = \Delta E_{\rm lh}^{\rm sh} = \Delta^{\rm so}/3$, $\Delta E_{\rm so}^{\rm sh} = -2\Delta^{\rm so}/3$. The $E_{\rm hh}$ and $E_{\rm lh}$ subbands are thus degenerate for the lattice-matched interface, and the topmost valence band lies at $\Delta^{\rm so}/3$ above $E_{v,{\rm av}}$.

The conduction-band and valence-band energies E_c and $E_{\rm hh}$, $E_{\rm lh}$,

$E_{\rm so}$, respectively, are obtained on an absolute scale from

$$\begin{aligned} E_c &= E_{v,\rm av} + \frac{\Delta^{\rm so}}{3} + E_{g,0} + \Delta E_c^{\rm hy}\,, \\ E_{\rm hh} &= E_{v,\rm av} + \Delta E_{v,\rm av}^{\rm hy} + \Delta E_{\rm hh}^{\rm sh}\,, \\ E_{\rm lh} &= E_{v,\rm av} + \Delta E_{v,\rm av}^{\rm hy} + \Delta E_{\rm lh}^{\rm sh}\,, \\ E_{\rm so} &= E_{v,\rm av} + \Delta E_{v,\rm av}^{\rm hy} + \Delta E_{\rm so}^{\rm sh}\,, \end{aligned} \tag{2.16}$$

where $E_{v,\rm av}$, $\Delta^{\rm so}$, and $E_{g,0}$ refer to stress-free bulk properties. For $\mathrm{Ga}_x\mathrm{In}_{1-x}\mathrm{As}$, we use $E_{g,0}$ [92]:

$$E_{g,0}|_{2K} = 0.4105 + 0.6337\, x_{\rm Ga} + 0.475\, x_{\rm Ga}^2$$

The band offsets for coherently strained well layers lattice-matched to stress-free barrier can thus be expressed as

$$\begin{aligned} V_{e,0} &= E_c(\text{barrier}) - E_c\,, \\ V_{\rm hh,0} &= E_{\rm hh} - E_v(\text{barrier})\,, \\ V_{\rm lh,0} &= E_{\rm lh} - E_v(\text{barrier})\,, \\ V_{\rm so,0} &= E_{\rm so} - E_v(\text{barrier})\,, \end{aligned} \tag{2.17}$$

where

$$\begin{aligned} E_v(\text{barrier}) &= E_{v,\rm av}^{\rm b} + \frac{\Delta^{\rm so,b}}{3}\,, \\ E_c(\text{barrier}) &= E_v(\text{barrier}) + E_{g,0}^{\rm b}\,. \end{aligned} \tag{2.18}$$

The band-edge energy of quantum well can also be determined by

$$E_A = \begin{cases} E_A^{\rm HH} = E_c - E_{\rm hh}, & \text{for heavy-hole} \\ E_A^{\rm LH} = E_c - E_{\rm lh}, & \text{for light-hole} \\ E_A^{\rm SO} = E_c - E_{\rm so}, & \text{for spin-orbit split-off}\,. \end{cases} \tag{2.19}$$

The results are schematically shown in Fig. 2.3.

In deriving physical parameters of the alloys used in the calculation, an interpolation scheme is adopted using the values of the related binary compounds. For a ternary compound $\mathrm{A}_x\mathrm{B}_{1-x}\mathrm{C}$, the parameter P is derived from

$$P_{\mathrm{A}_x\mathrm{B}_{1-x}\mathrm{C}} = xP_{\rm AC} + (1-x)P_{\rm BC}\,.$$

The parameters of the binary alloys are listed in Table 2.1 [8, 50, 51].

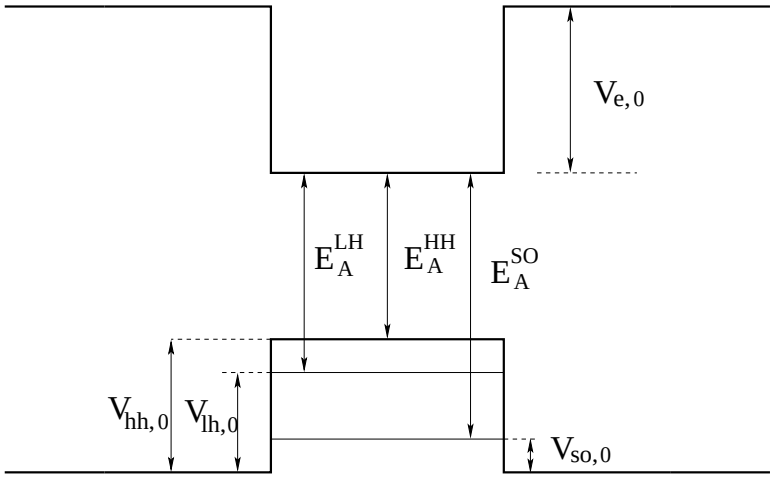

Figure 2.3: Schematic of the band-edge energies and the well potentials for hh, lh, and so subbands.

2.2.3 Wannier exciton in quantum well

To be definite, we concern ourselves with quasi-two dimensional finite quantum wells where electron and hole motion is quantized in the [001] direction. We assume that both electron and hole bands are parabolic and isotropic in the plane of the quantum well. The Hamiltonian of an exciton associated with either the hh or the lh band in the quasi-two dimensional quantum well can be expressed as [45]

$$\left[\frac{\mathbf{p}^2}{2\mu}+\frac{e^2\mathbf{A}^2}{2\mu}+e\left(\frac{1}{m_h^*}-\frac{1}{m_e^*}\right)\mathbf{A}\cdot\mathbf{p}+V(r)\right.$$
$$\left.-\frac{2e\hbar}{m_h^*+m_e^*}\mathbf{K}\cdot\mathbf{A}\right]\Phi(r) \;=E_r\Phi(r) \qquad (2.20)$$

where μ is the reduced effective mass of the exciton and $\mathbf{A}$ is the vector potential. The third term in the Hamiltonian is the Zeeman term which makes no contribution so long as we concern ourselves with exciton of S symmetry. The term involving the scalar product of $\mathbf{K}$ with $\mathbf{A}$ describes the coupling of the center-of-mass motion of the exciton to the magnetic field, for sufficiently small $\mathbf{K}$ this term can be neglected.

If we choose the cylindrical gauge such that

$$\mathbf{A}=\frac{1}{2}\mathbf{B}\cdot\mathbf{r}\,, \qquad (2.21)$$

Table 2.1: Parameters used in the calculation of the band-edge alignment in $Ga_xIn_{1-x}As$/InP QWs. l.i. represents linear interpolation.

parameters	units	GaAs	InAs	InP	$Ga_xIn_{1-x}As$
a_0	Å	5.6533	6.0584	5.8688	l.i.
E_g	eV	1.424	0.36	1.344	
$\Delta^{\rm so}$	eV	0.34	0.38	0.11	
γ_1		6.85	20.4	4.95	l.i.
γ_2		2.1	8.3	1.65	l.i.
γ_3		2.9	9.1	2.35	l.i.
C_{11}	10^{11} dyn/cm^2	11.879	8.329	10.11	l.i.
C_{12}	10^{11} dyn/cm^2	5.376	4.526	5.61	l.i.
$a_c - a_v$	eV	-9.77	-6.0	-8.6	l.i.
b	eV	-1.77	-1.8	-2.0	l.i.
$E_{v,\rm av}$	eV	-6.92	-6.67	-7.04	l.i.
$m^*_{e,z}/m_0$		0.067	0.027	0.077	l.i.
$m_{\rm hh,z}/m_0$†					
$m_{\rm lh,z}/m_0$		0.073	0.055	0.14	l.i.
$m_{\rm so,z}/m_0$		0.17	0.15	0.19	l.i.

† cite from [93]: $0.32 + 0.02x_{\rm Ga}$ for $Ga_xIn_{1-x}As$

then the form of the Hamiltonian which we need to solve is in cylindrical polar coordinates [46]

$$\left\{-\frac{\hbar^2}{2\mu}\left[\frac{1}{\rho}\frac{\partial}{\partial\rho}\left(\rho\frac{\partial}{\partial\rho}\right)+\frac{1}{\rho^2}\frac{\partial^2}{\partial\phi^2}\right]+\frac{e^2B^2}{8\mu}\rho^2+\frac{e}{2}\left(\frac{1}{m_h^*}-\frac{1}{m_e^*}\right)\quad Bm\hbar\right.$$
$$\left.-\frac{e^2}{4\pi\varepsilon_0}\frac{1}{r}\right\}\Phi(\rho,\phi)=E_r\Phi(\rho,\phi) \qquad (2.22)$$

where r is given by

$$\frac{1}{r}=\int_{-\infty}^{+\infty}\!\!\int\frac{|Z_e(z_e)|^2|Z_h(z_h)|^2}{\varepsilon_r(z_e,z_h)\left[\rho^2+(z_e-z_h)^2\right]^{1/2}}dz_e dz_h \qquad (2.23)$$

ε_r is the relative permittivity of the materials, $Z_e(z_e)$ and $Z_h(z_h)$ are the z-direction confined-state wave functions of electrons and holes as described in Sec.2.2.1.

The in-plane part of the wavefunction, $\Phi(\rho,\phi)$, can be expressed as

$$\Phi(\rho,\phi)=R_m(\rho)\,\frac{1}{\sqrt{2\pi}}\,e^{im\phi} \qquad (2.24)$$

with $m = 0, \pm 1, \pm 2, \cdots$. Therefore, Eq. (2.22) now takes the form as

$$\left\{ -\frac{\hbar^2}{2\mu}\left[\frac{\partial^2}{\partial\rho^2} + \frac{1}{\rho}\frac{\partial}{\partial\rho} - \frac{m^2}{\rho^2}\right] + \frac{e^2B^2}{8\mu}\rho^2 + \frac{e}{2}\left(\frac{1}{m_h^*} - \frac{1}{m_e^*}\right) Bm\hbar \right. \\ \left. -\frac{e^2}{4\pi\varepsilon_0}\frac{1}{r}\right\} R_m(\rho) = E_{n,m} R_m(\rho)\,. \tag{2.25}$$

2.2.4 Numerical treatment of the Wannier equation

To solve the Wannier equation, variational method [7, 93–95] and numerical integration method [6, 7, 46, 96, 97] have been well established. The remarkable advantage of the numerical integration method over the variational one is that it circumvents the necessity of inventing a trial wave function for each state. As we wish to calculate excited as well as ground exciton states in this work, we select the numerical integration method.

We first introduce "transverse-exciton units", which are analogous to the atomic units. The units of length, energy, and magnetic field are [95]

$$a_0 = \frac{4\pi\varepsilon_0\hbar^2}{\mu e^2}\,, \quad R_{\rm y} = \frac{e^2}{8\pi\varepsilon_0 a_0}\,, \quad \gamma = \frac{eB\hbar}{2\mu R_{\rm y}}\,. \tag{2.26}$$

Thus, Eq. (2.25) can be rewritten as

$$\left[-\frac{\partial^2}{\partial\rho^2} - \frac{1}{\rho}\frac{\partial}{\partial\rho} + \frac{m^2}{\rho^2} + \frac{1}{4}(\gamma\rho)^2 - \frac{2}{r}\right] R_m(\rho) = E'_{n,m}\, R_m(\rho)\,, \tag{2.27}$$

$$E_{n,m} = E'_{n,m} + \left(\frac{m_e^* - m_h^*}{m_e^* + m_h^*}\right)\gamma\, m\,. \tag{2.28}$$

Such procedure can in one way enhance physical insight and in the other way, make numerical treatment convenient, i.e., by avoiding dealing with very large or very small numbers in the computer.

We then transform it to two coupled first-order differential equations. Assuming that $X = \partial R_m/\partial\rho$, we have

$$\begin{cases} \frac{\partial R_m}{\partial\rho} = X\,, \\ \frac{\partial X}{\partial\rho} = -\frac{X}{\rho} - \left(\frac{2}{r} - \frac{\gamma^2\rho^2}{4} - \frac{m^2}{\rho^2} + E'_{n,m}\right) R_m\,. \end{cases} \tag{2.29}$$

Now the fourth-order Runge-Kutta algorithm can be performed easily.

To find the eigenvalues of Eq. (2.29), we use the shooting method. We first take a trial eigenvalue, for which we find out the leftmost *matching point*, $\rho_{\rm mat}$, by assuming the total confinement potential to equal this trial eigenvalue,

$$\frac{\gamma^2\rho^2}{4} + \frac{m^2}{\rho^2} - \frac{2}{r} = E'_{n,m}\,.$$

Then, we integrate toward $\rho_{\rm mat}$ from the origin ($\rho \to 0$) to generate a solution $R_m^<$, which oscillates in the region of $0 \sim \rho_{\rm mat}$, known as "classically allowed region". We also generate a second solution, $R_m^>$ by integrating from $\rho_{\rm max}$ to $\rho_{\rm mat}$, which increases exponentially in the so-called "classically forbidden region", as shown in Fig. 2.4.

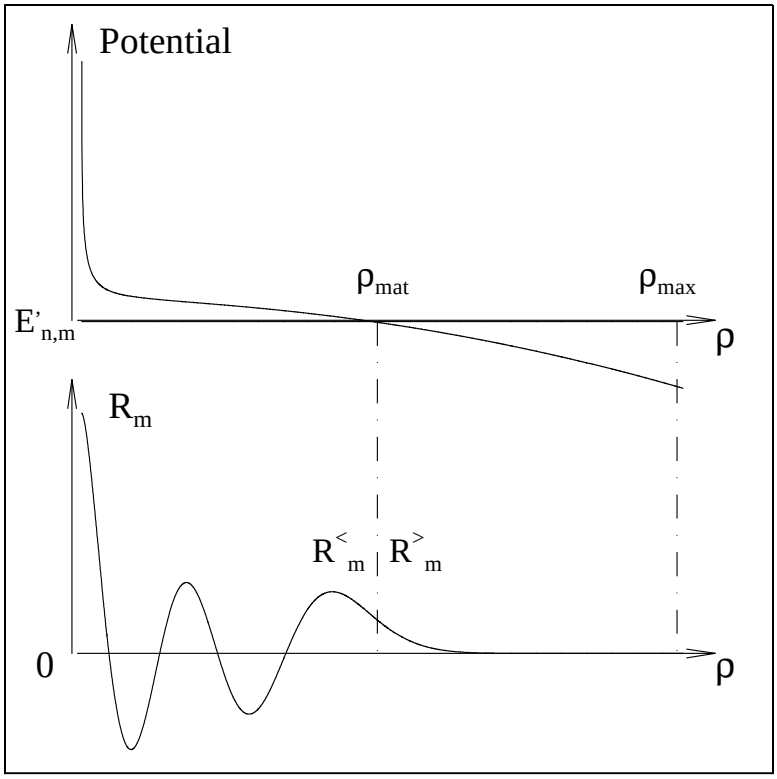

Figure 2.4: Upper: Schematic potential consisting both of Coulomb and magnetic field terms. Lower: Solutions $R_m^<$ and $R_m^>$ of the equation at an **arbitrary energy** E. $\rho_{\rm mat}$ is the (leftmost) matching point. When E is an eigenvalue, the derivative of the wavefunction will be continuous at the matching point.

The matching point here acts as a separator of the classically allowed and forbidden regions. Since both $R_m^<$ and $R_m^>$ satisfy a homo-

geneous equation, their normalizations can always be chosen so that the two functions are equal at the matching point $\rho_{\rm mat}$. An eigenvalue is found by the equality of the derivatives at the matching point,

$$\frac{d\,R_m^<}{d\,\rho}\Big|_{\rho_{\rm mat}} - \frac{d\,R_m^>}{d\,\rho}\Big|_{\rho_{\rm mat}} = 0\,.$$

With aid of the simple finite difference approach and the condition of R_m continuity, an equivalent condition is obtained using the points $\rho_{\rm mat}$ and $\rho_{\rm mat} - h$,

$$f \equiv \frac{1}{R_m^{<>}}\left[\,R_m^<(\rho_{\rm mat}-h)\;-\;R_m^>(\rho_{\rm mat}-h)\,\right] = 0\,,$$

where $R_m^{<>}$ is selected as the maximum value of $R_m^<$ and $R_m^>$ to make f typically of order unity. This integration process can serve to avoid numerical instability. As is well known, integrating into a classically forbidden region is likely to be inaccurate, since even at an exact eigenvalue where $R_<(\rho_{\rm max}) = 0$, there can be an admixture of the undesirable exponentially growing solution [48].

In Fig. 2.5, a numerical result is depicted for a $Ga_{0.4}In_{0.6}As/InP$ quantum well with well-width 10 nm, barrier-width 20 nm by using $m^*_{e,\rho} = 0.047m_0$, $\mu = 0.040m_0$, and other parameters listed in Table 2.1. Exciton diamagnetic shifts are predicted: energies of the exciton shift to higher values as the magnetic field increases. Fitting the calculation to the experimentally recorded diamagnetic shifts will lead to the determination of the exciton binding energy and reduced effective mass. We use this procedure in Chapter 4 [ref. Sec. 4.3 and Sec. 4.4] to deal with absorption measurements on GaInAs/InP QWs, and in Chapter 5 [ref. Sec. 5.5.2] to deal with reflectivity studies on ordered GaInP/AlGaInP QWs.

2.3 Strain effect on carrier effective masses and $\mathbf{k}\cdot\mathbf{p}$ model

In Sec. 2.2.2, we have considered strain effect on the band-edge alignment using model-solid theory. Now we set our sight onto strain effects on electron and hole effective masses.

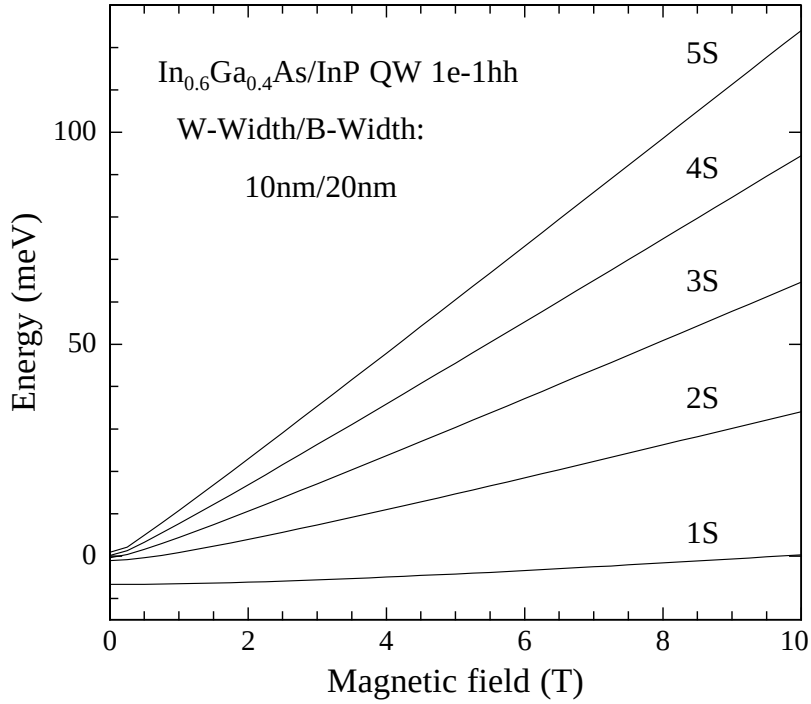

Figure 2.5: A theoretical calculation of exciton diamagnetic shifts as a function of magnetic fields for a $Ga_{0.4}In_{0.6}As/InP$ quantum-well. Parameters used are $m^*_{e,\rho} = 0.047m_0$, $\mu = 0.040m_0$, and those listed in Table 2.1.

The concept of effective mass is fundamental in the description of semiconductor properties. In two-dimensional (2D) systems, the electron (hole) mass is divided into a mass m^*_z perpendicular with respect to the growth plane, and a mass m^*_ρ parallel to it. Due to the isotropy of m^* in bulk materials, both m^*_z and m^*_ρ are often approximated by the bulk values [93]. However, the usefulness of this approximation rapidly decreases as the quantization effects increase. It is known, for instance, that in QWs m^*_z increases with subband indices [88].

2.3.1 $\mathbf{k}\cdot\mathbf{p}$ approximation

It has been established that the strain Hamiltonian H_ϵ for a $p-$like multiplet can be expressed as [53]

$$H_\epsilon = H^{(1)}_\epsilon + H^{(2)}_\epsilon\,, \tag{2.30}$$

where $H_\epsilon^{(1)}$ is the orbital-strain Hamiltonian of the valence bands, and can be written as [6, 53]

$$H_\epsilon^{(1)} = -a_v(\epsilon_{xx}+\epsilon_{yy}+\epsilon_{zz}) - 3b\left[\left(L_x^2 - \frac{L^2}{3}\right)\epsilon_{xx} + c.p.\right] \\ -\sqrt{3}\,d\left[(L_xL_y + L_yL_z)\epsilon_{xy} + c.p.\right], \quad (2.31)$$

ϵ_{ij} denotes the components of the strain tensor, $\mathbf{L}$ is the angular momentum operator and *c.p.* denotes cyclic permutation with respect to the indices x, y, z. a_v is the hydrostatic deformation potential of the valence band, b and d are the uniaxial deformation potentials appropriate to strains of tetragonal and rhombohedral symmetries, respectively. $H_\epsilon^{(2)}$ is the strain-dependent spin-orbit Hamiltonian, and can be described as

$$\begin{aligned} H_\epsilon^{(2)} = &- a_2(\mathbf{L}\cdot\sigma)(\epsilon_{xx}+\epsilon_{yy}+\epsilon_{zz}) \\ &- 3b_2\left[\left(L_x\sigma_x - \frac{1}{3}\mathbf{L}\cdot\sigma\right)\epsilon_{xx} + c.p.\right] \\ &- \sqrt{3}\,d_2\,\left[(L_x\sigma_y + L_y\sigma_x)\epsilon_{xy} + c.p.\right], \end{aligned}$$

where a_2, b_2 and d_2 are additional deformation potentials representing the effects of a strain on the spin-orbit interaction, and σ is the Pauli matrix vector. As it is not very significant [98], it is ignored here.

At $\mathbf{k} = 0$, the conduction-band minima for the diamond- and zinc-blende-type solids (except for Si and "zero" band-gap materials) is an anti-bonding $S-$state with symmetry $\Gamma_{2'}$ (Γ_1). The effect of a strain is to produce a hydrostatic shift given by

$$H_\epsilon^{(c)} = a_c\,(\,\epsilon_{xx}+\epsilon_{yy}+\epsilon_{zz}\,) \quad (2.32)$$

where a_c is the hydrostatic deformation potential of the $\Gamma_{2'}$ (Γ_1).

To explore the structure of the conduction- and valence bands near $\mathbf{k} = 0$, we use the $\mathbf{k}\cdot\mathbf{p}$ perturbation approach

$$H_k = \left(-\frac{\hbar^2}{2m}\right)\nabla^2 + V(r) + \left(\frac{\hbar^2k^2}{2m}\right) + \left(\frac{\hbar}{m}\right)\mathbf{k}\cdot\mathbf{p}\,. \quad (2.33)$$

Therefore, the total Hamiltonian can be written as

$$H = H_k + H_{\rm so} + H_\epsilon^{(c)} + H_\epsilon^{(1)}\,, \quad (2.34)$$

where $H_{\rm so}$ is the effect of the spin-orbit (SO) interaction.

2.3.2 Strain effect on in-plane hole effective mass

To study the strain effect on the in-plane hole effective mass $m^*_{h,\rho}$ in GaInAs/InP QWs, we first calculate the valence-band structure using the Chao-Chuang 6×6 $\mathbf{k}\cdot\mathbf{p}$ model [8], and then take a second-order derivative of the valence-band dispersion, that is

$$\frac{m_0}{m^*_\rho} = -\frac{m_0}{\hbar^2}\frac{\partial^2 E(k)}{\partial k^2}\,. \tag{2.35}$$

In Chapter 6 we will extend the model so as to be also able to account the CuPt-type ordering effect in GaInP/AlGaInP QWs.

Based on the theory of Luttinger-Kohn and Bir-Pikus, the valence-band structure of a strained bulk semiconductor can be described by the 6×6 Hamiltonian [8], which includes $\mathbf{k}\cdot\mathbf{p}$ perturbation term, SO coupling term, as well as strain term. Eq. (2.34) now takes the form:

$$H = -\begin{bmatrix} P+Q & -S & R & 0 & -\frac{1}{\sqrt{2}}S & \sqrt{2}R \\ -S^\dagger & P-Q & 0 & R & -\sqrt{2}Q & \sqrt{\frac{3}{2}}S \\ R^\dagger & 0 & P-Q & S & \sqrt{\frac{3}{2}}S^\dagger & \sqrt{2}Q \\ 0 & R^\dagger & S^\dagger & P+Q & -\sqrt{2}R^\dagger & -\frac{1}{\sqrt{2}}S^\dagger \\ -\frac{1}{\sqrt{2}}S^\dagger & -\sqrt{2}Q & \sqrt{\frac{3}{2}}S & -\sqrt{2}R & P+\Delta & 0 \\ \sqrt{2}R^\dagger & \sqrt{\frac{3}{2}}S^\dagger & \sqrt{2}Q & -\frac{1}{\sqrt{2}}S & 0 & P+\Delta \end{bmatrix} \tag{2.36}$$

with

$$\begin{aligned}
P &= P_k + P_\epsilon\,, \quad Q = Q_k + Q_\epsilon\,, \quad R = R_k + R_\epsilon\,, \quad S = S_k + S_\epsilon\,, \\
P_k &= \left(\frac{\hbar^2}{2m_0}\right)\gamma_1\left(k_x^2+k_y^2+k_z^2\right)\,, \quad Q_k = \left(\frac{\hbar^2}{2m_0}\right)\gamma_2\left(k_x^2+k_y^2-2k_z^2\right) \\
R_k &= \left(\frac{\hbar^2}{2m_0}\right)\sqrt{3}\left[-\gamma_2\left(k_x^2-k_y^2\right)+2i\gamma_3 k_x k_y\right]\,, \\
S_k &= \left(\frac{\hbar^2}{2m_0}\right)2\sqrt{3}\gamma_3\left(k_x - ik_y\right)k_z\,, \\
P_\epsilon &= -a_v(\epsilon_{xx}+\epsilon_{yy}+\epsilon_{zz})\,, \quad Q_\epsilon = -\frac{b}{2}(\epsilon_{xx}+\epsilon_{yy}-2\epsilon_{zz})\,, \\
R_\epsilon &= \frac{\sqrt{3}}{2}b(\epsilon_{xx}-\epsilon_{yy}) - id\epsilon_{xy}\,, \quad S_\epsilon = -d(\epsilon_{xx}-i\epsilon_{yz})\,.
\end{aligned} \tag{2.37}$$

The wave vector $\mathbf{k}$ is interpreted as a differential operator $-i\nabla$, γ_1, γ_2, and γ_3 are the Luttinger-Kohn parameters, the basis function $|j, m\rangle$ denotes the Bloch-wave function at the zone center. Here the zero-point of energy is taken to be at the top of the stress-free valence band.

In a strained-layer quantum well, by assuming that the growth direction is along the z axis and the strain caused by lattice mismatch is entirely elastically accommodated in the quantum well, the energies of the valence subband can be obtained by solving the effective mass equation

$$\begin{aligned} \textstyle\sum_\nu \, [\, H_{\mu\nu} + V_h(z)\delta_{\mu\nu} \,]\, G_\nu(k_\parallel, z) = E(k_\parallel)\, G_\mu(k_\parallel, z)\,, \\ \mu,\, \nu \,\in\, \left\{\, |\tfrac{3}{2}, \tfrac{3}{2}\rangle, |\tfrac{3}{2}, \tfrac{1}{2}\rangle, |\tfrac{3}{2}, -\tfrac{1}{2}\rangle, |\tfrac{3}{2}, -\tfrac{3}{2}\rangle, |\tfrac{1}{2}, \tfrac{1}{2}\rangle, |\tfrac{1}{2}, -\tfrac{1}{2}\rangle \right\}\,, \end{aligned} \quad (2.38)$$

where H is the Luttinger-Kohn Hamiltonian in Eq. (2.36) and $V_h(z)$ is the quantum-well potential for holes.

To solve it, an axial approximation has been previously adopted by Chao & Chuang to diagonalize the 6×6 Hamiltonian into two 3×3 blocks [8]. This can drastically reduce the computational effort. Then a finite-difference method is employed for the numerical simulations [37, 99, 100]. A detailed description of the procedure is discussed in Sec. 2.3.3. In chapter 6, we will extend this 6×6 $\mathbf{k}\cdot\mathbf{p}$ model to consider ordering effects [ref. Sec. 6.2]. Numerical results of the valence-band dispersion and effective mass in (Al)GaInP QWs will be presented, and differences caused by either using or not using the axial approximation will also be discussed.

2.3.3 Finite-difference procedure in $\mathbf{k}\cdot\mathbf{p}$ simulation

In practice, the differential operators in Eq. (2.36) can be expressed as $A(z)\cdot\,\partial^2/\partial z^2$ or $B(z)\cdot\partial/\partial z$, where $A(z)$ and $B(z)$ stand for position-dependent (well or barrier) inverse effective mass parameters. They have to be digitized through well- to barrier-layer in the first step of the numerical process by using the finite-difference method, in which the boundary-condition problem always should be taken into account. In the regime of variational methods, the boundary conditions are the requirement of the continuity of envelope functions and the continuity

of the unit-cell average of the normal component of the current, across the interfaces between the well and the barriers [8, 39, 101]. On the other hand, Baraff *et al.* found that the boundary conditions can be satisfied by requiring Hermiticity of the equation set [101]. As the Hermitian properties of the Hamiltonian can be obtained by using the following finite difference formulas

$$\begin{aligned} A(z)\frac{\partial^2 G}{\partial z^2}\Big|_{z=z_i} &\rightarrow \frac{\partial}{\partial z}\left(A(z)\frac{\partial G}{\partial z}\right)\Big|_{z=z_i} \simeq \frac{A(z_{i+1})+A(z_i)}{2(\Delta z)^2}\,G(z_{i+1}) \\ &- \frac{A(z_{i+1})+2A(z_i)+A(z_{i-1})}{2(\Delta z)^2}\,G(z_i) \\ &+ \frac{A(z_i)+A(z_{i-1})}{2(\Delta z)^2}\,G(z_{i-1})\,, \qquad (2.39) \\ B(z)\frac{\partial G}{\partial z}\Big|_{z=z_i} &\rightarrow \frac{1}{2}\left(B(z)\frac{\partial G}{\partial z}+\frac{\partial (BG)}{\partial z}\right)\Big|_{z=z_i} \\ &\simeq \frac{B(z_{i+1})+B(z_i)}{4\Delta z}\,G(z_{i+1}) - \frac{B(z_i)+B(z_{i-1})}{4\Delta z}\,G(z_{i-1})\,, \end{aligned}$$

which take into account the differences in the effective mass along the z-direction and the Luttinger-Kohn parameter in the well and barrier layers, the boundary conditions are also satisfied.

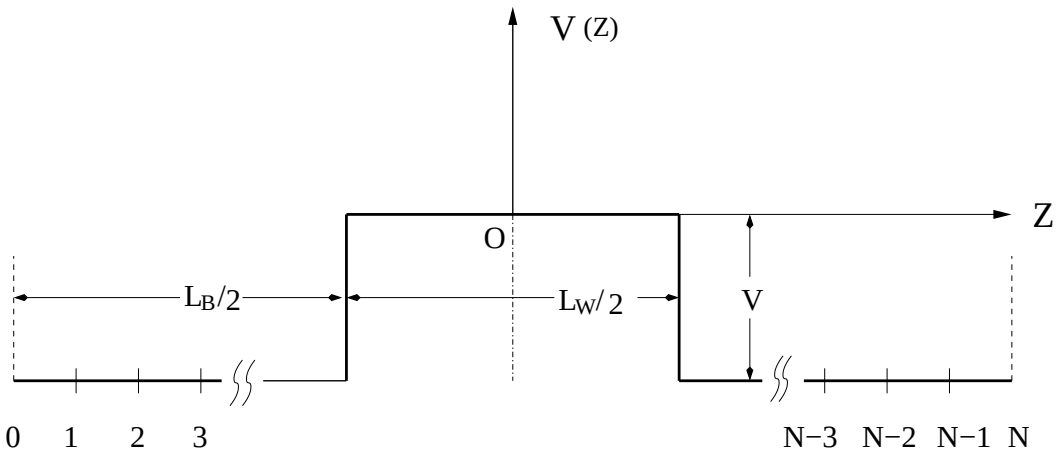

Figure 2.6: Schematic diagram of z-direction digitizing for a symmetric GaInP/ AlGaInP quantum well structure with coordinate origin at the center of the well-layer.

We deal in this work with a symmetric potential well, as shown in Fig. 2.6, and select its symmetric point to be at the center of the well-layer. Ordering the count-number i beginning from the left-side

barrier through the well layer to the right-side barrier, and assuming that the envelope function at the two ends [where $z_0 = -(L_{\rm W}+L_{\rm B})/2$, and $z_N = (L_{\rm W}+L_{\rm B})/2$] equals zero, we write out the finite-difference equations for each digitized point z_i, $i = 1, 2, \cdots, N-1$, and finally obtain an $6(N-1) \times 6(N-1)$ complex but Hermitian symmetric matrix. Thereby, the valence-band dispersion problem is reduced to find eigenvalues of the complex matrix, for which there are plenty of well-established numerical methods [102] ready to use.

2.3.4 Electron effective masses in strained GaInAs

To consider strain effects on the band-edge effective mass of electron, an 8×8 first-order $\mathbf{k} \cdot \mathbf{p}$ model is used. By choosing a set of bases to diagonalize the strain Hamiltonian for quantum wells grown coherently on (001) substrate, and taking the conduction-band edge as the energy origin, an 8×8 first-order $\mathbf{k} \cdot \mathbf{p}$ matrix can be obtained [6]. From it, an analytical expression for the band-edge effective mass of electron in bulk $\mathrm{Ga}_x\mathrm{In}_{1-x}\mathrm{As}$ can be derived [6, 53]:

$$\begin{aligned}
\frac{1}{m_{e,\rho}} &= \frac{1+D'}{m_0} + \frac{P^2}{3}\left[\frac{3}{E_A^{\rm HH}} + \frac{(\alpha-\sqrt{2}\beta)^2}{E_A^{\rm LH}} + \frac{(\beta+\sqrt{2}\alpha)^2}{E_A^{\rm SO}}\right], \\
\frac{1}{m_{e,z}} &= \frac{1+D'}{m_0} + \frac{2P^2}{3}\left[\frac{(\sqrt{2}\alpha-\beta)^2}{E_A^{\rm LH}} + \frac{(\sqrt{2}\beta+\alpha)^2}{E_A^{\rm SO}}\right], \qquad (2.40)
\end{aligned}$$

where $m_{e,\rho}$ and $m_{e,z}$ are the in-plane and $z-$direction effective masses of electron, respectively, $E_A^{\rm HH}$, $E_A^{\rm LH}$, and $E_A^{\rm SO}$ are the band-edge energies measured from the heavy hole, light hole and spin-orbit split-off valence subband to the conduction band, and have been determined in Sec. 2.2.2 [ref. Eq. (2.19), page 29]. D' is a second-order perturbation term in the 8-band $\mathbf{k} \cdot \mathbf{p}$ model describing the coupling between the conduction band and the SO valence subband. α and β represent the degree of mixing between light-hole and SO states described by

$$\begin{aligned}
\alpha &= \frac{2\sqrt{2}|Q_\epsilon|}{C}, \qquad \beta = \frac{(A-B)|Q_\epsilon|}{CQ_\epsilon}, \qquad A = \Delta_{\rm o} + Q_\epsilon \\
B &= \sqrt{\Delta_{\rm o}^2 + 2Q_\epsilon\Delta_{\rm o} + 9Q_\epsilon^2}, \qquad C = \sqrt{2B(B-A)}. \qquad (2.41)
\end{aligned}$$

P is the momentum matrix element showing the coupling between the conduction band and the valence band, which is related to the conduction-band-edge effective mass, m_{Γ_6}. It can be determined for the stress-free case by equation

$$P^2 = \frac{1}{2}\left[\frac{1}{m_{\Gamma_6}} - \frac{1+D'}{m_0}\right]\frac{E_g(E_g+\Delta_o)}{E_g+\frac{2}{3}\Delta_o}\,. \tag{2.42}$$

Here Δ_o is the spin-orbit splitting, E_g is band-gap energy of the (bulk) material. Both are in the absence of strain [6].

As shown by Sugawara *et al.* [6] in their magneto-optical study of $Ga_xIn_{1-x}As$ alloy on InP substrate, a qualitative agreement can be obtained between Eq. (2.42) and the experimentally determined magnetic-field dependence of the exciton resonance strength, by assuming that P and D' are strain-independent, and $D' = -6$. Therefore, we can calculate the effective masses in strained materials from m_{Γ_6}, using Eqs. (2.40-2.42). The results for $D' = 0$ and $D' = -6$, respectively, are plotted as a function of strain (Ga composition) in Fig. 2.7.

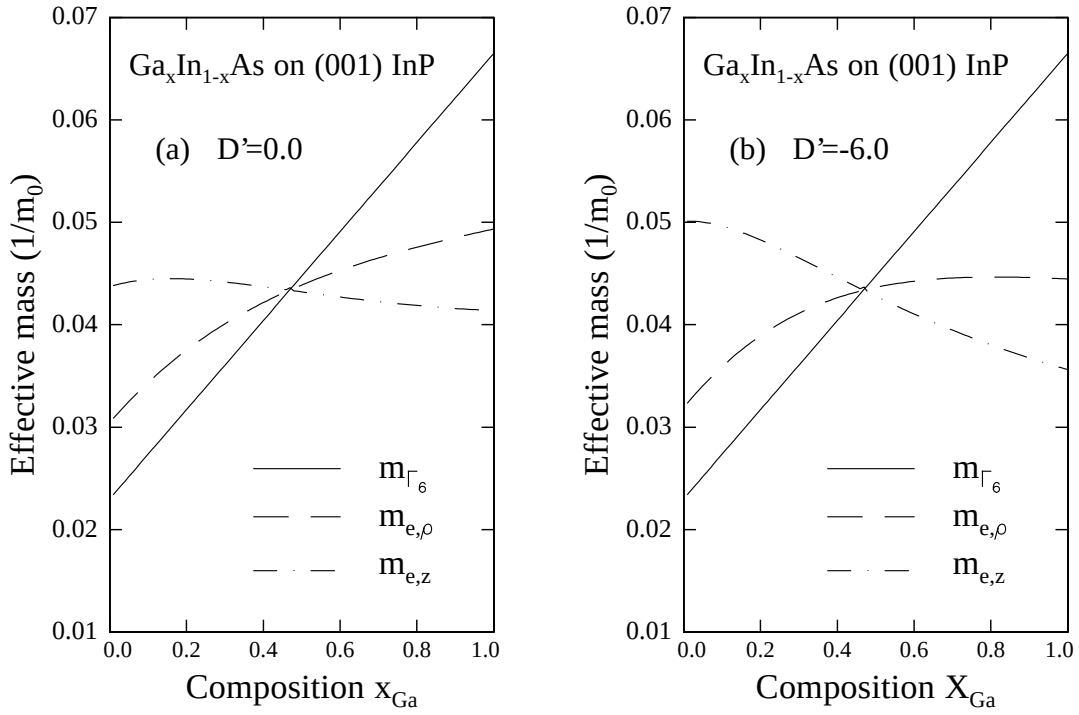

Figure 2.7: Band-edge electron effective masses of $Ga_xIn_{1-x}As$ on (001) InP as a function of Ga composition (strain).

Obviously, the electron mass shows anisotropy, $m_{\Gamma_6} > m_{e,\rho} > m_{e,z}$ under biaxially tensile strain ($x_{\mathrm{Ga}} > 0.468$), and $m_{\Gamma_6} < m_{e,\rho} < m_{e,z}$ under biaxially compressive strain ($x_{\mathrm{Ga}} < 0.468$).

Note that these effective masses are for strained $\mathrm{Ga}_x\mathrm{In}_{1-x}\mathrm{As}$ bulk, and thus do not represent any quantum confinement effect. Due to the non-parabolic effect in quantum wells, the in-plane and $z-$direction effective masses will increase, especially when the well gets narrower or, for a fixed well-width when the well-layer has a smaller band gap and thus a lighter conduction band mass [88, 103]. Therefore, we can expect that the effective masses determined here should be smaller than those we experimentally determined later in chapter 4 [ref. Sec. 4.3].

2.4 Ordering effects in GaInP_2 alloy

Spontaneous CuPt-type long range atomic ordering (LRO) of isovalent $\mathrm{A}_x\mathrm{B}_{1-x}\mathrm{C}$ semiconductor alloys has been observed in organometallic vapor phase growth of GaInP_2 [21,104–110], GaInAs [111,112], and many other III-V systems on (001) substrates. The ordered phase consists of alternate cation monolayer planes $\mathrm{A}_{x+\eta/2}\mathrm{B}_{1-x-\eta/2}$ and $\mathrm{A}_{x-\eta/2}\mathrm{B}_{1-x+\eta/2}$ stacked along the $[\bar{1}11]$ or $[1\bar{1}1]$ directions, depending upon the growth conditions and substrate misorientation. The η, $0 \leq \eta \leq 1$, is the long-range ordering parameter. $\eta = 0$ corresponds to the disordered phase, while $\eta = 1$ corresponds to the perfectly ordered phase. In spontaneously ordered semiconductor alloys, the ordering is not perfect. It depends on growth temperature, growth rates, III/V ratio, substrate misorientation, and doping. As known, an ordering parameter of $\eta \simeq 0.5$ is readily achievable with careful control of the growth parameters [113].

When the zinc-blende disordered alloy forms the long-range ordered CuPt-type super-lattice, the unit cell is doubled, the Brillouin zone is reduced by half, and the point-group symmetry is changed from tetrahedral (T_d) to trigonal (C_{3v}). The folding states from the $L-$point depress the Γ_6^c conduction band [23, 24, 30]. On the other hand, the LRO induces a lattice mismatch and therefore causes an additional quantization along [111] direction. These result in a series of predicted

and observed changes to material properties, e.g., effective masses [66, 114–116], band-gap reduction and valence-band splitting [30,106,112].

The effect of band-gap reduction can be described as

$$dE_g(\eta) = \eta^2 \Delta E_g(\eta = 1)\,, \tag{2.43}$$

which is mainly due to the depression of the conduction band. A theoretical value of ~ 0.71 [117] as well as a experimental value of ~ 0.80 [105] of the band-gap reduction was suggested from such a depression. Here $\Delta E_g(\eta = 1)$ is the band gap reduction of the perfectly ordered alloy relative to the perfectly random alloy. It is noteworthy that there exists an argument about this parameter in the literature. For example, Wei *et al.* predicted $\Delta E_g(\eta = 1) = -0.32$ eV for strain-free bulk alloy based on the first-principles, local density approximation method [25,26,106], while Ernst *et al.* gave a value of -0.471 eV based on photoluminescence excitation (PLE) measurements [31,32]; Geng proposed a value of $\Delta E_g(\eta = 1) = -0.405$ eV for compressively strained QW [118]. These will be identified in Sec. 5.7.1.

The effect of valence-band splitting is just like that caused by spin-orbit interaction, and can be described using a parameter similar to Δ^{so} [29,30],

$$\Delta^{\text{o}}_{111}(\eta) = \eta^2 \Delta^{\text{o}}_{111}(\eta = 1) \tag{2.44}$$

where $\Delta^{\text{o}}_{111}(\eta)$ is the crystal field splitting due to the atomic ordering, $\Delta^{\text{o}}_{111}(\eta = 1)$ is the value of the perfectly ordered bulk alloy. A value of $\Delta^{\text{o}}_{111}(\eta = 1) = 0.20$ eV is given by Wei *et al.* [25,26].

Regarding the fact that while many efforts have been made to investigate such effects on the band-edge electronic structure and effective mass in the **$GaInP_2$ alloy**, very limited work has been done for the GaInP/AlGaInP QWs. In this work we will first build a "modified" model-solid method including the ordering effects [ref. Sec. 5.7.1] to evaluate the band-edge electronic structure and transition energy in the QWs. Then in Sec. 5.5.2, we will carry out a reflectivity study of the effects on the exciton binding energy and reduced effective mass. In Chapter 6 we will further present an ordering-included 6-band $\mathbf{k}\cdot\mathbf{p}$ model and numerical results, illustrating ordering effects on valence band structure and band-edge effective mass.

Chapter 3

Experimental methods

3.1 Introduction

The magneto-optical measurements we made in this work are based on two major parts of the apparatus. One is a BOMEM DA3.01 Fourier transform infrared spectrometer (FTIR), the other is a Zeeman-cryostat.

The advantages of the FTIR over dispersive spectrometers are obvious. They can provide high resolution spectra quickly with high signal-to-noise ratios [119], which enable more informations, especially those from weak features in spectra, to be definitely identified, relative to a traditional dispersive spectrometer. In each measurement, a single detector is used to measure all of the signals simultaneously. Noises from this detector are shared among all of the recorded signals equally. This result is known as *multiplexing* or *Fellgett's advantage*. Compared with the dispersive spectrometer, the FTIR conducts more light to the detector with comparable resolution (since an increase of the resolution does not require a decrease of intensity), which is known as *throughput advantage* or *Jaquinot advantage* [120, 121].

The most important component of the FTIR is the Michelson interferometer. Schematically, it is illustrated in Fig. 3.1. Suppose the radiation from a measured sample is monochromatic light with an optical frequency σ. If the path difference Δ of the two beams (denoted as 1, and 2 in Fig. 3.1) varies linearly with time, $\Delta = \nu t$ (ν constant), the output signal is sinusoidally modulated. From the detector, a electrical signal with a frequency $\sigma \times (\nu/c)$ (c is the velocity of light) is obtained. If ν is known, the optical frequency (normally, the wavenumber) of the analyzed light is easily determined.

When the radiation from the measured sample contains multiple-frequency components, which is the realistic case, a complex harmonic analysis of the output signal of the interferometer must be done. The

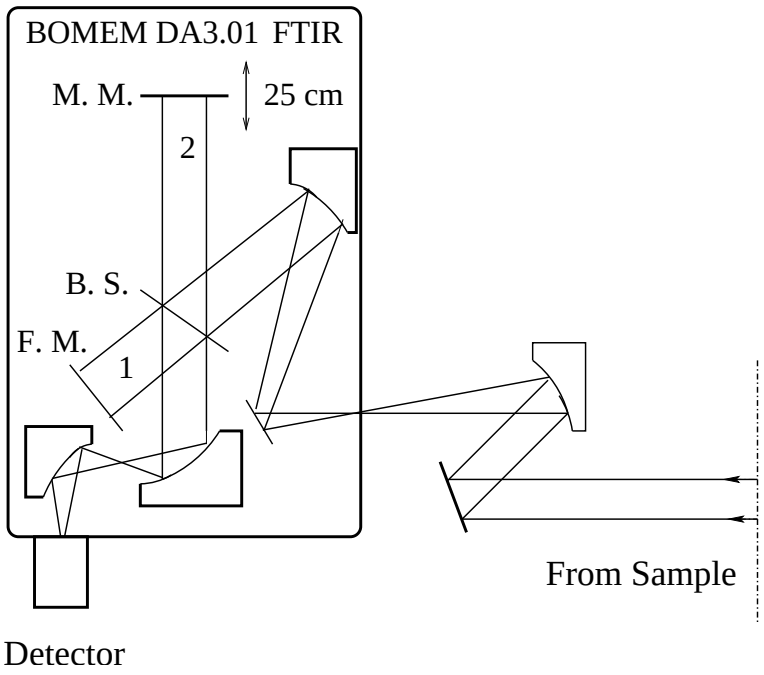

Figure 3.1: Schematic illustration of the part of the experimental apparatus involving the Fourier transform spectrometer.

well-known mathematical tool for this purpose is the Fourier transform, which will reconstruct the analyzed spectrum [122].

To obtain an interferogram, two "orthogonal" determinations are essentially necessary. The first determination is connected to the reciprocal mathematical relationship existing between Δ and σ in the Fourier transform. The second is that the intensity of the interferogram is a function of the Δ. The more accurately Δ is known, the more accurately the spectrum is calibrated. In the BOMEM DA3.01, the measurement of the Δ is achieved by using a simultaneously recorded additional interferogram of a He-Ne laser whose wavenumber is exactly known. This provides the FTIR another advantage of the ability to measure wavelength with very high accuracy and precision (up to 0.01 cm^{-1}).

For all the measurements, samples are placed in the center of the superconducting split-coil magnet built in a Zeeman cryostat, with superfluid helium at a temperature around 1.8 K around them. The magnetic field can be continuously changed from 0 through 6.8 T. The Faraday-configuration of the magnet is used, in which the magnetic

field is parallel to the light traveling out of the cryostat. The optical configuration for certain measurements is illustrated in Sec. 3.2.

3.2 Magneto-optical spectroscopy

In this work, magneto-optical absorption, reflectivity, as well as photoluminescence measurements have been carried out, with the following optical configuration.

3.2.1 Photoluminescence

Photoluminescence (PL), laser power-dependent PL, and magneto-PL were performed on ordered $Ga_xIn_{1-x}P$/AlGaInP quantum wells, to identify optical process in the QWs, and to estimate exciton binding energy and reduced effective mass. The optical arrangement used is schematically shown in Fig. 3.2, without the halogen-lamp involved part. An Ar^+-ion laser with wave-length set at 514.5 nm was used

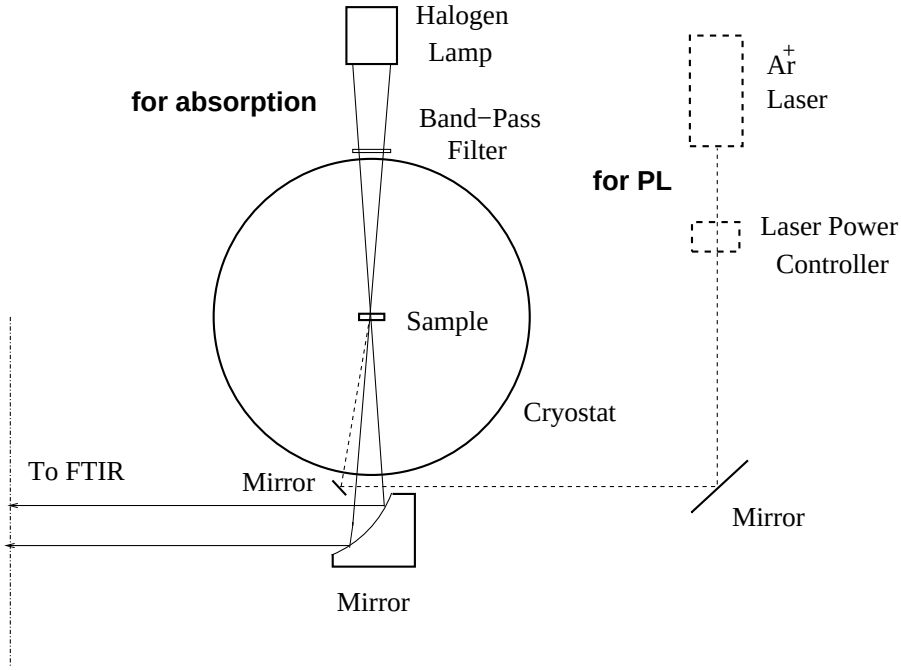

Figure 3.2: Experimental arrangement for PL and absorption. Laser beam path is depicted in dotted lines, whereas IR-path in full lines. For absorption the lamp is used.

as exciting source. Light from the laser first passed through a laser-power-controller, which kept the output power stable and drastically reduces the laser noise in a frequency range of $1-30$ kHz. With the aid of a small mirror, the light was directed to the sample as a spot with the radius of $\sim 300\mu$m. The size of the spot in one way insured an achievement of high excitation power-density without too high laser-power requirement, in the other way, and was very important, reduced the disturbance caused by the position change of the sample during the measurement. Due to the intrinsic property of the cryostat, the part of the sample rod immersed in the superfluid helium got shorter during the measurement, as the helium was exhausted. This resulted in a temperature change of the rod, and finally changed the sample position relative to the laser spot due to the thermal expansion of the rod. For the excitation-density dependent measurement, this change was estimated as $\sim 20\mu$m. For the magneto-PL, however, it was much larger, as the time available for the whole measurements covering $0-6.8$ T magnetic fields was much shorter (only about 3 hours, compared to about 7 hours for excitation-density dependent measurement). This will be seen in Sec. 5.4. Concerning the FTIR part, a quartz (visible) beam-splitter* and an LN_2-cooled Ge detector were used.

3.2.2 Absorption

Magneto-optical absorption has found its successful application in the study of the GaInAs/InP QWs in this work. In Fig. 3.2 the optical arrangement for the absorption measurement is illustrated. In this case, a halogen-lamp with 50 W output power was used as excitation source, but without the laser-involved parts. A band-pass filter constructed with a WG280 and a RG830 was used to reduce the sample-heating effect during the measurement. With the aid of a focusing lens ahead of the lamp, the light was focused onto the sample with a radius of $\sim$1.5mm. About the FTIR part, the quartz (visible) beam-splitter and a Ge-diode detector† were employed. The configuration insures a spectral range of $5,000-10,000$ cm^{-1} at a resolution of 4 cm^{-1} (0.5

*It covers a spectral range of $4,000-25,000$ cm^{-1}

†It covers a spectral range of $6,000-10,000$ cm^{-1}.

meV) to be accessible. To avoid the disturbance from the water and CO_2 absorption in the regime between 0.87 and 0.92 eV [70], the FTIR was evacuated. The optical path outside the FTIR was enclosed with a thin plastic film, and dried by an air-dryer*.

3.2.3 Reflectivity

Although absorption measurement is powerful in examining the transition processes in quantum well, as proved in studying GaInAs/InP QWs, its power is drastically reduced in studying GaInP/AlGaInP QWs due to the smaller energy gap of the GaAs substrate [ref. Sec. 5.2]. In contrast to absorption, reflectivity circumvents the disturbance of the GaAs substrate and/or the Fabry-Pérot interference in performing exciton related measurement, as will be discussed in Sec. 5.3.

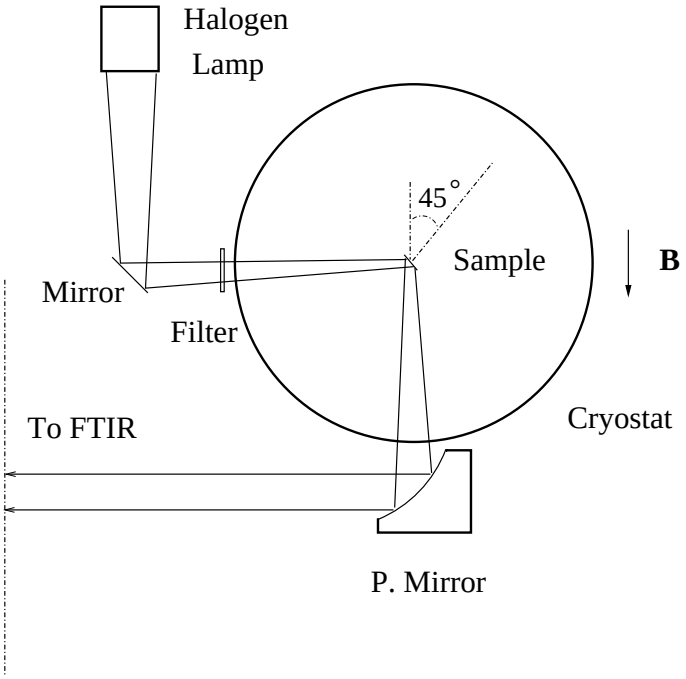

Figure 3.3: Sample arrangement in the cryostat for the reflectivity measurement.

Figure 3.3 shows sample configuration in the cryostat. The growth axis of the sample was rotated 45° relative to the magnetic field axis, and therefore the value of the magnetic fields given by the magnet

*Thanks to Enno Baars for his excellent work.

had to be scaled with a factor $\cos 45^\circ = 0.707$. A halogen lamp was used as excitation source, as in the absorption measurement. A band-pass filter constructed with KG3 and OG530 was inserted between the lamp and the cryostat. With the aid of a parabolic mirror, a light dot slightly larger than the sample surface was obtained to totally cover the sample. This insures the precise average transition energy of a sample over whole the sample surface to be recorded. The importance will be shown in Sec. 5.7. To gain a reflectivity spectrum, the quartz beam-splitter and a Si-diode detector* were used in the FTIR part. A spectral range of $11,500 - 18,000$ cm^{-1} at a resolution of 4 cm^{-1} (0.5 meV) was warranted.

3.3 Spectroscopic derivative

In order to employ the exciton theory described in Chapter 2 to analyze experimental absorption and reflectivity spectra, it is important first to accurately determine the resonance energy of excitonic features. However, it is not always easy to do so in tensile strained quantum well, or in which case there is a big band-gap at the Γ point of the $\mathbf{k}$ space, due to the weak excitonic feature†. Sugawara *et al.* found in their magneto-optical absorption study of strained GaInAs/InP QW that, while spectroscopic positions of the absorption peaks for compressively strained samples were easily determined, those for tensile strained ones were difficult to obtain because of large uncertainties in the broad and weak spectra [6]. The situation in GaInP/AlGaInP QWs is even worse, because of an additional Fabry-Pérot interference.

As known, in analyzing broad overlapped band of optical spectra, curve-fitting method has already found its use. However, to obtain accurate information, a clearly known number of peaks in the band and the profile function of each peak are required, which are in practice difficult to know in advance. Proper derivative operation on the experimental spectra can in part overcome these difficulties [54].

*It covers a spectral range of $8,500 - 50,000$ cm^{-1}.

†Excitonic absorption is inversely proportional to the exciton binding energy E_b, and the E_b takes a larger value for wider band gap material [47]

Since an infrared or visible spectrum can be interpreted as a mathematical function, its derivative can be calculated [56]. The derivative (accompanied by smoothing) of a spectrum can be taken a number of times, producing derivatives of different orders. One key feature of spectroscopic derivative is the observation that, relative to the original spectra bandwidth, the derivative centroid bandwidth decreases to 53%, 41%, and 34% in the second, fourth, and sixth orders, respectively, for Lorentzian bands. This feature forms the basis of resolution for overlapping bands, and facilitates the detection of poorly resolved absorption peaks arising from weak transitions. Another important issue is that derivatives can eliminate, or at least partially remove, the shifts of peak positions caused by background absorption (or reflectivity). This can be clearly seen in the following discussion.

In the case of a Lorentzian line shape of a particular peak, the absorption spectrum can be assumed as a summation of a Lorentzian function and a polynomial series for the background:

$$S(\nu) = \frac{AK}{1 + \pi^2 K^2 (\nu - \nu_0)^2} + \sum_{i=1}^{n} a_i \nu^i \,, \tag{3.1}$$

where $i \geq 1$, $K = 2/(\pi \Delta\nu)$, $\Delta\nu$ is the FWHM of the Lorentzian function. For the simplest case where the background is linear, $i = 1$, the peak of $S(\nu)$ does occur at $\nu \simeq \nu_0 + a_1/2A\pi^2K^3$, not at $\nu = \nu_0$. The shift of the peak maximum to higher energy is obvious, especially for a lower (A is small) and/or flatter ($\Delta\nu$ is large) peak incorporated on a stronger (a_1 is large) background. However, the peak maximum of the second-order derivative of $S(\nu)$ occurs obviously at $\nu = \nu_0$. In this way, the influence of a background on the peak position is totally eliminated. In practice, the background effect is nonlinear. The coefficients of higher order term a_i, however, turned out to be smaller than a_1 in the energy region we are interested in. Nevertheless, higher order derivatives diminish the background effect further, and sharpen the lines due to higher excited exciton states.

To calculate a spectroscopic derivative, the simplest way is the "point difference" method, where the difference in Y values between successive data points is calculated, then plotted versus wave-number. As a variant of it, the "gap" method, which can adjust the "gap" as

multiple integer of the data spacing in a spectrum. An advantage of this method is its increasing the signal-to-noise ratio (SNR) of derivative without introducing significant movement of the peak maximum if the data interval used is not as large as the half value of the FWHM of the peak. It is therefore especially fitted to deal with low SNR spectra. As general guidelines [57], it is better to take the derivatives step by step, e.g., two first-order derivatives rather than one second-order derivative. If necessary, smooth the derivative between each step as well. Note that, the differentiation will introduce additional noise into the spectrum, and therefore needs appropriate smoothing process to be performed after certain order derivative operation. We will show this later in chapter 4 [ref. Sec. 4.4], and discuss the proper derivative order in our case.

3.4 Control of multiple-beam interference

For layers of material which have little absorption at $h\nu < E_g$, light may travel through the sample many times to give rise to a multiple-beam interference. In certain cases, the wavelength difference of two adjacent constructive (or destructive) interference patterns is so small that this interference will hinder the real excitonic line from being detected. Figure 3.4 shows such a case for an absorption spectrum of a GaInP/AlGaInP QWs.

Consider the behavior of a ray of unit amplitude traveling through a medium of refractive index n_0 onto a layer of index n_1 and thickness d mounted on a base of index n_2 [123], as shown in Fig. 3.4. Assuming that the refractive index of the film is greater than that of the substrate, then the only phase change on reflection will be that of the directly reflected ray. The phase change on one traversal of the film is

$$\delta = \left(\frac{2\pi}{\lambda} \right) n_1 \left(\frac{d}{\cos \phi} \right) , \tag{3.2}$$

where ϕ is the angle of reflection in the film. The amplitude of the multi-reflected beam relative to the incident beam of unit amplitude

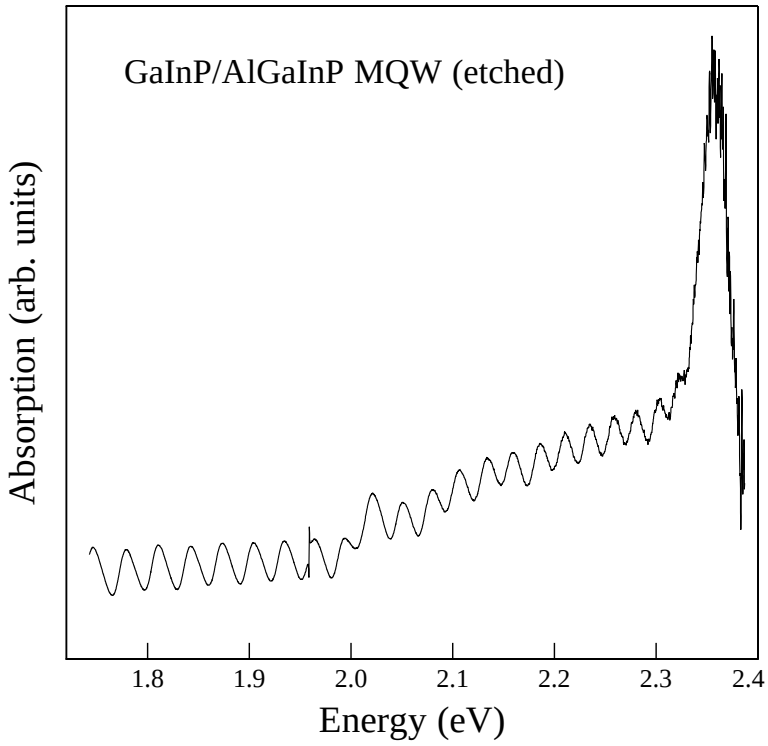

Figure 3.4: Absorption spectrum of an etched GaInP/AlGaInP QW. Fabry-Pérot interference is clearly seen.

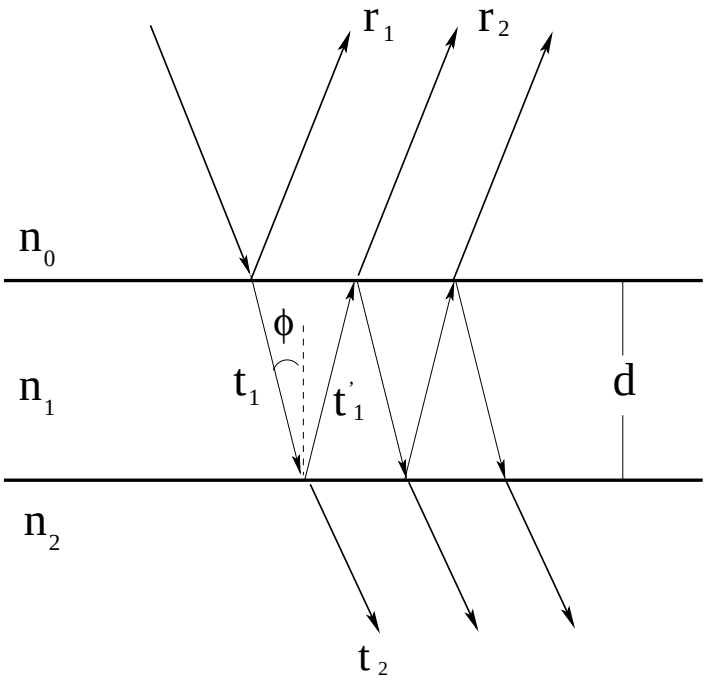

Figure 3.5: Multiple reflection in a high-index film ($n_0 < n_1 > n_2$).

is given by

$$r = -r_1 + t_1 t_1' r_2 e^{-i2\delta} \left(1 - r_1 r_2 e^{-i2\delta}\right)^{-1}, \tag{3.3}$$

and that of transmission is

$$t = t_1 t_2 e^{-i\delta} \left(1 - r_1 r_2 e^{-i2\delta} \right)^{-1} . \tag{3.4}$$

Maximal transmission occurs when the phase change is an integral number M of half wavelengths per traversal, i.e., $\delta = M\pi$; similarly, maximal reflectivity occurs when $\delta = (M + 1/2)\pi$.

By measuring the wavelengths of two adjacent maxima in absorption or reflectivity spectra, and applying the equations

$$\begin{aligned} 2n \left(\frac{d}{\cos\phi} \right) &= M\lambda_1 , \\ 2n \left(\frac{d}{\cos\phi} \right) &= (M+1)\lambda_2 , \end{aligned} \tag{3.5}$$

we have

$$2n \left(\frac{d}{\cos\phi} \right) = \left(\frac{1}{\lambda_2} - \frac{1}{\lambda_1} \right)^{-1} = \frac{1}{\Delta\nu} \tag{3.6}$$

Though it is valid only if n is independent of λ over the range, it can give us a qualitative understanding on the interference pattern in absorption measurement.

As an example, we consider the case shown in Fig. 3.4. We can easily obtain $2nd \simeq 250$ cm^{-1}. Assuming an refractive index n as 3.4 for all the layers (GaInP, AlGaInP) of the sample, we find $d \simeq 6$ μm, which is about the thickness of the whole layers except GaAs substrate for this sample. Indeed, the substrate was already removed in order to carry out the absorption measurements.

Bearing this results in mind, we can easily diminish the disturbance of the Fabry-Pérot interference by reducing the thickness of whole layers. Detailed discussion will be presented in chapter 5 [ref. Sec. 5.3].

Chapter 4

Effective mass and indirect valence-band in GaInAs/InP QWs

4.1 Introduction

Recently, many groups have engaged in experimentally determining the effective mass of the GaInAs/InP QW system by using different methods [1,2,6]. However, there still exist uncertainties, because of the drawback of the experimental or theoretical method used. Sugawara *et al.* [6,7] have carried out magneto-optical absorption measurements on a series of $Ga_xIn_{1-x}As$/InP MQW samples with gallium fraction x_{Ga} from 0.34 to 0.58, using single-pass monochromator together with lock-in technique. They succeeded in determining the in-plane effective masses of electrons and holes for compressively strained and lattice-matched samples. However, they couldn't evaluate those for tensile strained samples. The major reason was that the excitonic features of the tensile strained samples were weak and broad, and therefore their peak patterns were difficult to be accurately determined in the magnetic field range of $0-8$ T. Dalfors *et al.* [1] have evaluated the reduced effective masses in GaInAs/InP QWs as a function of strain and well width by means of magneto-photoluminescence excitation (PLE) method in magnetic fields up to 4.4 T, in which range exciton effects play an important role. But note that they have ignored excitonic effects in evaluating the effective masses. On the other hand, none of them was able to evaluate the out-of-plane effective masses of electrons and holes, $m^*_{e,z}$ and $m^*_{h,z}$, simultaneously.

From a fundamental physical point of view, it is interesting to note that while excitonic forbidden transition has been observed in Ga(InAs)/Ga(PAs) MQWs by magneto-PLE study in a magnetic field range of $0-20$ T [9], no similar observation in GaInAs/InP QW system was reported, to our knowledge. Also in this material system,

the indirect valence-band structure was experimentally evidenced by Michler *et al.* [58] and Härle *et al.* [59] in their time-resolved photoluminescence (PL) studies on undoped samples. A drastic increase of the measured radiative exciton lifetime for samples with $x_{\mathrm{Ga}} > x_c$, where x_c is Ga fraction and depends on well width ($x_c \simeq 0.58$ for 4.5 nm-thick quantum-well [58]), was observed, indicating that for $x_{\mathrm{Ga}} > x_c$ the valence band extreme is at $\mathbf{k}_{\parallel} \neq 0$, i.e., the band structure is indirect. Note that the reports on indirect band-structure were from time-resolved PL, also for other material systems [60]. No evidence from magneto-optical study was available.

As a useful tool, the 6-band $\mathbf{k} \cdot \mathbf{p}$ model has been widely employed to analyze the valence-band structure of this material system [6, 8]. However, due to the fact that $\mathbf{k} \cdot \mathbf{p}$ calculation relies to a degree on Luttinger-Kohn valence-band parameters, which are seldom experimentally determined for quantum well systems, it was expected to be difficult to gain a quantitative description of valence-band structure [124]. Sugawara *et al.* concluded that 6-band $\mathbf{k} \cdot \mathbf{p}$ calculations can properly describe their magneto-optical absorption measurements only if strongly reduced Luttinger-Kohn valence-band parameters (γ_1, $\overline{\gamma}$ about half values as large as those determined in Lawaetz's calculations) were adopted [6].

In order to remove the uncertainties, we carry out a systematic magneto-optical absorption study on a series of $\mathrm{Ga}_x\mathrm{In}_{1-x}\mathrm{As}$/InP MQW samples with Ga fraction x_{Ga} varying from 0.30 to 0.70, under magnetic fields up to 6.8 T. Combining experimental results to the theoretical description presented in chapter 2 [ref. Sec. 2.2], we trace out two types of forbidden transitions in compressively strained samples [ref. Sec. 4.3]. These result in a simultaneous determination of all the in-plane as well as out-of-plane (z-direction) effective masses of electrons and holes. Performing derivative operations on the spectra of tensile strained samples, we are able to identify the excitonic peak position accurately, and therefore to evaluate the in-plane reduced effective masses of exciton states unambiguously [ref. Sec. 4.4]. We evidence an indirect valence-band structure by analyzing the topmost valence-band hole effective masses in different exciton states [ref. Sec. 4.5],

and make a comparison with $\mathbf{k} \cdot \mathbf{p}$ simulation as well as with those obtained by magneto-PL on n-type modulation-doped QWs. The ability of $\mathbf{k} \cdot \mathbf{p}$ theory in describing valence-band structure is also discussed [ref. Sec. 4.6.2].

4.2 Experiment

In the experiments, 6 strained/lattice-matched $Ga_xIn_{1-x}As$/InP MQW samples were measured. They were grown by low-pressure metal-organic chemical vapor phase epitaxy at a temperature of 620 °C on the (001) surface of sulphur-doped InP substrates [55, 125]. First, a 150 nm undoped InP buffer layer was grown followed by 10 periods of 10 nm $Ga_xIn_{1-x}As$ QW and 20 nm undoped InP barrier. Finally, a 60 nm InP capping layer was added. The sample structure is schematically shown in Fig. 4.1. The gallium fraction x_{Ga} varies

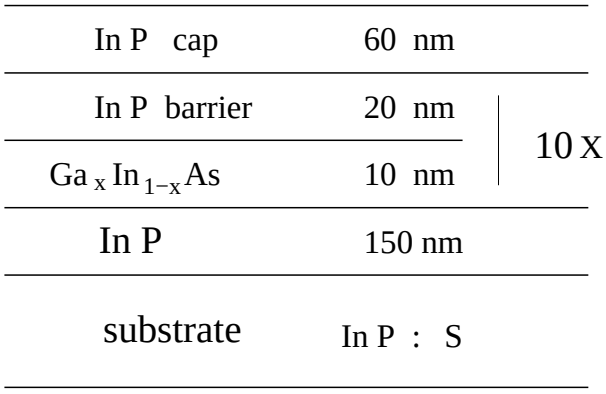

Figure 4.1: Schema of the $Ga_xIn_{1-x}As$/InP QWs' structure.

from 0.30 to 0.70, corresponding to a biaxial strain in QW layer of $\epsilon_{\parallel} = -1.16\% \sim +1.6\%$. As in previous epitaxial runs, composition, strain, and well width have been checked by low-temperature photoluminescence, x-ray diffraction, and absorption spectroscopy [71].

We employed the apparatus described in Sec. 3.2.2 [ref. page 47] to perform our magneto-optical absorption measurements. Figure 4.2 shows the absorption spectra of all the 6 samples under an external magnetic field of $B = 6.8$ T. One remarkable feature is that the spectroscopic position of the first exciton transition shifts to higher energy

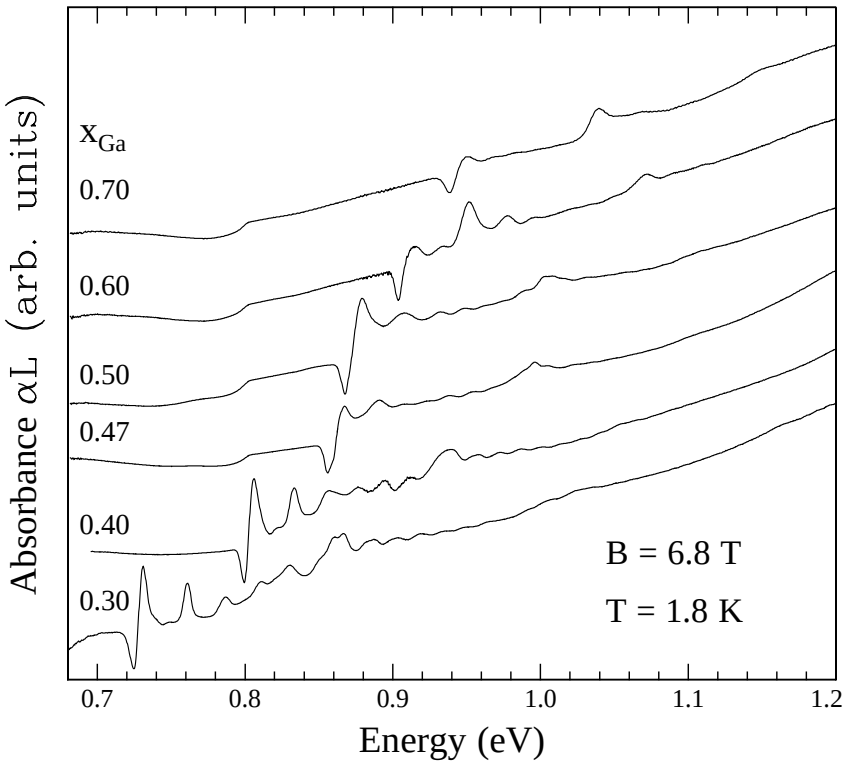

Figure 4.2: Absorption spectra for all 6 $Ga_xIn_{1-x}As/InP$ QW samples measured at low temperature ($T = 1.8$ K) under optimized instrumental conditions.

as x_{Ga} increases from 0.30 to 0.70, showing a well known strain effect: compressive strain reduces the band gap, while tensile strain increases it. Another obvious feature is that as x_{Ga} increases the intensity of the excitonic transition decreases, due to the reduction of the excitonic oscillator strength caused by the increase in the band gap [6]. The line-width (FWHM) also shows increase as x_{Ga} getting larger. It correlates to the Bohr radius of the exciton state. As in the compressively strained sample the Bohr radius is larger than that in the tensile strained ones, the uncertainty of the exciton state in $\mathbf{k}$ space is smaller, leading to a smaller uncertainty in the exciton transition energy (line-width). Taking Eq. (2.2) [see page 23] into account, we can see that the increase in the line-width means an increase of the in-plane reduced effective mass of the exciton state. Overall, the spectra are nearly free of water absorption disturbance, in contrast to a previous study [70]. And very important, they have much higher signal-to-noise ratios than those ever reported in the literature [1, 6, 70]. These let

us to trace out weak features in the spectra, and even to carry out mathematical derivative operation on the spectra [54].

4.3 Two types of forbidden transitions

In the infinite-well approximation, due to the orthogonality of the envelope wave function, only transitions between confined valence- and conduction-states with the same subband quantum indexes n, as shown in Eq. (2.3) [see page 24], are allowed. For finite-depth quantum-wells, however, the envelope wave functions are not exactly orthogonal, which could lead to the observation of transitions with different n, known as "forbidden transitions" [126–128]. Analyzing the allowed as well as forbidden transitions in the regime of the model-solid theory and finite-square-well model described in Sec. 2.2.1 and Sec. 2.2.2, the out-of-plane effective masses of electrons and holes, $m^*_{z,e}$, $m^*_{z,h}$ can be obtained. However, there isn't any report in the recently published work, to our knowledge.

On the other hand, optically forbidden transitions between Landau levels of electrons and holes with different Landau-level quantum numbers were observed in n-type modulation-doped strained GaAs/InGaAs quantum wells by magneto-PL spectroscopy [10, 129]. Recently, optically forbidden transitions of $P-$ and $D-$type exciton states were detected in undoped InGaAs/Ga(PAs) quantum wells by magneto-PLE spectroscopy under high magnetic fields (up to 20 T) [9]. Besides its physical meaning, an important usage of such forbidden transitions is that it can be used together with allowed transitions to determine optical in-plane effective masses of electrons and holes simultaneously, as mentioned before.

Figure 4.3 shows the absorption spectra of the samples (a) $x_{\mathrm{Ga}} = 0.30$ and (b) $x_{\mathrm{Ga}} = 0.40$, respectively, for $0-6.8$ T magnetic fields. The energies of the absorption peaks are shown in Fig. 4.4 as a function of the magnetic fields for both the samples, respectively.

According to the usual selection rule for exciton effects [52], only exciton states with S-symmetry (corresponding to $m = 0$ in Eq. (2.25) [see page 32]) are permitted. Therefore, we first assume $m = 0$ in

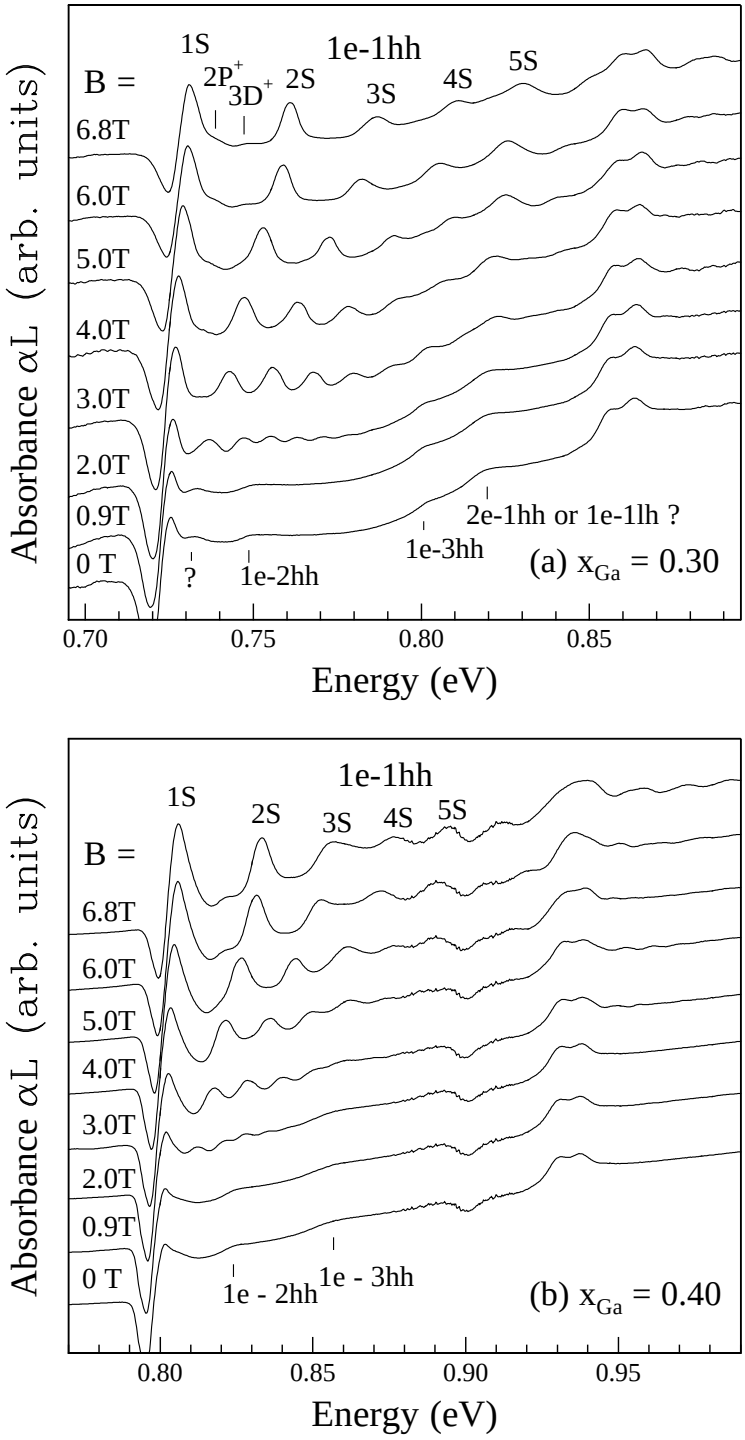

Figure 4.3: Optical absorption of $Ga_xIn_{1-x}As/InP$ QWs with (a) $x_{Ga} = 0.30$ and (b) $x_{Ga} = 0.40$ for different magnetic fields applied parallel to the growth direction of the samples at a temperature of $T = 1.8$ K. Up to $5S$ states of the $1e$-1hh exciton are labeled.

Eq. (2.25) and chose the in-plane reduced effective mass μ as an adjustable parameter for each S-type exciton state. The calculated re-

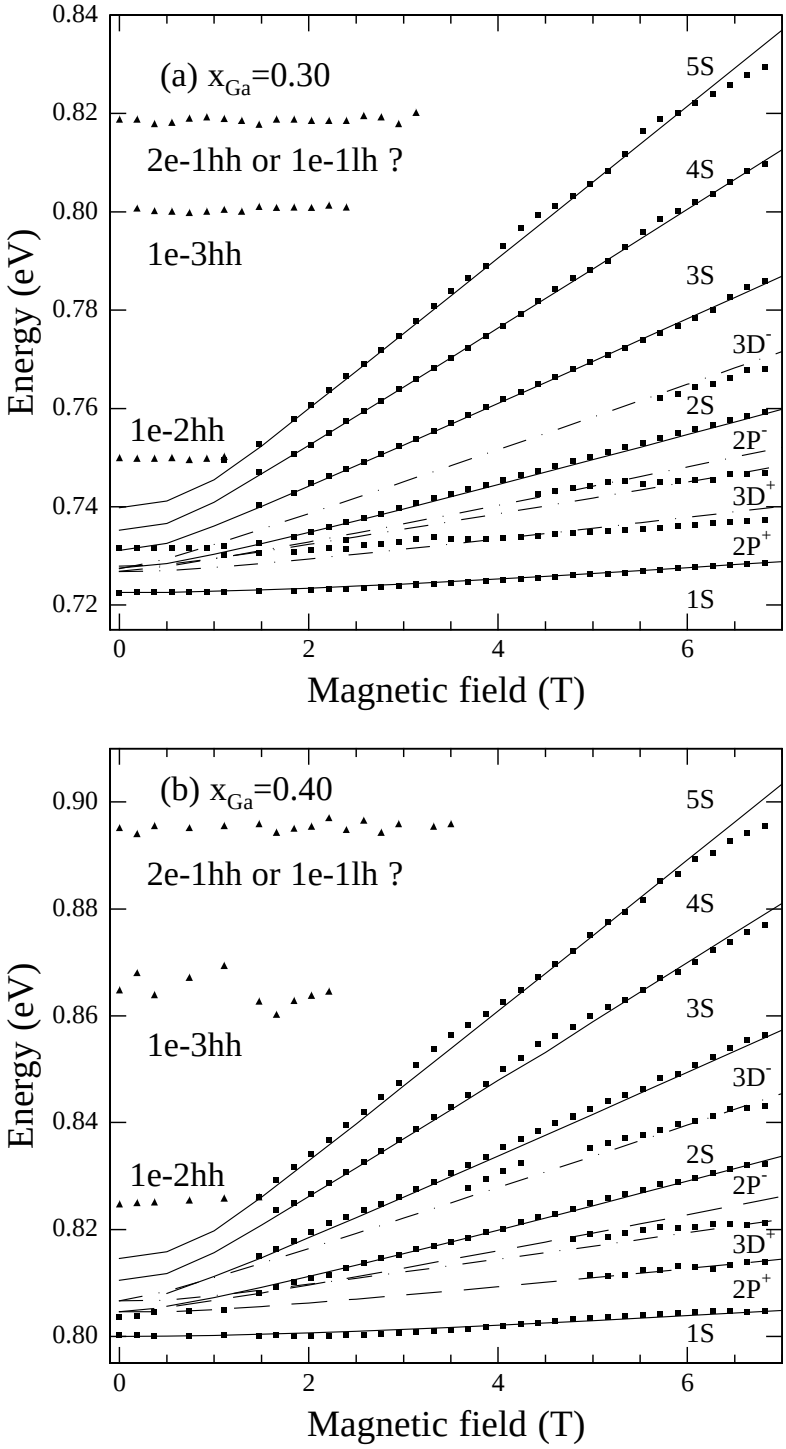

Figure 4.4: Calculated energies as a function of magnetic field for both allowed (solid lines) and forbidden (dash-dots) exciton transitions. Black squares and triangles represent experimental values. The triangles show the forbidden transitions between confined electron and hole states.

sults for the 1e-1hh heavy-hole exciton are shown by the solid lines in

Fig. 4.4. They are in very good agreement with the experimental data for up to $5S$ states. However, besides the S states, there still exist "forbidden" transitions located at low magnetic fields in the range of $0 \sim 2$ T (indicated by triangles in Fig. 4.4), and at high magnetic fields (denoted by squares between exciton ground state and the first two excited states), respectively.

4.3.1 Forbidden transitions of exciton states

In order to interpret the forbidden transition which occurs at high magnetic fields (≥ 4 T) as shown in Fig. 4.4, we assume that they are $P-$ and $D-$type solutions of Eq. (2.25) with $m = \pm 1, \pm 2$, respectively, in the exciton picture. We use the in-plane reduced effective mass of the $1S$ exciton state previously obtained as a constant. By adjusting $m^*_{e,\rho}$ (therefore $m^*_{h,\rho}$), we finally obtain a good agreement between $P-$, $D-$type solutions of the exciton equation (shown by dashed lines in Fig. 4.4) and the experimental data. The obtained effective masses of the electron and hole, $m^*_{e,\rho}$, $m^*_{h,\rho}$ are listed in table 4.1. Also listed are the $m^*_{e,\rho}$ values obtained from the magneto-PL

Table 4.1: Effective masses of electron and hole in the compressively strained $Ga_xIn_{1-x}As/InP$ QWs.

$m^*_{e,z}$ (m_0)	$m^*_{h,z}$ (m_0)	$m^*_{e,\rho}$ (m_0)	$m^*_{h,\rho}$ (m_0)	μ_ρ (m_0)	sample parameters	method
0.062	0.30	0.044	0.124	0.0325	$x_{\mathrm{Ga}} = 0.30$	magneto-optical
0.059	0.36	0.049	0.169	0.038	$x_{\mathrm{Ga}} = 0.40$	absorption
		0.050	0.099	0.033	$L_w = 7.2$ nm	
					$x_{\mathrm{Ga}} = 0.34$	magneto-optical
		0.047	0.099	0.032	$L_w = 9.7$ nm	absorption[a]
					$x_{\mathrm{Ga}} = 0.35$	
		0.047			$x_{\mathrm{Ga}} = 0.30$	magneto-photo-
		0.050			$x_{\mathrm{Ga}} = 0.40$	luminescence[b]

[a] Cite from Ref. [6]; [b] cite from Ref. [55] for n-doped samples

measurements on $n-$type modulation-doped GaInAs/InP QWs [55]. For the slightly larger $m^*_{e,\rho}$ from the magneto-PL on the n-doped samples, an explanation exists in the doping effect. As well known, the

conduction band effective mass is a function of doping. The bottom of the conduction band will become filled and the electron gas become degenerate when the doping level increases. The Fermi level moves up in the band and makes the non-parabolicity of the band significant. The electron mass increases with doping level for electron concentrations larger than 10^{18} cm^{-3} [130]. As the electron concentrations for the samples measured in Ref. [55] was estimated as just 10^{18} cm^{-3}, the doping effect was believed not so strong that significant change in $m^*_{e,\rho}$ would be expected. The agreement between the results of the two methods support the assumption of $P-$ and $D-$type exciton states we have made.

Note that the in-plane effective mass of the heavy-hole we determined is larger than that obtained by Sugawara *et al.* [6]. One reason is that the later was an average value of several low excitonic states. As will be shown in Table 4.5 [see page 83], the in-plane hole effective mass of the ground exciton state is larger than those of two lowest excited exciton-states. Dalfors *et al.* [1] had obtained a much smaller in-plane reduced effective mass $(0.0278\pm0.0003)m_0$ for samples with x_{Ga} =0.33 and 13.5 nm well-width. But they had neglected excitonic effects under a lower magnetic field (below 4.4 T), in which range the excitonic effects still play an important role, as observed in our study.

It should be pointed out that such excitonic forbidden transitions are not detected in lattice-matched and tensile strained samples in our measurements. For the possible reason of the observation of such transitions, scattering mechanisms (impurities, interface roughness or alloy disorder) and the presence of electric fields have been discussed in the literature [9, 96, 129]. As the $P-$, $D-$type transitions are not detected experimentally in the lattice-matched GaInAs/InP QWs with the same sample structure and preparation process, the presence of electric fields should not be the major reason. We note that a weaker peak just above the $1S$ state of the $1e$-1hh exciton is clearly seen for both the compressively strained samples under a low magnetic field, but not for the lattice-matched sample. Such a splitting of the exciton peak can be well described by +1% gallium composition (or equivalent strain) fluctuation. This leads us to assume a scattering mechanisms

here: Due to the alloy composition (or equivalent strain) fluctuation, the electronic states in the quantum well become localized in "imperfect", which forms scattering center. Increasing the magnetic field leads to more excitonic states separating from the absorption continuum, thereby increases the scattering probability, and causes the forbidden transition to show up. On the other hand, decreasing the confining potential height which is the case in the tensile strained samples can substantially reduce the localization tendency and hinder the forbidden transitions from occurring. This is the reason why no forbidden transitions are observed in the tensile strained samples, though the alloy composition fluctuation should also exist under the same sample-preparation condition. However, it shouldn't be unreasonable to expect that it will be observable under much higher magnetic field, when the line shape of the excitonic transition becomes more sharper, letting weak feature to be resolved easily.

4.3.2 Forbidden transitions of confined electron and hole states

To identify the "forbidden" transitions occurring at lower magnetic fields ($0 \sim 2$ T), we use Eq. (2.3) [see page 24]. We analyze several possible transitions from the (m) valence- to (n) conduction-states. The calculated energy difference $\Delta E_{n,m}$ between ne-$m$hh and 1e-1hh is listed in Table 4.2. The measured energy difference ΔE_l between "forbidden" and 1e-1hh 1S state at zero magnetic field is also listed.

Table 4.2: Calculated ($\Delta E_{n,m}$) and measured (ΔE_l) energy differences between ne-$m$hh and 1e-1hh transitions of the compressively strained $Ga_xIn_{1-x}As$/InP QWs at $B = 0$ T. Energy in meV

x_{Ga}	$m^*_{e,z}$ (m_o)	$m^*_{h,z}$ (m_o)	ΔE_{12}	ΔE_{13}	ΔE_{21}	ΔE_{22}	ΔE_1	ΔE_2	ΔE_3	ΔE_4
0.30	0.036	0.326	27.1	72.3	130.5	157.6	27.3	77.8	96.8	127.0
0.40	0.040	0.328	26.5	70.7	116.0	142.5	24.7	64.2	94.2	124.1

As can be seen, the theoretical results are only qualitatively in agreement with the experimental data, especially for the values of

ΔE_{21} and ΔE_3. The reason is straightforward: we have empirically selected the value of $z-$direction electron and hole effective masses $m^*_{e,z}$, $m^*_{h,z}$ as the band-edge effective masses of the corresponding bulk materials, for electrons it is selected as m_{Γ_6} [93]. No strain effect on the effective masses is considered. According to the theoretical results reported by Sugawara *et al.* [6], however, the electron effective mass in GaInAs/InP is anisotropic, and $m_{\Gamma_6} < m^*_{e,\rho} < m^*_{e,z}$ under biaxially compressive strain ($x < 0.468$) [ref. Sec. 2.3.4]. We note that the relation among the m_{Γ_6}, used $m^*_{e,z}$, and determined $m^*_{e,\rho}$ (shown in Table 4.1) is not the case at all. By adjusting $m^*_{e,z}$, $m^*_{h,z}$, and fitting the calculated results to the experimental data, a good agreement is obtained. The results are shown in Table 4.3. Obviously, there exists

Table 4.3: Good agreement between theoretical ($\Delta E_{n,m}$(meV)) and experimental (ΔE_l) data based on new selected $m^*_{e,z}$, $m^*_{h,z}$ values.

$x_{\rm Ga}$	$m^*_{e,z}$ (m_o)	$m^*_{h,z}$ (m_o)	ΔE_{12}	ΔE_{13}	ΔE_{21}	ΔE_{22}	ΔE_1	ΔE_2	ΔE_3	ΔE_4
0.30	0.062	0.30	28.9	77.2	96.5	125.4	27.3	77.8	96.8	127.0
0.40	0.059	0.36	24.7	65.7	94.5	119.2	24.7	64.2	94.2	124.1

now a relation just as aforementioned, $m_{\Gamma_6} < m^*_{e,\rho} < m^*_{e,z}$. To exclude other possible reasons, we have also tried to assume the forbidden transition as "partially allowed", i.e., 1e-3hh, 1e-5hh, 1e-7hh. While the obtained effective mass $m^*_{e,z}$ is nearly identical, however, $m^*_{h,z}$ should be much larger ($> 1.0m_0$), which is ruled out. This provides a direct experimental evidence supporting Sugawara *et al.*'s theory, and demonstrates that the forbidden transitions indicated by the triangles in Fig. 4.4 are between the confined valence- and conduction-states with different quantum numbers, caused by the finite quantum well effect and/or perturbation of the alloy composition.

Note that such forbidden transitions diminish as the magnetic field increases. The reason is that they merge into the allowed excitonic transitions because of their weak oscillator strengths. It has been established that with increasing the magnetic fields the exciton oscillator strength is enhanced [131,132]. Also noteworthy is as shown in Fig. 4.3 and Fig. 4.4 that we could not firmly interpret the "forbidden" tran-

sition near 0.82 eV [in Fig. 4.4(a)] as the 2e-1hh, and that near 0.86 eV [in Fig. 4.4(b)] as the 1e-3hh neither, because the 1e-1lh light hole transition should also be in this region, according to our calculation. Fortunately, this doesn't hinder us from determining the $z-$direction effective mass of the electron and heavy hole.

4.4 Tensile strained QWs studied by derivative technique

Figure 4.5 illustrates optical absorption spectra of two tensile strained samples (a) $x_{\mathrm{Ga}} = 0.60$ and (b) $x_{\mathrm{Ga}} = 0.70$, respectively, recorded under external magnetic fields ranging from 0 to 6.8 T.

Comparing it with Fig. 4.3 [see page 59], an obvious feature is that for the tensile strained samples much fewer and flatter peaks can be identified under the same magnetic fields. It is therefore difficult to accurately determine the peak energy in the tensile strain case. The situation is made clear in Fig. 4.6, where the transition energies of the ground exciton state are plotted as a function of the magnetic fields for a compressively strained (a) $x_{\mathrm{Ga}} = 0.30$, and a tensile strained (b) $x_{\mathrm{Ga}} = 0.70$ QWs, respectively.

Clearly, the diamagnetic shift of the compressively strained sample can be easily fitted to the theoretical calculation with high accuracy. That of the tensile strained sample, however, is difficult or even impossible to be modeled by theoretical results. This indicates that, although absorption spectra of tensile strained samples also possess high signal-to-noise ratio, they cannot be used directly to determine the in-plane effective mass. An important reason resulting in such a difference is that the excitonic feature of the absorption spectra for tensile strained samples is much broader and flatter than that for compressively strained samples [6], making the determination of the peak-position uncertain.

Recalling from the intrinsic property of the derivative operation discussed in Sec. 3.3, we now try to apply derivative operations on the absorption spectra, so as to be able to determine excitonic resonance energy better and thereby gain information on the effective mass and

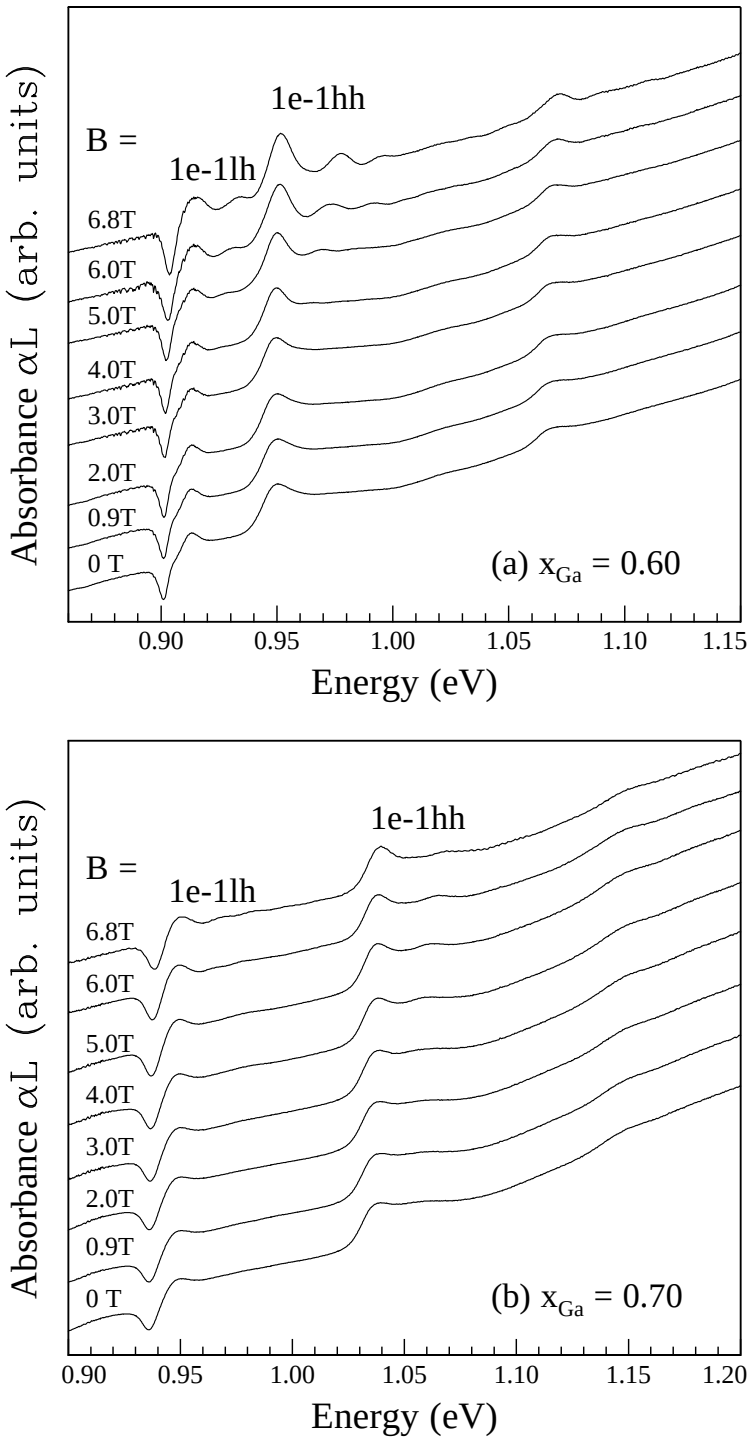

Figure 4.5: Optical absorption of tensile strained $Ga_xIn_{1-x}As$/InP QWs with (a) $x_{Ga} = 0.60$ and, (b) $x_{Ga} = 0.70$, for different magnetic fields applied parallel to the growth direction at low temperature ($T = 1.8$ K).

exciton binding energy.

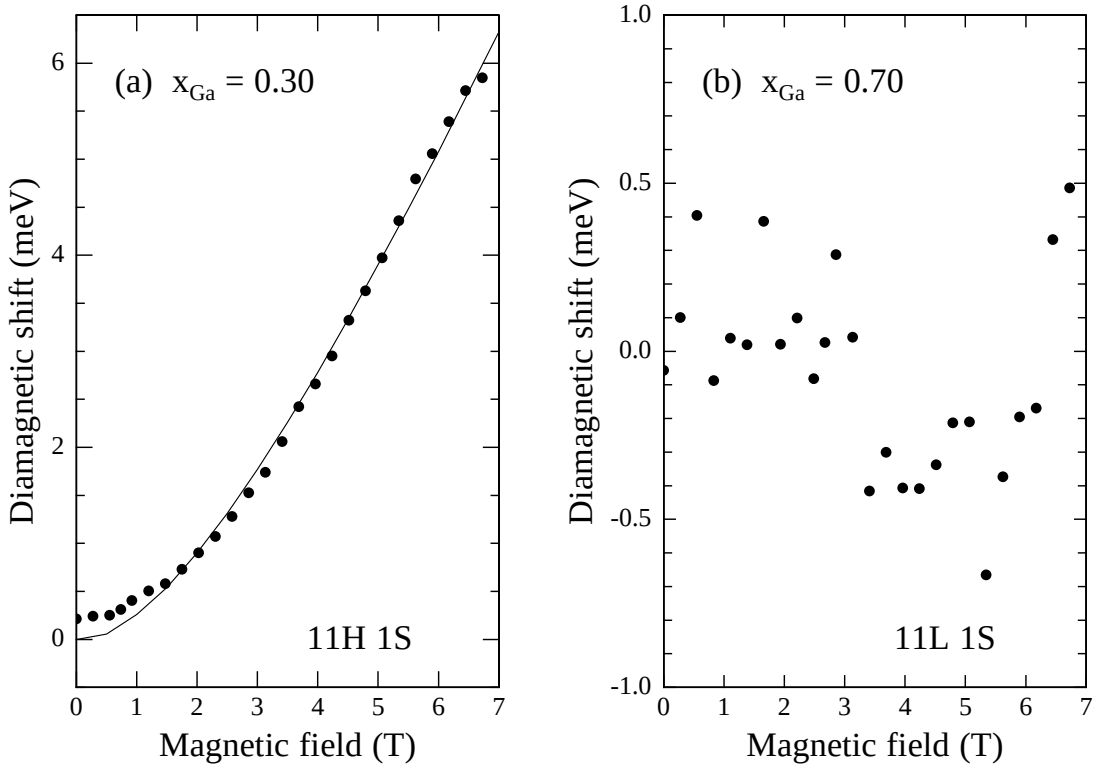

Figure 4.6: Diamagnetic shifts of the first excitonic transition for compressively strained (a) $x_{\mathrm{Ga}} = 0.30$ and, tensile strained (b) $x_{\mathrm{Ga}} = 0.70$ GaInAs /InP QW samples.

4.4.1 Derivative operations for strained samples

Firstly, we probe the possibility and reliability of taking derivative operations on the absorption spectra.

By employing the derivative method described in Sec. 3.3, we evaluate even order derivatives from the absorption spectra for all the samples. Higher order derivatives are obtained by successively operating first-order derivative [57]. After every even order derivative operation, a medium smoothing [133] is performed to keep the derivative spectra having a reasonable signal-to-noise ratio. The derivative spectra are multiplied by -1 necessary to keep their maxima to correspond to the maxima in absorption spectra for second- and sixth-order derivatives.

Figure 4.7 shows the second- and fourth-order derivatives as well as absorption spectra at $B = 5$ T for the (a) $x_{\mathrm{Ga}} = 0.30$, and (b) $x_{\mathrm{Ga}} = 0.70$ samples, respectively. As an important feature, derivatives show more peaks, therefore weak feature shows up, which are difficult to be detected in the absorption spectra. Another remarkable phenomenon

is that the line-widths of excitonic peaks are drastically narrowed, especially for tensile strained samples which have broad line shape in the absorption spectra, making it possible to determine the peak position with higher accuracy. Also the background vanishes. With these advantages, derivatives promise a possible manner in an accurate study of effective mass and exciton binding energy for tensile strained samples.

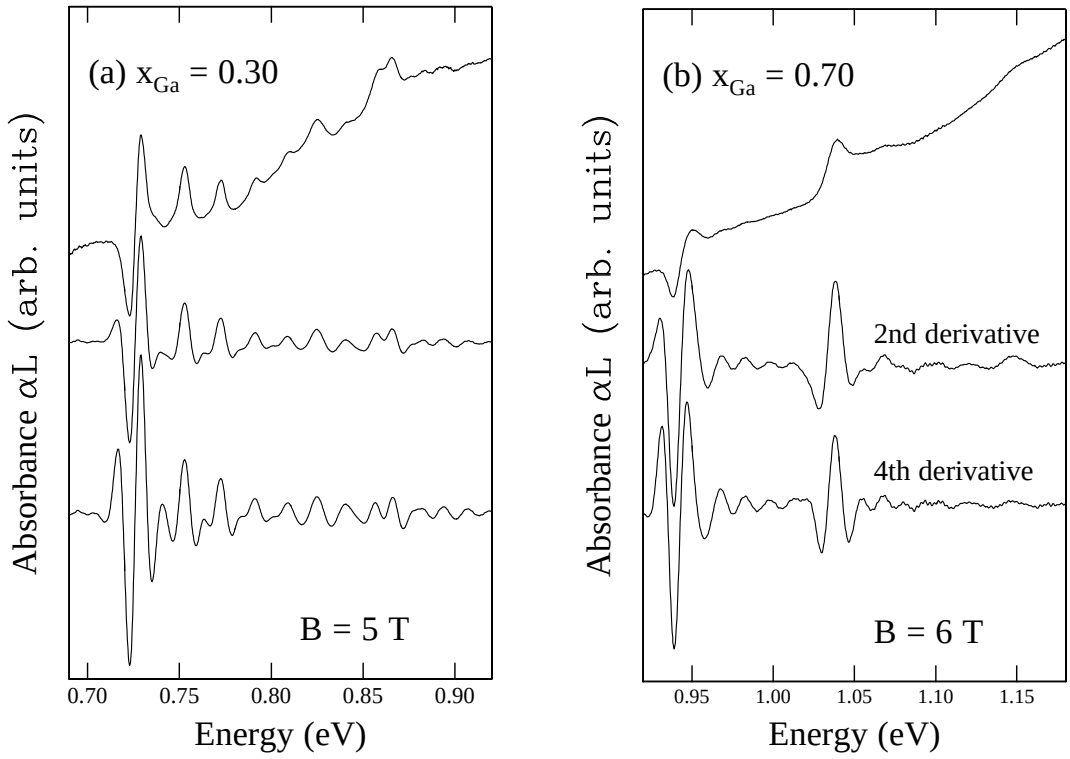

Figure 4.7: Absorption spectra and their second-, fourth-order derivatives for compressively strained (a) $x_{\mathrm{Ga}} = 0.30$ and, tensile strained (b) $x_{\mathrm{Ga}} = 0.70$ $\mathrm{Ga}_x\mathrm{In}_{1-x}\mathrm{As/InP}$ QW samples.

In Fig. 4.8, the diamagnetic shift of the first excitonic transition for the samples with (a) $x_{\mathrm{Ga}} = 0.30$, (b) $x_{\mathrm{Ga}} = 0.40$, (c) $x_{\mathrm{Ga}} = 0.60$, and (d) $x_{\mathrm{Ga}} = 0.70$ are plotted, respectively. They are determined from the absorption spectra (denoted as black squares), as well as from their various order derivatives (denoted as triangles, cross, etc.). The lines in the figures are theoretical fits to the experimental results, based on solving the quasi-two dimensional effective mass equation of the exciton [Eq. (2.25), see page 32].

It is clear that derivatives make no difference to the spectroscopic

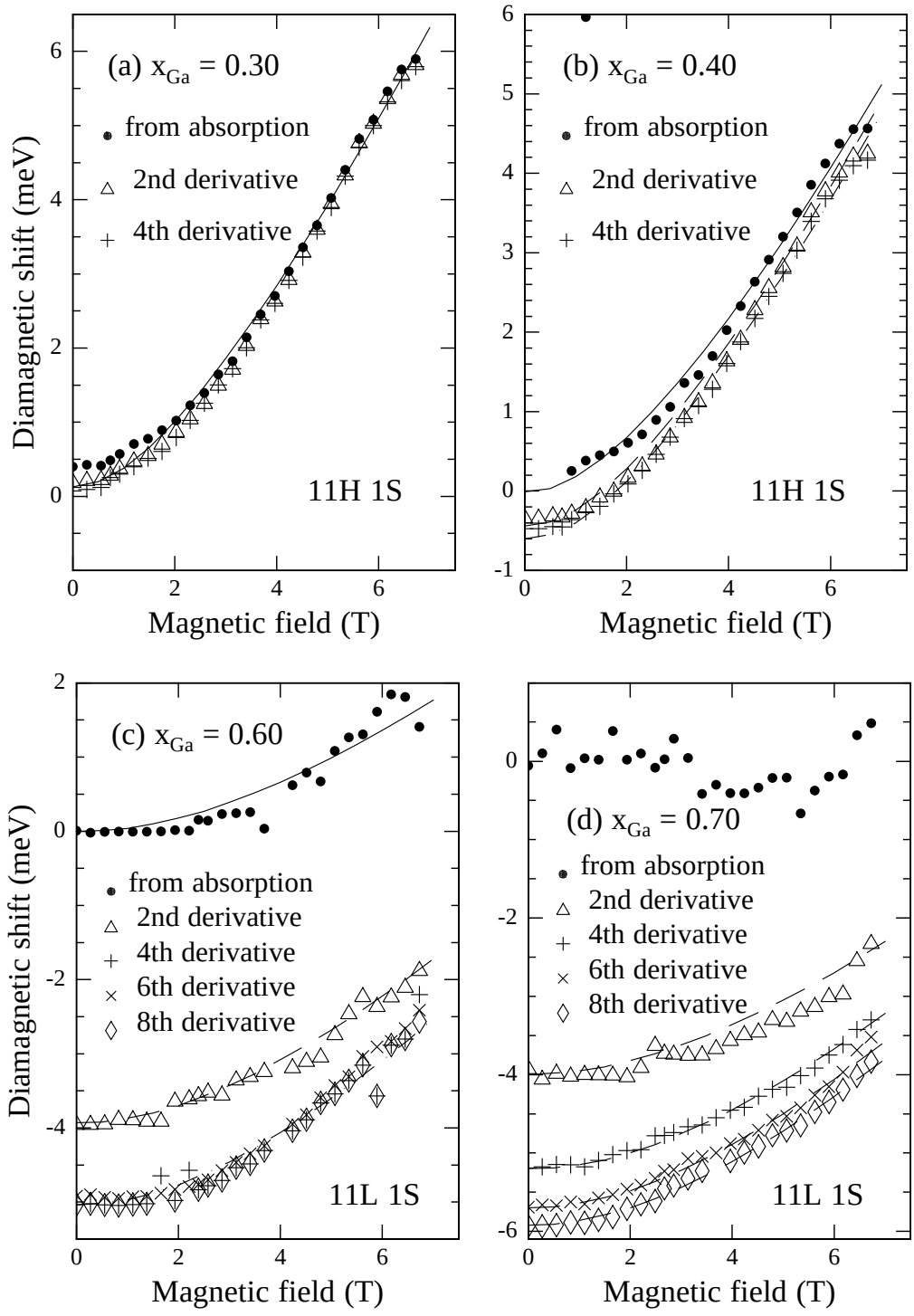

Figure 4.8: Diamagnetic shifts of the first excitonic transition for (a) $x_{\mathrm{Ga}} = 0.30$, (b) $x_{\mathrm{Ga}} = 0.40$, (c) $x_{\mathrm{Ga}} = 0.60$ and (d) $x_{\mathrm{Ga}} = 0.70$ $\mathrm{Ga}_x\mathrm{In}_{1-x}\mathrm{As/InP}$ QW samples. Lines are theoretical results from Eq. (2.25).

position of the peak for the sample with $x_{\mathrm{Ga}} = 0.30$, very little difference for the that with $x_{\mathrm{Ga}} = 0.40$. The second- and fourth-order

derivatives give the same reduced effective mass and exciton binding energy for the compressively strained quantum wells. On the other hand, derivatives take a profound effect on the tensile strained samples. The peak position of the derivative spectrum shifts significantly to lower energies, especially at lower magnetic fields and/or for higher tensile strain. This results in a relatively small reduced effective mass and exciton binding energy to be determined from the derivative spectra. However, it is important to note that the spectroscopic position of the peaks tend to approach a low-energy limit as increasing the derivative order. Recalling the discussion in Sec. 3.3 [ref. page 49], we can firmly conclude that this "red-shift" of the spectroscopic positions of the peak is caused by diminishing the effect of background absorption. The peak will be set to its "real" position after the "background" is totally eliminated by high enough order derivative operation.

With confidence in both the possibility and the reliability of the derivative operation, we can now set our sight on the determination of the exciton effective mass for the tensile strained samples.

4.4.2 Reduced effective mass in tensile strained QW

Though the whole valence band structure is non-parabolic, we can assume without big error that for each individual $S-$type 1e-1h exciton state, it has a parabolic feature, regarding the fact that under the magnetic fields available in this work, the 1e-1h exciton states are near the Brillouin-zone center ($\mathbf{k}_{\|} \simeq 0$) in $\mathbf{k}$ space, and there the degeneracy of the light-hole and heavy-hole subband is well removed by tensile strain*. Such an assumption can be verified by the judgment that if a single μ value can well describe a particular exciton state in the whole range of the magnetic fields or not. By adjusting the reduced effective mass in the quasi-two-dimensional effective mass equation [ref. Eq. (2.25), page 32] we fit theoretical calculations to the experimental results obtained by the absorption spectra and their derivatives, respectively. Thereby, we determine the exciton binding energy and in-plane reduced effective mass.

*We note that the diamagnetic shift of up to 5S exciton are still significantly smaller that the lh-hh valence-subband spacing.

In Fig. 4.9, we plot the diamagnetic shifts of all exciton resonances determined in the (a) absorption spectra, and (b) their second-order derivatives, for the $x_{\mathrm{Ga}} = 0.70$ sample. Obviously, in Fig. 4.9(b) more measured points corresponding to higher S-type exciton states are shown by the second-order derivatives. And very important, good theoretical fits (solid and dashed lines corresponding to heavy-hole and light-hole exciton transitions, respectively) to the experimental data are obtained for up to $5S$ exciton states. This supports the assumption of parabolic dispersion for each individual exciton state. Similar work are also done for higher even-order derivatives, and for the $x_{\mathrm{Ga}} = 0.60$ sample.

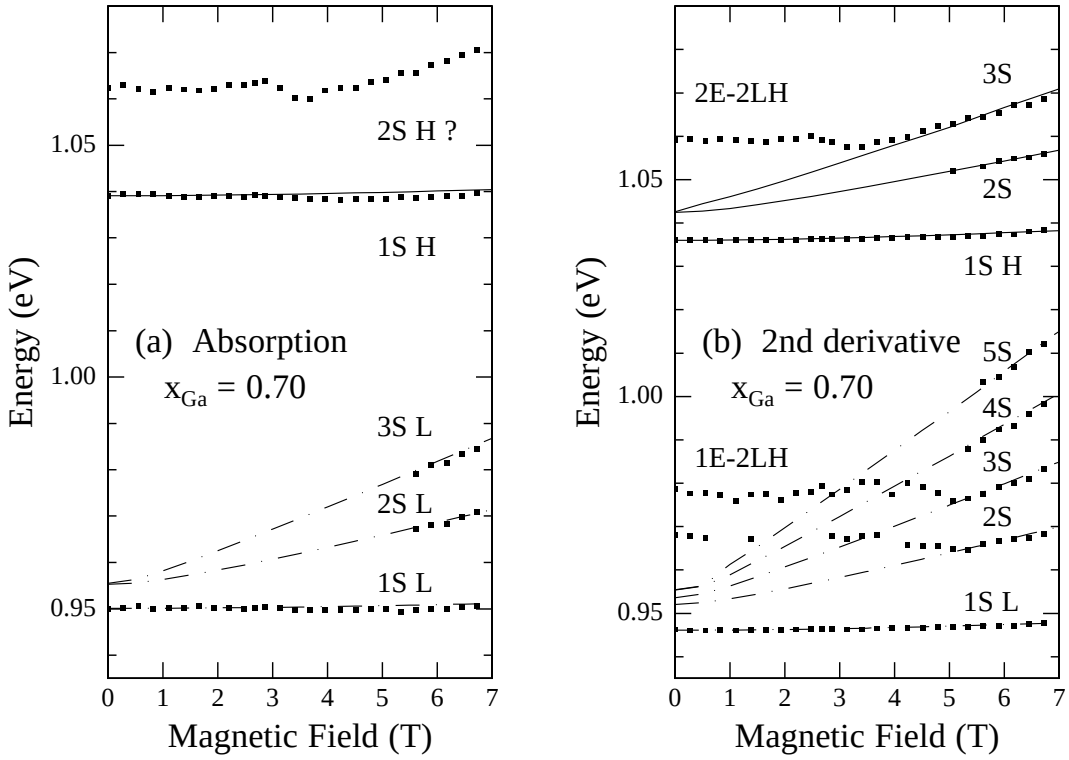

Figure 4.9: Diamagnetic shifts of all excitonic resonances determined in (a) absorption spectra and (b) second-order derivatives for the $x_{\mathrm{Ga}} = 0.70$ $\mathrm{Ga}_x\mathrm{In}_{1-x}\mathrm{As/InP}$ QW sample. Lines are theoretical results from Eq. (2.25).

The derivatives lead the ground exciton state to be definitely determined, as also shown in Fig. 4.8. Besides, they reveal more excited exciton states. And very important, the second- and higher order derivatives obviously show the $2S$ and $3S$ excited states of the $1e$-1hh exciton, which are only partially observable and difficult to be identified in the absorption spectra.

The effective masses of different exciton states determined by the absorption spectra and their derivatives, respectively, are listed in Table 4.4 [see page 82].

Based on the discussions, we can make two conclusions:

1. For the ground exciton state in a tensile strained sample, up to fourth-order derivative is needed to obtain a *near to real* value of the reduced effective mass or exciton binding energy.

2. For the excited exciton states, second-order derivative is already sufficient to evaluate the reduced effective masses and to check weak features which can't be identified in the original absorption spectra.

Overall, the derivatives provide an excellent description of the exciton states in the tensile strained quantum wells. Using them, the effective masses and exciton binding energy can be reliably determined.

4.5 Effective masses of particular exciton states

To obtain the effective masses of particular exciton states for all the samples, we make two assumptions. First, we assume a parabolic dispersion for each individual state of the 1e-1h exciton under medium magnetic fields, as made in Sec. 4.4.2, though the whole dispersion is non-parabolic. We fit the theoretical model to each exciton state by adjusting the reduced effective mass μ_{hh} (μ_{lh}), and can achieve an excellent agreement for up to $4S$ states of the compressively strained, and for up to $3S$ states of the lattice-matched and tensile strained samples. Even for the higher excited exciton states (e.g., $5S$ in Fig. 4.4, page 60) at the high-end magnetic field we used (~ 6.8 T), the agreement between the experimental data and theoretical result is only slightly degraded, due to a small downward deviation of the experimental data from the theoretical result. The possible reason causing the slight difference is the interaction of the excited exciton states with the higher subband states, making the non-parabolic effect significant. The determined reduced effective mass for each exciton state of each sample is listed in Table 4.5 [see page 83].

Then, based on the reports [10] that the conduction band is parabolic for energies approaching 50 meV above the band gap*, we make the second assumption as the parabolic dispersion of conduction band over the energy range we concern ($\leq$ 50 meV). This means we can use one identical value of the in-plane electron-effective-mass for the excited as well as ground exciton states. Using the electron effective masses we determined from the $P-$ and $D-$type exciton forbidden transitions [ref. Sec. 4.3], and those available in the literature [55], the in-plane hole-effective-mass for each exciton state is also evaluated, and listed in Table 4.5 [see page 83].

The results indicate that for highly compressive strain ($x_{\mathrm{Ga}} = 0.30$), the heavy-hole in-plane effective masses of different exciton states are almost identical, showing a nearly parabolic dispersion of the heavy-hole valence subband in $\mathbf{k}_{\parallel}$ space near the Brillouin-zone center. As the compressive strain decreases, the non-parabolic effect shows up, especially at $\mathbf{k}_{\parallel} \simeq 0$. At high $\mathbf{k}_{\parallel}$ value, the value tends to increase, especially for the sample with Ga fraction of $x_{\mathrm{Ga}} = 0.40$.

For the lattice-matched sample, the heavy-hole effective masses of the first three exciton states are much heavier than those of higher states. The light-hole effective mass of the ground exciton state is even negative, whereas the excited states have positive values. These predict a highly non-parabolic dispersion. For the tensile strained samples, the light-hole effective mass of the ground exciton state is negative, while those of the excited states keep their sign in positive. For highly tensile strain, the heavy-hole effective mass of the ground state or even all detectable excited states is also negative, indicating a strong non-parabolic nature.

The results are understood as follows. In the lattice-matched and slightly tensile strained samples, the heavy-hole and light-hole valence subband are nearly degenerate. This results in a high non-parabolicity to the subband dispersion. Under compressive strain, the large heavy hole-light hole subband splitting lifts the subbands, and removes the degeneracy, especially in the highly compressive strain case. It results in a rather parabolic dispersion. Under tensile strain, the first light-

*A support is/will be established in Sec. 4.3.1 and 4.6.1 that in this energy range of conduction band, the electron effective mass only shows very slight change

hole subband is the topmost valence subband. Due to the repulsion from the lower heavy-hole subbands and the coupling to the split-off band, the light-hole exciton has a large reduced effective mass and the light-hole valence-subband has a negative effective mass. On the other hand, repulsions from upper light-hole subband and from lower subbands for the highly tensile strain sample will cause the first heavy-hole subband to have a very large effective mass [6]. Later in Sec. 4.6.2 [see page 4.6.2], we will present a schematic illustration based on a 6-band second-order $\mathbf{k} \cdot \mathbf{p}$ simulation.

4.6 Evidence for indirect valence band

In this section, our major interest is to explore the possible evidence for indirect valence-band structure by means of magneto-optical method and the effective-mass concept.

Magneto-PL study on n-type modulation-doped QWs is another method used to determine the effective mass in quantum wells [55], besides magneto-optical absorption study on undoped QWs. With this method, Reyher had evaluated the effective masses of the electron and hole in n-doped SQWs with the same well width as that of our undoped QW samples.

4.6.1 Effective masses from different measurements

Figure 4.10 shows the composition dependence of the hole effective mass for the ground state of the 1e-1h conduction band-topmost valence subband exciton, which is heavy-hole-like for $x_{\mathrm{Ga}} \leq 0.50$ and light-hole-like for $x_{\mathrm{Ga}} = 0.60$ and $x_{\mathrm{Ga}} = 0.70$, according to a theoretical analysis based on the model-solid theory [ref. Sec. 2.2.2]. It also shows the effective masses determined by Reyher [55] in his magneto-PL study of n-type modulation-doped single quantum well samples as unfilled stars.

For the compressively strained and lattice-matched samples, the effective masses of the 1S state determined by the absorption study is qualitatively in agreement with those presented by the PL study on $n-$doped SQW. The quantitative difference can be ascribed to the

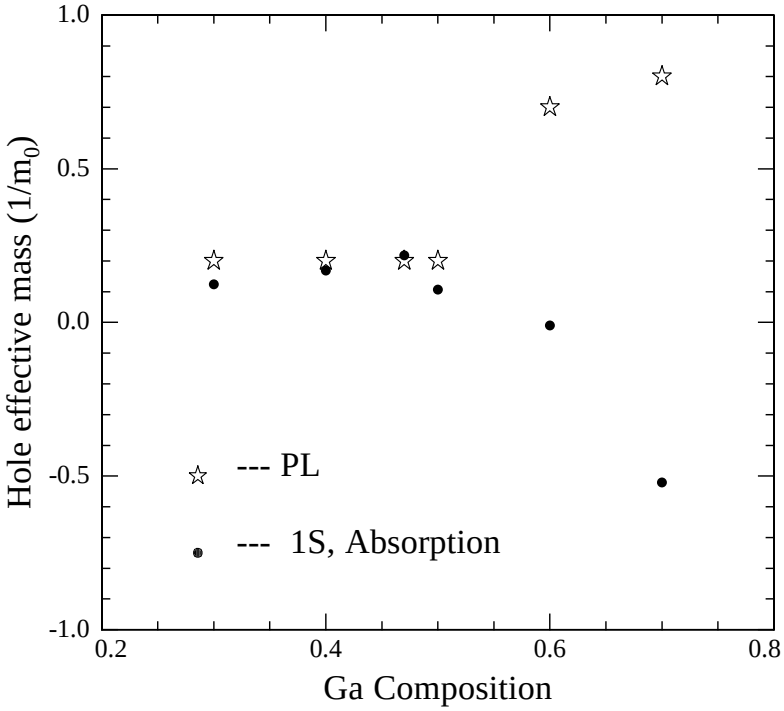

Figure 4.10: Hole effective masses of 1s state of the topmost valence-band exciton, determined by absorption for $Ga_xIn_{1-x}As$/InP QWs. Those from PL are according Reyher [55].

experimental error in the PL study [55] and slight difference in the sample structures *. For the tensile strained samples, however, while the effective masses from the PL study are always positive and increase with x_{Ga}, those from our absorption study are negative. This can't be explained as a result of experimental error. Normally, the negative effective mass of the topmost valence-subband in absorption can be assumed due to the repulsion from lower heavy-hole subband [6]. But it is difficult to explain the always positive value from the PL study in the same manner. We will discuss this below.

In Fig. 4.11, the effective masses of the lowest three states ($1S$, $2S$ and $3S$) of the topmost valence subband-conduction band exciton, determined by the absorption study, are plotted against the Ga fraction. It is clearly seen that for the compressively strained and lattice-matched samples, the effective masses of the different exciton

*The barrier thickness of the MQW is 20 nm, while that of the SQW is visually thicker (5 nm separating layer plus 10 nm InP:S plus 60 nm/150 nm InP capping/buffer layer); MQW is undoped, while SQW is n-doped.

states are positive and only slightly differ from each other for the same sample; for the tensile strained samples, however, while the effective mass of the $1S$ state is negative (also indicated in Fig. 4.10), those of the excited ($2S$, $3S$) states are positive. These suggest that the valence subband structure in the Brillouin-zone center ($\mathbf{k}_{\|} \simeq 0$) is rather parabolic for compressive strain, and is highly non-parabolic for tensile strain. Furthermore, it is clear that while the effective masses from the PL study for tensile strain are significantly different from those of the $1S$ exciton state determined by the absorption study (as shown in Fig. 4.10), they are in the range of the effective mass of the $2S$ or $3S$ state.

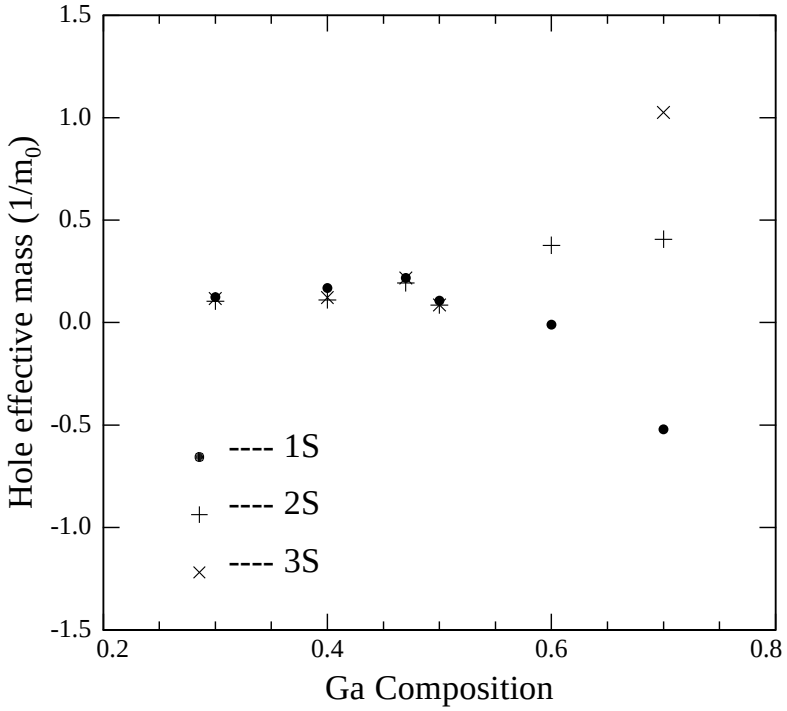

Figure 4.11: Effective masses of the lowest three states of the topmost valence subband-conduction band exciton, for all the $Ga_xIn_{1-x}As$/InP QW samples.

The exciton transition in absorption can be understood as follows. At a low temperature (1.8 K) and a low magnetic field, the exciton concentration created by a low-excitation is very limited in undoped QWs with exciton momentum $\mathbf{K}_{\|} \sim 0$ [refer to Eq. (2.2) on page 23]. These exciton states locate in the region of the valence subband around $\mathbf{k}_{\|} \simeq 0$ [134] [ref. the footnote on page 79]. Under a higher magnetic

field, more exciton states ($2S$, $3S$, ...) are separated from the absorption continuum, as a result of increasing magnetic confinement energy. They appear at higher energy, corresponding to a higher $\mathbf{k}_\parallel$ value in the $\mathbf{k}_\parallel$ space. For the compressively strained and lattice-matched conditions, the exciton ground state has a positive hole effective mass, and shows a sharp peak in the absorption spectrum [83]. It means that the extreme of the valence subband is at $\mathbf{k}_\parallel = 0$. The transition is direct with high probability. For tensile strain, however, the exciton ground state corresponding to the topmost valence subband has a negative hole effective mass, and a flat and weak feature in the absorption spectrum [54]. Only the excited states occurring at higher $\mathbf{k}_\parallel$ value (with higher energy) have a positive hole effective mass. The extreme of the topmost valence subband is therefore at $\mathbf{k}_\parallel > 0$. Note that in the tensile strained samples the topmost valence subband is light-hole like, which has weaker oscillator strength than the heavy-hole subband does [134]. This is the reason why the $1S$ transition is weaker than it is in the compressively strained samples.

In the n-doped SQWs studied by magneto-PL, the concentration of the electrons is estimated to be 1×10^{12} cm^{-2} [55]. The electrons fill the conduction band up to $\Delta E = E_F - E_g \simeq 40 - 50$ meV and correspondingly $k^f_{\parallel,F} \sim 0.25$ nm^{-1} *. In the case where the extreme of the topmost valence subband occurs at $\mathbf{k}_\parallel \neq 0$ but in the range of $k_\parallel < k^f_\parallel$, the filled-up conduction band will make the transition from conduction band to "indirect" extreme as "direct", that is $\Delta\mathbf{k}_\parallel = 0$. And the LO phonon-assisted transition plays a minor role. The hole effective mass is therefore corresponding to the dispersion around the valence-band extreme, and is positive. The difference in transition mechanism between PL of n-doped and absorption of undoped QWs is schematically shown in Fig. 4.12.

Based on the discussions above, the following conclusions can be made: (i) The absorption transition in undoped QWs corresponds to the excitonic transition with its ground state of 1e-1h occurring at $\mathbf{k}_\parallel \simeq 0$, and excited states at $\mathbf{k}_\parallel > 0$, while PL transition in n-doped

*using the relation $k_\parallel = \sqrt{2\pi n_{2D}}$, where n_{2D} is the $2D$ density of electron states, and selecting the electron effective mass as $0.05m_0$. Here parabolic band is assumed.

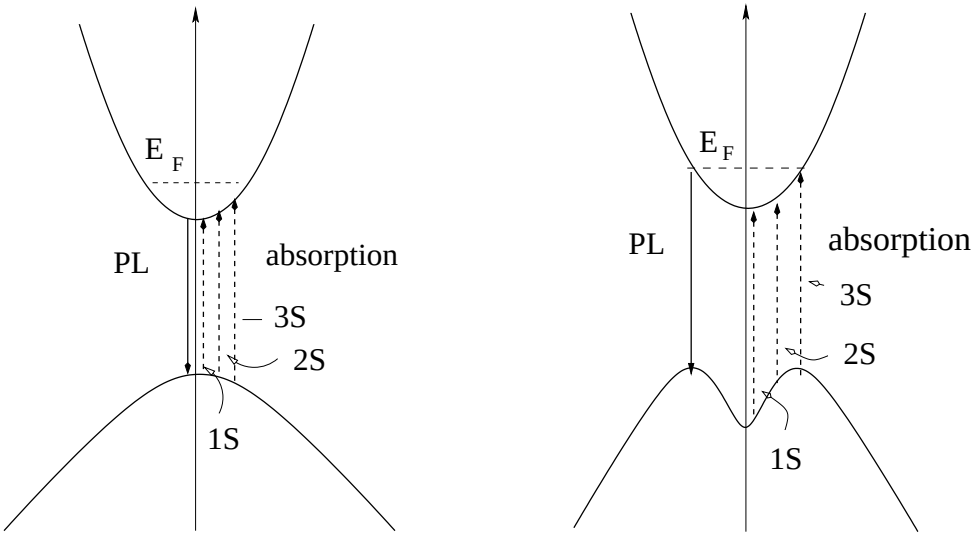

(a) compressive strain (b) tensile strain

Figure 4.12: Schematic of possible transition for absorption in undoped, and PL in n-doped $Ga_xIn_{1-x}As$/InP QW samples, with (a) compressive strain and (b) tensile strain.

QWs tends to occur at the valence-band extrema; (ii) With strain changing its property from compressive through absence of strain to tensile strain, the extreme of the topmost valence subband moves to $\mathbf{k}_{\|} > 0$, according to the determined effective masses in the absorption study, and an indirect band gap occurs. The initiation of the indirect band is in the range of around $x_{\mathrm{Ga}} \sim 0.60$ for 10 nm quantum wells, where the effective mass of the exciton ground state begins to be negative, in our case. This is in agreement with the results from time-resolved photoluminescence study [58, 59]; (iii) Though both the PL study on n-doped and the absorption study on undoped QWs can be employed to evaluate effective masses, the latter is a better choice as it provides a real picture of the valence subband structure near the Brillouin-zone center, and therefore can serve as a good candidate for experimentally detecting indirect band structure.

4.6.2 Can the $\mathbf{k} \cdot \mathbf{p}$ model quantitatively describe the valence-band structure ?

To make a comparison of the hole effective mass with theory, we carried out a 6-band second-order $\mathbf{k} \cdot \mathbf{p}$ simulation [8, 37]. The calculated ef-

fective mass as well as band structure of the topmost valence-subband is plotted in Fig. 4.13, for $x_{\mathrm{Ga}} = 0.30$ and 0.70, respectively, with a well-width of 10 nm. The effective masses determined by the absorption study are plotted as black dots.

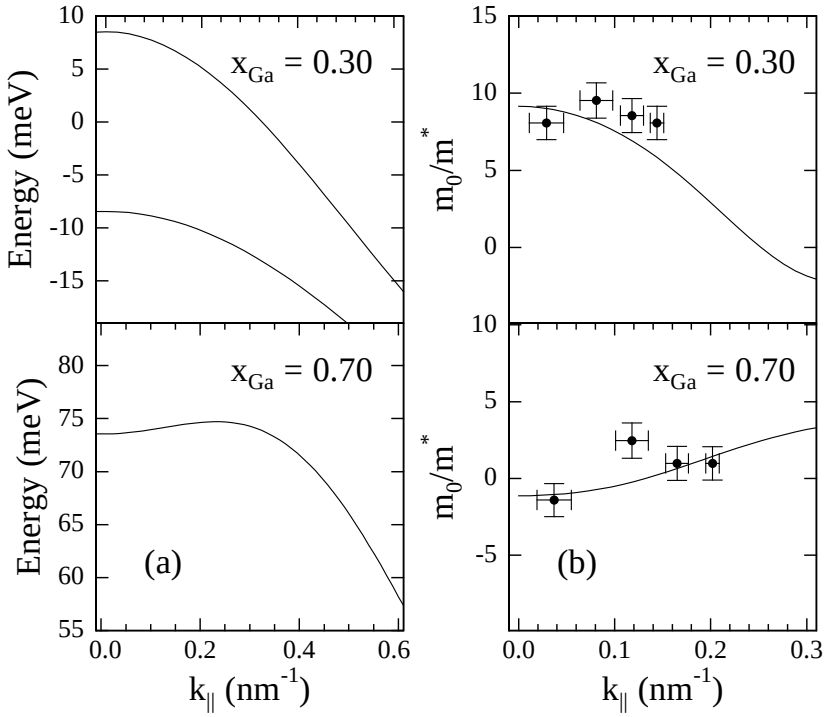

Figure 4.13: Numerical band structure (a) and effective mass (b) calculations using 6-band $\mathbf{k}\cdot\mathbf{p}$ theory for 10 nm $Ga_xIn_{1-x}As/InP$ quantum wells.

The $\mathbf{k}_{\|}$ value corresponding to each exciton-state is estimated with Eq. (2.1) at the magnetic field in which the excited exciton states beginning to be detectable, e.g., $B \simeq 2$ T for the $x_{\mathrm{Ga}} = 0.30$ sample and $B \simeq 4$ T for the $x_{\mathrm{Ga}} = 0.70$ one*. The uncertainty of the exciton state in $\mathbf{k}$ space is estimated from the line-width (FWHM) of the exciton transition, ~ 6 meV and 10 meV for the $x_{\mathrm{Ga}} = 0.30$ and 0.70 samples, respectively, and shown by the error-bars in Fig. 4.13(b). We found that a qualitative agreement can be obtained for compressive strain by using the Luttinger-Kohn parameters proposed by Sugawara *et al.* [6], $\gamma_1 = 10.8 - 6.6\,x_{\mathrm{Ga}}$, and $\overline{\gamma} = 4.4 - 3.0\,x_{\mathrm{Ga}}$, which were significantly smaller than the values calculated by Lawaetz [135] (about one-half

*As $\mathbf{K} = \mathbf{k}_e + \mathbf{k}_h$ and for exciton transition $\Delta\mathbf{k} = 0$, there is $\mathbf{k}_{\|} = \mathbf{K}/2$

of the Lawaetz's values). For tensile strain, however, normal values (nearly the same as Lawaetz's values) have to be used. To understand the difference, we rely on the Bohr radius of the exciton state and the relation between the Luttinger-Kohn parameters and the hole effective masses, $m^*_{\rm hh} = m_0/(\gamma_1 - 2\overline{\gamma})$ and $m^*_{\rm lh} = m_0/(\gamma_1 + 2\overline{\gamma})$ [6]. For the tensile strained samples, the Bohr radius of the ground exciton state is near to the well-width in our case, while for the compressively strained samples, the radius is two times as large as the well-width. It makes the well-layer in the compressively strained samples much like a two-dimensional case. Stronger quantum-confinement effect in compressively strained samples leads to a heavier in-plane hole effective mass, and therefore a set of smaller Luttinger-Kohn parameters. The calculation shows that, for compressive strain, valence-band structure is rather parabolic with its extreme occurring at $\mathbf{k}_{\|} = 0$. The effective mass of the heavy-hole is positive over a large range in $\mathbf{k}$ space. For tensile strain, however, the topmost valence-band is highly non-parabolic and has its extreme occurring at $\mathbf{k}_{\|} \neq 0$. Effective mass is negative at zone-center, but positive over valence-band extreme. This supports what the absorption results predict. It also makes clear that, in describing valence-band structures in quantum wells with $\mathbf{k} \cdot \mathbf{p}$ theory, the Luttinger-Kohn parameters used will play a crucial role. For the rather two-dimensional case, i.e., the Bohr radius of the ground exciton state is larger than the width-width, the Luttinger-Kohn parameters for bulk materials will result in a bad description.

4.7 Conclusion

By recording magneto-optical absorption spectra with FTIR spectrometer in high signal-to-noise ratio and reasonable resolution and performing theoretical and numerical operations, we have presented direct evidence for two types of forbidden transitions in compressively strained $Ga_xIn_{1-x}As$/InP QWs. Using these forbidden transitions together with the allowed ones, we evaluated all the out-of-plane and in-plane effective masses of electrons and holes. This procedure resulted in a direct support to the theoretical prediction of $m_{\Gamma_6} < m^*_{e,\rho} < m^*_{e,z}$

for compressive strain [6]. We showed that derivative operation can provide a good pathway to the exciton states in tensile strained QWs, where excitonic transitions have flat and weak features with strong background disturbance. We obtained reliable values of exciton binding energy and effective mass of up to $5S$ exciton states for all the $Ga_xIn_{1-x}As$/InP QWs with x_{Ga} from 0.30 to 0.70. We compared the values with those determined by magneto-PL on $n-$doped strained $Ga_xIn_{1-x}As$/InP SQWs. We found that the two kinds of transitions (PL in $n-$doped and absorption in undoped QWs) have different mechanisms. Absorption in undoped QWs corresponds to the excitonic transition in the regime of $\Delta\mathbf{k} = 0$ with its ground state occurring at $\mathbf{k}_{\|} \simeq 0$ (at $B \simeq 0$), and excited states (at $B > 0$) at $\mathbf{k}_{\|} > 0$; whereas PL in n-doped QW tends to occur at valence-band extreme due to the fact that the conduction band is filled up. The former can therefore describe the valence-band structure near the Brillouin-zone center, and serve as a good candidate for experimentally tracing indirect band-gap. The effective masses determined by absorption show that with strain changing its property from compressive through absence of strain to tensile strain, the extreme of the topmost valence subband move to $\mathbf{k}_{\|} > 0$, and indirect band gap occurs. A 6-band second-order $\mathbf{k} \cdot \mathbf{p}$ calculation supports our results, and on the other hand, makes clear that to predict valence-band structure with $\mathbf{k} \cdot \mathbf{p}$ theory, unique Luttinger-Kohn parameters cannot be used throughout.

x_{Ga}	spectra	E_b^{hh}	μ_{hh} (m_0)					E_b^{lh}	μ_{lh} (m_0)				
		(meV)	$1S$	$2S$	$3S$	$4S$	$5S$	(meV)	$1S$	$2S$	$3S$	$4S$	$5S$
0.60	absorp.	-9.1	0.075	0.041	0.038	0.040	0.043	-8.6	0.068	0.056			
	2nd deri.	-8.1	0.060	0.038	0.038	0.040	0.042	-8.1	0.060	0.048			
	4th deri.	-7.5	0.053	0.038	0.038	0.040	0.042	-7.8	0.056	0.045			
	6th deri.	-7.5	0.053	0.038	0.038	0.040	0.042	-7.8	0.056	0.045			
	8th deri.	-7.5	0.053	0.038	0.038	0.040	0.042	-7.8	0.056	0.045			
0.70	absorp.	-9.4	0.080[a]	?	?			-9.9	0.090[a]	0.054	0.054		
	2nd deri.	-8.0	0.060	0.059	0.061			-9.1	0.075	0.050	0.054	0.054	0.055
	4th deri.	-8.0	0.060	0.059	0.061			-8.4	0.064	0.050	0.052	0.053	0.054
	6th deri.	-8.0	0.060	0.059	0.061			-8.2	0.062	0.050	0.052	0.053	0.054
	8th deri.	-8.0	0.060	0.059	0.061			-8.2	0.062	0.050	0.052	0.053	0.054

Table 4.4: Reduced effective masses of exciton states in the tensile strained $Ga_xIn_{1-x}As$/InP QWs determined by absorption spectra and their derivatives.

[a]Estimated without reasonable theoretical support

x_{Ga}	ϵ_ρ	$m^*_{e,\rho}$	$E_{\mathrm{b}}^{\mathrm{hh}}$		μ_{hh}	(m^*_{hh})			$E_{\mathrm{b}}^{\mathrm{lh}}$		μ_{lh}	(m^*_{lh})	
	(%)	(m_0)	(meV)	$1S$	$2S$	$3S$	$4S$	$5S$	(meV)	$1S$	$2S$	$3S$	$4S$
0.30	-1.16	0.044	-5.29	0.0325	0.0310	0.0320	0.0325	0.0330					
				(0.124)	(0.105)	(0.117)	(0.124)	(0.132)					
0.40	-0.47	0.049	-5.99	0.038	0.034	0.035	0.0355	0.0360					
				(0.169)	(0.111)	(0.123)	(0.129)	(0.136)					
0.47	0.01	0.052	-6.42	0.042	0.041	0.042	0.036	0.037	-7.37	0.053	0.038	0.044	0.038
				(0.218)	(0.194)	(0.218)	(0.117)	(0.128)		(-2.756)	(0.141)	(0.286)	(0.141)
0.50	0.22	0.051	-5.71	0.0345	0.032	0.032	0.033	0.0345	-5.38	0.0315	0.030	0.031	0.033
				(0.107)	(0.086)	(0.086)	(0.094)	(0.107)		(0.083)	(0.073)	(0.079)	(0.094)
0.60	0.91	0.055	-7.50	0.053	0.038	0.038	0.040	0.042	-7.79	0.056	0.048		
				(1.458)	(0.123)	(0.123)	(0.147)	(0.178)		(-0.01)	(0.377)		
0.70	1.60	0.057	-8.04	0.060	0.059	0.061			-8.35	0.064	0.050	0.054	0.054
				(-1.14)	(-1.682)	(-0.869)				(-0.521)	(0.407)	(1.026)	(1.026)

Table 4.5: Exciton binding energy and in-plane effective masses of up to $5S$ exciton states in $\mathrm{Ga}_x\mathrm{In}_{1-x}\mathrm{As}$ /InP QWs.

Chapter 5

Bandedge electronic structure in ordered (Al)GaInP QWs

5.1 Introduction

In order to explore ordering effects and further, to establish an appropriate method being suitable for determining effective mass and exciton binding energy in GaInP/AlGaInP QWs even in medium magnetic fields, we try out in this chapter the optical spectroscopy of absorption [Sec. 5.2], PL [Sec. 5.4] and reflectivity [Sec. 5.5]. We adjust the QW sample structure with the aid of the Fabry-Pérot theorem to fit our measurements [Sec. 5.3]. The assumptions available in the literature of band-edge structure, i.e., spatially type-II band alignment caused by ordering and band-tails due to shallow traps, are checked and a new model is proposed, which originates from the concept of the domain distribution function and shows to describe experimental phenomena very well. We conclude that the optical transition is significantly affected by the spread of the domain distribution, which is estimated for all the samples in this work [Sec. 5.6]. Effective masses and exciton binding energies are also obtained, and ordering effects are discussed. The results show that to determine the effective mass and exciton binding energy in this material system, the magneto-optical reflectivity spectroscopy together with derivative technique is appropriate.

We extend the "model-solid" method described in chapter 2 to deal with ordering as well as strain effect on the band-offset and interband transition energies in ordered quantum wells [Sec. 5.7]. The results indicate that, (i) measuring the first excitonic transition energy can lead to a reasonable estimation of the ordering parameter η in the QWs; (ii) For lattice-matched and compressively strained samples, the first excitonic transition has a relatively heavy out-of-plane effective mass; (iii) While $\Delta E_g(\eta = 1) = -0.471$ eV [31, 32] gives a best

fit for lattice-matched samples, $\Delta E_g(\eta = 1) = -0.405$ eV [118], which taking strain-correction into account, leads to a good fit for compressively strained samples; (iv) Compressive strain tends to weaken the ordering effects; (v) Ordering causes conduction band-offset ratio Q_c to increase, especially under the lattice-matched and tensile strained conditions.

5.2 Difficulty of measuring the absorption

Magneto-optical absorption spectroscopy is powerful in dealing with magneto-exciton related phenomena in $Ga_xIn_{1-x}As$/InP QW structures, as discussed in chapter 4. However, due to the strong absorption of the GaAs substrate, it can be used in (GaAs-based) GaInP /AlGaInP QWs only if the GaAs substrate is (partially) removed.

Four $Ga_xIn_{1-x}P/(Al_{0.66}Ga_{0.34})_{0.52}In_{0.48}P$ QW samples were measured, which were grown by metal organic vapor-phase epitaxy with a susceptor at a reactor pressure of 120 hPa. The structure of the samples is schematic shown in Fig. 5.1. The gallium fraction x_{Ga} of

GaInP	2 nm	
$(Al_{0.66}Ga_{0.34})_{0.52}In_{0.48}P$	3000 nm	
GaInP	10 nm	
$(Al_{0.66}Ga_{0.34})_{0.52}In_{0.48}P$	4 nm	6 X
GaInP	10 nm	
$(Al_{0.66}Ga_{0.34})_{0.52}In_{0.48}P$	3000 nm	
GaInP	2 nm	
GaAs buffer	30 nm	
substrate	a) GaAs : 0 ° b) GaAs : 6 °−$(111)_A$	

Figure 5.1: Schema of the $Ga_xIn_{1-x}P/(Al_{0.66}Ga_{0.34})_{0.52}In_{0.48}P$ QWs.

the $Ga_xIn_{1-x}P$ well-layer is 0.4 and 0.52, respectively. Two kinds of

(001) GaAs substrates oriented in $6^\circ - (111)_\mathrm{A}$ and 0°, respectively, were used. In order to obtain a relatively high mechanical stability of the QWs, a thick $(Al_{0.66}Ga_{0.34})_{0.52}In_{0.48}P$ buffer layer was inserted on each side of the QWs. A small part of the substrate (about 1 mm^2) was etched for each sample to let source light used for the absorption measurement travel through.

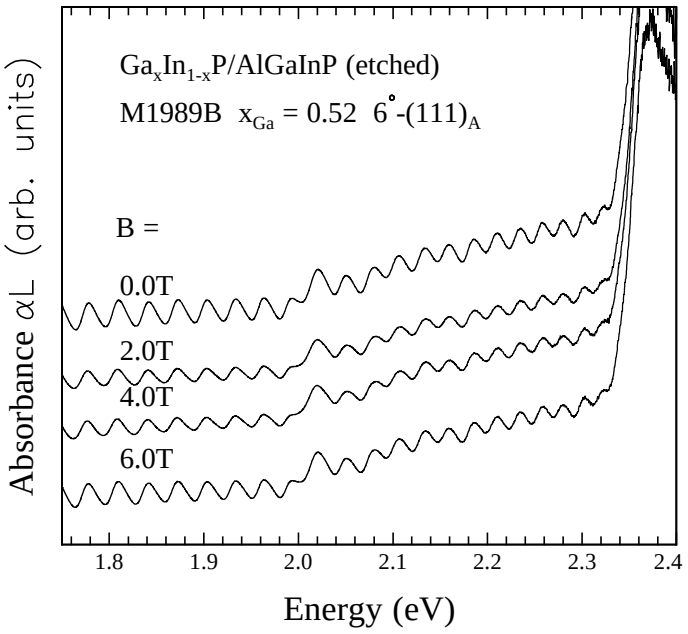

Figure 5.2: Absorption spectra of the $Ga_xIn_{1-x}P$/AlGaInP QW sample with $x_{Ga} = 0.52$, recorded in different magnetic fields at a low temperature ($T = 1.8K$).

Figure 5.2 shows typical absorption spectra of the sample with $x_{Ga} = 0.52$. Similar spectra were also recorded for the other samples in magnetic fields ranging of $0 - 6.8$ T. Unlike the study of GaInAs/InP QWs, here we cannot see exciton feature clearly but only periodic oscillations, which are caused by the Fabry-Pérot multiple-beam interference. Attempting to see possible magneto-exciton effect, we divide the absorption spectra recorded at $B \neq 0$ by the absorption spectrum recorded at $B = 0$. The results are depicted in Fig. 5.3. They are rather noisy. At ∼1.96 eV, a sharp line occurs, due to the disturbance from the He-Ne laser in the BOMEM DA3.01 spectrometer. Under high magnetic fields, small dips can be seen at ∼1.83 eV and ∼1.88 eV, respectively. They are most probably from excitonic transitions. However, no useful information can be extracted. To identify exci-

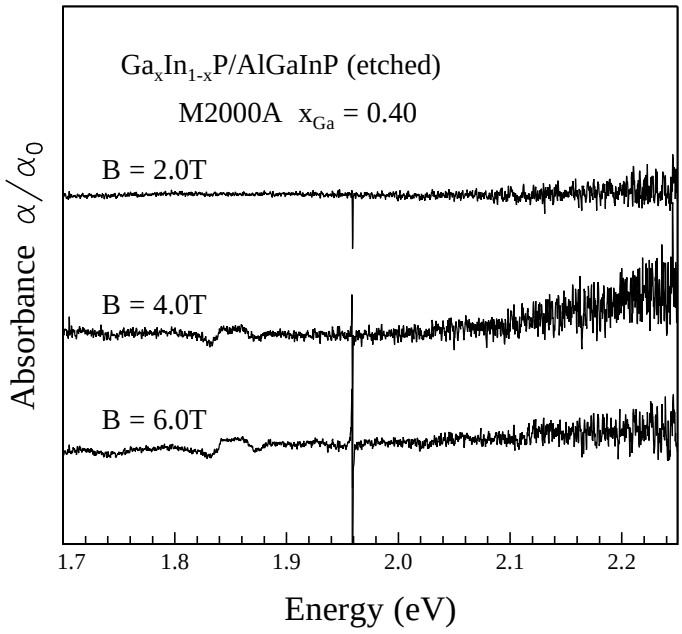

Figure 5.3: Magnetic field-induced absorption change at $B \neq 0$ relative to $B = 0$ in $Ga_xIn_{1-x}P$/AlGaInP QWs.

tonic transitions, the oscillation in the absorption spectrum should be reduced.

5.3 Sample structure: optimized for reflectivity measurement

Recalling the discussion in Sec. 3.4, there exists a relation of $\Delta\nu \propto 1/d$ for the Fabry-Pérot interference, where $\Delta\nu$ is the energy difference between two adjacent oscillation peaks, and d is the thickness of the layer. We can conclude that the reduction of the total thickness of the sample layer (except GaAs substrate) is crucially needed for diminishing the interference. On the other hand, a multiple-well-layer structure in the sample is also important, as it can enhance absorption and reduce the intensity of the Fabry-Pérot interference. Based on the analysis of the electronic structure in GaInP/AlGaInP QWs [ref. Sec. 5.7.1], and the demand of derivative operation [ref. Sec. 5.5], $\Delta\nu$ should be safely selected as $\sim$ 200 meV or even larger, to enable the transitions from heavy-hole (hh), light-hole (lh) and split-off (so) valence subbands be unambiguously identified. This means that the

thickness of the total layers should drop from $\sim 6\mu$m to $< 1\mu$m. Such a thin layer, however, will make it difficult to remove an appropriate part of the substrate without destroying the QWs. The absorption measurements in GaAs-based GaInP/AlGaInP QWs therefore cannot easily be carried out. Other magneto-optical methods are therefore required. In the following, we will employ reflectivity spectroscopy to perform our investigation. An important advantage gained by measuring reflectivity is that it is not necessary to etch the GaAs substrate and therefore possible to reduce the thickness of AlGaInP buffer layer dramatically.

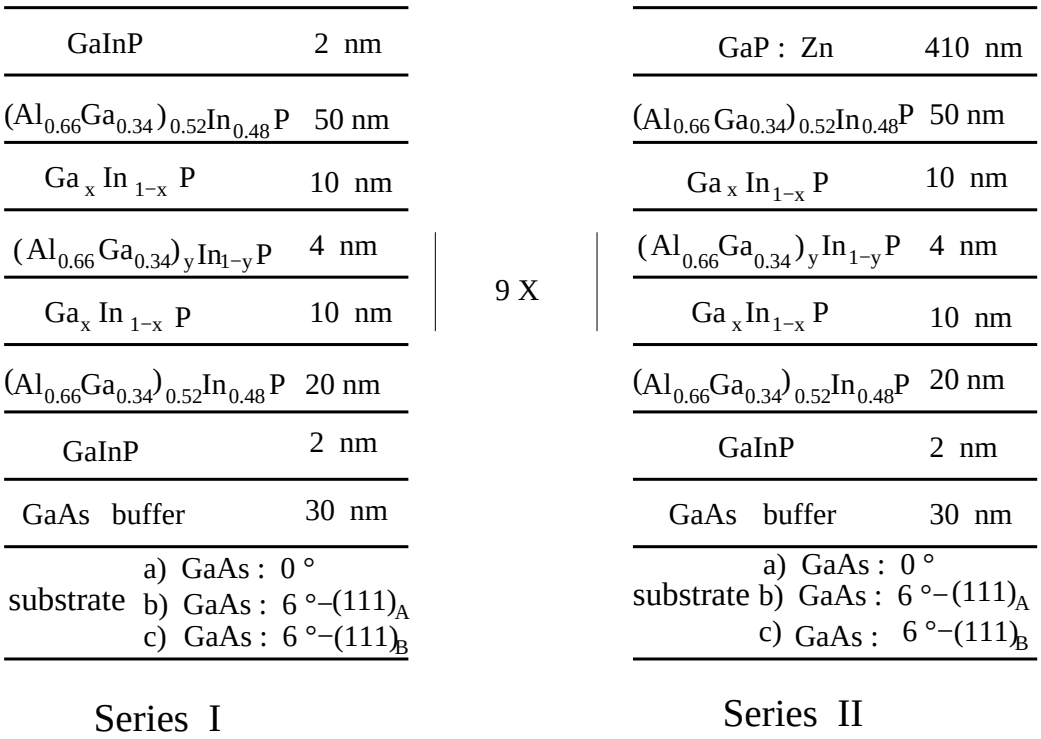

Figure 5.4: Schematic structure of the two series of ordered $Ga_xIn_{1-x}P$/AlGaInP QW samples optimized for reflectivity measurements. A distinct difference exists in the capping-layer.

Two series of $Ga_xIn_{1-x}P/(Al_{0.66}Ga_{0.34})_yIn_{1-y}P$ QW samples were prepared by metal organic vapor-phase epitaxy*, each consisting of 6 samples grown on (001) Si-doped GaAs substrate with different misorientation, i.e., 0°, 6° off toward $[111]_A$, 6° off toward $[111]_B$, respectively.

*They were prepared by Dr. Rolf Winterhoff in *4. Physikalisches Institut*, to whom I'd like to say: *Dankschön!*.

The structures are schematically shown in Fig. 5.4. The first series, prepared at $T = 700$ °C, has a 2-nm-thick GaInP capping layer, while the second series, prepared at $T = 700$ °C for three lattice-matched samples and at $T = 750$ °C for strained ($x_{\mathrm{Ga}} = 0.4, y = 0.76$) samples, has a 410-nm-thick Zn-doped GaP capping layer, which is intended for electro-reflectivity or photocurrent measurement in the near future. The well-layer of the samples is below the critical thickness predicted by Geng *et al.* [136] following the theory of Matthews *et al.* [137] or that of van de Merve *et al.* [138]. The thickness of the total layers (except substrate and GaAs buffer layer) is ~ 212 nm for the first series, and ~ 618 nm for the second. A survey of the samples is given in Table 5.1.

Table 5.1: $\mathrm{Ga}_x\mathrm{In}_{1-x}\mathrm{P}/(\mathrm{Al}_{0.66}\mathrm{Ga}_{0.34})_y\mathrm{In}_{1-y}\mathrm{P}$ QW samples with their substrate, growth temperature T_g, and composition.

sample		M 2421			M 2447			M 2517			M 2518		
		a	b	c	a	b	c	a	b	c	a	b	c
T_g	700	x	x	x	x	x	x	x	x	x			
($°C$)	750										x	x	x
x_{Ga}	0.4	x	x	x							x	x	x
	0.52				x	x	x	x	x	x			
y	0.52				x	x	x	x	x	x			
	0.76	x	x	x							x	x	x
substrate	0°	x			x			x			x		
	6°-$(111)_A$		x				x		x			x	
	6°-$(111)_B$			x		x				x			x

To qualitatively show the improvement due to the adjustment of sample structure, two reflectivity spectra for samples with $d \sim 6\mu$m and $d \sim 0.618\mu$m, respectively, are shown in Fig. 5.5. Note that, for the reflectivity measurement, the incident light will be reflected mainly at the upper surface of the AlGaInP layer, due to its larger refractive index and the strong absorption of the GaAs substrate, the visual layer-thickness for the $\sim 6\mu$m sample is therefore reduced to $\sim 3\mu$m. This is the reason that the oscillating period of the thinner sample is about 5 times large that that of the thicker sample, as can be seen in Fig. 5.5. Also noteworthy is that the oscillating period of the thicker sample (M2000A) is about that in the absorption spectrum

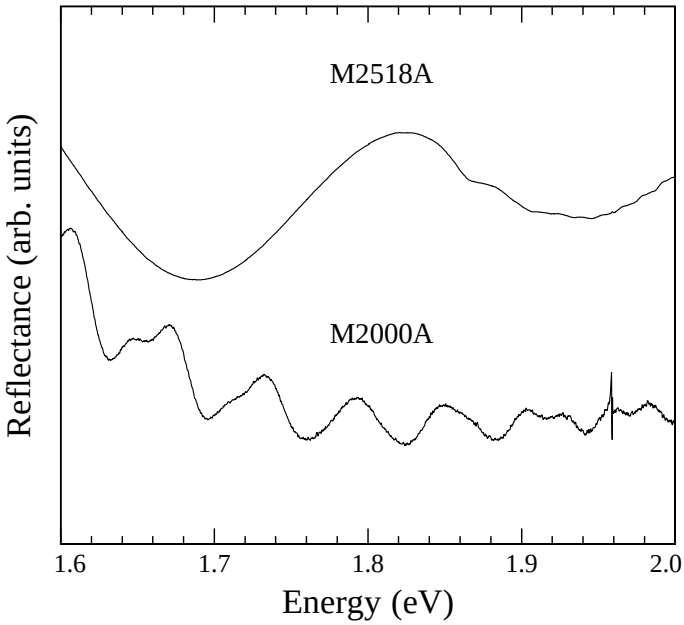

Figure 5.5: Reflectivity spectra from two $Ga_xIn_{1-x}P$/AlGaInP QW samples with different layer thickness. Upper line: $\sim 0.6\mu$m; lower line: $\sim 6\mu$m.

[see Fig. 5.2 on page 86] multiplied by 1.4. It can be well explained in the regime of the Fabry-Pérot interference. The enlarged separation of two adjacent maxima in the spectrum enables the numerical derivative operation and an indirect identification of the exciton transitions. Detailed discussion will be presented in Sec. 5.5.

5.4 Photoluminescence study

PL and magneto-PL have been employed to investigate ordering effects in $GaInP_2$ bulk material by Ernst *et al.* [61, 114]. It was known that at low temperature, PL spectra from ordered $GaInP_2$ bulk alloy can be classified in three types: (i)Type-I, which is mostly for disordered case, has one single, narrow and symmetric PL peak, and doesn't show any excitation-density dependence in a range from 50 mW/cm^2 to 500 W/cm^2; (ii) Type-II, which has a single but relatively broad (or asymmetric) PL peak. The peak shifts to higher emission energies with increasing the excitation intensity and tends to become narrower; (iii) Type-III, which shows two more or less separated peaks and exhibit a very characteristic behavior that while the "low-energy" emission is

strongly influenced by excitation intensity, the "high-energy" emission does not show any dependence on excitation level, neither in peak energy nor in peak line-width. To understand the phenomena two models were proposed, one of which was based on an assumption of spatially indirect recombination which was believed to occur at the type-II boundaries located at domain boundaries of different degree of ordering [61–65] (as shown in Fig. 5.6(a)); the other assumed a band-tail states due to, e.g., shallow traps [61], as shown by shaded region in Fig. 5.6(b).

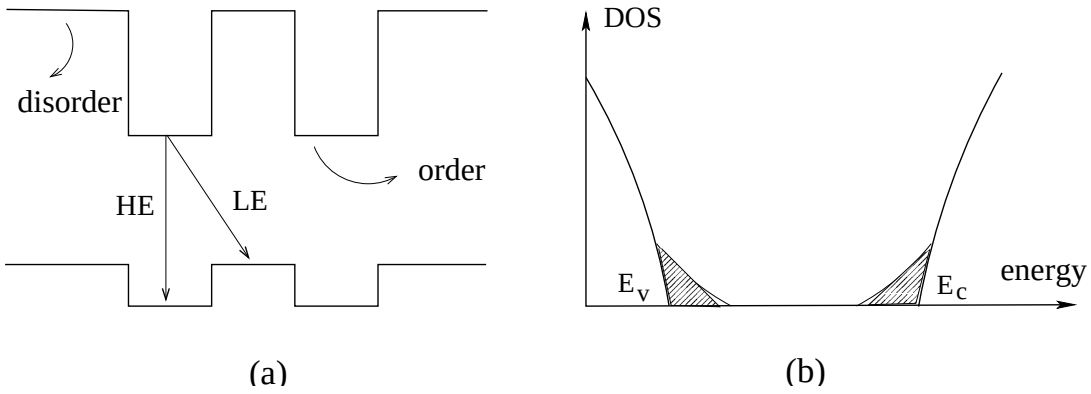

Figure 5.6: Schematics of (a) energy band diagram of ordered $GaInP_2$ alloy proposed in the literature and (b) average electronic density of states proposed by Ernst *et al.* [61] for explaining the excitation-density dependence of the PL in ordered $GaInP_2$ bulk material.

Also, it has been experimentally shown that the ordering causes changes in the effective mass [114, 115]. Emanuelsson *et al.* presented optically detected cyclotron resonance measurements [115] and concluded that the conduction-band effective mass in an ordered $GaInP_2$ sample decreases to $m_c = (0.088 \pm 0.003)m_0$ from $m_c = (0.092 \pm 0.003)m_0$ in the disordered alloy. Ernst *et al.* [114] reported magneto-PL study of ordered $GaInP_2$ with varying degree of order from $\eta \sim 0.0$ to $\eta \sim 0.54$ and found that the in-plane reduced effective mass is lower than that of the disordered alloy, the exciton binding energy is nearly independent of the ordering parameter. In the QW systems, however, the effective mass is far away from being well studied, because of its intrinsic property. As theoretically predicted, high electron effective mass m_e^* causes a weak and flat feature of the excitonic transition with small diamagnetic shift under medium magnetic field ($\sim$ 1 meV

by 4 T), which is in the range of uncertainty of the often used PLE method [15,17,18,81]. The only study, to our knowledge, was made on compressively strained and disordered QW by magneto-optical reflectivity under magnetic fields up to 45 T [20]. Effective mass and exciton binding energy of heavy-hole exciton were estimated. But no information on light-hole exciton was given. A possible reason is that there still exists strong Fabry-Pérot interference, making the unambiguous identification of the transitions difficult. Further, the experimental uncertainty in that work was large due to weak and flat features of the excitonic transitions.

In the following, we first examine the excitation-density dependence of the optical transitions. We then try to estimate the effective mass and exciton binding energy by magneto-PL spectroscopy.

5.4.1 Low-temperature photoluminescence

Photoluminescence measurements were carried out for all the samples at low temperature (1.8 K). Instruments were configured as described in Sec. 3.2.1. In Fig. 5.7, PL from the (a) lattice-matched and (b) compressively strained quantum well samples are shown. Dashed lines represent the PL from the series-II, and solid lines from the series-I samples.

Unlike observed before [61], here only two types are identified: one is with a single-peak, and is for all the lattice-matched samples and the compressively strained ones with 0° and $6^\circ - (111)_\mathrm{B}$ substrate-misorientations; the other has a less separated double-peak, and is only for the $6^\circ - (111)_\mathrm{A}$ compressively strained samples. The spectroscopic peak positions exhibit dependence on substrate misorientation. According to the established knowledge, samples with $6^\circ - (111)_\mathrm{B}$ substrates have the highest ordering, while those with $6^\circ - (111)_\mathrm{A}$ the lowest under the same sample-preparation condition [114], and the stronger the ordering the larger the band-gap reduction [23, 31]. For the lattice-matched samples shown in Fig. 5.7(a), a good agreement is seen: the PL peaks occur at highest energies for the samples with $6^\circ - (111)_\mathrm{A}$ substrate (to simplify the discussion, they will be

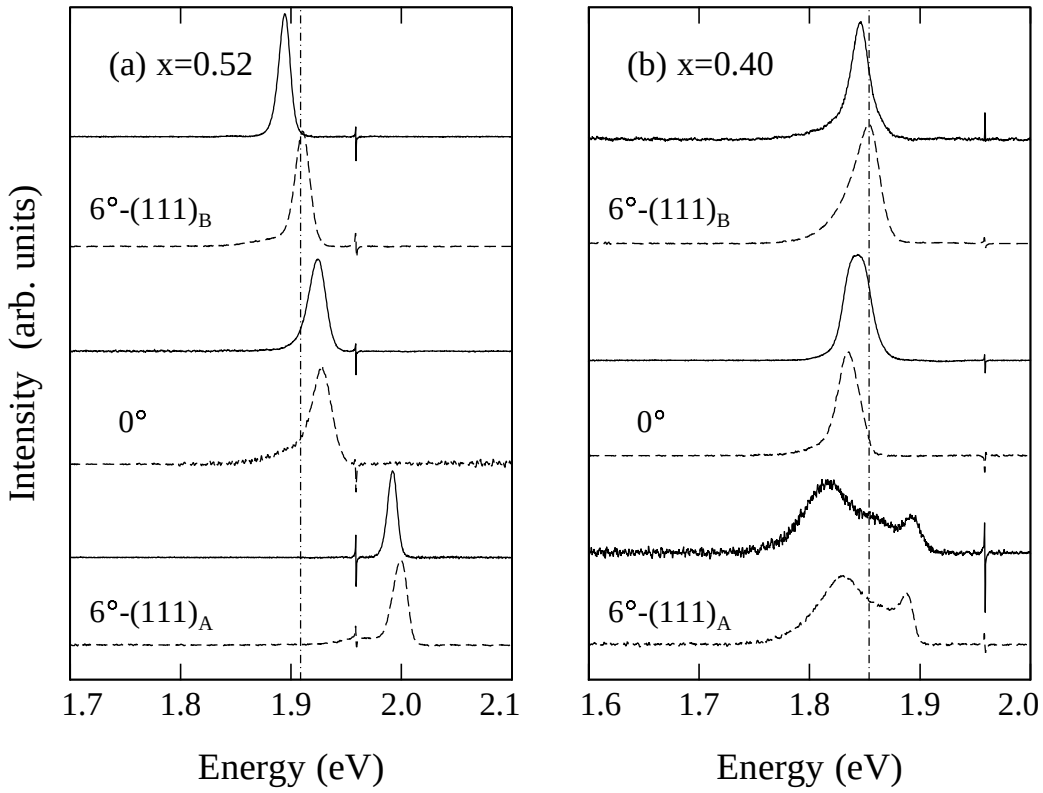

Figure 5.7: PL from ordered and (a) lattice-matched or (b) compressively strained $Ga_xIn_{1-x}P$/AlGaInP quantum wells. Dashed lines represent those from series II, and solid lines from series I samples.

noted as "low ordering" in the following discussion*.), while those with $6^\circ - (111)_B$ substrate show up at lowest energies (noted as "high ordering"). For the compressively strained samples shown in Fig. 5.7(b), however, two exceptions occur. One is that a sample with (expected) high ordering (M2518C) has higher PL energy than those with 0° substrate (noted as "medium ordering"). The other is that the "low-energy" peak of the samples with low ordering even occurs at the lowest energy position in the same series of the samples.

5.4.2 Excitation-density dependent photoluminescence

In order to gain deep insight into ordering effects on PL transitions, the excitation-intensity dependence of the PL was checked. In Fig. 5.8 the typical tendency of the peak energy is shown as a function of the

*The ordering parameter will be given in Table 5.2 on page 98.

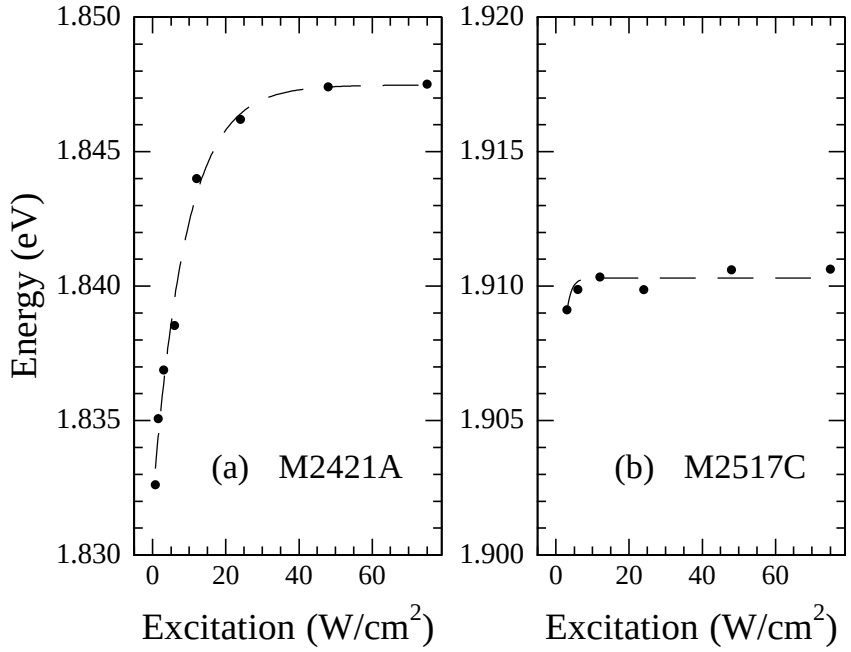

Figure 5.8: Excitation-density dependence of the PL peak energy for (a) compressively strained with medium ordering and, (b) lattice-matched with high ordering (Al)GaInP QW samples. Dashed lines are fitted to the measuring points to guide eyes.

excitation level. Fig. 5.8(a) is for a compressively strained sample with medium ordering, and (b) for a lattice-matched one with high ordering. For the single-peak samples, the PL peak first shifts rapidly to higher energies with increasing the excitation level in the range below ≤ 15 W/cm^2. It then slows down, and finally does not show the dependence of excitation level any more in the range ≥ 40 W/cm^2. This was not the case for the measurement on $GaInP_2$ bulk material [61], whereby the blue shift was manifested to be strong over the excitation of 500 W/cm^2. Also observed is that the blue shift varies with order and strain. It takes a value of about 5 meV per decade of excitation-density increase for medium ordering, and of about $1 \sim 2$ meV for high ordering. For absence of strain and low ordering, the blue shift is below 1 meV per decade of excitation-density increase.

Concerning the excitation-density dependence, the line-width for all the single-peak samples first decreases ($\sim$ 0.5-1.5 meV) as the excitation intensity increases up to $\sim$15 W/cm^2, then keeps nearly unchanged for higher excitation density, as shown in Fig. 5.9. The change in the FWHM is also ordering-dependent. For the lattice-

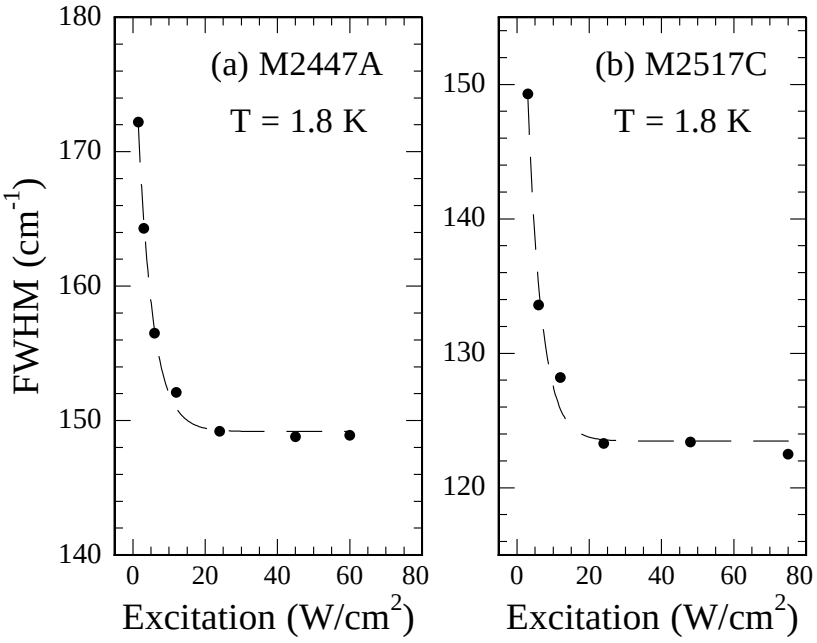

Figure 5.9: FWHM of the PL peak determined by curve-fitting process for lattice-matched $Ga_xIn_{1-x}P$/AlGaInP quantum wells with (a) middle ordering and (b) high ordering as a function of excitation density. Dashed lines are fitted to the measuring points to guide eyes.

matched samples, the middle as well as high ordering corresponds to a sharper narrowing of the peak than the low ordering does. Similar comparison for the compressively strained samples is difficult, as the low ordering corresponds to a slightly separated double-peak for which the FWHM is difficult to determine. An exception exists for a lattice-matched sample with low ordering (M2447C) that the FWHM shows a slight increase (∼1.5 meV)! We note that it corresponds to only 0.2 meV blue shift as the excitation-density increases.

It is interesting to note that there is a general relation between the blue shift and the stable line-width of the PL peak measured at high excitation densities ($\sim$ 50 W/cm^2): larger blue shift corresponds to larger stable FWHM. The lattice-matched samples with high ordering have relatively smaller FWHM, $12.2 - 15.3$ meV, similar to those with low ordering. In contrast, those with medium ordering have a large value, $18.6 - 23.2$ meV. Similar but enlarged results are obtained for the series-I compressively strained samples: 20.0 meV for high ordering and 27.1 meV for medium ordering. For the series-II compres-

sively strained samples however, that with high ordering (M2518C) has broader lines (29.8 meV) than that with medium ordering (23.4 meV) in the same series. But the line shape of the former is obviously asymmetric with its maximum occurring at higher energy than that with medium ordering, suggesting a bad sample quality. Further evidence will be obtained by magneto-PL as well as reflectivity measurements.

5.4.3 Magneto-photoluminescence

In order to identify the property of the PL emission and further possibly to estimate band-edge effective mass of the quantum wells, magneto-PL measurements were performed with an excitation power-density of ~ 15 W/cm^2.

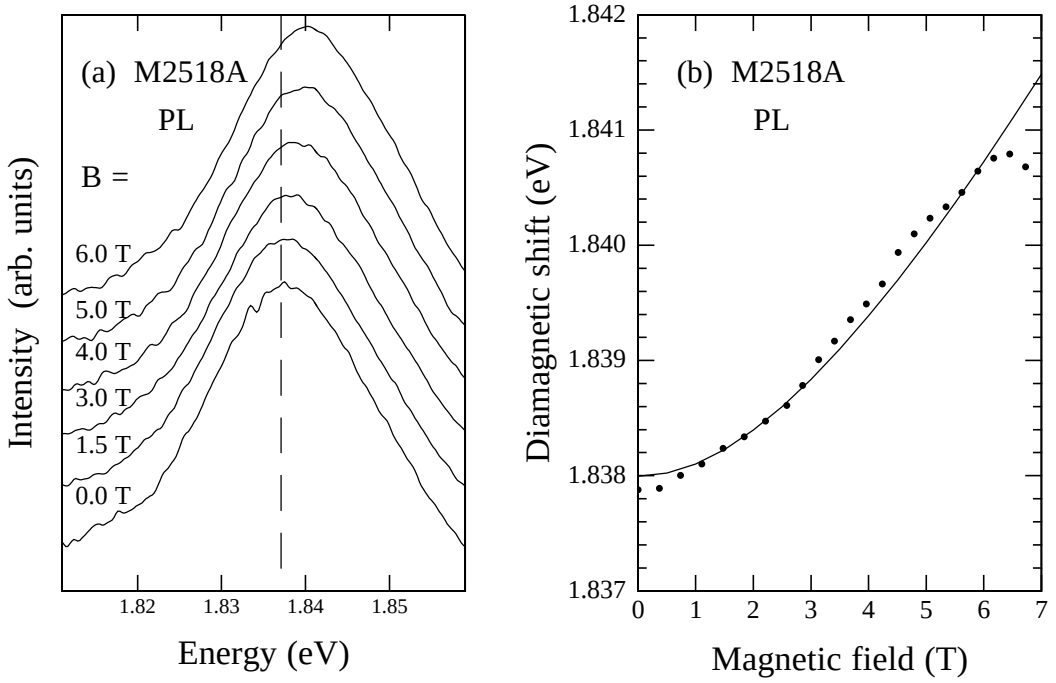

Figure 5.10: (a) PL spectra recorded at different magnetic fields; (b) magnetic field-dependent spectroscopic position of the PL peak for a strained GaInP/AlGaInP QW with medium ordering (M2518A).

Figure 5.10 shows a series of PL spectra (a) and magnetic field-dependent spectroscopic positions of the PL peaks (b-d). It represents typical phenomena for most of the samples we measured. Obviously, the PL peak shifts to higher energies under higher magnetic

fields. Such a "diamagnetic shift" is a direct evidence indicating that the PL peak from the QW is excitonic. With regard to the valence band structure*, the lattice-matched and disordered sample has a very high in-plane effective mass and exciton binding energy, which makes the diamagnetic shift very small under medium magnetic fields. Figure 5.11(a) shows such a case. Figure 5.11(b) is the only case ob-

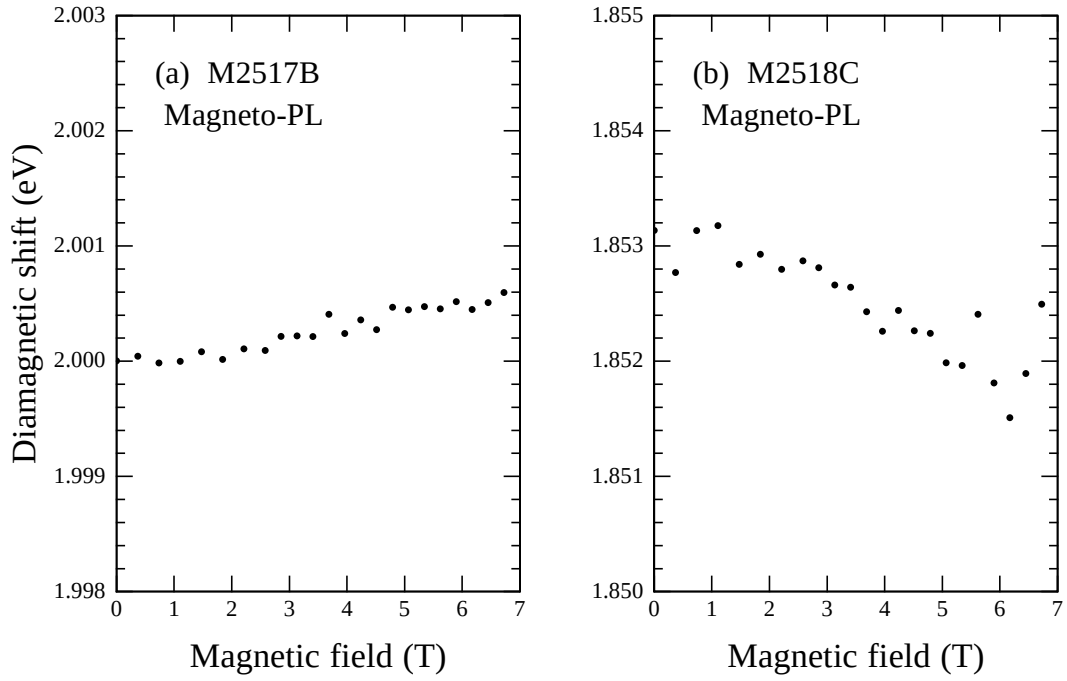

Figure 5.11: Magnetic field-dependent spectroscopic position of the PL peak for ordered $Ga_xIn_{1-x}P$/AlGaInP QW.

served in the measurements and is from the compressively strained sample with high ordering, M2518C. It does not show any normal diamagnetic shift. For the possible reason, we assume bad sample quality. As aforementioned, its PL energy should be lower than those with the same strain but lower ordering. A remarkable feature of the spectrum is that it is highly asymmetric with obvious low-energy tail. There should be significant defects, most probably caused by the interaction between high compressive strain and high ordering. As a result no exciton state exists. Measurements under excitation-densities of $\sim 45 - 60$ W/cm^2 as well as of ~ 1.5 W/cm^2 for compressively

*will be numerically analyzed in Sec. 6.4

strained samples with middle and high ordering (M2421A,C) were also performed and similar diamagnetic shift was detected.

5.4.4 Estimation of reduced effective mass

For the samples showing a diamagnetic shift as illustrated in Fig. 5.10(a) and (b), we have estimated the effective mass and exciton binding energy by numerically solving the Wannier exciton effective mass equation [ref. Eq. (2.25) on page 32] and fitting the theoretical calculations to the experimental diamagnetic shifts. The solid line in Fig. 5.10(b) shows such a fit. The obtained reduced effective mass and exciton binding energy are listed in Table 5.2.

Table 5.2: Exciton binding energy and reduced effective mass in ordered GaInP /AlGaInP QWs estimated by magneto-PL. Ordering parameter η is also listed, for which the determining procedure will be given in Sec. 5.7.

Sample	M2421A	M2421C	M2518A	M2447B	M2517A	M2517B
x_{Ga}	0.4	0.4	0.4	0.52	0.52	0.52
η	0.32	0.35	0.31	0.47	0.32	0.20
$\mu(m_0)$	0.068	0.078	0.043	0.09	0.06	0.09
E_{b} (meV)	-10.9	-11.7	-8.4	-12.7	-10.3	-12.7

It is obvious that both the exciton binding energy and effective mass are strain and ordering dependent. The exciton binding energy is in the range of a theoretical prediction for disordered quantum wells [14]. Roughly, compressively strained samples have relatively smaller reduced effective mass and exciton binding energy. Such a strain effect was also observed in other QW systems, e.g., GaInAs/InP QWs. On the other hand, different substrate misorientations, corresponding to different degrees of ordering, lead to a different value of the effective mass. For compressively strained samples, ordering results in an increase to reduced effective mass and exciton binding energy. This is qualitatively in agreement with ordering-included 6-band $\mathbf{k} \cdot \mathbf{p}$ calculations [ref. Chapter 6]. For the lattice-matched samples however, medium ordering corresponds to smaller effective mass. It can be explained as follows. For the low ordering, the valence-band is nearly degenerate, the effective mass determined by PL is a averaged value

from both the hh- and lh-exciton. For the middle ordering however, the degeneracy is removed, and the effective mass is mainly determined by hh-exciton, which is smaller than that of the lh-exciton. For high ordering, the hh-exciton effective mass increases due to the further ordering effect.

It is noteworthy that the PL spectra can only show one peak from the quantum well, which is always corresponding to upper valence-subband-involved transition [ref. Sec. 4.6.1], not as heavy-hole and light-hole peaks shown in absorption spectra. Therefore the results of reduced effective mass and exciton binding energy can not reveal the detailed structure of the valence-band. In Sec.5.5, further insight will be gained into the ordering effects on the valence band structure and effective mass by derivative-assisted magneto-optical reflectivity measurements.

5.5 Reflectivity study

To gain further support for the assumption of the excitonic PL transition and the sample-quality, optical reflectivity measurements were performed. As known, the direct reflectivity spectrum shows sharp features at the exciton resonance energies [139–141]. Although the energies of the reflectivity minima do not coincide with those of the exciton resonance accurately but instead, lie slightly above, the difference in energy however, is much less than exciton binding energies [140–142].

We employed the experimental instruments illustrated in Sec. 3.2.3 to carry out optical reflectivity measurements, and performed the second-order derivative operation described in Sec. 4.4. The hh- and lh-like exciton transition energies are determined and further, the exciton binding energy and reduced effective mass for hh- and lh-excitons are evaluated. Based on the experimental observation, the assumptions of spatially indirect recombination as well as band-tail states will be reconsidered and a new model can be proposed in Sec. 5.6 to fully explain the experimental phenomena.

5.5.1 Derivative-assisted reflectivity

Figure 5.12 shows the reflectivity spectra from the compressively strained samples with (a) medium and (b) high ordering. Typically, the reflectivity spectrum is broad with weak, narrow features located at, say, ~ 1.86 eV for M2518A. Combining it with the corresponding PL spectrum, a slight blue-shift of the minimum relative to PL-maximum is evident [32, 61, 142, 143]. We therefore assume the minimum to be an exciton-associated transition.

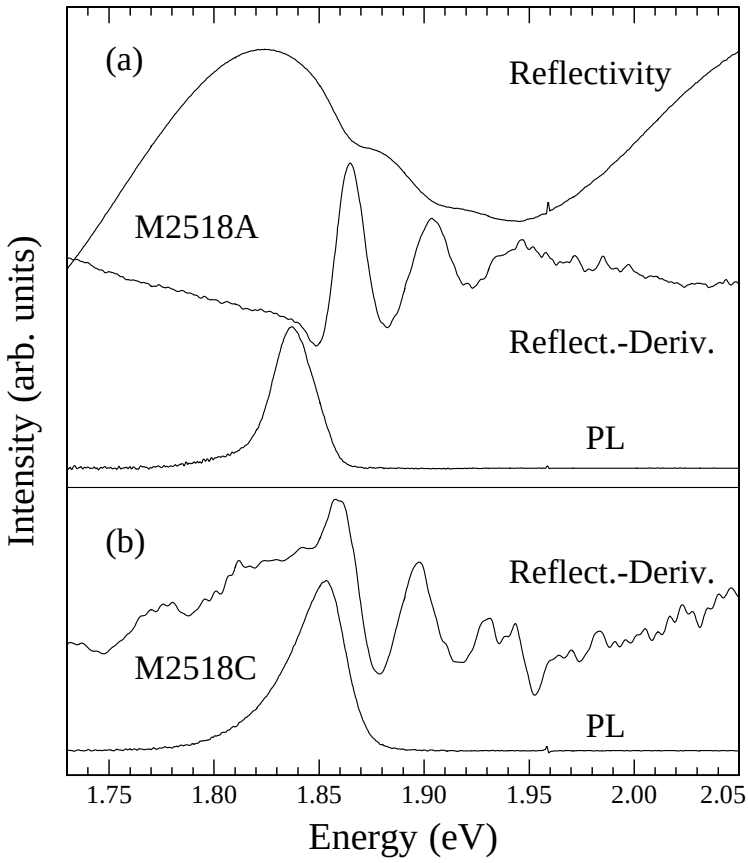

Figure 5.12: Reflectivity and its second-order derivative, as well as PL spectrum of the $Ga_{0.4}In_{0.6}P$/AlGaInP QW sample with (a) middle ordering (M2518A) and (b) high ordering (M2518C).

As established in Sec. 4.4, the derivative operation can diminish a background on which the signal is superposed, sharpen the signal, and thereby improve the sensitivity of detection. It lets weak features show up without causing significant error [54]. In order to identify the spectroscopic position of the reflectivity minima, second-order deriva-

tive operation is performed. The second-order derivative of reflectivity (SODR) spectrum is also shown in Fig. 5.12(a). Clearly, the SODR manifests clear peaks and dips around the minima in the reflectivity spectrum. This is a direct evidence showing that exciton states are formed in the QWs. Similar phenomena are observed in other samples. The only exception is shown in Fig. 5.12(b), where SODR and PL spectrum are shown for the compressively strained series-II sample with high ordering (M2518C), which is guessed to have a bad quality. As can be seen, in the low energy side of the first SODR maximum, there is no dip at $\sim$ 1.86 meV as that shown in Fig. 5.12(a) at the same energy. This suggests that no hh-like exciton state exists and supports the assumption of bad quality of the sample made above. Employing this combination-method, the transition energies are determined (as listed in Table 5.3), which provide a pathway to analyze band-offset and ordering effects in the QWs.

Table 5.3: Transition energies of ordered $Ga_xIn_{1-x}P$/AlGaInP QW samples determined by reflectivity derivative (SODR) at 1.8 K (in eV).

	M2421			M2447		
sample	A	B	C	A	B	C
1st transition	1.8636 ±0.0001	1.8896 ±0.0002	1.857 ±0.0001	1.9485 ±0.0002	1.9144 ±0.0002	1.9991 ±0.0004
2nd transition	1.9059 ±0.0002	1.9296 ±0.0006	1.9017 ±0.0003	1.9665 ±0.0005	1.9410 ±0.0001	2.0077 ±0.0005
3rd transition	1.9522 ±0.0005	- -	1.9594 ±0.0007	2.0487 ±0.001	2.0268 ±0.0002	2.0888 ±0.0009
	M2517			M2518		
sample	A	B	C	A	B	C
1st transition	1.9683 ±0.0007	1.9974 ±0.0006	1.9327 ±0.0002	1.8646 ±0.0001	1.9032 ±0.0003	1.8588 ±0.0005
2nd transition	1.9853 ±0.0008	2.0052 ±0.0006	1.9573 ±0.0001	1.9034 ±0.0002	1.9408 ±0.0006	1.8975 ±0.0001
3rd transition	2.0681 ±0.0006	2.0525 0.0006	2.0387 ±0.0003	1.9490 ±0.0002	2.0194 ±0.0005	1.9309 ±0.0002

It is found that the Stokes shift of the first SODR maximum relative to the corresponding PL peak at stable position (corresponding to high excitation-density of $\sim$50 W/cm^2) is ordering-dependent. The samples with medium ordering manifest the highest value of about

16.2 $\sim$ 35.7 meV, whereas those with high ordering take middle values of 10.3 $\sim$ 22.1 meV, and the lattice-matched samples with low ordering have the lowest value of $\leq$ 7.0 meV. Regarding to the FWHM of the first SODR peak, we note that the lattice-matched sample with medium ordering has a broader peak (17.1 meV for M2447A) than high ordering does (14.7 meV for M2447B), similar to the case for compressive strain ($\sim$16.4 meV for M2421A and $\sim$15.5 meV for M2421C). By assuming a similar line shape, e.g., Lorentzian form to the hh-like exciton transition for different samples, we can conclude a similar relationship among the FWHM of the hh-like exciton lines in their reflectivity spectra. Nevertheless, the FWHM of the peak in the (zero-order) reflectivity spectrum will be about two times as large as that in the corresponding SODR spectrum [57]. With this estimation in mind, we notice that the Stokes shift is smaller than the FWHM of the first peak in the reflectivity spectrum for all the single-peak samples.

5.5.2 Exciton binding energy and effective mass

For the magneto-reflectivity measurement, the growth axis of the samples was rotated 45° relative to the magnetic field direction and therefore the values of the magnetic fields given have been scaled with the factor $\cos 45^\circ = 0.707$. The coupling effect between the geometric and the magnetic confinement caused by the tilt angle between the magnetic field and the QW growth direction has not been taken into account [1, 144].

In Fig. 5.13, the peak position determined by the second-order derivative of the reflectivity spectra are shown as filled squares and points, as a function of magnetic fields for the compressively strained samples M2421A [Fig. 5.13(a)] and M2518A [Fig. 5.13(b)], and the lattice-matched samples M2447A [Fig. 5.13(c)] and M2447B [Fig. 5.13(d)], respectively. Obviously, the compressively strained samples (a and b) and the lattice-matched sample with high ordering (d) show two transitions. Based on the band-edge electronic structure calculations [described in Sec. 5.7.1, page 112, and Sec. 5.7.2, page 114], it is concluded that the first transition is heavy-hole like (with heavier out-of-plane

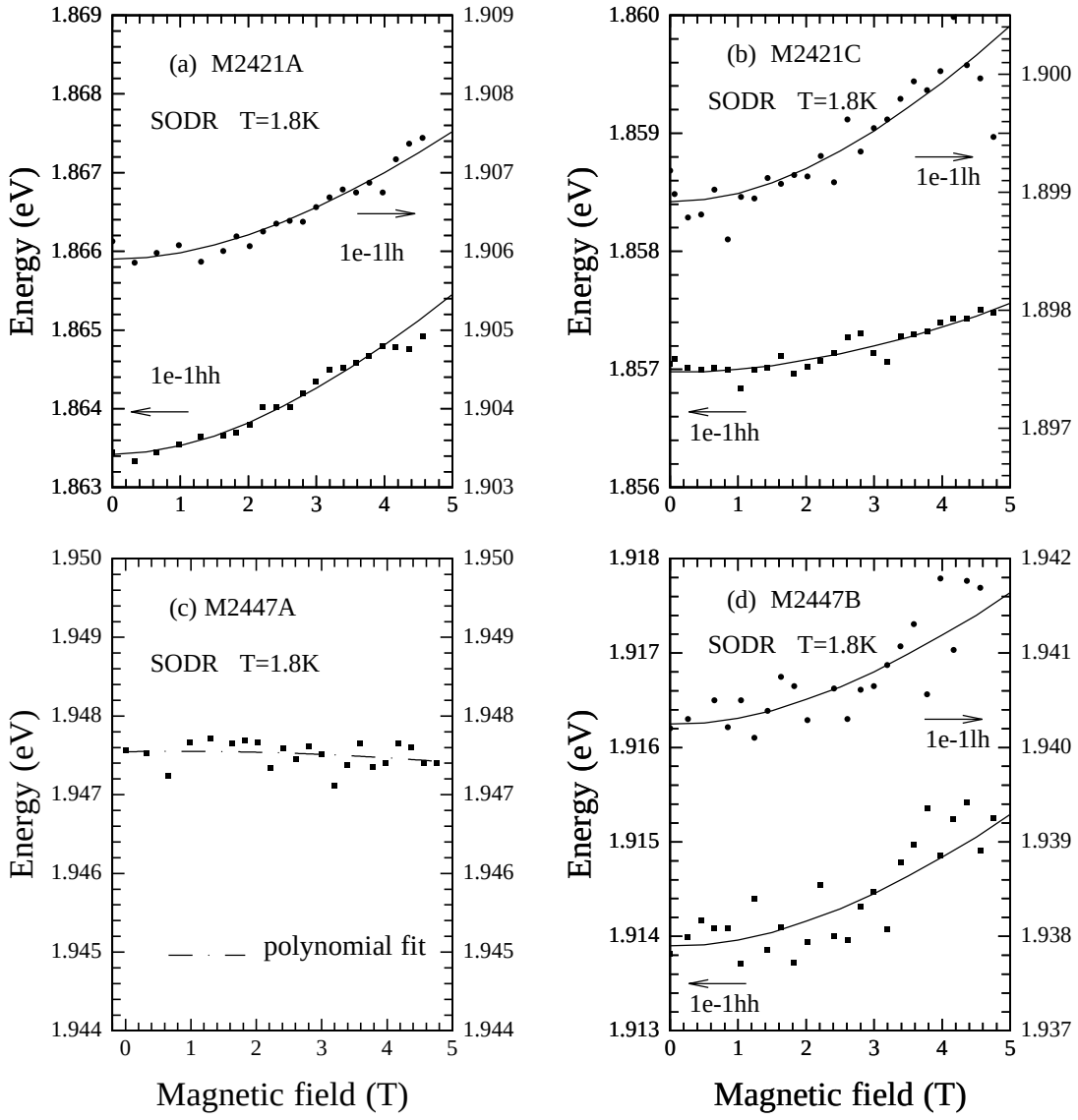

Figure 5.13: Peak energy of the second-order derivative of reflectivity (SODR) from the compressively strained (a and b) and lattice-matched (c and d) $Ga_xIn_{1-x}P$/AlGaInP QW, plotted against magnetic fields as filled squares and dots. The solid lines show theoretical fit, while the dash-dot represents a polynomial fit to serve as a guide to the eye.

hole effective mass), while the second is light-hole like. It is noteworthy that here we call the first transition as *heavy-hole like*, not *heavy-hole*. The reason is straightforward: as soon as the ordering sets in, the valence-sub-band states will be mixtures of all the three sub-bands. Therefore, *heavy-hole* or *light-hole* loses its physical meaning. For the sake of conventional understanding, we still use *heavy-hole like* to show a state with relatively heavier out-of-plane effective mass.

In order to evaluate the effective mass and exciton binding energy,

the effective-mass equation [Eq. (2.25), page 32] was numerically solved to fit experimental transition energies. The material parameters used in the calculations are adopted from Ref. [14, 18, 115], and listed in Table 5.5. The numerical results are shown as solid lines in Fig. 5.13 corresponding to the measured points. Fitting the theoretical calculation to experimental data leads to a determination of the reduced effective mass and exciton binding energy listed in Table 5.4. Not as reported by Kinder *et al.* [20], here both the hh- and lh-exciton transitions are unambiguously characterized. The fact that only the ground exciton state can be identified, on the other hand, is due to low available magnetic fields. It can be seen in Fig. 5.13, the scattering of the measured points around theoretical line is a little larger for the second (lh-like) transition. The reason is that in this energy range the reflectivity spectra are noisy because of low intensity of the second transition, and introduce a higher uncertainty to the determination of the peak position, relative to the first transition (hh-like). However, the overall uncertainty can be assumed as ~ 0.3 meV.

Similarly, the sample M2421C has also been studied. The determined effective mass and exciton binding energy are also listed in Table 5.4.

Table 5.4: Reduced effective masses and exciton binding energies in ordered $Ga_xIn_{1-x}P$/AlGaInP QWs estimated by reflectivity-derivative. E_b in meV, μ in m_0

Sample	$T_g(^oC)$	θ	x_{Ga}	η	μ_{hh}	E_b^{hh}	μ_{lh}	E_b^{lh}
M2421A	700	0^o	0.4	0.32	0.043	-8.38	0.049	-8.84
M2518A	750	0^o	0.4	0.31	0.044	-8.50	0.044	-8.30
M2421C	700	$6^o - [111]_B$	0.4	0.35	0.08	-11.87	0.051	-9.04
M2447B	700	$6^o - [111]_B$	0.52	0.47	0.052	-9.51	0.052	-9.51
M2447A	700	0^o	0.52	0.38	-	-	-	-

It is obvious that the exciton binding energy and reduced effective mass for the hh-exciton are ordering-dependent and increase as ordering gets stronger. This is qualitatively in agreement with our magneto-PL results [ref. Sec. 5.4.4]. The quantitative difference is believed to be due to different domains involved in the PL and reflectivity process [145]: the PL corresponds to extremely high ordering domains and therefore to a larger effective mass and exciton binding energy. It is also consistent with a 6-band $\mathbf{k} \cdot \mathbf{p}$ simulation including

the ordering effects, which predicts an increase of hh effective mass with ordering [ref. Chapter 6]. However, that that of the lh should be slightly decrease according to the same $\mathbf{k} \cdot \mathbf{p}$ simulation is not the case of our measurement. As a possible reason, the uncertainty of the evaluation may play a role.

It is noteworthy that our results seem to contradict with the reports of Ernst *et al.* on magneto-PL study of $GaInP_2$ bulk material [114], in which the diamagnetic shift measured at $\mathbf{B}\|$ [001] was smaller for ordered (η=0.54) than for disordered alloy, and it was therefore concluded that ordering caused a reduction to the reduced effective mass. But note that there the change of the reduced effective mass solely caused by the effect of the valence-band splitting was not considered. For disordered bulk alloy, the valence-band was degenerate, and the measured reduced effective mass from PL corresponded to an average of the hh- and lh-exciton. Due to the ordering the valence-band degeneracy was significantly removed, which caused the reduced effective mass from PL measurement to correspond to hh-exciton, and hence a relative smaller value. In the case of compressively strained QWs, valence-band degeneracy is well removed before ordering is introduced. Therefore the ordering effect on the effective mass can be clearly identified. At this point, we can conclude that to investigate ordering-dependence of the effective mass, the PL method can be applicable only when the valence-band degeneracy is well removed in advance, either by the CuPt-type ordering or by the compositional strain.

For the lattice-matched sample with low ordering only one transition shows up (c) and its effective mass cannot be estimated due to none obvious diamagnetic shift. The sample with high ordering, however, again shows two transitions like those of compressively strained samples do and its effective mass is accessible. But we have to take caution not to simply conclude that ordering in the lattice-matched samples reduces the effective mass. The reason is as follows: For the sample shown in Fig. 5.13(c), the energetic separation of the hh- and lh-exciton transitions is about 18 meV, which is similar to the FWHM of the SODR peak. The peak energy determined is in the middle of

the both indeed. Regarding the fact that the height of the peak can be regarded to be proportional to the exciton oscillator strength in QWs and magnetic fields enhance the oscillator strength by shrinking the wave function [132], it can be expected that the diamagnetic shift of the peak energy will be "reduced" if the enhancement of the oscillator strength of the lower-energy (hh-exciton in our case) transition is more significant than that of the higher-energy (lh-exciton) transition as the magnetic field gets stronger, no matter whether the reduced effective mass of the hh exciton increases or decreases as ordering gets higher. To obtain further evidence, the SODR spectra as well as the peak energies as a function of the magnetic fields are depicted for the lattice-matched sample with lowest ordering in Fig. 5.14. There is only

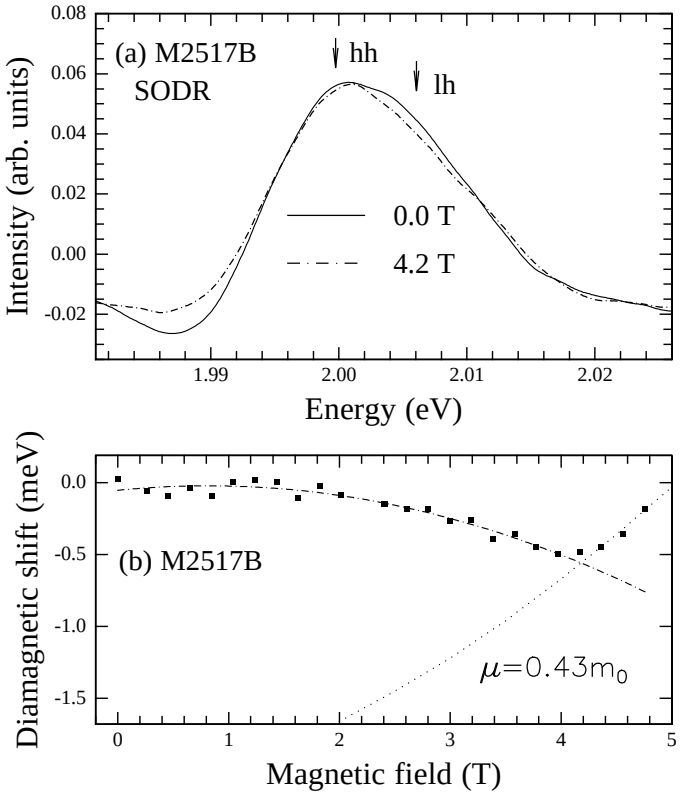

Figure 5.14: (a) Segments of the SODR spectra for the lattice-matched sample with lowest ordering (M2517B) containing the peak from the QWs for two magnetic fields. (b) Diamagnetic shift of the peak. The squares represent experimental values and the dash-dots is a least-square-fit to the points as a guide to the eye.

one (broader) peak in the SODR spectrum with a weak shoulder occurring at the high-energy side. The shoulder is identified as lh- while

the near maximum of the peak as hh-exciton transition, as marked by arrows in Fig. 5.14(a). It is noteworthy that as the peak height around the hh-arrow is identical for the two magnetic fields, the signal around lh-arrow for $B = 4.2$ T is significantly weak relative to that for $B = 0.0$ T. Regarding the fact that the height of the peak can be regarded to be proportional to the exciton oscillator strength in QWs and magnetic fields enhance the oscillator strength by shrinking the wave function [132], this observation can therefore serve as a support of the assumption of different enhancements to the oscillator strength for the hh- and lh-exciton transitions. In Fig. 5.14(b), the diamagnetic shift of the total peak is even negative, because the energetic separation between the hh- and lh-exciton transitions is only ~ 8 meV and obviously smaller than the line-width (full-width at half-maximum) of the SODR peak, which is ~ 15 meV. Such a "negative" diamagnetic shift at lower magnetic fields ($\leq$4 T) occurs due to the smaller diamagnetic shift and the different magnetic-field enhancements of the oscillator strength of the hh- and lh-exciton. For the higher fields, the peak energy is mainly determined by the hh transition, and therefore normal diamagnetic shift shows up. As shown in Fig. 5.14(b) as dot-line, the peak energy can be fitted with an exciton solution using a reduced effective mass of $0.43\mathrm{m}_0$!

In summary, we have shown in this section that the combination of optical reflectivity spectroscopy with derivative technique is powerful in studying exciton binding energy and reduced effective mass based on diamagnetic shift, even under a medium magnetic field, in GaInP/AlGaInP QW system. The determined effective mass and exciton binding energy for some samples indicate both are ordering-dependent.

5.6 Band-edge model for ordered QWs

Now we are in the position to explain the excitation-density dependence of the PL measurements. First, we note that the assumption of spatially indirect recombination [61–65] cannot be considered as a candidate due to the following two reasons:

1. in the regime of spatially indirect recombination, no quadratic diamagnetic shift should be observed [143], and

2. about 20% of the band-gap reduction introduced by ordering is due to valence-band shifting upward [105], which removes the possibility of the spatially type-II band-offset in ordered $GaInP_2$!

The assumption of band-tail states however, seems to be able to explain the excitation-density dependent phenomena, i.e., blue shift and narrowing of the PL peak. But it does not explain the general observation that a large blue shift corresponds to a large stable line-width (FWHM) and both the blue shift and line-width are ordering dependent. We therefore propose a new band-edge model for ordered GaInP/AlGaInP QW system, based on the observation of the Stokes shift being smaller than the FWHM of the first peak in the reflectivity spectrum for all the single-peak samples and the arguments reported by Horner *e*t al. [27] that:

- The local ordering parameter is a function of surface and bulk chemical potentials and bulk inter-diffusion, and it is likely that domains characterized by a distribution function $\mathrm{F}(\eta)$ of ordering parameter η in the range of $0 \leq \eta \leq 1$ will be formed, where $\int_0^1 F(\eta)\, d\eta = 1$;

- PL intensity is dominated by a contribution from small-band-gap domains with values of η above η_{p}, where η_{p} corresponds to the value where $\mathrm{F}(\eta)$ has its maximum.

First we assume a Gaussian form to the function $F(\eta)$,* and plot two functions with their maximum occurring at η_{p} but different FWHM in Fig. 5.15(a). Taking into account the order-induced band-gap reduction, we obtain the band-edge as a function of ordering, as illustrated in Fig. 5.15(b). The dash-dot line is moved slightly down to make the black lines easy to see. Obviously, larger line-width of the distribution function corresponds to larger energy difference between E_{p} and E_{H}. Here E_{p} correlates with reflectivity energy while E_{H} with the PL energy at low excitation density.

*The Lorentzian form gives similar results. Discussion of real feature of the function $F(\eta)$ is out of our interest.

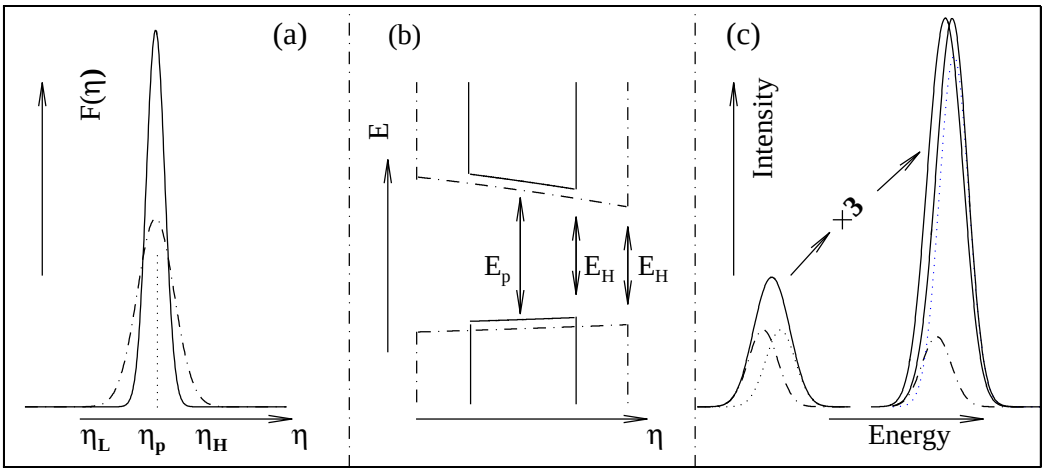

Figure 5.15: (a) Schema of the domain distribution function $F(\eta)$. (b)Band-edge structure in ordered QWs due to the $F(\eta)$. (c) Superposition of two adjacent peaks with identical intensity in the left part, and higher energetic peak (depicted as dots) being 5 times as strong as the lower energetic one (dash-dot) in the right part. The summation from the left part is enlarged with a factor of 3 and moved to overlay on the right part to make a direct comparison of both the line-width and the energetic position of the summations.

With this model, we can explain the blue shift and narrowing of the PL peak in a simplified manner by assuming that the PL is composed of two components occurring at extremely high (η_{H}) and lower ordering (η_{p}) domains, respectively. At low temperature, the density of electrons and holes is very small at low excitation level. Most probably, the carriers diffuse into domains with extremely high ordering and recombine there. It corresponds to low-energy emission (dash-dots in Fig. 5.15(c)). As the domains with extremely high ordering has a very low density, the part of the PL via them is weak and saturates rapidly at low excitation-density. The part of the PL via the domains with lower ordering on the other hand, will get stronger and stronger as the excitation-density increases (shown by dot-line in Fig. 5.15(c)). The shift of the total PL peak to higher energy with increasing the excitation power-density will therefore be drastic at very low excitation level and stop at a particular level when the part of the PL from the lower ordering domains (near to η_{p}) gets strong enough to dominate the total PL peak. The change in the line-width (FWHM) can be easily explained in the same way. Note that if the $F(\eta)$ function is very sharp, the two part of the PL shown in Fig. 5.15(c) will nearly

occur at the same energetic position. The blue shift will be very small, corresponding to a small narrowing or even a broadening of the total peak. This is just the observation in a lattice-matched sample with low ordering (M2447C). According to this model, the PL emission is always excitonic, even at a very low excitation-density. This is in agreement with our measurements. It is worthy to mention that our model is consistent with the experimental observation in the $GaInP_2$ bulk material that the two parts of PL transition are from distinct spatial locations, which was ascribed to spatially indirect recombination before [64].

The general relation between the blue shift and the stable line-width shown in the excitation-dependent measurements is explicable: large blue shift means large scattering of the $F(\eta)$ distribution and small $F(\eta)$ near to the $\eta_{\rm p}$, and therefore corresponds to large stable line-width. The difference existing in excitation-dependent PL measurements on QWs and on $GaInP_2$ bulk material can also be well interpreted. As established, there is a direct correlation between the density of domain boundaries and the relative strength of the excitonic PL peak [65]. From 3-dimensional bulk to (quasi-) two-dimensional QW layer, the density of domains as well as their boundaries may be drastically reduced. The intensity of the PL transition from the domains with extremely high ordering will rapidly saturate in QWs. This will cause a saturation to the blue shift as well as the narrowing of the PL peak at a not-too-high excitation level ($\geq$40 W/cm^2).

The Stokes shift and the FWHM of the first SODR peak are also explicable. As known, the reflectivity peak corresponds to a space-averaged transition [142]. In our case it means that the peak energy is near to $E_{\rm p}$ shown in Fig. 5.15(b), and the FWHM of the (reflectivity) peak is $\sim (E_{\rm L} - E_{\rm H})/2$. On the other hand, the stable PL peak energy $E_{\rm PL}$ is estimated from the corresponding Stokes shift to be between $E_{\rm p}$ and $E_{\rm H}$ and near to the middle point, as shown in Fig. 5.15(b). Obviously, for larger scattering of $F(\eta)$ distribution both the Stokes shift and the FWHM of the SODR peak will take larger values.

Note that our model can not explain the PL from the slightly separated-two-peak samples, which are compressively strained with

low ordering. We note that the Stokes shift of the first SODR peak relative to the low-energy peak in the PL spectrum is significantly larger than the FWHM of the first peak in the reflectivity spectrum, showing that the energy of the low-energy peak is even smaller than that of the transition from extremely high ordering domain. This removes the possibility of relating the low-energy PL peak to (extremely high) ordering domain. As the origin of the low-energy peak can not be clearly identified in our work, we guess it should be caused by strain-related defects occurring especially in the $6^\circ - (111)_\mathrm{A}$ misoriented-substrate case.

From the model and the experimental observations, we can deduce that the scattering of the domain distribution $F(\eta)$ around $\eta(\mathrm{p})$ is more significant for medium ordering, less significant for high ordering and small for low ordering in the lattice-matched samples. Connecting with the experience of best GaInP lasers being from disordered material and $6^\circ - (111)_\mathrm{B}$ misorientation being preferable for achieving ordering [146], we think the scattering of the domain distribution $F(\eta)$ plays a crucial role in the optoelectronic application. Compressive strain causes a degradation of the ordering-homogeneity and probably a bad quality to the samples with $6^\circ - (111)_\mathrm{A}$ and $6^\circ - (111)_\mathrm{B}$ misoriented-substrates.

5.7 Ordering effects on band-offset and transition energy

Band-offset determination for GaInP/AlGaInP structures has been carried out by several groups. Liedenbaum *et al.* [14] obtained a ratio of $\Delta E_c/\Delta E_g = 0.65$ for lattice-matched structure by PLE measurements; Dawson *et al.* [17, 18] determined $\Delta E_c/\Delta E_g = 0.67$ for compressively strained ($x_\mathrm{Ga} = 0.44$) and, $\Delta E_c/\Delta E_g = 0.70$ for tensile strained QWs by low-temperature PLE spectroscopy; Kowalski *et al.* [19] evaluated $\Delta E_c/\Delta E_g^\mathrm{LH} = 0.7/0.3$ and $0.61/0.39$ for the $+0.56\%$ and $+0.71\%$ strained samples by hydrostatic-pressure-dependent low-temperature PL measurements; Zhang *et al.* [34] predicted a ratio of $\Delta E_c/\Delta E_g = 0.65$ for $\mathrm{Ga_{0.5}In_{0.5}P/Al}_z\mathrm{Ga}_{0.5-z}\mathrm{In_{0.5}P}$ heterostructure

with $z = 0.3 \sim 0.35$ by using the first-principles pseudopotential method with virtual crystal approximation. However, no report concerned ordering effect on the band-offset. As the ordering phenomenon is widely observed in vapor phase growth of GaInP systems on (001) substrates [21, 43, 106, 136], and also shows up in the PL and reflectivity studies of the QW structures in the last sections, ignoring it will cause systematic errors.

In this section, first the model-solid method is extended to include ordering effects as well as strain and spin-orbit split-off terms. After obtaining a good fit between experimental and theoretical results, an analysis of the band-offset in ordered and strained $Ga_xIn_{1-x}P$/AlGaInP QW structures is carried out.

5.7.1 Model-solid method for ordering effects

In the following we incorporate two major effects of CuPt-type ordering: band-gap reduction and valence-band splitting [ref. Sec. 2.4], into the model-solid theory to get a theoretical perspective of the ordering-dependent band-offsets and transition energies.

Introducing both the effects into the model-solid theory [49–51], a general description of the band lineup of $Ga_xIn_{1-x}P$ QW layer including the interaction of the (111) CuPt-type ordering with the (001) strain can be obtained as follows:

$$\begin{aligned} E_v^i &= E_{v,\mathrm{av}} + \Delta E_{v,\mathrm{av}}^{\mathrm{hy}} + E_i\,, \qquad (i = 1, 2, 3) \\ E_c &= E_{v,\mathrm{av}} + \Delta E_c^{\mathrm{hy}} + E_g(\epsilon = 0, \eta = 0) \\ &\quad + \frac{1}{3}\left(\Delta^{\mathrm{so}} + \eta^2 \Delta_{111}^{o}(\eta = 1)\right) + dE_g(\eta)\,, \end{aligned} \tag{5.1}$$

where E_v^i and E_c are the valence-band and conduction-band edge energies on an absolute scale. $i = 1, 2, 3$ represents the hh, lh and so valence-subband, respectively. $E_{v,\mathrm{av}}$ is weighted average energy over the three topmost valence bands at Γ point, and taken as a reference energy level [49]. $\Delta E_{v,\mathrm{av}}^{\mathrm{hy}}$ and ΔE_c^{hy} are energy shifts of $E_{v,\mathrm{av}}$ and E_c induced by the hydrostatic strain component, and can be determined by Eq. (2.12)-(2.13) [see page 27]; E_i are valence subband shifts relative

to their weighted average ($E_{v,\mathrm{av}}$) caused by both the uniaxial strain component and atomic ordering. They correspond to the eigenvalue of the following Hamiltonian:

$$H_v = \frac{1}{3}\begin{bmatrix} \Delta_{001}^{\mathrm{sh}} & -\Delta_{111}^{o} - i\Delta^{\mathrm{so}} & -\Delta_{111}^{o} & 0 & 0 & \Delta^{\mathrm{so}} \\ -\Delta_{111}^{o} + i\Delta^{\mathrm{so}} & \Delta_{001}^{\mathrm{sh}} & -\Delta_{111}^{o} & 0 & 0 & -i\Delta^{\mathrm{so}} \\ -\Delta_{111}^{o} & -\Delta_{111}^{o} & -2\Delta_{001}^{\mathrm{sh}} & -\Delta^{\mathrm{so}} & i\Delta^{\mathrm{so}} & 0 \\ 0 & 0 & -\Delta^{\mathrm{so}} & \Delta_{001}^{\mathrm{sh}} & -\Delta_{111}^{o} + i\Delta^{\mathrm{so}} & -\Delta_{111}^{o} \\ 0 & 0 & -i\Delta^{\mathrm{so}} & -\Delta_{111}^{o} - i\Delta^{\mathrm{so}} & \Delta_{001}^{\mathrm{sh}} & -\Delta_{111}^{o} \\ \Delta^{\mathrm{so}} & i\Delta^{\mathrm{so}} & 0 & -\Delta_{111}^{o} & -\Delta_{111}^{o} & -2\Delta_{001}^{\mathrm{sh}} \end{bmatrix} \tag{5.2}$$

where $\Delta_{001}^{\mathrm{sh}}$ is due solely to the uniaxial component of the compositional strain, and determined by Eq. (2.15) [see page 28]; $E_g(\epsilon = 0, \eta = 0)$, the band-gap of strain-free and totally random $\mathrm{Ga}_x\mathrm{In}_{1-x}\mathrm{P}$ alloy, is adopted from Ref. [18],

$$E_g(x) = 1.42 + 0.778\,x + 0.702\,x^2\,.$$

According to Wei and Zunger [30], the ordering modifies the lattice constant, and affect on the valence-band in the manner similar to the spin-orbit interaction. It causes a crystal field splitting described by Δ_{111}^{o} [ref. Sec. 2.4]. $dE_g(\eta)$ is the ordering-induced band-gap reduction at the Γ_6^c [ref. Eq. (2.43), on page 43].

The band lineup for $(\mathrm{Al}_y\mathrm{Ga}_{1-y})_{1-z}\mathrm{In}_z\mathrm{P}$ barrier layer, lattice mismatched to (001) GaAs, can be expressed similar to those of $\mathrm{Ga}_x\mathrm{In}_{1-x}\mathrm{P}$ [Eq. (5.1)], but ignoring ordering effect. That is, E_i can be described as:

$$\begin{aligned} E_1(\mathrm{barrier}) &= \frac{\Delta^{\mathrm{so}}}{3} + \frac{\Delta_{001}^{\mathrm{sh}}}{3}\,, \\ E_2(\mathrm{barrier}) &= -\frac{\Delta^{\mathrm{so}}}{6} - \frac{\Delta_{001}^{\mathrm{sh}}}{6} \\ &\quad + \frac{1}{2}\left((\Delta^{\mathrm{so}})^2 - \frac{2}{3}\Delta^{\mathrm{so}}\Delta_{001}^{\mathrm{sh}} + (\Delta_{001}^{\mathrm{sh}})^2\right)^{1/2}\,. \end{aligned} \tag{5.3}$$

Note that here both the Δ^{so} and $\Delta_{001}^{\mathrm{sh}}$ are of the barrier-layer. We use only the value $E_i(\mathrm{barrier})$ of the topmost valence-sub-band. The

band-gap of strain-free and ordering-free $Al_xGa_yIn_{1-x-y}P$ alloy is also adopted from Ref. [18],

$$E_g(x,y) = 1.42 + 1.84\,x + 0.778\,y + 1.682\,xy + 1.14\,x^2 + 0.702\,y^2$$

The material parameters used as the basis of the modeling are listed in Table 5.1 [18, 51]. Parameters for the ternary and quaternary are linearly interpolated between the binary values, expect for $E_{v,av}$, which takes bowing parameter into account [18]. For $Al_xGa_yIn_{1-x-y}P$, we have

$$\begin{aligned} E_{v,\mathrm{av}} &= z\,E_{v,\mathrm{av}}(\mathrm{InP}) + x\,E_{v,\mathrm{av}}(\mathrm{AlP}) + y\,E_{v,\mathrm{av}}(\mathrm{GaP}) \\ &\quad +3\,z(1-z)\,[a_v(\mathrm{Al_xGa_{1-x}P}) - a_v(\mathrm{InP})] \\ &\quad \times [a_0(\mathrm{InP}) - a_0(\mathrm{Al_xGa_{1-x}P})]\;/a_0(x,y)\,, \end{aligned}$$

where $z = 1 - x - y$, and a_i is the lattice constant for compound i.

We therefore obtain band-gap offsets and band-offset ratios of the ordered $Ga_xIn_{1-x}P$/(AlGa)InP QW:

$$\begin{aligned} \Delta E_c &= E_c(\mathrm{barrier}) - \mathrm{E_c}\,, \\ \Delta E_v^i &= E_v^i - E_v(\mathrm{barrier})\,, \\ Q_c &= \frac{\Delta E_c}{\Delta E_c + \Delta E_v^1}\,. \end{aligned} \tag{5.4}$$

To determine confinement energies $E^z_{e,n}$ and $E^z_{h_i,n}$ (h_i represents h_1, h_2 and h_3, respectively) in quantum well, we use finite-deep square-well model, as described in Eqs. (2.5)−(2.11) [see Sec. 2.2.1, page 25]. The effective masses are also listed in Table 5.5 [51].

Finally, we obtain all the three band-to-band (i.e., e−h_1, e−h_2, e−h_3) transition energies:

$$E_{i,n} = E^z_{e,n} + |E^z_{h_i,n}| + E_c - E_{v,i}\,, \qquad (i = 1,2,3) \tag{5.5}$$

The energy difference of the first two transitions is straightforward,

$$\Delta E^w_{12} = E_{1,n} - E_{2,n}\,. \tag{5.6}$$

5.7.2 Band-to-band transition energies

Based on the experimental results obtained in Sec. 5.5.1, and the modified model-solid method, we first consider the dependence of the band-to-band transition energies on the ordering parameter. Using the data

Table 5.5: Material parameters used to calculate transition energy and band offset in ordered $Ga_xIn_{1-x}P$/AlGaInP QWs [18], l.i. stands for linear interpolation.

parameter	GaP	InP	AlP	$Ga_xIn_{1-x}P$	$(Al_yGa)In_zP$
a_0 (Å)	5.45	5.8686	5.462	l.i..	l.i.
a_v (eV)	1.70	1.27	3.15	l.i.	l.i.
a_c (eV)	-7.14	-5.04	-5.54	l.i.	l.i.
b (eV)	-1.5	-1.6	-1.6	l.i.	l.i.
C_{11} (10^{11}dyn/cm^2)	14.39	10.22	13.2	l.i.	l.i.
C_{12} (10^{11}dyn/cm^2)	6.52	5.76	6.30	l.i.	l.i.
$E_{v,av}$ (eV)	-7.40	-7.04	-8.09		
Δ^{so} (eV)	0.08	0.11	0.07		
m_e^z/m_0	0.15	0.064	0.22	l.i.	
m_{hh}^z/m_0	0.41[a]	0.048[a]	0.52[a]	l.i.	l.i.
m_{lh}^z/m_0	0.16[a]	0.014[a]	0.22[a]	l.i.	l.i.
m_{so}^z/m_0	0.23[a]	0.019[a]	0.34[a]	l.i.	l.i.

[a] Reference [51]

listed in Table 5.5, we numerically solve Eq. (5.5), and plot as lines in Fig. 5.16 the band-to-band transition energies as functions of the ordering parameter η for lattice-matched ($x \simeq 0.52$) and compressively strained ($x = 0.4$) samples, respectively.

We also plot measured transition energies as points in Fig. 5.16 by the following procedure:

1. first, we assume all exciton binding energies to be 12 meV [81], and include them in transferring the measured excitonic transition energies to band-to-band values;

2. We then fit the first transition energy (black squares) to the first theoretical line in Fig. 5.16. This results in a determination of ordering parameter η.

3. Finally, we plot the other transition energies against these η values into Fig. 5.16.

For both the lattice-matched and strained samples, there is very good agreement for the second-transition between the theoretical results and the experimental values. For the third-transition, however, the agreement is not so good, especially for the lattice-matched samples. We assume two possible reasons, (i) the third-transition in the reflectivity spectrum has a much weaker and flatter peak than the

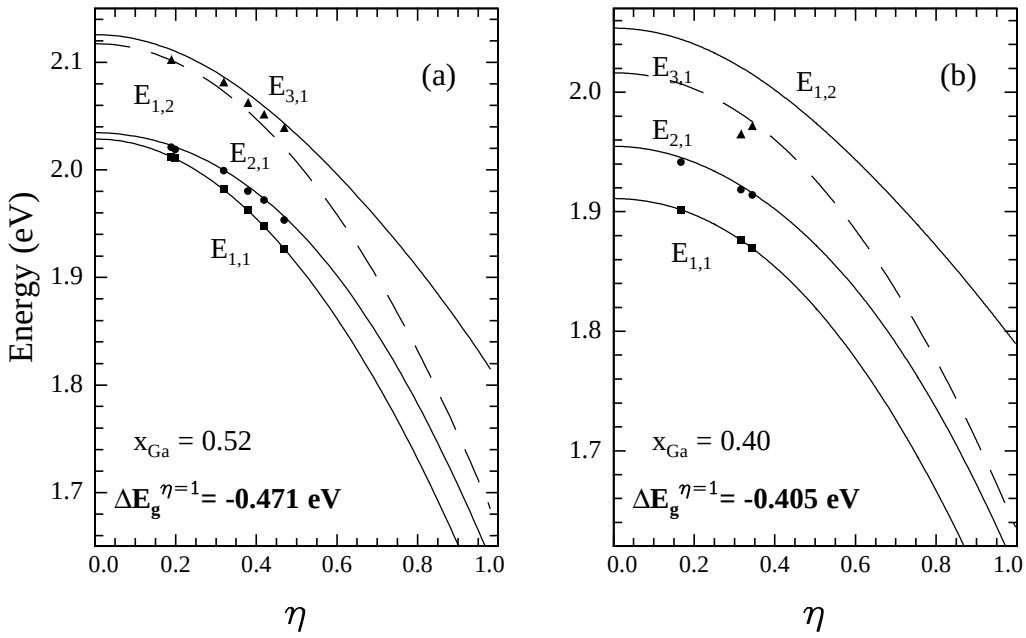

Figure 5.16: Band-to-band transition energy as a function of ordering parameter η for (a) lattice-matched ($x \simeq 0.52$, $y = 0.52$) and, (b) compressively strained ($x = 0.40$, $y = 0.76$) $Ga_xIn_{1-x}P/(Al_{0.66}Ga_{0.34})_yIn_{1-y}P$ QW. Experimental data are plotted as solid dots. $E_{1,1}, E_{2,1}, E_{3,1}$, and $E_{1,2}$ represent the transition energies of $1e-1h_1$, $1e-1h_2$, $1e-1h_3$, and $2e-2h_1$, respectively.

first two transitions, which results in a significant uncertainty in the resonance energy determination; (ii) for the lattice-matched samples, the transition energy of the first excited state of the topmost valence-subband ($E_{1,2}$) is close to that of the ground state of the third valence-subband ($E_{3,1}$) under a low degree of ordering. This will cause further uncertainty to the corresponding peak-position determination.

It is noteworthy that, all the experimental values of valence-band splitting are slightly smaller (in absolute value) than theoretical prediction. A similar phenomenon was also observed in GaInP bulk alloy [30], and was explained as a result of clustering-type short range order (SRO). Such clustering was predicted to reduce the band gap without introducing a crystal field splitting. In our case it is most probably caused by the assumption that the first two excitonic transitions have a equal exciton binding energy. According to an ordering-included 6-band $\mathbf{k} \cdot \mathbf{p}$ simulation [ref. Chapter 6] the second transition corresponds to a relatively large in-plane hole effective mass. It means that the exciton binding energy for the second transition

will be larger than that for the first transition. Assuming equality will therefore cause the valence-band splitting to be underestimated. Note that if the difference of the exciton binding energy between the first two excitonic transitions is accounted for, which is significant for compressively strained samples with high ordering and in a range of a few meV, a better agreement for the valence-band splitting can be obtained.

We have also tried to fit the experimental values with other assumptions, but all gave bad results. In Fig. 5.17 we plot a theoretical

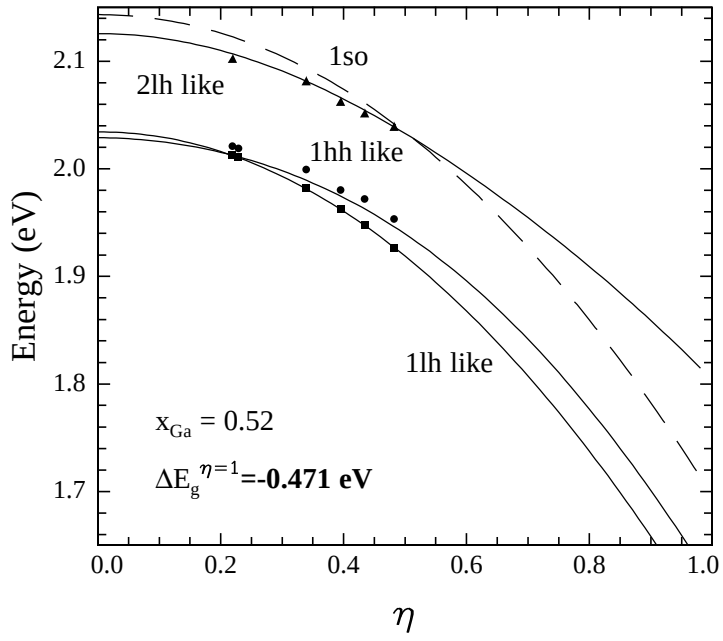

Figure 5.17: Bad description caused by assuming the first subband transition as light-hole like for the lattice-matched and ordered $Ga_xIn_{1-x}P$/AlGaInP quantum wells.

result assuming that the first transition corresponding to a relatively light out-of-plane valence-subband effective mass, i.e., $m_{\rm lh}^z$ listed in Table 5.5.

For the possible error introduced by the assumed value of the exciton binding energy, we note that the deviation of the assumed value from the real value is only a few meV, which is much smaller than the line-width (full-width at half-maximum, FWHM) of the corresponding exciton line in the reflectivity spectrum (estimated to be larger than 24 meV). As an estimate, a 3 meV change in the first transition energy only causes ~ 0.01 change to the η, which falls in the range

of ordering scattering in the QW layer[ref. Sec. 5.6] Therefore the ordering parameter determined by measuring the first band-to-band transition energy and fitting it to the theoretical values can serve as a plausible parameter describing the ordering phenomena in the QWs.

An argument exists here is that fitting the energy difference of the first two transitions, ΔE_{12}, to the numerical simulation could also lead to the determination of η. That was indeed widely used in the study of $GaInP_2$ bulk material [114]. But note that the ΔE_{12} is insensitive to the change of η, especially in the compressively strained samples where a difference of 0.1 in η corresponds to just $\sim$ 1.5 meV change in the ΔE_{12} but about 20 meV change in the $E_{1,1}$. The accurate knowledge of the exciton binding energies of the first two transitions becomes crucially important, which is generally difficult to establish in this material system [20].

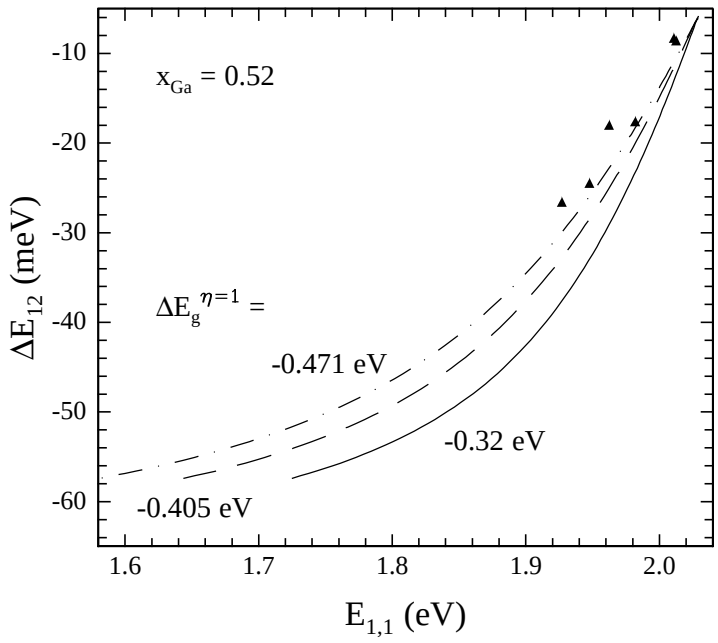

Figure 5.18: Correlation between ΔE_{12} and E_1 (energy of first transition) based on different $\Delta E_g(\eta = 1)$ values for the lattice-matched $Ga_xIn_{1-x}P$ /AlGaInP QWs. The experimental values are plotted as solid triangles.

In Fig. 5.18 we show results based on the $\Delta E_g(\eta = 1)$ values of Geng and Wei *et al.* as well as Ernst *et al.* for the lattice-matched samples. Note that the $\Delta E_g(\eta = 1)$ values from Wei *et al.* and Ernst *et al.* are for the $GaInP_2$ bulk material, while that from Geng is adjusted for

the GaInP QWs with strain. It is clear that Ernst *et al.*'s value

$$\Delta E_g(\eta = 1) = -0.471\,\text{eV} \quad \text{(for bulk)}$$

gives the best fit. Similar work on strained ($x = 0.4$) samples shows, however, Geng's value

$$\Delta E_g(\eta = 1) = -0.405\,\text{eV} \quad \text{(for QWs)}$$

is a better choice for the compressive strain. This suggest that effects of (111) atomic ordering in compressively strained QWs may be weakened, due to the interaction with the (001) elastic strain.

Overall, our results suggest that:

- The modified theoretical model can reasonably predict band-to-band transitions in ordered $Ga_xIn_{1-x}P$ /AlGaInP QWs;
- The first transition has a relatively heavier out-of-plane effective mass than the second does for all the lattice-matched and compressively strained samples, which is similar to disordered situation;
- Measuring the first transition energy will result in a determination of the ordering parameter;
- Under a similar growth condition, compressively strained samples have small ordering parameters relative to the lattice-matched samples. It means that compressive strain tends to weaken the ordering effects;
- While Ernst *et al.*'s experimentally determined $\Delta E_g(\eta = 1)$ value leads to a best fit for lattice-matched QWs, Geng's value, which is based on Ernst *et al.*'s value but including a theoretically predicted strain-correction for strained quantum well, does mostly fit for strained samples. This may suggest that the compressive strain weakens the ordering effect of band-gap reduction.

5.7.3 Ordering effect on band-offsets

Being sure that the theoretical model can reasonably well predict the band-to-band transitions in the ordered $Ga_xIn_{1-x}P$/AlGaInP QWs,

we now set our sights on determining the conduction-band discontinuity, which is crucial for modeling and optimizing opto-electronic device behavior. Using the data listed in Table 5.5, we numerically solve Eq. (5.4), and plot the band-offset ratio as a function of strain and ordering parameter, respectively, in Fig. 5.19. We find that or-

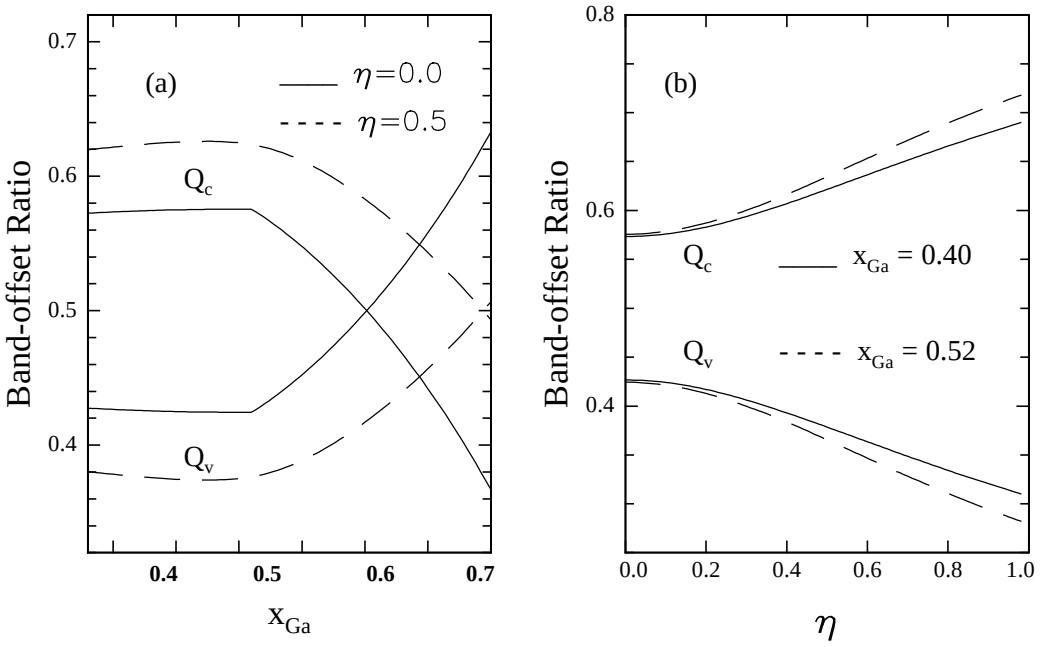

Figure 5.19: Band-offset ratios as a function of (a) strain and, (b) ordering parameter for the $Ga_xIn_{1-x}P/(Al_{0.66}Ga_{0.34})_{0.52}In_{0.48}P$ QW.

dering causes the conduction band-offset ratio to increase, and topmost valence-sub-band offset ratio to decrease, as shown in Fig. 5.19. Meanwhile, ordering removes the cusp, which is caused by $E_{\rm lh}$ and $E_{\rm hh}$ switching order, in Fig. 5.19(a) at $x \sim 0.52(\epsilon = 0)$ for $\eta = 0$. The reason is that even a small amount of atomic ordering will mix equal amount of light-hole and heavy-hole states at $\epsilon = 0$, so the slope of the topmost sub-band $\partial E_1/\partial\epsilon$ at $\epsilon = 0$ is continuous [30].

Note that our results for disordered QWs suggest a nearly constant conduction band-offset ratio $Q_c \simeq 0.58$ for the absence of strain (lattice-matched case) and compressive strain, but a significant drop for tensile strain. It is in excellent agreement with the results given in Ref. [18] predicted by the Krijn formalism of the model-solid theory [51]. The only small difference, if there is any, is believed due to different material parameters having been used. However, our re-

sults differ significantly from Dawson *et al.*'s [18] prediction. An obvious reason is the different definition of Q_c in Ref. [18] and in this work. We have employed a similar definition as that used by Krijn, $Q_c = \Delta E_c/(\Delta E_c + \Delta E_v^1)$, ΔE_v^1 is the confinement of the topmost valence subband. Dawson *et al.* defined $Q_c = \Delta E_c/(\Delta E_c + \Delta E_{\rm hh})$, where $\Delta E_{\rm hh}$ is the confinement energy of the heavy-hole subband, this leads Q_c to a larger value in the range of tensile strain.

Also noteworthy is that our theoretical Q_c is in good agreement with Liedenbaum *et al.*'s experimental value $Q_c = 0.60 \pm 0.05$ obtained by fitting of PLE spectra for $Ga_xIn_{1-x}P$ QW sandwiched by $(Al_{0.66}Ga_{0.34})_{0.52}In_{0.48}P$, but slightly smaller than those recently reported by other workers: Cockburn *et al.* [82] obtained $Q_c = 0.65$ for $GaInP/(Al_{0.66}Ga_{0.34})_{0.52}In_{0.48}P$ by pressure-dependent PL measurements; Dawson *et al.* [17, 18] obtained $Q_c = 0.67$ for $Ga_{0.56}In_{0.44}P/(Al_{0.7}Ga_{0.3})_{0.52}In_{0.48}P$, and 0.70 for $Ga_{0.59}In_{0.41}P/(Al_{0.7}Ga_{0.3})_{0.52}In_{0.48}P$. A common reason is that those Q_c values were determined as an adjustable parameter in the fitting of the ΔE_{12} observed in QWs assuming that the hh- and lh-exciton have an identical binding energy [17]. The fact that the exciton binding energy for lh-exciton is larger than that for hh-exciton makes ΔE_{12} to be underestimated for the compressively strained and lattice-matched QWs, which will cause Q_c to be overestimated. This indicates again that to use the ΔE_{12} in QWs, the exciton binding energies must be accurately known in advance. Another reason, as discussed above, is that Dawson *et al.* have used a different definition of Q_c.

In summary, we have measured ordered and compressively strained /lattice-matched GaInP/AlGaInP QW samples by low-temperature optical-reflectivity spectroscopy to determine the excitonic resonance energies. We incorporated the ordering effects into the model-solid theory so as to account both the strain and ordering effects on the band-edge electronic structures in the quantum wells. The results indicate that:

1. Measuring the first band-to-band transition energy can lead to a reasonable estimation of the ordering parameter in the QWs.

2. For the lattice-matched and compressively strained QWs, the first transition has a heavy out-of-plane (and a light in-plane) effective mass relative to the second transition, even if ordering exists, showing that ordering does not change the valence-subband's order (e.g., the order of hh, lh and so for compressive strain).

3. While Ernst *et al.*'s value of $\Delta E_g(\eta = 1) = -0.471$ eV for the bulk material gives a best fit for the lattice-matched QWs, Geng's value of -0.405 eV for QWs leads to a good fit for compressively strained samples.

4. Compressive strain tends to weaken the ordering effects in the QWs.

5. Ordering causes the conduction band-offset ratio to increase. For the lattice-matched and compressively strained QWs, Q_c falls into a range of $0.58 - 0.7$ as η changes from 0 through 1.

6. For the disordered and lattice-matched/compressively strained QWs, Q_c has a nearly constant value, $Q_c \sim 0.58$.

5.8 Conclusion

In this chapter, the difficulty of carrying out magneto-optical absorption measurements on the ordered $Ga_xIn_{1-x}P$/AlGaInP QW system was pointed out. The sample's structure was then adjusted according the multi-beam interference theorem to fit reflectivity measurement with possibly small Fabry-Pérot interference disturbance. The detailed PL and magneto-PL measurements showed that, in the $Ga_xIn_{1-x}P$/AlGaInP QW structure, the CuPt-type ordering will most probably not result in a type-II electronic band structure. A model of band-structure caused by the ordering was proposed based on the fact that ordering parameter η isn't a unique value but a certain range of distribution, to well explain the experimental observation that the PL-peak shows blue shift with increasing excitation-intensity, and finally tends to saturation. The exciton binding energy and reduced effective mass evaluated by the magneto-optical PL suggest both are ordering-dependent. The transition energies of the first three valence-subband

were determined by the derivative-assisted reflectivity measurement. A modified model-solid method including the ordering effects can well describe ordering phenomena in the $Ga_xIn_{1-x}P$/AlGaInP QWs. Measuring the first transition energy by reflectivity can lead the ordering parameter to be reasonably determined. Proper values of ordering-induced band-gap reduction for lattice-matched [$\Delta E_g(\eta = 1) = -0.471$ eV] and compressively strained [$\Delta E_g(\eta = 1) = -0.405$ eV] have been presented. Also, a band-offset ratio $Q_c \simeq 0.58$ was obtained for disordered and compressively strained and lattice-matched cases. As soon as ordering sets in, Q_c will increase with η, mostly due to the fact that band-gap reduction caused by ordering is mainly from conduction band shifting downward. The derivative-assisted reflectivity experiment indicates that it can serve to evaluate the exciton binding energy and reduced effective mass of this QW system even under medium magnetic fields. The results suggested that ordering has a significant effect on the effective masses: for compressive strain, ordering causes both heavy-hole-like and light-hole-like bands to have a heavier effective mass. Further discussion based on 6-band $\mathbf{k} \cdot \mathbf{p}$ simulation will be presented in Chapter 6.

Chapter 6

Ordering-included 6-band $\mathbf{k} \cdot \mathbf{p}$ simulation

6.1 Introduction

In the past several years, many authors have employed multi-band effective mass theory in dealing with $Ga_xIn_{1-x}P$/AlGaInP quantum well systems. For example, Kamiyama *et al.* [33, 40] first used a conventional 4×4 Luttinger-Kohn Hamiltonian in analyzing the valence subband structures and the optical gain of $Ga_xIn_{1-x}P$/AlGaInP strained-quantum-wells, taking into account the valence subband mixing. Domen *et al.* [42] reported their comparison study with and without the split-off band effect based on a second-order $\mathbf{k} \cdot \mathbf{p}$ method. The axial approximation was used with $\gamma = (\gamma_2 + \gamma_3)/2$. They showed that neglecting the split-off band effect may cause an overestimate of the optical gain because of a small spin splitting energy for GaInP making higher non-parabola of the valence bands. The split-off band effect is particularly significant under tensile strain, since it makes the effective mass very large due to the large interaction between the split-off and light-hole bands. Moritz *et al.* [43, 44] carried out a 6-band $\mathbf{k} \cdot \mathbf{p}$ calculation for quantum-wells based on a Luttinger-Kohn Hamiltonian including strain and ordering as well as split-off band effects. They predicted that as there should exist a strong warping in the valence bands of GaInP even in the case of disordering, no axial approximation could be applied. Therefore they solved a full 6-band problem (without axial approximation) with the z-envelope functions expanded in the quantized solutions of the single finite quantum well at $k = 0$. Note that as they only included the bound states of the z-envelope functions, the results obtained were questionable [147].

In this chapter, we present a finite-difference solution of the 6-band problem, with and without axial approximation. We first derive an ordering as well as strain and split-off-band included 6-band model.

We then employ the finite-difference method to perform the numerical simulation of the model for full 6-band and axial-approach-assumed cases, respectively. The difference between the two cases (with and without axial approximation) are checked. We at last carried out the simulations of the valence subbands (dispersion and effective mass) for the strained and/or ordered quantum-wells to realize a comparison with the experimental work done in Chapter 5.

6.2 Ordering-included 6-band $\mathbf{k}\cdot\mathbf{p}$ model

In an envelope-function approximation the wave function of the valence band in a quantum well is given by [148, 149]

$$\psi_{mk_\parallel(\mathbf{r})} = \sum_{\nu}^{6} G_m^\nu(\mathbf{k}_\parallel, z)\, e^{i\mathbf{k}_\parallel\cdot\rho}\, U^\nu(\mathbf{r})\,, \tag{6.1}$$

where m is a valence subband index; G_m^ν is the envelope function, $U^\nu(\mathbf{r})$ is the cell periodic part of the Bloch function at the zone center, $\mathbf{k}_\parallel = k_x\hat{\mathbf{x}} + k_y\hat{\mathbf{y}}$, and $\rho = x\hat{\mathbf{x}} + y\hat{\mathbf{y}}$. The envelope function $G_m^\nu(\mathbf{k}_\parallel, z)$ satisfies the *multi-band effective-mass equation* [148, 149]:

$$\sum_{\nu}\left[H_{\mu\nu}(\mathbf{k}_\parallel, -i\frac{\partial}{\partial z}) + V(z)\delta_{\mu\nu}\right] G_m^\nu(\mathbf{k}_\parallel, z) = E_m\, G_m^\mu(\mathbf{k}_\parallel, z)\,, \tag{6.2}$$

where $V(z)$ is the quantum-well potential, $H_{\mu\nu}$ is the Luttinger-Kohn Hamiltonian taking the form, e.g., as Eq. (2.36) [ref. page 37].

In constructing the $H_{\mu\nu}$ for the case all the (001) elastic strain, (111) atomic ordering and spin-orbit split-off effects should be taken into account, we assume that the three types of effects are additive. That is

$$H_{\text{total}} = H_k + H_{\text{so}} + H_\epsilon^{(1)} + H_o\,, \tag{6.3}$$

where H_k is the energy in the absence of strain, ordering and spin-orbit coupling; H_{so} and $H_\epsilon^{(1)}$ are the same as defined in Eq. (2.34) [see page 36], which represent the effect of the spin-orbit interaction and the orbital-strain Hamiltonian of the valence bands.

For the CuPt-type ordering widely observed in the GaInP material system, the fourth term can be expressed as [30]

$$H_o^{111,v} = \frac{1}{3}\,\Delta_{111}^{O}(\eta)\begin{bmatrix} 0 & -1 & -1 \\ -1 & 0 & -1 \\ -1 & -1 & 0 \end{bmatrix} \tag{6.4}$$

in the (x, y, z) Cartesian representation for the bulk material, as shown by Wei *et al.* [30]. Here $\Delta_{111}^{O}(\eta)$ is the crystal field splitting due to the atomic ordering. As it has been shown that purely from the symmetry point of view, the Hamiltonian of the ordering has the same symmetry as that of a cubic crystal subjected to a [111] uniaxial stress. Thus, it has the same form as (111) strain, except that $\Delta_{111}^{O}(\eta)$ is a function of the ordering parameter η. The total Hamiltonian for QW can therefore be directly derived from Eq. (2.36) [see page 37], by replacing d-related terms with $\epsilon_{xy} = \epsilon_{yz} = \epsilon_{zx}$ and $d\epsilon_{xy} = -\Delta_{111}^{O}/3\sqrt{3}$.

6.2.1 Consideration of strain effect

In order to take the advantage of using the axial approximation without rewriting the Hamiltonian , we express the ordering term separately from the other terms. The first three terms of the right side of the Eq. (6.3) constitute the 6×6 $\mathbf{k}\cdot\mathbf{p}$ Hamiltonian, H, already used in the calculation of GaInAs/InP QWs, which is well established by Chao *et al.* [8] to take the form of Eq. (2.36) [ref. page 37] in the basis set of

$$\begin{aligned}
|\tfrac{3}{2},\tfrac{3}{2}\rangle &= -\frac{1}{\sqrt{2}}\,|(x+iy)\uparrow\rangle \\
|\tfrac{3}{2},\tfrac{1}{2}\rangle &= \frac{1}{\sqrt{6}}\,|-(x+iy)\downarrow+2z\uparrow\rangle \\
|\tfrac{3}{2},-\tfrac{1}{2}\rangle &= \frac{1}{\sqrt{6}}\,|(x-iy)\uparrow+2z\downarrow\rangle \\
|\tfrac{3}{2},-\tfrac{3}{2}\rangle &= \frac{1}{\sqrt{2}}\,|(x-iy)\downarrow\rangle \\
|\tfrac{1}{2},\tfrac{1}{2}\rangle &= \frac{1}{\sqrt{3}}\,|(x+iy)\downarrow+z\uparrow\rangle \\
|\tfrac{1}{2},-\tfrac{1}{2}\rangle &= \frac{1}{\sqrt{3}}\,|(x-iy)\uparrow-z\downarrow\rangle\,.
\end{aligned} \tag{6.5}$$

Closely following the method described by Chao *et al.* [8], we express $\mathbf{k}_\parallel$ in polar coordinates, $\mathbf{k}_\parallel = k_x\hat{\mathbf{x}} + k_y\hat{\mathbf{y}} = k_\parallel e^{i\phi}$, and rewrite Eq. (2.37) on page 37 as

$$\begin{aligned} P_k &= \left(\frac{\hbar^2}{2m_0}\right)\gamma_1\left(k_\parallel^2 + k_z^2\right) \qquad Q_k = \left(\frac{\hbar^2}{2m_0}\right)\gamma_2\left(k_\parallel^2 - 2k_z^2\right) \\ R &= -\left(\frac{\hbar^2}{2m_0}\right)\sqrt{3}\left[\left(\frac{\gamma_2+\gamma_3}{2}\right)e^{-2i\phi} + \left(\frac{\gamma_2-\gamma_3}{2}\right)e^{2i\phi}\right]k_\parallel^2 \\ S &= \left(\frac{\hbar^2}{2m_0}\right)2\sqrt{3}\,\gamma_3\,k_\parallel k_z\,e^{-i\phi}\,. \end{aligned}$$

By choosing a new basis set

$$\begin{aligned} |u_1\rangle &= \frac{1}{\sqrt{2}}\left(|\frac{3}{2},\frac{3}{2}\rangle\,e^{-i(3/2)\phi} - i|\frac{3}{2},-\frac{3}{2}\rangle\,e^{i(3/2)\phi}\right), \\ |u_2\rangle &= \frac{1}{\sqrt{2}}\left(i|\frac{3}{2},\frac{1}{2}\rangle\,e^{-i(1/2)\phi} - |\frac{3}{2},-\frac{1}{2}\rangle\,e^{i(1/2)\phi}\right), \\ |u_3\rangle &= \frac{-1}{\sqrt{2}}\left(i|\frac{1}{2},\frac{1}{2}\rangle\,e^{-i(1/2)\phi} + |\frac{1}{2},-\frac{1}{2}\rangle\,e^{i(1/2)\phi}\right), \\ |u_4\rangle &= \frac{1}{\sqrt{2}}\left(|\frac{3}{2},\frac{3}{2}\rangle\,e^{-i(3/2)\phi} + i|\frac{3}{2},-\frac{3}{2}\rangle\,e^{i(3/2)\phi}\right), \\ |u_5\rangle &= \frac{-1}{\sqrt{2}}\left(i|\frac{3}{2},\frac{1}{2}\rangle\,e^{-i(1/2)\phi} + |\frac{3}{2},-\frac{1}{2}\rangle\,e^{i(1/2)\phi}\right), \\ |u_6\rangle &= \frac{1}{\sqrt{2}}\left(i|\frac{1}{2},\frac{1}{2}\rangle\,e^{-i(1/2)\phi} - |\frac{1}{2},-\frac{1}{2}\rangle\,e^{i(1/2)\phi}\right), \end{aligned} \tag{6.6}$$

the Hamiltonian H [Eq. (2.36)] can be separated into two block-diagonalized 6×6 matrices,

$$H' = H_{6\times6}^{\mathrm{Re}} + \underline{i}\,H_{6\times6}^{\mathrm{Im}}\,,$$

$$H_{6\times6}^{\mathrm{Re}} = \begin{bmatrix} H_{3\times3}^{1} & 0 \\ 0 & H_{3\times3}^{1\dagger} \end{bmatrix}, \qquad H_{6\times6}^{\mathrm{Im}} = \begin{bmatrix} 0 & H_{3\times3}^{2} \\ H_{3\times3}^{2} & 0 \end{bmatrix} \tag{6.7}$$

where

$$H_{3\times3}^{1} = \begin{bmatrix} -(P+Q) & R_\rho + R_\rho^- \cos 4\phi + iS_\rho & \sqrt{2}(R_\rho + R_\rho^-\cos 4\phi) - \frac{i}{\sqrt{2}}S_\rho \\ R_\rho + R_\rho^-\cos 4\phi - iS_\rho & -(P-Q) & -\sqrt{2}Q - i\sqrt{\frac{3}{2}}S_\rho \\ \sqrt{2}(R_\rho + R_\rho^-\cos 4\phi) + \frac{i}{\sqrt{2}}S_\rho & -\sqrt{2}Q + i\sqrt{\frac{3}{2}}S_\rho & -(P+\Delta) \end{bmatrix}$$

$$
\begin{aligned}
H^2_{3\times3} &= \begin{bmatrix} 0 & R^-_\rho \sin 4\phi & \sqrt{2}R^-_\rho \sin 4\phi \\ -R^-_\rho \sin 4\phi & 0 & 0 \\ -\sqrt{2}R^-_\rho \sin 4\phi & 0 & 0 \end{bmatrix}, \\
R_\rho &= -\left(\frac{\hbar^2}{2m_0}\right)\sqrt{3}\left(\frac{\gamma_2+\gamma_3}{2}\right)k^2_\parallel, \\
R^-_\rho &= -\left(\frac{\hbar^2}{2m_0}\right)\sqrt{3}\left(\frac{\gamma_2-\gamma_3}{2}\right)k^2_\parallel, \quad S_\rho = \left(\frac{\hbar^2}{2m_0}\right)2\sqrt{3}\,\gamma_3\,k_\parallel k_z\,.
\end{aligned}
$$

It is obvious that if $\gamma_2 = \gamma_3$, all the R^-_ρ-related terms in $H^1_{3\times3}$ and $H^2_{3\times3}$ will vanish. The Hamiltonian $H^{'}$ is then block-diagonalized with independence of ϕ, resulting in the subband energies to be ϕ independent. The problem is reduced to search eigenvalues of 3×3 Hamiltonian. The computational efforts can therefore be drastically reduced. This is actually the axial approximation, and has been used in the valence-band analysis in the $Ga_xIn_{1-x}As/InP$ QWs.

In practice, real subband dispersion is not isotropic but possessing C_{4h} symmetry at $k_\parallel > 0$, due to $\cos 4\phi = \cos 4(n\pi/2+\phi)$ and $\sin 4\phi = \sin 4(n\pi/2+\phi)$, $n = 1, 2, \cdots$. The assumption of $|\gamma_2 - \gamma_3| \ll |\gamma_2 + \gamma_3|$ is therefore not so reasonable in the $Ga_xIn_{1-x}P/AlGaInP$ QWs.

6.2.2 Consideration of ordering effect

To get an appropriate expression of the ordering effect, we first transform the ordering term [Eq. (6.4), on page 126] to the basis of Eq. (6.5),

$$
\begin{aligned}
H_o^{111,v} &= \frac{\Delta^O_{111}(\eta)}{3\sqrt{3}} \times \\
&\times \begin{bmatrix} 0 & 1+i & i & 0 & \frac{1}{\sqrt{2}}(1+i) & \sqrt{2}i \\ 1-i & 0 & 0 & i & 0 & \frac{-\sqrt{3}}{\sqrt{2}}(1+i) \\ -i & 0 & 0 & -1-i & \frac{-\sqrt{3}}{\sqrt{2}}(1-i) & 0 \\ 0 & -i & -1+i & 0 & \sqrt{2}i & \frac{1}{\sqrt{2}}(1-i) \\ \frac{1}{\sqrt{2}}(1-i) & 0 & \frac{-\sqrt{3}}{\sqrt{2}}(1+i) & -\sqrt{2}i & 0 & 0 \\ -\sqrt{2}i & \frac{-\sqrt{3}}{\sqrt{2}}(1-i) & 0 & \frac{1}{\sqrt{2}}(1+i) & 0 & 0 \end{bmatrix}
\end{aligned}
$$

then take it to the basis set of Eq. (6.6) to reach a explicit ϕ-dependent description:

$$H_{o'}^{111,v} = \frac{\Delta_{111}^{O}(\eta)}{3\sqrt{3}} \left(H_o^{\mathrm{Re}} + \underline{i} H_o^{\mathrm{Im}} \right), \tag{6.8}$$

where

$$H_o^{\mathrm{Re}} = \begin{bmatrix} 0 & -Si2 & -\sqrt{2}Si2 & 0 & Sm & -\frac{1}{\sqrt{2}}Sm \\ -Si2 & 0 & 0 & -Sm & 0 & \sqrt{\frac{3}{2}}Sm \\ -\sqrt{2}Si2 & 0 & 0 & \frac{1}{\sqrt{2}}Sm & -\sqrt{\frac{3}{2}}Sm & 0 \\ 0 & -Sm & \frac{1}{\sqrt{2}}Sm & 0 & -Si2 & -\sqrt{2}Si2 \\ Sm & 0 & -\sqrt{\frac{3}{2}}Sm & -Si2 & 0 & 0 \\ -\frac{1}{\sqrt{2}}Sm & \sqrt{\frac{3}{2}}Sm & 0 & -\sqrt{2}Si2 & 0 & 0 \end{bmatrix},$$

$$H_o^{\mathrm{Im}} = \begin{bmatrix} 0 & Sp & -\frac{1}{\sqrt{2}}Sp & 0 & Co2 & \sqrt{2}Co2 \\ -Sp & 0 & -\sqrt{\frac{3}{2}}Sp & -Co2 & 0 & 0 \\ \frac{1}{\sqrt{2}}Sp & \sqrt{\frac{3}{2}}Sp & 0 & -\sqrt{2}Co2 & 0 & 0 \\ 0 & Co2 & \sqrt{2}Co2 & 0 & -Sp & \frac{1}{\sqrt{2}}Sp \\ -Co2 & 0 & 0 & Sp & 0 & \sqrt{\frac{3}{2}}Sp \\ -\sqrt{2}Co2 & 0 & 0 & -\frac{1}{\sqrt{2}}Sp & -\sqrt{\frac{3}{2}}Sp & 0 \end{bmatrix},$$

$$\begin{aligned} Si2 &= \sin 2\phi\,, \quad Co2 = \cos 2\phi\,, \\ Sp &= \sin\phi + \cos\phi\,, \quad Sm = \sin\phi - \cos\phi\,. \end{aligned}$$

Eqs. (6.7) and (6.8) constitute the basis for carrying out our valence-band simulations

$$H'_{\mathrm{total}} = H' + H_{0'}^{111,v}\,. \tag{6.9}$$

Note that even under the axial approximation, the valence band warping will still exist. Due to the (111) atomic ordering, the valence-subband dispersion will only have C_{1h} symmetry. This can be concluded from Eq. (6.8), as $\cos\phi = \cos(2\pi+\phi)$ and $\sin\phi = \sin(2\pi+\phi)$. Numerical details, which give a explicit picture, will be presented in next Section. Eqs. (6.7) and (6.8) form the Hamiltonian in Eq. (6.2) by replacing k_z with $-i\partial/\partial z$.

6.3 (Al)GaInP QW: valence band dispersion

As an example, we calculate the valence-band structure in ordered $Ga_xIn_{1-x}P/(Al_{0.66}Ga_{0.34})_{0.52}In_{0.48}P$ QWs on (001) GaAs substrates. For simplicity, we assume the (AlGa)InP barrier-layer is totally disordered. The Ga composition x_{Ga} is selected as 0.40, 0.514, and 0.63, corresponding to -0.84% compressive strain, absence of strain, and +0.86% tensile strain in well-layer. The well width is 10 nm, and the barrier width is 4 nm. The number of the finite-difference points, N, is set at 51 [ref. Fig. 2.6 on page 39]. We use

$$E_g(x) = 1.42 + 0.778\, x_{Ga} + 0.702\, x_{Ga}^2$$

for composition-dependence of the bulk band-gap energy in $Ga_xIn_{1-x}P$ [18], 2.3 eV for direct gap energy of the barrier, and the ordering-induced crystal field splitting $\Delta^o_{111}(\eta = 1)$ of 0.20 eV for the well-layer. We use the valence-band discontinuity, $\Delta E_v/\Delta E_g = 0.35$ in the literature [34], and assume it is independent of ordering*. Other parameters used in the calculations are derived from those of corresponding binary compounds, most of which are listed in Table 5.5, by linear interpolation. The Luttinger-Kohn effective-mass parameters are listed in Table 6.1 [87, 150].

Table 6.1: Luttinger effective-mass parameters for GaInP and AlGaInP. l.i. stands for linear interpolation

parameter	GaP	InP	AlP	$Ga_xIn_{1-x}P$	$(Al_{0.66}Ga_{0.34})_yIn_{1-y}P$
γ_1	4.20	6.28	3.47	l.i.	l.i.
γ_2	0.98	2.08	0.06	l.i.	l.i.
γ_3	1.66	2.76	1.15	l.i.	l.i.

With the obtained valence-band dispersion, we also estimate the in-plane hole effective mass according to Eq. (2.35) [see page 37].

Note that almost all the studies already reported have employed the axial approximation in the simulation to simplify the problem and to reduce the computational effort. Moritz *et al.* suggested that because the intrinsic warping of GaInP is strong even for the totally

*As discussed in Sec. 5.7.3, for partially ordered with small ordering parameter $\eta \leq 0.4$, the valence-band discontinuity only slightly changes with η.

disordered case, the axial approach can't be applied [43]. But it was left unknown how is the difference between the calculations with and without the axial approximation. In this section, we carry out an analysis of the angle-dependent valence-band dispersion by using two methods, that is, with and without the axial approximation and make a simple comparison. We also investigate the intrinsic warping (due to $\gamma_2 \neq \gamma_3$) and the warping purely introduced by the ordering.

6.3.1 Importance of non-axial contributions

Figures 6.1-6.3 show in the (100)-, (110)- and $(1\bar{1}0)$-direction, respectively, the valence-band dispersions for the disordered and partially ordered ($\eta = 0.5$) QWs with Ga fraction of $x_{\mathrm{Ga}} = 0.40$ (Fig. 6.1), 0.514 (Fig. 6.2), and 0.63 (Fig. 6.3). They are calculated with (indicated by the dashed lines) and without (indicated by the solid lines) the axial approach, respectively. The subbands are ordered with **hh** and **lh**, which represent *heavy-hole* and *light-hole*, respectively, and are determined by the model-solid theory established in Sec. 5.7.1 [ref. page 112].

It is obvious that

1. *Ordering causes the valence-band to shift upward for all the compressive strain, absence of strain and tensile strain conditions.*

   This makes clear that in the band-gap reduction due to the ordering, besides the contribution of the conduction-band moving downward, that the valence-band moving upward also plays a role.

   By making a quantitative estimation, we find a value of about 50 meV for the compressive and tensile strain, and some 60 meV for the absence of strain, in the case of total order ($\eta = 1.0$).

   Recalling the results obtained in Sec. 5.7.2, we can conclude that about 13% of the band-gap reduction is from the valence-band shifting upward. This, from the theoretical point of view, does not suggest that the ordering in the QW-layer could cause a type-II electronic substructure [see Sec. 5.4.1, page 92]. It is noteworthy

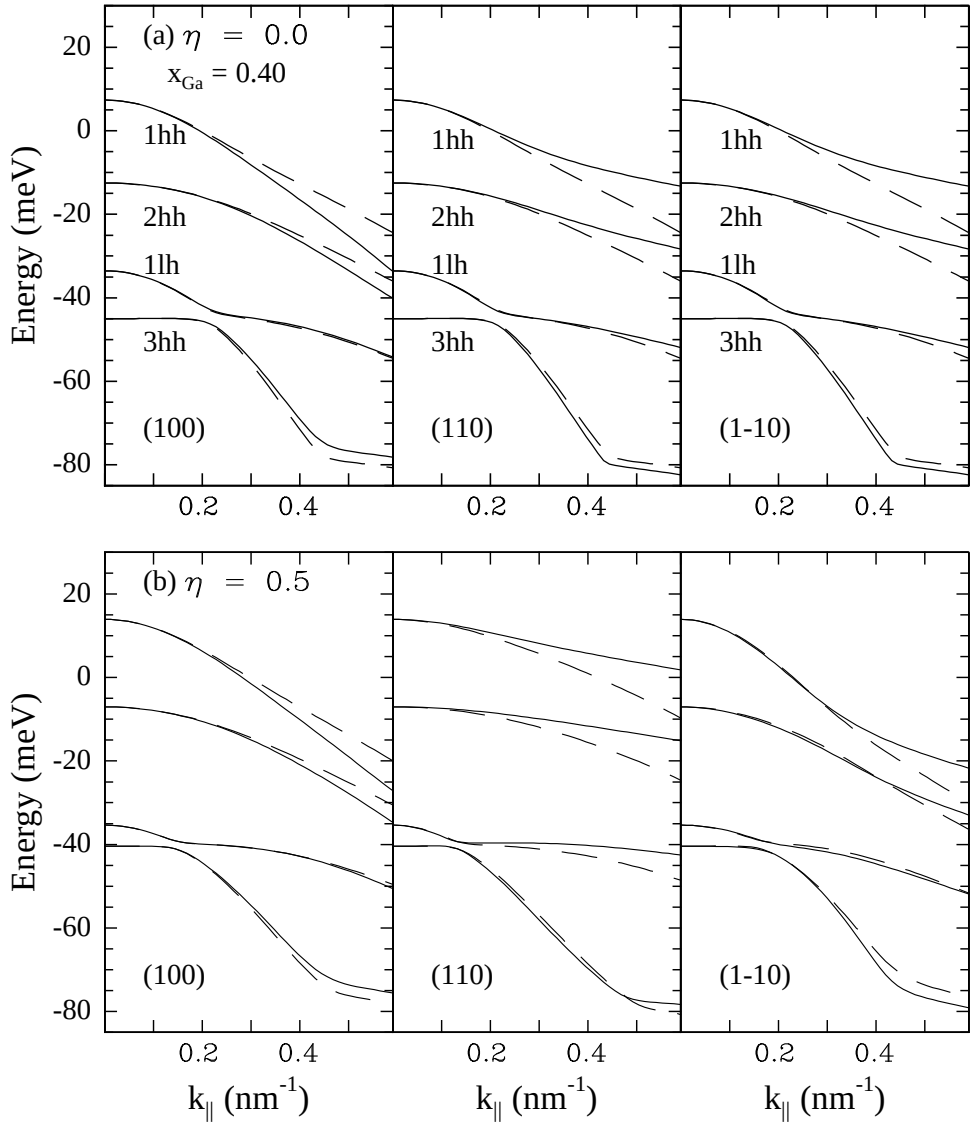

Figure 6.1: Dispersion relation for the disordered (a) and ordered (b) $Ga_xIn_{1-x}P$/AlGaInP QWs with **compressive strain** ($x_{Ga} = 0.40$), in the (100), (110) and (1$\bar{1}$0) directions. Solid-line indicates without axial approach, dash-line with axial approach.

that recently a slightly larger value ($\sim$20%) for $GaInP_2$ alloy was reported based on electro-absorption measurements [105].

2. *The strain-dependent valence-band dispersion is similar to that of the* $Ga_xIn_{1-x}As$/InP *QWs.*

   For the compressive strain, the maxima of the first three valence subbands are at the Brillouin-zone center ($k_{\|} = 0$). The difference caused by with and without the axial approach is undetectable

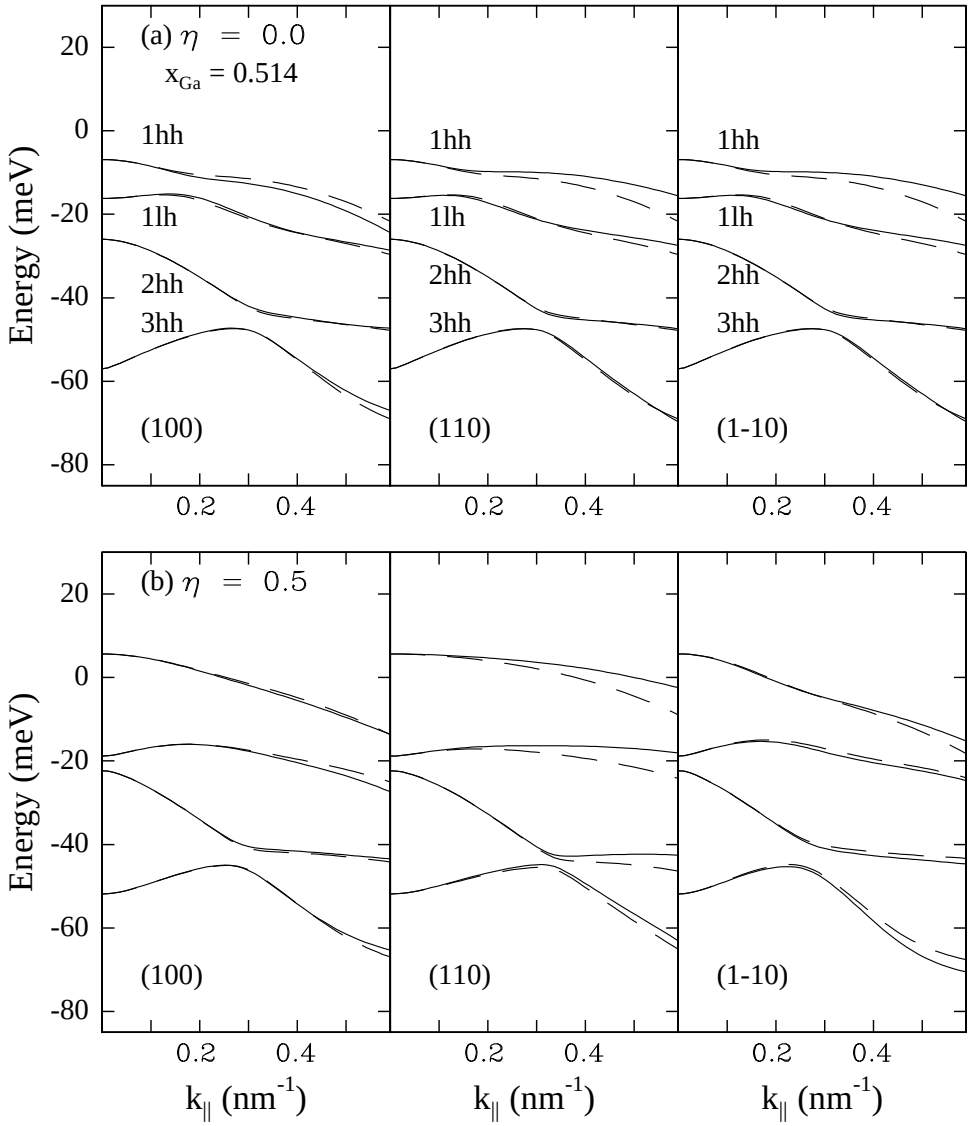

Figure 6.2: Same as Fig. 6.1, but for the **lattice-matched** QWs, $x_{\rm Ga} = 0.514$.

in the zone center, but becomes significant at $\mathbf{k}_{\|} > 0.2$ nm^{-1}.

For the absence of strain, while the maxima of the first and third subbands are at the zone center ($k_{\|} = 0$), that of the second subband is away from the zone center, and appears at $k_{\|} \simeq 0.15$ nm^{-1}. This is understood as a result of the strong repulsion from the lower hh-like band (here is the third subband). It can be seen from Figs. 6.1-6.3 that the separation between the second and the third subbands is much smaller for the absence of strain than for compressive strain. The difference caused by with and without the axial approach for the absence of strain is smaller than for

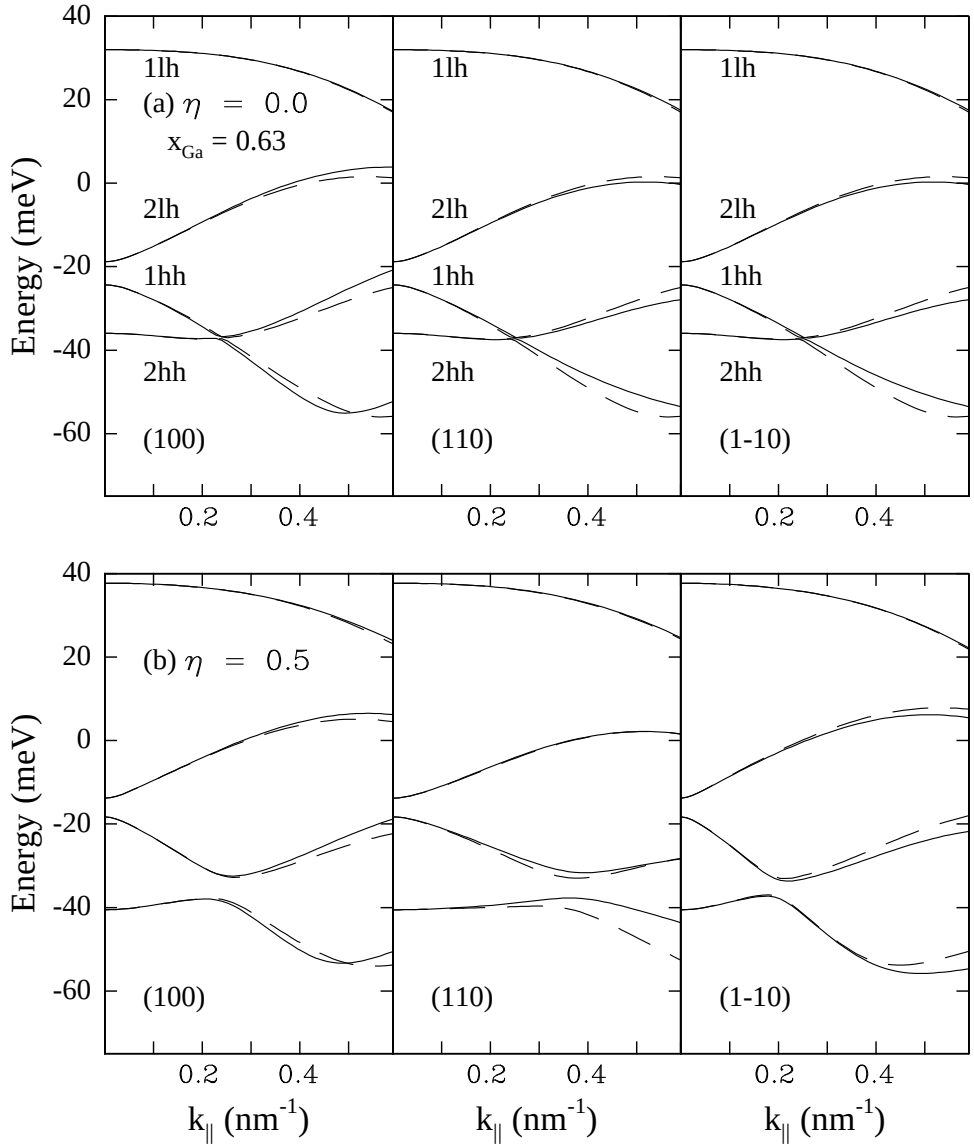

Figure 6.3: Same as Fig. 6.1 and Fig. 6.2, but for the **tensile strain** QWs, $x_{\mathrm{Ga}} = 0.63$.

the compressive strain, especially for the partial order.

For the tensile strain, the dispersion of the first subband is much flatter than those of the compressive strain and absence of strain. Similar to the (disordered) $\mathrm{Ga}_x\mathrm{In}_{1-x}\mathrm{As/InP}$ QW, the first subband is lh-like with a heavier in-plane effective mass. The difference between the calculations with and without the axial approach is nearly undetectable for the first subband, even at $k_{\|} > 0$. The ordering increases the separation between the first two bands, but decreases that between the second and the third, caus-

ing an obvious change to the dispersion-shape of the second subband.

3. *There is a difference between the dispersions of three different directions from the full 6-band calculations (without the axial approximation).*

   For disorder ($\eta = 0$), those of the (110) and (1$\bar{1}$0) are identical but differ from that of (100), especially for the compressive strain and absence of strain, due to the fact that the valence-band dispersion is anisotropic at the valence-band maximum, and the effect is most pronounced for the hh-band which has a strongly direction-dependent effective mass with a larger mass along (111) direction compared to the (100) direction.

   For ordering ($\eta = 0.5$), however, that of the (110) is drastically different from those of the (100) and (1$\bar{1}$0), especially for the first two subbands in the compressive strain and absence of strain, which show rather flat dispersions as that in the tensile case. This, on the other hand, is caused by the (111) ordering. As can be predicted, the ordering is analogous to the (1$\bar{1}$1)-direction compressive strain [ref. Eq. (6.4)], which causes compressive-strain effect along the (1$\bar{1}$0)-, and tensile-strain effect along (110)-direction in the well plane.

6.3.2 Valence-band warping of disordering

Figure 6.4 shows the angle-dependent energy (a) and inverse effective mass (b) of the first three subbands at $k_{\|} = 0.2$ and 0.4 nm^{-1}, for *disordered* $Ga_xIn_{1-x}P$/AlGaInP QWs with $x_{Ga} = 0.40$, 0.514 and 0.63, respectively, calculated *without axial approach.* The inverse effective mass is calculated according to Eq. (2.35) [see page 37], which represents the second-order derivative of the dispersion against $k_{\|}$.

We can see that the dispersion of the first subband is strongly angle-dependent for the compressive strain and absence of strain, at $k_{\|} > 0$, where it has its energy *maximum* at $(2n+1)\times 45°, n = 0, 1, 2, 3$, against $\mathbf{k_x}$, that is, along (110)-, ($\bar{1}$10)-, ($\bar{1}\bar{1}$0)-, and (1$\bar{1}$0)-direction. The warping in the tensile strain, however, is much weaker in the $k_{\|}$ range

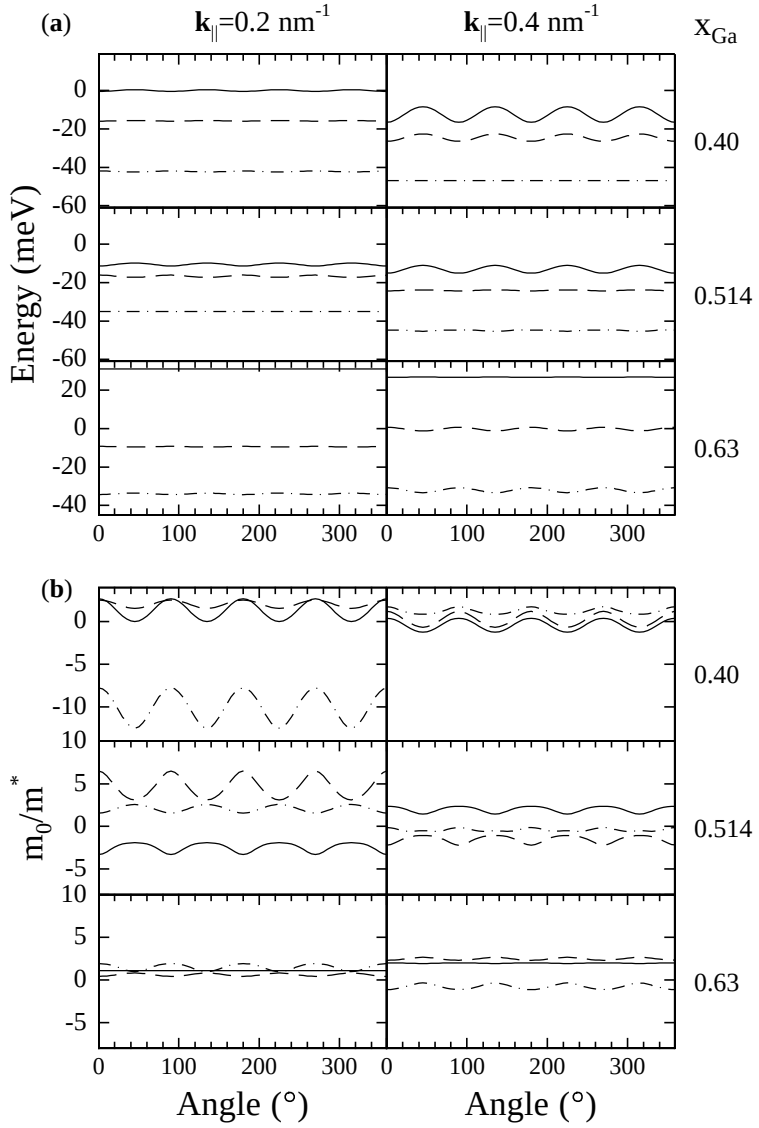

Figure 6.4: Angle-dependent energy (a) and inverse effective mass (b) of the first three subband for **disordered** GaInP/AlGaInP QWs with $x_{\mathrm{Ga}} = 0.40$, 0.514, and 0.63, respectively, obtained **without the axial approach**. Solid lines indicate the first subband, dashed the second and dash-dot the third. The inverse effective mass is calculated with $m_0/m^*_\rho = -(m_0/\hbar^2)\partial^2 E(k)/\partial k^2$.

calculated. This provides a possibility to use the axial approach in 6-band $\mathbf{k}\cdot\mathbf{p}$ simulation of valence-band dispersion in the *Brillouin-zone center* for the *totally disordered* tensile strained GaInP/AlGaInP QW (though it is very difficult to obtain in the sample preparation) without big error, despite of the fact that the difference between γ_2 and γ_3 of this material system is much bigger than that of GaInAs. Thereby the computational effort involved can be significantly reduced [8,39,41,42].

Looking at it closely, we find that the effective mass of the first subband for the compressive strain and absence of strain (hh) takes its maximum, while that of the third subband for the compressive strain and the first subband for the tensile strain (lh) takes its minimum along the $(2n+1)\times 45°, n = 0, 1, 2, 3$, directions. This result is consistent with the following facts: As well established, in bulk material the effective mass of heavy- as well as light-hole valence band can be defined in terms of the Luttinger γ parameters, γ_1, γ_2, γ_3 with [151]

$$m^*_{\mathrm{hh},(001)} = (\gamma_1 - 2\,\gamma_2)^{-1}\,, \quad m^*_{\mathrm{lh},(001)} = (\gamma_1 + 2\,\gamma_2)^{-1}\,,$$
$$m^*_{\mathrm{hh},(111)} = (\gamma_1 - 2\,\gamma_3)^{-1}\,, \quad m^*_{\mathrm{lh},(111)} = (\gamma_1 + 2\,\gamma_3)^{-1}\,.$$

Because of $\gamma_2 < \gamma_3$ [see Table 6.1, page 130], the hh subband has a larger while the lh subband has a smaller effective mass along the (111) direction than that calculated with the axial approach, $\bar{\gamma} = (\gamma_2+\gamma_3)/2$. In the well-plane, this will lead a larger value of the effective mass to the hh and a smaller one to the lh along the (110) and equivalent $[(2n+1)\times 45°,\ n = 0, 1, 2, 3]$ directions.

6.3.3 Pure ordering effect from axial approach

In Fig. 6.5-6.7, we plot the numerical results of the angle-dependent energy (a) and inverse effective mass (b) for the compressive strain ($x_{\mathrm{Ga}} = 0.40$), absence of strain and tensile strain ($x_{\mathrm{Ga}} = 0.63$), respectively, by using the *axial approach*.

For disordering ($\eta = 0.0$), the subband-energy and effective mass are not angle-dependent at any $k_\parallel$ value, due to the axial approach. With the ordering parameter increasing, the subband-energy becomes angle-dependent at $k_\parallel > 0.0$. Such a tendency is very significant for the compressive strain and absence of strain, where the energy maximum occurs in the (110)- and $(\bar{1}\bar{1}0)$-direction, and the minimum in the $(1\bar{1}0)$- and $(\bar{1}10)$-direction. This is also the case for the band-edge effective mass ($k_\parallel = 0$) of the first two subbands, though the situation will be very complicated at higher $k_\parallel$ region, where band-mixing may be strong. Recalling the fact that the $[111]_{\mathrm{B}}$ ordering can be considered as "strain" along (111)-direction, the angle-dependence of the energy and effective mass is easily understood with assuming that

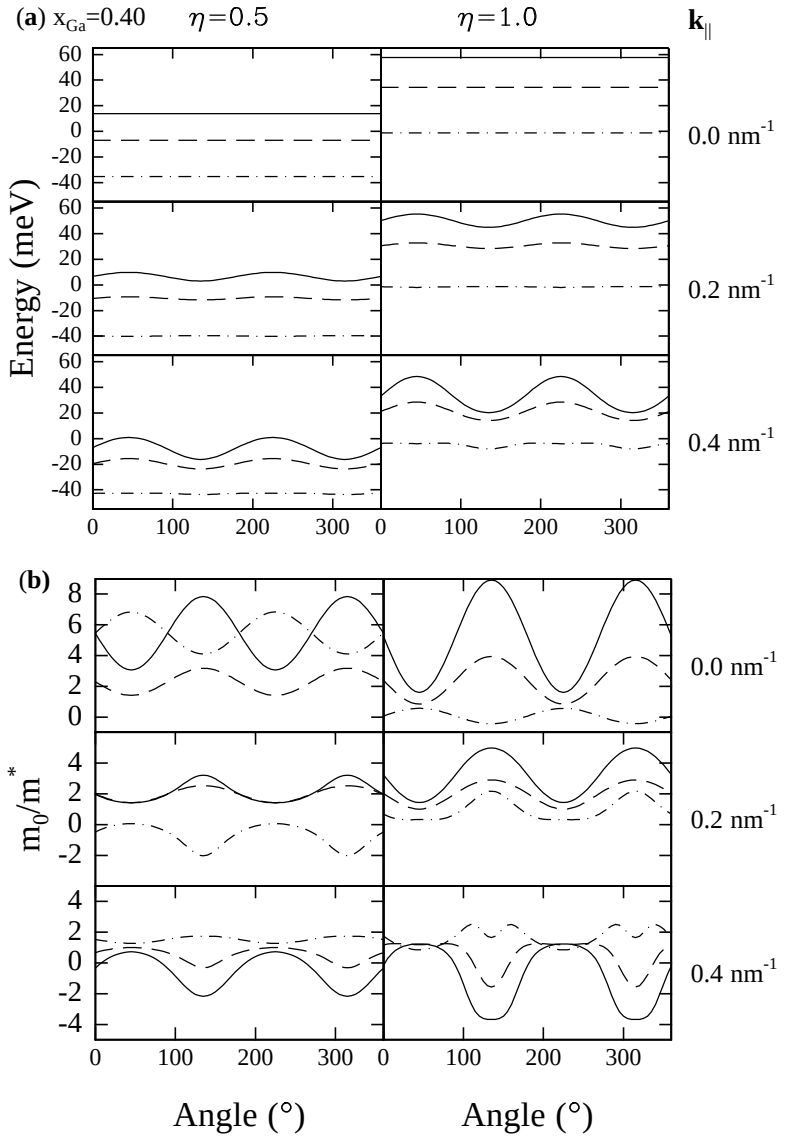

Figure 6.5: Angle-dependent energy (a) and inverse effective mass (b) of the first three subbands by using the **axial approach**, for the **compressive strain** $Ga_xIn_{1-x}P$/AlGaInP QWs. Solid lines indicate the first subband, dashed lines the second and dash-dot the third.

the "strain" is compressive along $(1\bar{1}1)$-direction [or $(\bar{1}11)$-direction]. Such a "strain" has two components in the (x, y, z) coordinate. One of which is along $(1\bar{1}0)$-direction [or $(\bar{1}10)$-direction], and causes a further reduction to the effective mass as well as energy as that done by compressive strain. On the other hand, its equivalent tensile strain along the (110)-direction [or $(\bar{1}\bar{1}0)$-direction] results in an increase to the effective mass as well as energy in this direction.

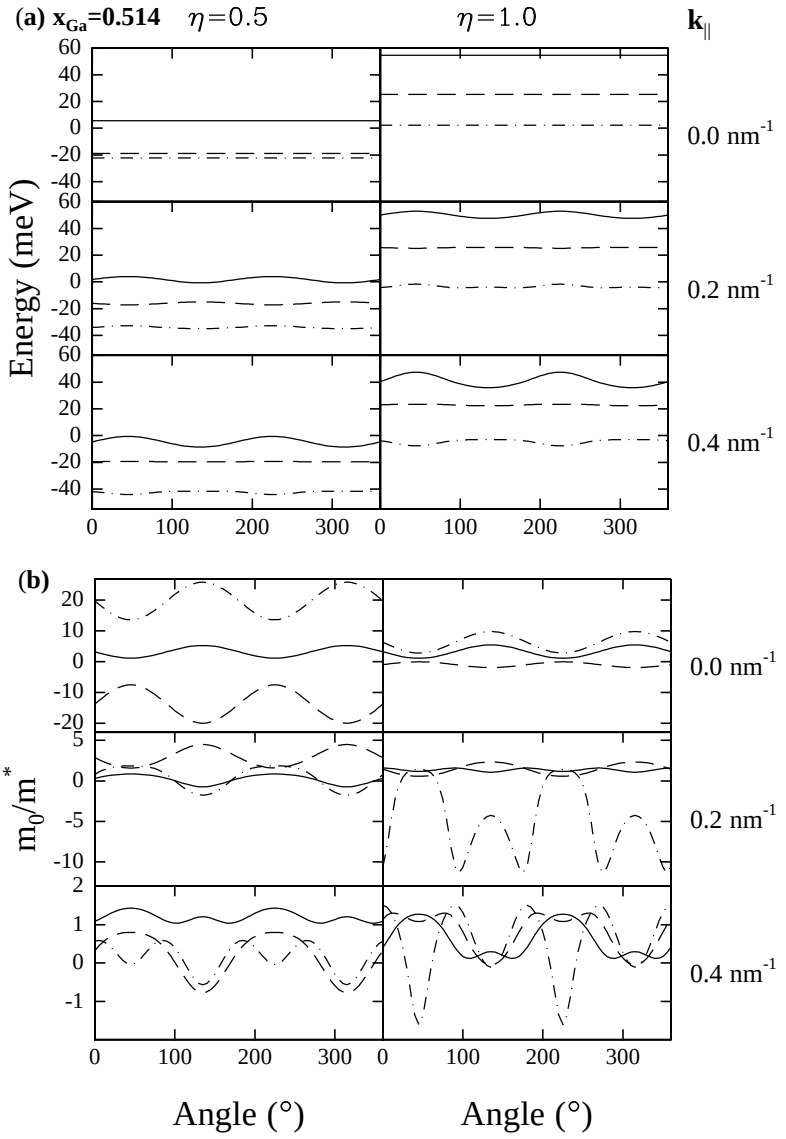

Figure 6.6: Same as Fig. 6.5, but for **lattice-matched** QWs.

The warping of the first subband caused by pure ordering is stronger than that of the second subband for the compressive strain, in contrast to the case for tensile strain, where nearly no warping detected for the first subband (lh-like). Though ordering results in significant warping effect to the band energy at high $k_{\|}$ value, its dominant influence on the subband effective mass also occurs at the Brillouin-zone center, which is most important in understanding various experimental results, such as magneto-PL, and excitonic properties. Also clearly seen is that even partial ordering can result in significant warping to the valence-band

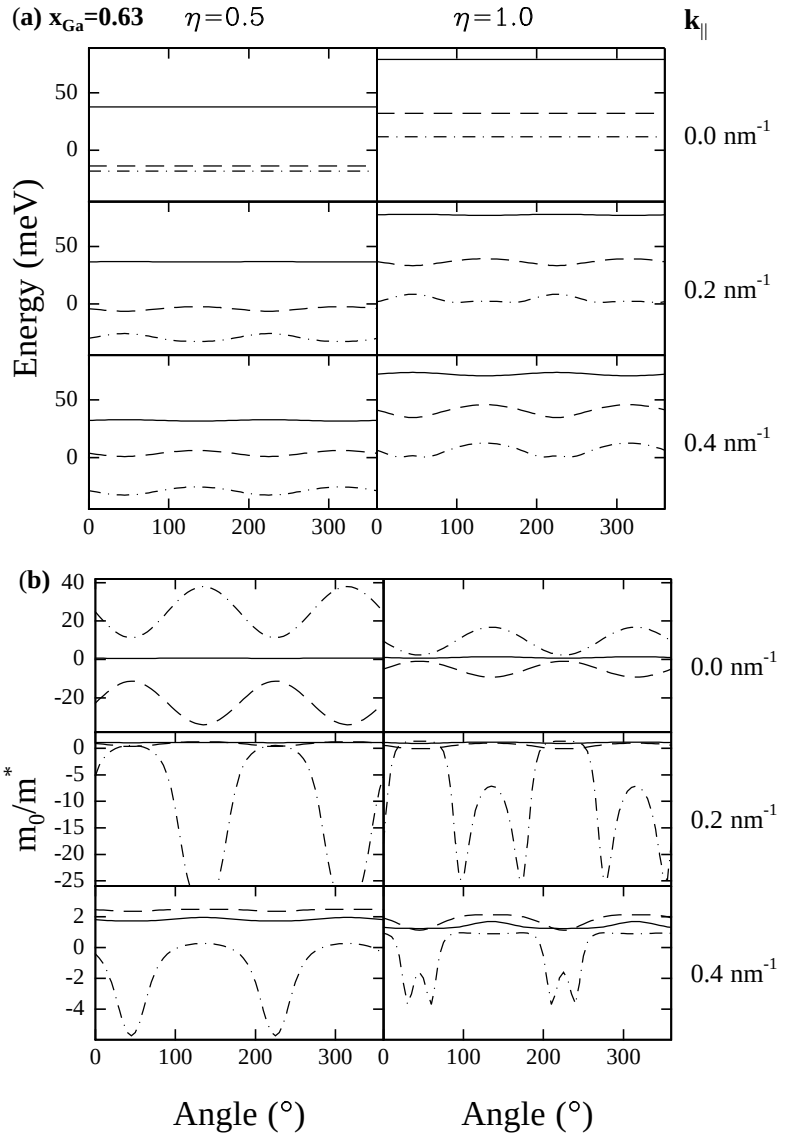

Figure 6.7: Same as Fig. 6.5 and Fig. 6.6, but for **tensile strain** QWs.

effective mass. This shows the necessity of including ordering into the valence-band effective mass analysis.

6.3.4 Conclusion: Is the axial approach applicable?

From the above discussion we learn that the intrinsic warping (due to $\gamma_2 \neq \gamma_3$, calculated without the axial approach) produces a in-plane valence-band anisotropy with the maximum of the subband energy as well as of effective mass occurring in the directions of $(2n+1) \times 45°, n = 0, 1, 2, 3$, against $\mathbf{k_x}$, in the disordered QWs. The CuPt-type

ordering, on the other hand, causes further warping effect. It acts as a tensile strain along the (110)-, and a compressive strain along the ($\bar{1}$10)-direction. For any strain, the ordering shifts the valence-subband upward. The value is about 13% of the ordering-induced band-gap reduction.

In the compressively strained and lattice-matched $Ga_xIn_{1-x}P$/AlGaInP QWs, due to the strong intrinsic warping, the axial approach cannot be reasonably used. Also, the ordering-induced warping is significant for the valence-band dispersion as well as band-edge effective mass. They should be considered in the band-structure analysis. Therefore a full 6-band $\mathbf{k} \cdot \mathbf{p}$ model is needed.

For the tensile strain, however, the intrinsic warping of the valence-band dispersion as well as the band-edge effective mass is nearly undetectable for the first subband, and very weak for the second. The ordering-induced warping, however, can be ignored for the first subband, but not for the second. Therefore only in the disordered and/or very low level ordered tensile strained QWs, the axial approximation can be used, which achieves a drastic reduction of the computational effort.

6.4 Valence-band effective mass in QWs

In this section, we perform numerical analysis of the valence band effective mass by using the full-6-band (*without axial approach*) method. A comparison with our experimental values evaluated by optical reflectivity [see Sec. 5.5.2, page 102] is also made.

6.4.1 Effective mass in disordered quantum well

Figure 6.8 shows the (100)-direction inverse subband effective mass as a function of $k_{\|}$ for totally disordered QWs with Ga fraction $x_{\mathrm{Ga}} = 0.40, 0.514$ and 0.63, respectively. The well-width was selected as 10 nm in all cases. The solid lines represent the first subband, which is in the Brillouin-zone center hh subband for the compressive strain and absence of strain, and is lh subband for the tensile strain. The dashed lines represent the second subband, and is the first lh subband for the

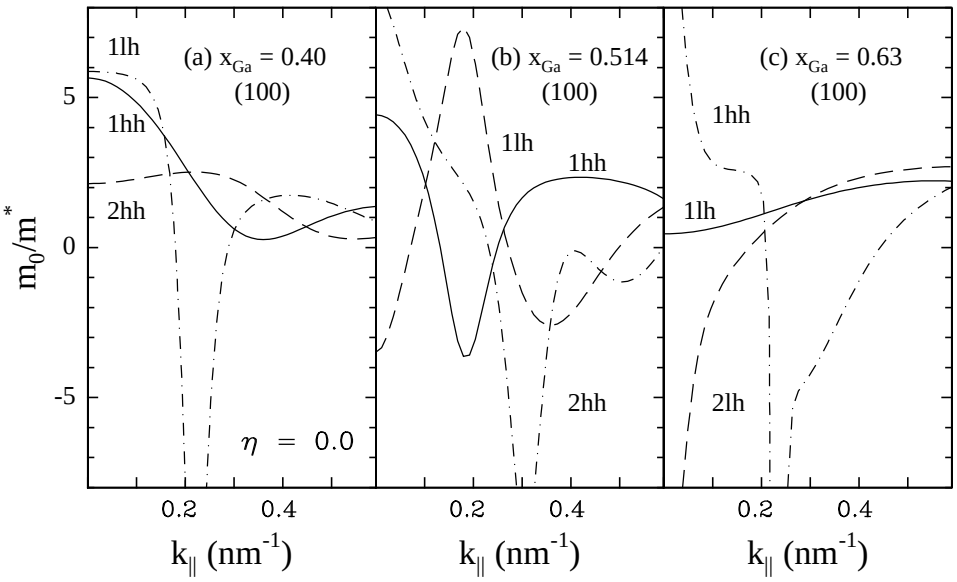

Figure 6.8: (100)-direction inverse subband effective mass of totally disordered QWs with Ga fraction $x_{\mathrm{Ga}} = 0.40$ (a), 0.514 (b), and 0.63 (c). Solid lines indicate the first subband, dashed lines the second and dash-dots the third.

absence of strain. As the third subband, the dash-dots represent the first lh subband for the compressive strain and the first hh subband for the tensile strain.

As can be seen, at the band-edge,

- the compressive strain corresponds to very small 1hh and 1lh effective mass, both are positive;
- the tensile strain corresponds to very heavy effective mass for the 1lh band, and very small for the 1hh band;
- for the absence of strain, however, while the effective mass for the 1hh band is a little heavier than that of the compressive strain, that for the 1lh is negative.

Similar phenomena were observed by several groups in disordered $\mathrm{Ga}_x\mathrm{In}_{1-x}\mathrm{P}$/AlGaInP QWs [41, 42]. The results can be understood as follows. For the compressive strain, the energy difference between the 1hh and 1lh is larger due to the shear deformation energy. The reduction of the mixing between the 1hh and 1lh results in a small effective mass at the band-edge. As the $k_{\|}$ value increases, the 1hh band couples with lh, split-off as well as other hh bands [ref. Fig. 6.1 on page

132]. This leads the effective masses of the 1hh to increase. For the tensile strain, the lh subband is lifted at the band-edge [ref. Fig. 6.3 on page 134]. It couples with split-off band, therefore corresponds to a very large in-plane effective mass. For the absence of strain, the small energy difference between the 1hh and 1lh [ref. Fig. 6.2 on page 133] results in a relative large heavy-hole effective mass in comparison with the compressive strain. Strong coupling between the 1lh and split-off, however, leads the lh to have a negative in-plane effective mass.

6.4.2 Ordering effect on effective mass

Ordering effects on inverse band-edge effective mass are shown in Fig. 6.9. Similar to that shown in Fig. 6.5-6.7, here again indicates that for disorder ($\eta = 0.0$) with any strain, the effective mass at the band-edge ($k_{\|} = 0.0$) is independent of angle, that is, there is no warping effect. Note that the results for $k_{\|} = 0$ is identical with those from using the axial approach [see Sec. 6.3.3, page 137]. This is expected from Eq. (6.7) [see page 127]. As $k_{\|} = 0$ causes all ϕ related terms to vanish, no difference will exist between that of with and without the axial approach.

For $k_{\|} > 0$ and $\eta > 0$, the intrinsic warping (due to $\gamma_2 \neq \gamma_3$) and ordering-induced warping come into action. Therefore the warping will be determined by both effects.

Concerning the warping effect in the compressive strain and absence of strain, we note that the ordering enhances the intrinsic warping of the 1hh subband along the (110) and $(\bar{1}\bar{1}0)$ directions. In the $(1\bar{1}0)$ and $(\bar{1}10)$ directions, however, the ordering causes a contrary effect to the intrinsic warping, which reduces the effective mass, and therefore forms the dip in Fig. 6.9(b,i). For total ordering ($\eta = 1$), the minimum of the effective mass will nearly occur in these direction. Nevertheless, an obvious difference still exists between those with and without the intrinsic warping [ref. Fig. 6.5(b) on page 138]. This suggests that for the compressive strain and absence of strain, the intrinsic warping should be considered no matter what degree of the ordering exists.

For the tensile strain ($x_{\mathrm{Ga}} = 0.63$), the ordering only slightly changes the anisotropy of the first (lh-like) subband effective mass. It reduces

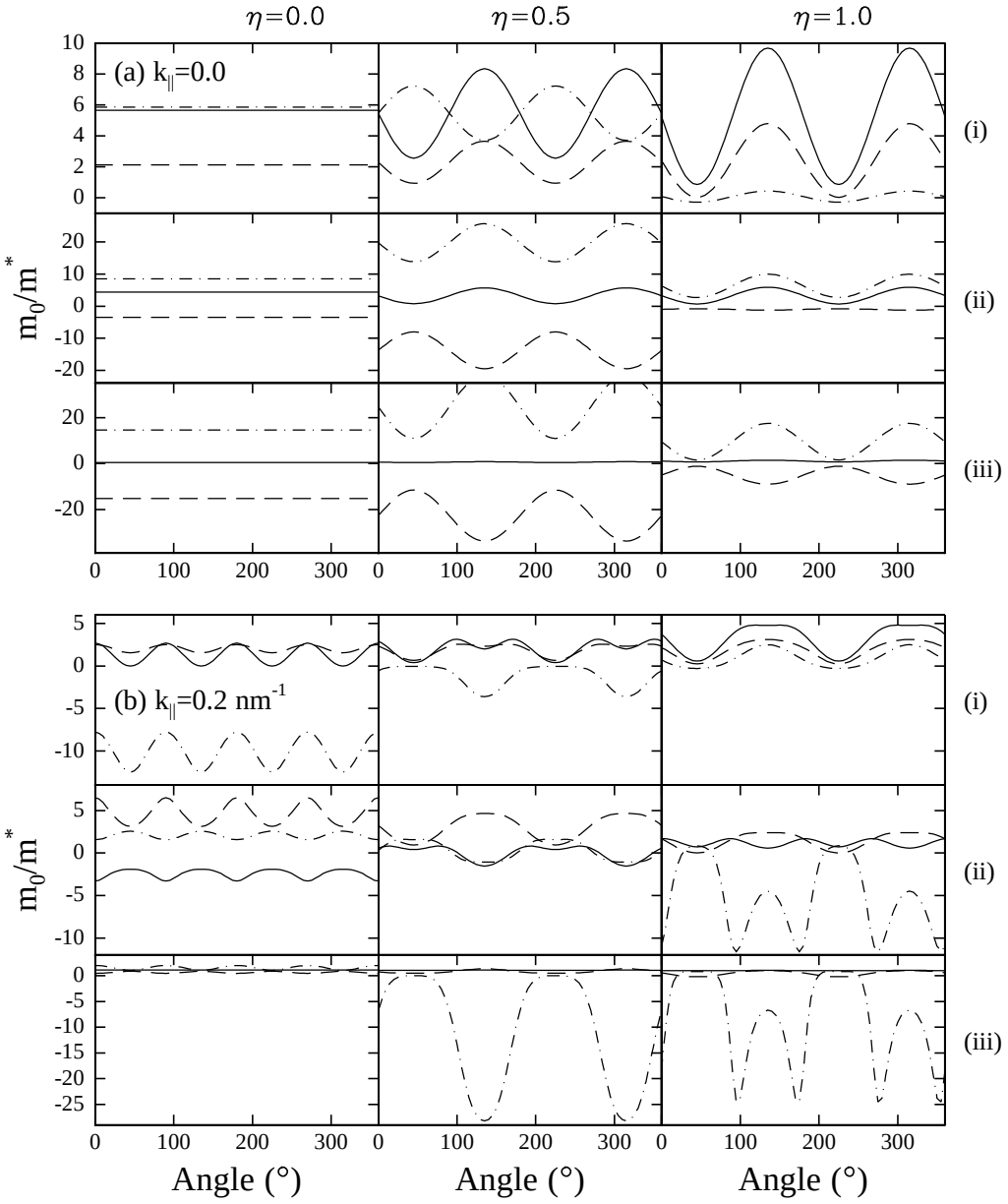

Figure 6.9: Ordering effect on the inverse effective mass of the first three subbands at (a) $k_{\|} = 0$ and (b) $k_{\|} = 0.2$ nm^{-1} for the QWs with Ga fraction $x_{\mathrm{Ga}} = 0.40$ (i), 0.514 (ii), and 0.63 (iii). Solid lines indicate the first subband, dashed the second and dash-dots the third.

the effective mass in the $(\bar{1}10)$ and $(1\bar{1}0)$ directions, in which effective-mass reaches its minimum, but increases the value in the other two directions. However, it significantly changes that of the second and especially the third subbands. The tendency of the change to the third subband (1hh as indicated above) is similar to that of the first subband in the compressive strain.

Figure. 6.10 shows the dependence of the band-edge ($k_{\|} = 0$) effec-

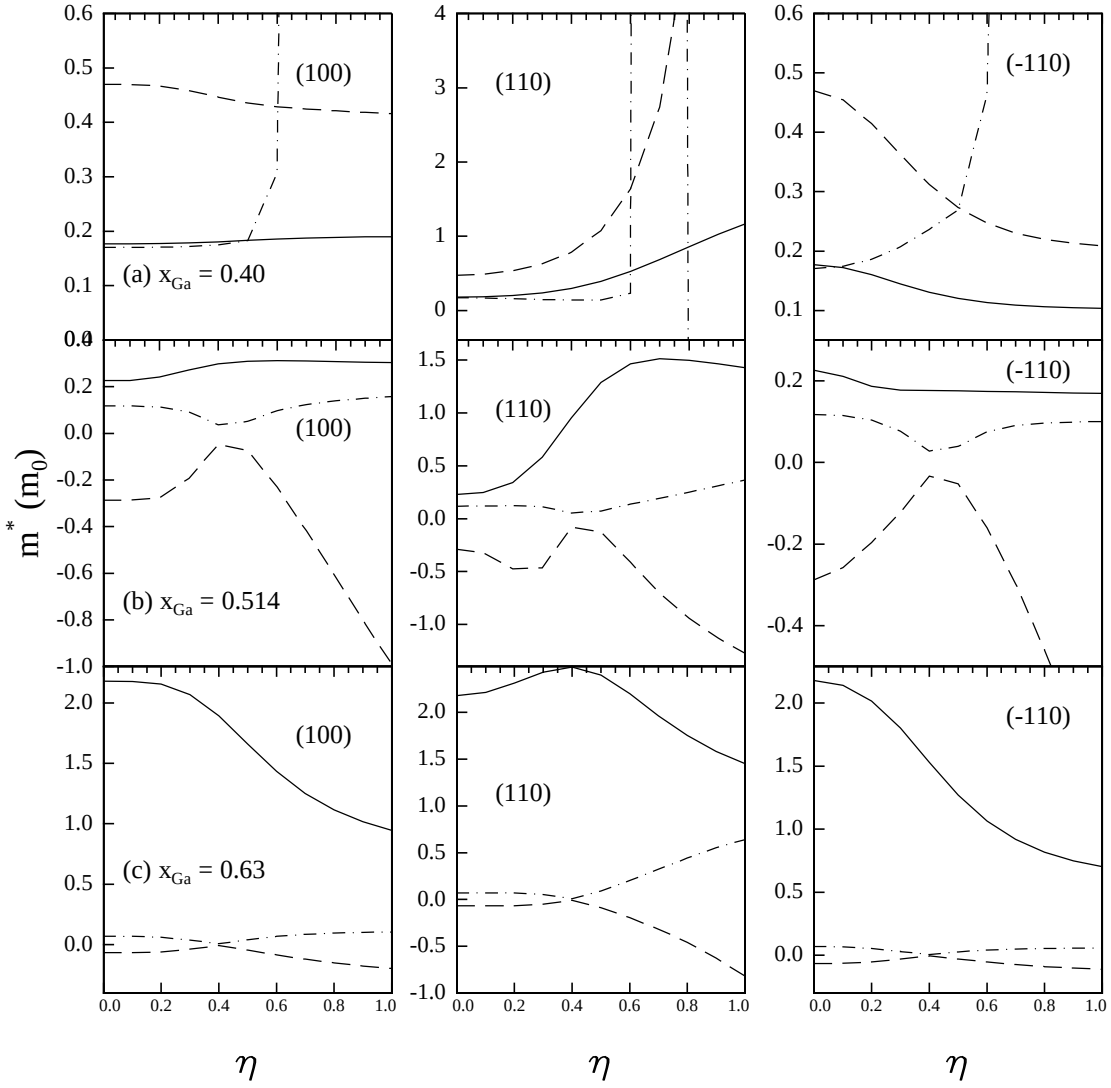

Figure 6.10: Ordering effect on band-edge effective mass in (100), (110), and ($\bar{1}$10) directions, for (a) compressive strain, (b) absence of strain, and (c) tensile strain. Solid lines indicate the first subband, dashed the second and dash-dots the third.

tive mass on the ordering in three special directions, (100), (110) and ($\bar{1}$10). Obviously, the ordering causes the effective masses of the first subband to increase in the (110) direction in a range of $0 \leq \eta \lesssim 0.4$. On the other hand, it results in a reduction to that of the first subband in the ($\bar{1}$10) direction. In the (100) direction, the ordering increases the hh subband effective mass for the compressive strain and absence of strain. It also increases that of the lh subband for the compressive strain, in contrast it slightly decreases that in the absence of strain and tensile strain. These effects are coincident with the interpreta-

tion of $[111]_B$ ordering as compressive strain along $(\bar{1}11)$ direction. Note that it is difficult to compare our results with those obtained by Zhang *et al.* [66], due to different coordinate systems was used and only $GaInP_2$ bulk alloy was treated there. Another remarkable feature herein is that the situation becomes very complicated for higher ordering, due to the enhanced band coupling which will be shown in Fig. 6.11 [see page 147].

Due to the warping effect caused by the ordering, we cannot use a single value of effective mass in one direction, say, $\mathbf{k_x}$, to explain particular experimental results from unpolarized magneto-PL, reflectivity, etc. For this purpose, an averaged value of the band-edge effective mass over angle in the $\mathbf{k_x}-\mathbf{k_y}$ plane is estimated, with the relation $1/m^*_{\rm av} = \oint(1/m^*)d\phi/\oint d\phi$.

To achieve our aim, we first have to make clear if the subband's order of the valence band changes with the ordering. In Fig. 6.11, the band-edge energies of the topmost four subbands are illustrated as a function of the ordering parameter η. Clearly, **(i)** for the compressive strain the first two subbands are 1hh and 2hh, respectively, and do not change their order as the ordering parameter gets larger. The third subband, however, is 1lh at $\eta \leq 0.6$, and will be 3hh as η gets larger. **(ii)** For the absence of strain, while the first subband is always 1hh, the second is 1lh at $\eta \leq 0.45$ and changes to 2hh for larger η. **(iii)** The change also happens to the tensile strain, where the second subband is 2hh for $\eta \leq$ and becomes 1hh for other η values. The first subband keeps to be 1lh.

Based on the established knowledge [66]:

1. The attraction between hh and lh subbands may play an important role. Soon as the ordering sets in, the hh effective mass may decrease as the induced coupling between the hh and lh gets stronger. Meanwhile, the coupling will make the lh effective mass increase;

2. For the tensile strain the coupling between the conduction band and the lh subband significantly affects the effective mass. As the band-gap reduces, the coupling gets stronger, which causes a reduction to the lh effective mass,

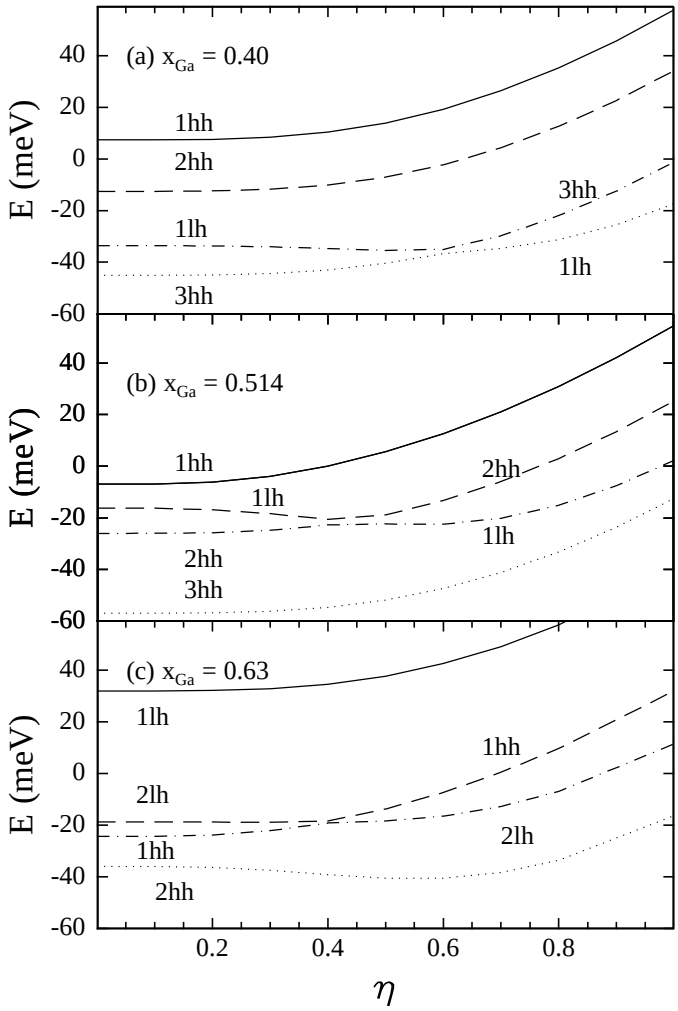

Figure 6.11: Band-edge energy as a function of the ordering parameter η for the (a) compressive strained $x_{\mathrm{Ga}} = 0.40$, (b) lattice-matched $x_{\mathrm{Ga}} = 0.514$, and (c) tensile strained $x_{\mathrm{Ga}} = 0.63$ $\mathrm{Ga}_x\mathrm{In}_{1-x}\mathrm{P}$/AlGaInP QWs.

the change of the valence-band effective mass can be predicted, from Fig. 6.11, as follows:

- For the compressive strain, as the energetic separation between the 1hh and 1lh subbands increases with the ordering η, the attraction between the two subbands is reduced, leading to a increase to the 1hh effective mass. As the separation between the 1lh and 3hh decreases in the range of $\eta \leq 0.6$, the 1lh effective mass is also expected to get larger in that η range.

- For the absence of strain, the 1lh lie between the 1hh and 2hh and the separation between the 1lh and 2hh first decreases in

the range of $\eta \leq 0.45$, and then increases for the larger η. The effective mass of the 1lh will therefore increase in the range of small η and decrease for the larger η. The separation between the 1hh and 1lh, on the other hand, gets enlarged in the whole η range as η increases. The effective mass of the 1hh is hence expected to slightly increase.

- For the tensile strain, the topmost subband is lh. As η increases the band-gap between the 1lh and the conduction band decreases, therefore the 1lh effective mass will decrease. Meanwhile, the separation between the 2lh and 1hh decreases as η increases in the range of $\eta \leq 0.4$, the 1hh effective mass in this η range will also decrease.

It is interesting to note that all these predictions are, in general, consistent with what the numerical result indicates. In Fig. 6.12, we depict the direction-averaged band-edge ($k_{\|} = 0$) effective mass is plotted as a function of the ordering parameter η for the absence of strain as well as compressive and tensile strain. It shows that **(i)** for the compressive strain, the averaged ordering effect on the 1hh and 1lh subbands at $\eta \leq 0.6$ is resulting in an increase to the effective mass, though it has different effect in the (110) and ($\bar{1}$10) direction; **(ii)** for the absence of strain, the 1hh still has a positive effective mass, which is a little larger than that of the compressive strain. As the ordering increases, the value increases. The 1lh, however, has a negative value, which increases with ordering only in a small region ($\eta \leq 0.45$). For $\eta \gtrsim 0.4$ it becomes positive and increases from a very small value; **(iii)** for the tensile strain, the 1lh has a large positive effective mass. As ordering increases, the value decreases. The 1hh subband, however, has a small positive value, which first decreases and begins to increase after $\eta \gtrsim 0.45$.

To make a comparison with the experimental data obtained in Chap. 5, we first notice that the experimentally determined reduced effective mass of the both the 1hh and 1lh exciton increases with the ordering for the compressively strained samples, which in a qualitative point of view agrees with the numerical results. For the drastic quantitative difference clearly shown in Fig. 6.12(a), in which black

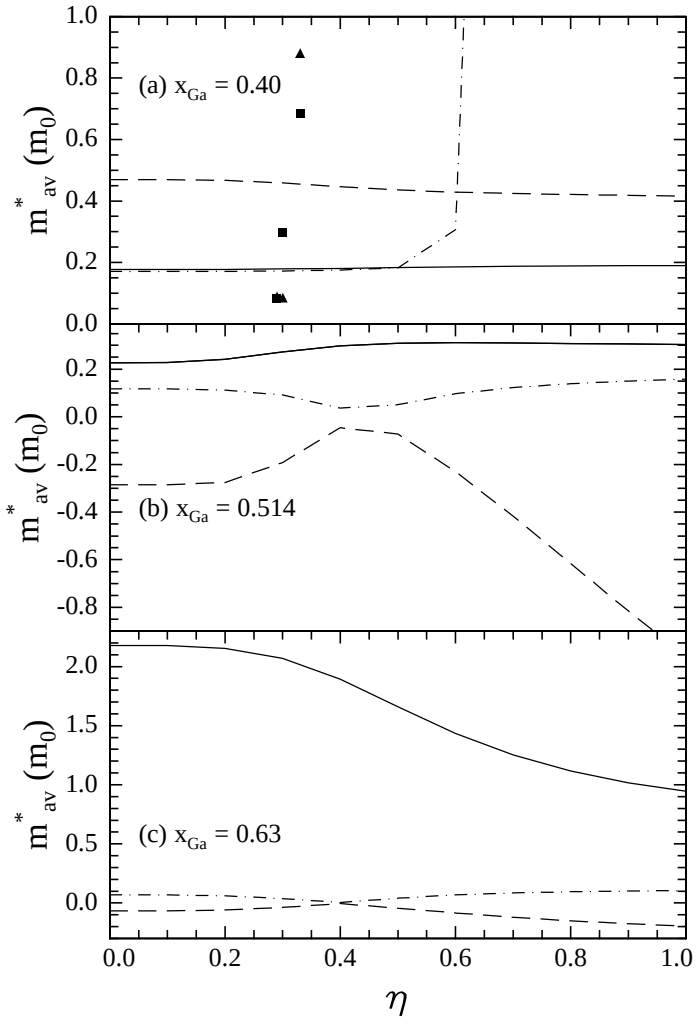

Figure 6.12: Direction-averaged band-edge ($k_{\|} = 0$) effective mass as a function of the ordering parameter η for the (a) compressive strain $x_{\mathrm{Ga}} = 0.40$, (b) absence of strain $x_{\mathrm{Ga}} = 0.514$, and (c) tensile strain $x_{\mathrm{Ga}} = 0.63$. Solid lines indicate the first subband, dashed the second and dash-dots the third. Black squares and triangles in (a) are deduced from the results of the PL and reflectivity study with $m_e^* = 0.088 m_0$.

squares and triangles represent the hole effective mass deduced from the reduced effective mass determined in the PL and reflectivity measurements with an electron effective mass m_e^*, $m_e = 0.088 m_0$, we first have to point out that the electron effective mass and its ordering-dependence is unknown in our work. Using 0.088 for m_e^* will certainly not lead to the **real** m_{hh}^* and/or m_{lh}^*. We also recall the discussion in Sec. 4.6.2 that to obtain a quantitative description of the valence-band effective with $\mathbf{k} \cdot \mathbf{p}$ simulation, appropriate Luttinger-Kohn parameters are called for, which are different from the values for the bulk

material and rely on advanced experiments. It is also possible that to determine the valence-band effective mass, the remote bands, e.g., $L-$point conduction band, may play a significant role

6.5 Conclusion

In this Chapter, an ordering-included 6-band $\mathbf{k}\cdot\mathbf{p}$ model has been established in an angle-explicit format, which enables a straightforward comparison of the difference caused by either or not using the axial approach. Numerical simulations were performed by using the finite-difference algorithm. The results indicate that the CuPt-type ordering in strained and lattice-matched quantum wells causes the topmost valence-subband to move upward. About 13% band-gap reduction due to the ordering is from such a upward-shift. This does not support the assumption widely used in the literature that type-II band alignment may be caused by ordering.

Intrinsic warping of the valence band, due to $\gamma_2 \neq \gamma_3$, is strong for compressive strain and absence of strain, especially for the heavy-hole subband, in the $Ga_xIn_{1-x}P$/AlGaInP QWs. It results in a maximum of the valence-band energy as well as band-edge effective mass occurring in the direction of $(2n+1)\times 45^\circ, n = 0, 1, 2, 3$. For tensile strain, the warping is nearly undetectable for the topmost valence subband.

The ordering causes further warping effect to the valence band. It acts as tensile strain along (110)-, and compressive strain along $(\bar{1}10)$-direction. The ordering-induced warping is also stronger in compressive strain and absence of strain, than in tensile strain. This enables the axial approach in the tensile strained, disordered or very low-level ordered $Ga_xIn_{1-x}P$/AlGaInP QWs, which may drastically reduce computational effort. On the other hand, the results suggest that a full 6-band problem should be numerically treated for compressively strained and lattice-matched $Ga_xIn_{1-x}P$/AlGaInP QWs.

For the valence-band effective mass, it has been shown that, the ordering causes the effective masses of the first subband to increase in the (110) direction in a range of $0 \leq \eta \lesssim 0.4$, and to decrease in the $(\bar{1}10)$ direction. The (in-plane) direction-averaged dependence of

effective mass upon ordering shows that, (i) For compressive strain, the 1hh effective mass increases and the 1lh effective mass is also expected to get larger in the range of $\eta \leq 0.6$. (ii) For absence of strain, the effective mass of the 1lh increases in the range of small η and decreases for the larger η. Meanwhile, the effective mass of the 1hh slightly increases. (iii) For tensile strain, the 1lh effective mass decreases, while the 1hh effective mass in the range of $\eta \leq 0.4$ will also decrease. A comparison was made with the experimental data obtained in Chap. 5, and a qualitative agreement was obtained. To obtain a quantitative description of the valence-band effective with $\mathbf{k} \cdot \mathbf{p}$ simulation, appropriate Luttinger-Kohn parameters are called for, which are different from the values for the bulk material and rely on advanced experiments.

List of Symbols

$\mathbf{A}$	vector potential
a_0	lattice constant of substrate
a_f	equilibrium lattice constant of quantum-well layer
a_{B}^*	effective Bohr radius
a_c, a_v	hydrostatic deformation potentials for conduction and valence band
B	magnetic field
b	shear deformation potential for a strain of tetragonal symmetry
C_{11}, C_{12}	stiffness constants
D'	second-order perturbation term describing the coupling between the conduction band and the SO valence subband
E_A	band-edge energy of quantum well
E_{b}, $E_{\mathrm{b}}^{\mathrm{hh}}$, $E_{\mathrm{b}}^{\mathrm{lh}}$	exciton binding energy, that of heavy-hole-, light-hole-exciton
E_c	conduction band energy
$E_{v,av}$	average valence band energy
$E_{\mathrm{hh}}, E_{\mathrm{lh}}, E_{\mathrm{so}}$	absolute energies for hh, lh, so valence subband
$E_A^{\mathrm{HH}}, E_A^{\mathrm{LH}}, E_A^{\mathrm{SO}}$	band-edge energies from hh, lh, so valence subband to conduction band
$E_{c,n}^z, E_{h,n}^z$	electron, hole energy level in finite quantum well
$E_{n,m}$	exciton diamagnetic energy
$\Delta E_{n,m}$	energy difference between $ne{-}m$hh transition and $1e-1$hh transition
ΔE_g	band-gap reduction due to ordering
$\Delta_{111}^o(\eta)$	crystal field splitting due to atomic ordering

Δ^{so}	spin-orbit splitting in absence of strain
E_g	band-gap energy of bulk material
E_{sp}	spin-splitting energy of the exciton resonance
e	electron, electron charge
$\epsilon_{\parallel}, \epsilon_{\perp}$	biaxial, uniaxial strain
ϵ_{ij}	component of strain tensor
ε_0	dielectric constant in vacuum
ε_r	relative permittivity in well or barrier layer
ε_ρ	lattice mismatch
η	ordering parameter
$F(\eta)$	distribution of the domains in ordered material
EMA	effective mass approximation
FTIR	Fourier transform infrared spectrometer
FWHM	full-width at half-maximum
γ	magnetic field of transverse-exciton units
$\gamma_1, \gamma_2, \gamma_3$	Luttinger-Kohn parameter
H	Hamiltonian operator
H_ϵ	strain Hamiltonian
H_k	Hamiltonian term for $\mathbf{k}\cdot\mathbf{p}$ disturbance
H_{so}	Hamiltonian term for spin-orbit interaction
$\hbar$	Plank constant
hh, lh, so	heavy-hole, light-hole, spin-orbit split-off
k	wave vector
LRO	long-range ordering
$L_{\mathrm{B}}, L_{\mathrm{W}}$	width of barrier or well layer
m	orbital quantum number

m_0	free electron mass
m_e^*, m_h^*	electron, hole effective mass
$m_{e,\rho}^*, m_{h,\rho}^*$	in-plane electron or hole effective mass
$m_{e,z}^*, m_{h,z}^*$	z-direction electron or hole effective mass
μ, $\mu_{\rm hh}$, $\mu_{\rm lh}$	reduced effective mass, that of heavy-hole-, light-hole-exciton
μ_B	Bohr magneton
μ_ρ	in-plane reduced effective mass
PL	photoluminescence
PLE	photoluminescence excitation
Q_c	conduction band-offset ratio
QW	quantum well
SODR	second-order derivative of reflectivity
R_y^*	effective Rydberg energy
ρ_{mat}	matching point in shorting method
T	temperature, in Kelvin (K)
$V_{e,0}$	well-potential for electron
$V_{\rm hh,0}, V_{\rm lh,0}, V_{\rm so,0}$	well-potential for hh, lh, and so
$x_{\rm Ga}$	Ga fraction in QW layer
$Z_s(z)$	confined-state envelope wave function of electron or hole

Bibliography

[1] J. Dalfors, T. Lundström, P. O. Holtz, H. H. Radamson, B. Monemar, J. Wallin, and G. Landgren, "The effective masses in strained InGaAs/InP quantum wells deduced from magnetoexcitation spectroscopy," Appl. Phys. Lett. **71,** 503 (1997).

[2] C. Wetzel, R. Winkler, M. Drechsler, B. K. M. U. Rössler, J. Scriba, J. P. Kotthaus, V. Härle, and F. Scholz, "Electron effective mass and nonparabolicity in $Ga_{0.47}In_{0.53}As$/InP quantum wells," Phys. Rev. B **53,** 1038 (1996).

[3] C. Wetzel, A. L. Efros, A. Moll, B. K. Meyer, P. Omling, and P. Sobkowicz, "Dependence on quantum confinement of the in-plane effective mass in $Ga_{0.47}In_{0.53}As$/InP quantum wells," Phys. Rev. B **45,** 14052 (1992).

[4] B. K. Meyer, M. Drechsler, C. Wetzel, V. Härle, F. Scholz, H. Linke, P. Omling, and P. Sobkowicz, "Composition dependence of the in-plane effective mass in lattice-mismatched, strained $Ga_{1-x}In_xAs$/InP single quantum wells," Appl. Phys. Lett. **63,** 657 (1993).

[5] K. Oettinger, T. Wimbauer, M. Drechsler, and B. K. Meyer, "Dispersion relation, electron and hole effective masses in $In_xGa_{1-x}As$ single quantum wells," J. Appl. Phys. **79,** 1481 (1996).

[6] M. Sugawara, N. Okazaki, T. Fujii, and S. Yamazaki, "Conduction-band and valence-band structures in strained $In_{1-x}Ga_xAs$/InP quantum wells on (001) InP substrates," Phys. Rev. B **48,** 8102 (1993).

[7] M. Sugawara, N. Okazaki, T. Fujii, and S. Yamazaki, "Diamagnetic shift and oscillator strength of two-dimensional excitons under a magnetic field in $In_{0.53}Ga_{0.47}As$/InP quantum wells," Phys. Rev. B **48,** 8848 (1993).

[8] C. Y.-P. Chao and S. L. Chuang, "Spin-orbit-coupling effects on the valence-band structure of strained semiconductor quantum wells," Phys. Rev. B **46,** 4110 (1992).

[9] M. Volk, S. Lutgen, T. Marschner, W. Stolz, and E. O. Göbel, "Carrier effective masses in symmetrically strained (GaIn)As/Ga(PAs) multiple-quantum-well structures," Phys. Rev. B **52,** 11096 (1995).

[10] E. D. Jones, S. K. Lyo, I. J. Fritz, J. F. Klem, J. E. Schirber, C. P. Tigges, and T. J. Drummond, "Determination of energy-band dispersion curves in strained-layer structures," Appl. Phys. Lett. **54,** 2227 (1989).

[11] A. Moritz, R. Wirth, S. Heppel, C. Geng, J. Kuhn, H. Schweizer, F. Scholz, and A. Hangleiter, "Intrinsic modulation bandwidth of strained GaInP/AlGaInP quantum well lasers," Appl. Phys. Lett. **71,** 650 (1997).

[12] R. W. Herrick and P. M. Petroff, "Improved reliability of red GaInP vertical-cavity surface-emitting lasers using bias-induced annealing," Appl. Phys. Lett. **72,** 1799 (1998).

[13] P. M. Smowton, P. Blood, and W. W. Chow, "Comparison of experimental and theoretical gain-current relations in GaInP quantum well lasers," Appl. Phys. Lett. **76,** 1522 (2000).

[14] C. T. H. F. Liedenbaum, A. Valster, A. L. G. J. Severens, and G. W. 't Hooft, "Determination of the GaInP/AlGaInP band offset," Appl. Phys. Lett. **57,** 2698 (1990).

[15] M. D. Dawson and G. Duggan, "Exciton localization effects and heterojunction band offset in (Ga,In)P-(Al,Ga,In)P multiple quantum wells," Phys. Rev. B **47,** 12598 (1993).

[16] O. P. Kowalski, J. W. Cockburn, D. J. Mowbray, M. S. Skolnick, R. Teissier, and M. Hopkinson, "GaInP-AlGaInP band offsets determined from hydrostatic pressure measurements," Appl. Phys. Lett. **66,** 619 (1995).

[17] M. D. Dawson and G. Duggan, "Band-offset determination for GaInP-AlGaInP structures with compressively strained quantum well active layers," Appl. Phys. Lett. **64,** 892 (1994).

[18] M. D. Dawson, G. Duggan, and D. J. Arent, "Optical measurements of electronic band structure in tensile strain (Ga,In)P-(Al,Ga,In)P quantum wells," Phys. Rev. B **51,** 17660 (1995).

[19] O. P. Kowalski, J. W. Cockburn, D. J. Mowbray, M. S. Skolnick, M. D. Dawson, G. Duggan, and A. H. Kean, "Hydrostatic-pressure determination of tensile-strained $Ga_xIn_{1-x}P$-$(Al_yGa_{1-y})_{0.52}In_{0.48}P$ quantum-well band offsets," Phys. Rev. B **53,** 10830 (1996).

[20] D. Kinder, S. L. Wong, A. N. Priest, R. J. Nicholas, G. Duggan, M. D. Dawson, S. P. Najda, and A. H. Kean, "Magneto-optical studies of compressively strained GaInP/AlGaInP multiple quantum wells," Solid-state Electronics **40,** 597 (1996).

[21] A. Zunger and S. Mahajan, in *Handbook of Semiconductors*, 2nd ed. (Elsevier, Amsterdam, 1994), Vol. 3, p. 1399, and references therein.

[22] E. P. O'Reilly, G. Jones, A. Ghiti, and A. R. Adams, "Improved performance due to suppression of spontaneous emission in tensile-strain semiconductor lasers," Electron. Lett. **27,** 1417 (1991).

[23] S.-H. Wei and A. Zunger, "Band gaps and spin-orbit splitting of ordered and disordered $Al_xGa_{1-x}As$ and $GaAs_xSb_{1-x}$ alloys," Phys. Rev. B **39,** 3279 (1989).

[24] S.-H. Wei and A. Zunger, "Band-gap narrowing in ordered and disordered semiconductor alloys," Appl. Phys. Lett. **56,** 662 (1990).

[25] D. B. Laks, S.-H. Wei, and A. Zunger, "Evolution of alloy properties with long-range order," Phys. Rev. Lett. **69,** 3766 (1992).

[26] S.-H. Wei, D. B. Laks, and A. Zunger, "Dependence of the optical properties of semiconductor alloys on the degree of long-range order," Appl. Phys. Lett. **62,** 1937 (1993).

[27] G. S. Horner, A. Mascarenhas, S. Froyen, R. G. Alonso, K. Bertness, and J. M. Olson, "Photoluminescence-excitation-spectroscopy studies in spontaneously ordered $GaInP_2$," Phys. Rev. B **47,** 4041 (1993).

[28] R. B. Capaz and B. Koiller, "Partial-ordering effects in $In_xGa_{1-x}P$," Phys. Rev. B **47,** 4044 (1993).

[29] S.-H. Wei and A. Zunger, "Strain effects on the spectra of spontaneously ordered $Ga_xIn_{1-x}P$," Appl. Phys. Lett. **64,** 757 (1994).

[30] S.-H. Wei and A. Zunger, "Optical properties of zinc-blende semiconductor alloys: Effects of epitaxial strain and atomic ordering," Phys. Rev. B **49,** 14337 (1994).

[31] P. Ernst, C. Geng, F. Scholz, H. Schweizer, Y. Zhang, and A. Mascarenhas, "Band-gap reduction and valence-band splitting of ordered $GaInP_2$," Appl. Phys. Lett. **67,** 2347 (1995).

[32] P. Ernst, C. Geng, G. Hahn, F. Scholz, H. Schweizer, F. Phillipp, and A. Mascarenhas, "Influence of domain size on optical properties of ordered $GaInP_2$," J. Appl. Phys. **79,** 2633 (1996).

[33] S. Kamiyama, T. Uenoyama, M. Mannoh, Y. Ban, and K. Ohnaka, "Theoretical analysis of valence subband structures and optical gain of GaInP/AlGaInP compressive strained-quantum wells," IEEE Photon. Technol. Lett. **4,** 439 (1993).

[34] X. H. Zhang, S. J. Chua, and W. J. Fan, "Band offsets at GaInP/AlGaInP(001) heterostructures lattice matched to GaAs," Appl. Phys. Lett. **73,** 1098 (1998).

[35] J. M. Luttinger and W. Kohn, "Motion of electrons and holes in pertubed periodic fields," Phys. Rev. **97,** 869 (1955).

[36] L. C. Andreani, A. Pasquarello, and F. Bassani, "Hole subbands in strained GaAs-$Ga_{1-x}Al_xAs$ quantum wells: Exact solution of the effective-mass equation," Phys. Rev. B **36,** 5887 (1987).

[37] D. Ahn, S. L. Chuang, and Y.-C. Chang, "Valence-band mixing effects on the gain and the refractive index change of quantum-well lasers," J. Appl. Phys. **64,** 4056 (1988).

[38] T. B. Bahder, "Eight-band $\mathbf{k} \cdot \mathbf{p}$ model of strained zinc-blende crystals," Phys. Rev. B **41,** 11992 (1990).

[39] S. L. Chuang, "Efficient band-structure calculations of strained quantum wells," Phys. Rev. B **43,** 9649 (1991).

[40] S. Kamiyama, T. Uenoyama, M. Mannoh, Y. Ban, and K. Ohnaka, "Analysis of GaInP/AlGaInP compressive strained multiple quantum well laser," IEEE J. Quantum Electron. **30,** 1363 (1994).

[41] S. Kamiyama, T. Uenoyama, M. Mannoh, and K. Ohnaka, "Theoretical studies of GaInP-AlGaInP strained quantum-well lasers including spin-orbit split-off band effect," IEEE J. Quantum Electron. **31,** 1409 (1995).

[42] K. Domen, H. Ishikawa, M. Sugawara, M. Kondo, and T. Tanahashi, "Effect of spin-orbit split-off band on optical gain in AlGaInP/GaInP strained quantum wells," Appl. Phys. Lett. **66,** 466 (1995).

[43] A. Moritz and A. Hangleiter, "Optical gain in ordered GaInP/AlGaInP quantum wells," Appl. Phys. Lett. **66,** 3340 (1995).

[44] A. Moritz, Ph.D. thesis, 4. Physikalisches Institut der Universität Stuttgart, 1997.

[45] R. S. Knox, "Theory of excitons," in *Solid State Physics* (Academic Press, New York, 1963), Vol. Supplement 5.

[46] G. Duggan, "Theory of heavy-hole magnetoexcitons in GaAs-(Al,Ga)As quantum-well heterostructures," Phys. Rev. B **37,** 2759 (1988).

[47] H. Haug and S. W. Koch, *Quantum Theory of the Optical and Electronic Properties of Semiconductors* (World Scientific, Singapore, 1993).

[48] S. E. Koonin, *Computational Physics* (The Benjamin/Cummings Publishing Company, Inc., Menlo Park, Califonia, 1986).

[49] C. G. van de Walle, "Band lineups and deformation potentials in the model-solid theory," Phys. Rev. B **39,** 1871 (1989).

[50] T. Y. Wang and G. B. Stringfellow, "Strain effects on $Ga_xIn_{1-x}As$/InP single quantum wells grown by organometallic vapor-phase epitaxy with $0 \leq x \leq 1$," J. Appl. Phys. **67,** 344 (1990).

[51] M. P. C. M. Krijn, "Heterojunction band offsets and effective masses in III-V quaternary alloys," Semicond. Sci. Technol. **6,** 27 (1991).

[52] C. Weisbuch and B. Vinter, *Quantum Semiconductor Structures* (Academic Press, INC, 1991).

[53] F. H. Pollak, in *Semiconductors and Semimetals* (Academic, New York, 1990), Vol. 32, Chap. 2.

[54] J. Shao, D. Haase, A. Dörnen, V. Härle, and F. Scholz, "Tensile strained InGaAs/InP multiple-quantum-well structures studied by magneto-optical spectroscopy," J. Appl. Phys. **87,** 4303 (2000).

[55] G. Reyher, Master's thesis, Universität Stuttgart, 1994.

[56] H. H. Perkampus, *UV-VIS Spectroscopy and Its Applications* (Springer-Verlag, 1992).

[57] G. Talsky, *Derivative Spectrophotometry* (VCH, Weinheim, Germany, 1994).

[58] P. Michler, A. Hangleiter, A. Moritz, G. Fuchs, V. Härle, and F. Scholz, "Direct-to-indirect energy-gap transition in strained $Ga_xIn_{1-x}As/InP$ quantum wells," Phys. Rev. B **48,** 11991 (1993).

[59] V. Härle, H. Bolay, E. Lux, P. Michler, A. Moritz, T. Forner, A. Hangleiter, and F. Scholz, "Indirect-band-gap transition in strained GaInAs/InP quantum-well structures," J. Appl. Phys. **75,** 5067 (1994).

[60] J. Ringling, Y. Kawamura, L. Schrottke, H. T. Grahn, K. Yoshimatsu, A. Kamada, and N. Inoue, "Direct evidence of the indirect energy gap in InAlAs/AlAsSb multiple quantum wells by time-resolved photoluminescence," Appl. Phys. Lett. **72,** 1620 (1998).

[61] P. Ernst, C. Geng, F. Scholz, and H. Schweizer, "Ordering in $GaInP_2$ studied by optical spectroscopy," Phys. Stat. Sol. (b **193,** 213 (1996).

[62] M. C. DeLong, W. D. Ohlsen, I. Viohl, P. C. Taylor, and J. M. Olson, "Evidence for spatially indirect recombination in $Ga_{0.52}In_{0.48}P$," J. Appl. Phys. **70,** 2780 (1991).

[63] J.-R. Dong, Z.-G. Wang, X.-L. Liu, D.-C. Lu, D. Wang, and X.-H. Wang, "Photoluminescence of ordered $Ga_{0.5}In_{0.5}P$ grown by metalorganic vapor phase epitaxy," Appl. Phys. Lett. **67,** 1573 (1995).

[64] M. J. Gregor *et al.*, "Near-field optical characterization of the photoluminescence from partially ordered (GaIn)P," Appl. Phys. Lett. **67,** 3572 (1995).

[65] H. M. Cheong, A. Mascarenhas, S. P. Ahrenkiel, K. M. Jones, J. F. Geisz, and J. M. Olson, "Effect of microstructure on excitonic luminescence of spontaneously ordered $Ga_{0.52}In_{0.48}P$ alloys," J. Appl. Phys. **83,** 5418 (1998).

[66] Y. Zhang and A. Mascarenhas, "Conduction- and valence-band effective masses in spontaneously ordered $GaInP_2$," Phys. Rev. B **51,** 13162 (1995).

[67] D. Gershoni, H. Temkin, M. B. Panish, and R. A. Hamm, "Excitonic transitions in strained-layer $In_xGa_{1-x}As/InP$ quantum wells," Phys. Rev. B **39,** 5531 (1989).

[68] L. V. Butov, V. D. Kulakovskii, E. Lach, A. Forchel, and D. Grützmacher, "Magnetoluminescence study of many-body effects in homogeneous quasi-two-dimensional electron-hole plasma in undoped $In_xGa_{1-x}As/InP$ single quantum wells," Phys. Rev. B **44,** 10680 (1991).

[69] J. C. Ryan and T. L. Reinecke, "Band-gap renormalization of optically excited semiconductor quantum wells," Phys. Rev. B **47,** 9615 (1993).

[70] J. Dalfors, T. Lundström, P. O. Holtz, H. H. Radamson, B. Monemar, J. Wallin, and G. Landgren, "The electronic structure of InGaAs/InP quantum wells measured by Fourier transform photoluminescence excitation spectroscopy," J. Appl. Phys. **80,** 6855 (1996).

[71] V. Härle *et al.*, "Determination of the in-plane mass in strained GaInAs/InP quantum wells," In *Proceedings of the International Conference on Indium Phosphide and Related Compounds*, p. 221 (Sapporo, Japan, 1995).

[72] D. K. Sengupta *et al.*, "*p*-type InGaAs/InP quantum well infrared photodetector with peak response at 4.55 μm," Appl. Phys. Lett. **69,** 3209 (1996).

[73] K. Ogawa and Y. Matsui, "Time-frequency spectroscopy of an InGaAs/InP quantum-well exciton Bragg reflector," Appl. Phys. Lett. (1999).

[74] S. D. Gunapala, B. F. Levine, D. Ritter, R. A. Hamm, and M. B. Panish, "InGaAs/InP hole intersubband normal incidence quantum well infrared photodetector," J. Appl. Phys. **71,** 2458 (1992).

[75] M. Sugawara, "Theoretical calculation of optical gain in $In_xGa_{1-x}As/InP$ quantum wells under biaxially compressive and tensile strain," Appl. Phys. Lett. **60,** 1842 (1992).

[76] P. J. A. Thijs, In *Digest of the 13th IEEE International semiconductor laser conference*, p. 2 (1992).

[77] S. S. Ou, J. J. Yang, R. J. Fu, and C. J. Hwang, "High-power 630-640 nm GaInP/GaAlInP laser diodes," Appl. Phys. Lett. **61,** 892 (1992).

[78] J. A. Lott and J. R. P. Schneider, "Electrically injected visible (639-661 nm) vertical cavity structure emitting lasers," Electron. Lett. **29,** 830 (1993).

[79] T. Katsuyama, I. Yoshida, J. Shinkai, J. Hashimoto, and H. Hayashi, "Very low threshold current $AlGaInP/Ga_xIn_{1-x}P$ strained single quantum well visible laser diode," Electron. Lett. 26 (1990).

[80] A. Valster, C. J. van de Poel, M. N. Finke, and M. J. B. Boermans, In *Digest of 13th IEEE International Semiconductor Laser Conference*, p. 152 (1992).

[81] J. R. P. Schneider, R. P. Bryan, E. D. Jones, and J. A. Lott, "Excitonic transitions in InGaP/InAlGaP strained quantum wells," Appl. Phys. Lett. **63,** 1240 (1993).

[82] O. P. Kowalski, J. W. Cockburn, D. J. Mowbray, M. S. Skolnick, R. Teissier, and M. Hopkinson, "GaInP-AlGaInP band offsets determined from hydrostatic pressure measurements," Appl. Phys. Lett. **66,** 619 (1995).

[83] J. Shao, A. Dörnen, D. Haase, E. Baars, V. Härle, and F. Scholz, submitted to Phys. Rev. B (unpublished).

[84] J. Shao, A. Dörnen, R. Winterhoff, and F. Scholz, submitted to Phys. Rev. B (unpublished).

[85] J. Shao, A. Dörnen, R. Winterhoff, and F. Scholz, "Effective mass and exciton binding energy in ordered (Al)GaInP quantum wells evaluated by derivative of reflectivity," J. Appl. Phys. **91,** 2553 (2002).

[86] E. I. Rashba and M. D. Sturge, in *Excitons*, Vol. 2 of *Modern problems in condensed matter sciences*, V. M. Agranovich and A. A. Maradudin, eds., (North-Holland Publishing Company, New York, 1982).

[87] *Numerical Data and Functional Relationship in Science and Technology*, Vol. 17a of *New Series, Group III*, landolt-börnstein ed., K. H. Hellwege, ed., (Springer, Berlin, 1982).

[88] G. Bastard, J. A. Brum, and R. Ferreira, in *Solid State Physics* (Academic, New York, 1991), Vol. 44, p. 229.

[89] C. G. van de Walle and R. M. Martin, "Theoretical calculations of heterojunction discontinuities in the Si/Ge system," Phys. Rev. B **34,** 5621 (1986).

[90] C. G. van de Walle and R. M. Martin, "Theoretical study of band offsets at semiconductor interfaces," Phys. Rev. B **35,** 8154 (1987).

[91] S. Satpathy, R. M. Martin, and C. G. van de Walle, "Electronic properties of the (100) (Si)/(Ge) strained-layer superlattices," Phys. Rev. B **38,** 13237 (1988).

[92] K. H. Goetz, D. Bimberg, H. Jürgensen, J. Selders, A. V. Solomonov, G. F. Glinski, and M. Razeghi, "Optical and crystallographic properties and impurity incorporation of $Ga_xIn_{1-x}As$ ($0.44 < x < 0.49$) grown by liquid phase epitaxy, vapor phase epitaxy, and metal organic chemical vapor deposition," J. Appl. Phys. **54,** 4543 (1983).

[93] K. S. Lee, Y. Aoyagi, and T. Sugano, "Modified perturbational method for the magnetoexciton ground state in quantum wells," Phys. Rev. B **46,** 10269 (1992).

[94] R. L. Greene and K. K. Bajaj, "Binding energies of Wannier excitons in GaAs-$Ga_{1-x}Al_xAs$ quantum well structures," Solid State Commun. **45,** 831 (1983).

[95] X. L. Zheng, D. Heiman, and B. Lax, "Magnetoexciton ground state in a quantum well: A variational and perturbation approach," Phys. Rev. B **40,** 10523 (1989).

[96] L. Viña, G. E. W. Bauer, M. Potemski, J. C. Maan, E. E. Mendez, and W. I. Wang, "Term spectrum of magnetoexcitons in quasi-two-dimensional systems," Phys. Rev. B **41,** 10767 (1990).

[97] L. Viña, L. Muñoz, N. Mestres, E. S. Koteles, A. Ghiti, E. P. O'Reilly, D. C. Bertolet, and K. M. Lau, "Valence-band-shape modification due to band coupling in strained quantum wells," Phys. Rev. B **47,** 13926 (1993).

[98] F. H. Pollak, "Modulation spectroscopy under uniaxial stress," Surface Science **37,** 863 (1973).

[99] A. Niwa, T. Ohtoshi, and T. Kuroda, "Orientation dependence of optical properties in long wavelength strained quantum-well lasers," IEEE J. Select. Topic. Quant. Electron. **1,** 211 (1995).

[100] C.-S. Chang and S.-L. Chuang, "Modeling of strained quantum-well lasers with spin-orbit coupling," IEEE J. Select. Topic. Quant. Electron. **1,** 218 (1995).

[101] G. A. Baraff and D. Gershoni, "Eigenfunction-expansion method for solving the quantum-wire problem: Formulation," Phys. Rev. B **43,** 4011 (1991).

[102] W. H. Press, S. A. Teukolsky, W. T. Vetterling, and B. P. Flannery, *Numerical Recipes in Fortran: The Art of Scientific Computing*, 2nd ed. (Cambridge University Press, 1992).

[103] U. Ekenberg, "Quantum well enhancement of nonparabolicity effects on the effective electron mass," J. de Phys. **48,** 207 (1987).

[104] S. Smith, H. M. Cheong, B. D. Fluegel, J. F. Geisz, J. M. Olson, L. L. Kazmerski, and A. Mascarenhas, "Spatially resolved photoluminescence in partially ordered $GaInP_2$," Appl. Phys. Lett. **74,** 706 (1999).

[105] T. Kippenberg, J. Krauss, J. Spieler, P. Kiesel, G. H. Döhler, R. Stubner, R. Winkler, O. Pankratov, and M. Moser, "L-point backfolding in ordered $GaInP_2$ determined by electroabsorption," Phys. Rev. B **60,** 4446 (1999).

[106] S.-H. Wei and A. Zunger, "Fingerprints of CuPt ordering in III-V semiconductor alloys: Valence-band splittings, band-gap reduction, and x-ray structure factors," Phys. Rev. B **57,** 8983 (1998).

[107] J. S. Luo, J. M. Olson, S. R. Kurtz, D. J. Arent, K. A. Bertness, M. E. Raikh, and E. V. Tsiper, "Optical anisotropy and spontaneous ordering in $Ga_{0.5}In_{0.5}P$: An investigation using reflectance-difference spectroscopy," Phys. Rev. B **51,** 7603 (1995).

[108] S.-H. Wei, A. Franceschetti, and A. Zunger, "E_1, E_2, and E_0' transitions and pressure dependence in ordered $Ga_{0.5}In_{0.5}P$," Phys. Rev. B **51,** 13097 (1995).

[109] G. Schmiedel, P. Kiesel, G. H. Döhler, E. Greger, K. H. Gulden, H. P. Schweizer, and M. Moser, "Electroabsorption in ordered and disordered GaInP," J. Appl. Phys. **81,** 1008 (1997).

[110] T. Mattila, S.-H. Wei, and A. Zunger, "Electronic Structure of "Sequence Mutations" in Ordered $GaInP_2$ Alloys," Phys. Rev. Lett. **83,** 2010 (1999).

[111] R.Wirth, H. Seitz, M. Geiger, F. Scholz, A. Hangleiter, A. Mühe, and F. Phillipp, "Single variant ordering in GaInAs/InP," Appl. Phys. Lett. **71,** 2127 (1997).

[112] R.Wirth, H. Seitz, M. Geiger, J. Porsche, F. Scholz, and A. Hangleiter, "Valence-band splitting and band-gap reduction in ordered GaInAs/InP," J. Appl. Phys. **83,** 6196 (1998).

[113] H. M. Cheong, A. Mascarenhas, J. F. Geisz, J. M. Olson, M. W. Keller, and J. R. Wendt, "Statistical distribution of the order parameter in spontaneously ordered $Ga_{0.52}In_{0.48}P$ alloys," Phys. Rev. B **57,** R9400 (1998).

[114] P. Ernst, Y. Zhang, F. A. J. M. Driessen, A. Mascarenhas, E. D. Jones, C. Geng, F. Scholz, and H. Schweizer, "Magnetoluminescence study on the effective mass anisotropy of $CuPt_B$-ordered $GaInP_2$ alloys," J. Appl. Phys. **81,** 2814 (1997).

[115] P. Emanuelsson, M. Drechsler, D. M. Hofmann, B. K. Meyer, M. Moser, and F. Scholz, "Cyclotron resonance studies of GaInP and AlGaInP," Appl. Phys. Lett. **64,** 2849 (1994).

[116] A. Franceschetti, S.-H. Wei, and A. Zunger, "Effects of ordering on the electron effective mass and strain deformation potential in $GaInP_2$: Deficiencies of the $\mathbf{k} \cdot \mathbf{p}$ model," Phys. Rev. B **52,** 13992 (1995).

[117] S. Froyen, A. Zunger, and A. Mascarenhas, "Polarization fields and band offsets in GaInP/GaAs and ordered/disordered GaInP superlattices," Appl. Phys. Lett. **68,** 2852 (1996).

[118] C. Geng, Ph.D. thesis, University of Stuttgart, 1997.

[119] *Advances in Applied Fourier Transform Infrared Spectroscopy*, M. W. Mackenzie, ed., (John Wiley & Sons, 1988).

[120] B. C. Smith, *Fundamentals of Fourier Transform Infrared Spectroscopy* (CRC Press, Inc., 1996).

[121] R. Williams, *Spectroscopy and the Fourier Transform: An interactive tutorial* (VCH, New York, 1996).

[122] *Spectrometric Techniques*, G. A. Vanasse, ed., (Academic Press, Inc., New York, 1981), Vol. II.

[123] T. S. Moss, G. J. Burrell, and B. Ellis, *Semiconductor Optoelectronics* (Butterworths, London, 1973).

[124] E. P. O'Reilly, "Valence band engineering in strained-layer structures," Semicond. Sci. Technol. **4,** 121 (1989).

[125] V. Härle, Ph.D. thesis, Universität Stuttgart, 1995.

[126] R. Dingle, W. Wiegmann, and C. H. Henry, "Quantum states of confined carriers in very thin $Al_xGa_{1-x}As$-GaAs-$Al_xGa_{1-x}As$ heterostructures," Phys. Rev. Lett. **33,** 827 (1974).

[127] R. C. Miller, D. A. Kleinman, J. W. A. Nordland, and A. C. Gossard, "Luminescence studies of optically pumped quantum wells in GaAs-$Al_xGa_{1-x}As$ multilayer structures," Phys. Rev. B **22,** 863 (1980).

[128] R. C. Miller, D. A. Kleinman, O. Munteanu, and W. T. Tsang, "New transitions in the photoluminescence of GaAs quantum wells," Appl. Phys. Lett. **39,** 1 (1981).

[129] S. K. Lyo, E. D. Jones, and J. F. Klem, "Breaking of the usual selection rule for magnetoluminescence in doped semiconductor quantum wells," Phys. Rev. Lett. **61,** 2265 (1988).

[130] V. Swaminathan and A. T. Macrander, *Materials Aspects of GaAs and InP Based Structures* (Prentice Hall, Englewood Cliffs, New Jersey, 1991).

[131] M. Sugawara, "Magnetic-field-induced enhancement of exciton oscillator strength in $In_{0.53}Ga_{0.47}As$/InP quantum wells," Phys. Rev. B **45,** 11423 (1992).

[132] T. Tanaka, Z. L. Zhang, M. Nishioka, and Y. Arakawa, "Magnetic field dependence of exciton oscillator strength by measurements of magnetoexciton-polariton mode splitting in quantum wells with a microcavity," Appl. Phys. Lett. **69,** 887 (1996).

[133] *A triangular filter function having its cutoff point at 60% towards the end of the corresponding interferogram is used.*

[134] F. Ancilotto, A. Fasolino, and J. C. Mann, "Hole-subband mixing in quantum wells: A magnetooptic study," Phys. Rev. B **38,** 1788 (1988).

[135] P. Lawaetz, "Valence-band parameters in cubic semiconductors," Phys. Rev. B **4,** 3460 (1971).

[136] C. Geng, M. Moser, R. Winterhoff, E. Lux, J. Hommel, B. Höhing, H. Schweizer, and F. Scholz, "Ordering in strained $Ga_xIn_{1-x}P$ quantum wells grown by metalorganic vapor phase epitaxy," J. Cryst. Growth **145,** 740 (1994).

[137] J. W. Matthews and A. E. Blakeslee, "Defects in epitaxial multilayers, *I. Misfit dislocations*," J. Cryst. Growth **27,** 118 (1974).

[138] J. H. van der Merve and W. A. Jesser, "An exactly solvable model for calculating critical misfit and thickness in epitaxial superlattices: Layers of equal elastic constants and thicknesses," J. Appl. Phys. **63,** 1509 (1988).

[139] W.-M. Zhou, M. Dutta, D. D. Smith, J. Pamulapati, H. Shen, P. Newman, and R. Sacks, "Magneto-optical studies of strain effects on the excitons in $In_xGa_{1-x}As/Al_yGa_{1-y}As$ strained quantum wells," Phys. Rev. B **48,** 5256 (1993).

[140] B. V. Shanabrook, O. J. Glembocki, , and W. T. Beard, "Photoreflectance modulation mechanisms in GaAs-$Al_xGa_{1-x}As$ multiple quantum wells," Phys. Rev. B **35,** 2540 (1987).

[141] A. F. Terzis, X. C. Liu, A. Petrou, B. D. McCombe, M. Dutta, H. Shen, D. D. Smith, M. W. Cole, M. Taysing-Lara, and P. G. Newman, "Line-shape analysis of reflectance spectra from GaAs/AlAs multiple-quantum-well structures," J. Appl. Phys. **67,** 2501 (1990).

[142] Y. Ishitani, S. Minagawa, T. Kita, T. Nishino, H.Yaguchi, and Y. Shiraki, "The optical processes in AlInP/GaInP/AlInP quantum wells," J. Appl. Phys. **80,** 4592 (1996).

[143] S. H. Kwok, P. Y. Yu, J. Zeman, S. Jullian, G. Martinez, and K. Uchida, "Optical studies of GaInP(ordered)/GaAs and GaInP(ordered)/GaP/GaAs heterostructures," J. Appl. Phys. **84,** 2846 (1998).

[144] M. Bayer, A. A. Dremin, V. D. Kulakovskii, A. Forchel, F. Faller, P. A. Knipp, and T. L. Reinecke, "Coupling of geometric confinement and magnetic confinement in $In_{0.09}Ga_{0.91}As$/GaAs quantum wells in magnetic fields with varying orientations," Phys. Rev. B **52,** 14728 (1995).

[145] J. Shao, A. Dörnen, R. Winterhoff, E. Baars, and F. Scholz (unpublished).

[146] F. Scholz, C. Geng, M. Burkard, H.-P. Gauggel, H. Schweizer, R. Wirth, A. Moritz, and A. Hangleiter, "Ordering in GaInP: Is it relevant for devices?," Physica E **2,** 8 (1998).

[147] private communication from Achim Dörnen.

[148] S. Seki, T. Yamanaka, W. Lui, Y. Yoshikuni, and K. Yokoyama, "Theoretical analysis of pure effects of strain and quantum confinement on differential gain in InGaAsP/InP strained-layer quantum-well lasers," IEEE J. Quantum Electron. **30,** 500 (1994).

[149] D. Ahn and S. L. Chuang, "The theory of strained-layer quantum-well lasers with bandgap renormalization," IEEE J. Quantum Electron. **30,** 350 (1994).

[150] *Numerical Data and Functional Relationship in Science and Technology*, Vol. 22a of *New Series, Group III-V*, landolt-börnstein ed., K. H. Hellwege, ed., (Springer, Berlin, 1986).

[151] *Properties of Indium Phosphide*, No. 6 in *EMIS Datareviews Series* (The Institution of Electrical Engineers, New York, 1991).

Curriculum Vitæ

Jun Shao

Born on May 19, 1965 in Jiangsu, China, married Jing Huang with one daughter. Parents: Xingzi Shao and Shanrong Liu.

02/72 – 07/82	Primary/High school, Ganyu, Jiangsu, China.
09/82 – 07/86	Study of **radio physics and Electronics** in Nanjing University, China. **Bachelor of Science**.
09/86 – 06/89	Study of **Acoustics** in the *Institute of Acoustics*, Nanjing University, supervised by Prof. G. R. Sun. **Master thesis**: *Modulation-Transfer-Function method for estimating speech intelligibility in communications.*
06/1989	**Master of Science** .
07/89 – 08/94	**Lecturer** on electronics & fundamental physics, Huaihai University, Lianyungang, China.
09/94 – 05/96	Study **toward PhD** in the *Institute of Acoustics*, Nanjing University, supervised by Prof. J. Z. Sha. Aim: *actively controlled acoustical noise barrier.*
06/96 – 09/96	Language (German) training in the *Goethe-Institut* in Mannheim, Germany.
10/1996–	Study **toward PhD** in the *4. Physikalisches Institut*, Universität Stuttgart, supervised by Prof. Dr. M. H. Pilkuhn and PD Dr. A. Dörnen.
01/2001	**Diplomarbeit** entitled *Optical and magneto-optical study of ZnTe:Ti^{3+}*, supervised by PD Dr. A. Dörnen.
05/2001	**Hauptdiplom Prüfungsgespräch** (oral exam) with Prof. Dr. Mahler and Prof. Dr. Schweitzer.

Danksagung

An dieser Stelle möchte ich allen, die zum Gelingen dieser Arbeit beigetragen haben, herzlich danken.

Mein besonderer Dank gilt Herrn Priv. Doz. Dr. A. Dörnen, der mich und meine Arbeit auf vielfältige Weise betreuet und gefördert hat, insbesondere in einer schwierigen Anfangszeit. Mit seinem Enthusiasmus und seiner Improvisationsgabe konnte er mich immer wieder neu für die Physik begeistern.

Herrn Prof. Dr. M. H. Pilkuhn danke ich für die Aufnahme in sein herausragendes Institut und die mir gebotenen Arbeitsmöglichkeiten.

Herrn Prof. Dr. G. Denninger danke ich für die Übernahme des Mitberichts.

Eine Einführung in die experimentellen Grundlagen habe ich von Dr. B. Kaufmann und Dr. D. Haase erhalten, von denen ich in der Anfangsphase der Arbeit vieles gelernt habe.

Besonders danken möchte ich den Mitgliedern meiner Arbeitsgruppe: Dr. Berthold Kaufmann, Dr. Dieter Haase, Enno Baas, Cordula Kersten und Anne Hasenkopf für das freundschaftliche Arbeitsklima und vielerlei Hilfen.

Neben vielen anderen Institutsmitgliedern möchte ich besonders Enno Baars, Anne Hasenkopf, Liwei Fu, und Feng Gao für mancherlei Diskussionen und Hilfestellungen danken.

Für die Herstellung und die Präparation der Proben danke ich Dr. F. Scholz, Dr. V. Härle und Dr. R. Winterhoff.

Ganz besonders bedanken möchte ich mich bei meiner Frau für ihr Verständnis, und bei meinen Eltern danken, die mir das Studium ermöglichten.

Die finanzielle Förderung dieser Arbeit erfolgte aus Doktoranden Programm für Chinesische Physiker der Volkswagen-Stiftung und des Deutschen Akadamischen Austaushdienstes (DAAD).